MOLECULAR ASSEMBLY BASED NANO-COMPOSITE STRUCTURES FOR MEMORY APPLICATIONS

RAJU KUMAR GUPTA

NATIONAL UNIVERSITY OF SINGAPORE

2010

MOLECULAR ASSEMBLY BASED NANO-COMPOSITE STRUCTURES FOR MEMORY APPLICATIONS

RAJU KUMAR GUPTA
(B. Tech., Indian Institute of Technology, Roorkee)

A THESIS SUBMITTED
FOR THE DEGREE OF DOCTOR OF PHILOSOPHY
DEPARTMENT OF CHEMICAL & BIOMOLECULAR ENGINEERING
NATIONAL UNIVERSITY OF SINGAPORE

2010

Dedicated to my mother and my father,

the two most important people in my life,

for their endless love and support.

Acknowledgements

The research work presented in this thesis was carried out at Department of Chemical and Biomolecular Engineering, National University of Singapore during the period January 2006 – January 2010. When I look back on my four years at NUS, I realize how time flies. It was a very valuable and fruitful period for me, although of course at times I struggled with obstacles and failures. I have learned and experienced many things at NUS. The completion of this research was in large part due to the support of many people. I would like to acknowledge some people who have made a major contribution in completing my Ph.D.

First and foremost, my heartfelt thanks and my deepest appreciation to my supervisor, Assoc. Prof. Srinivasan Madapusi, P for his incalculable guidance and direction throughout this research work. It is him who led me to the field of organic electronics. His patience and timely advice, continuous encouragement and confidence provided me an inspiration to complete my research work with prolific mode. His constructive criticisms and numerous suggestions have helped me a lot in getting the thesis in present form. This thesis would have been a distant goal without his support, direction and encouragement. His patience and kind understanding has motivated and spurred me through the long and arduous experiments. Constant words of encouragement, support, and the invaluable academic interaction which has guided me from the various “dead-ends” of the project are duly acknowledged. He is also my learning models of the scientific spirits and positive attitude.

Heartfelt thanks to Dr. Sivashankar Krishnamoorthy from Institute of Materials Research and Engineering (IMRE), Singapore for his fruitful technical discussions as well as encouragement for my future academic career.

My sincere thanks to Assoc. Prof. Pooi See, LEE from School of Materials Science and Engineering, NTU, Dr. AKKIPEDDI Ramam from IMRE, Singapore, Dr. Jianyong Ouyang from Department of Materials Science and Engineering, NUS and Dr. Nalam Satyanarayana from Mechanical Engineering department, NUS for their valuable advices and timely assistance throughout my research.

Due acknowledgement has been made of the research work done by others in the literature on the organic nonvolatile memory devices over the years, by referring them appropriately in the respective Chapters of the Thesis. Due to vast amount of literature on the topic of the Thesis, it has not been possible to quote all the available references and any omissions are due to oversight or to error in judgment, which may be condoned.

Special thanks to all research staff and lab officers Dr. Rajarathnam, Mr. Rajamohan, Mr. Chia, Ms. Samantha, Mr. Mao Ning, Ms. Chai Keng, Ms. Novel, Ms. Yanfang, Ms. Tay Kaisi, Mr. Boey and Dr. Yuan for their help and understanding. I would like to express my profound thanks to my lab seniors Dr. Zhang Fengxiang and Dr. Sreenivasa Reddy Puniredd, my lab mates Yeong Sai Hooi, Sundaramurthy Jayaraman, Huang Meiyu Stella, Ng Su Peng, Vignesh Suresh, Zhou Ruitao and all my FYP students for rendering their continuous help and for involving directly or indirectly in my research work.

My heartiest appreciation to all my friends Bipin Kumar, Yogesh Sharma, Mohan Singh Dhoni, Vishal Sharma, Balaji Parasumanna Gokulan, Atul D Karande and

Sujit Barik for keeping a fruitful and enjoyable environment at home during my stay with them.

I wish to express my deepest gratitude to Shri Vishnuswaroop Brahamchariji Maharaj. By his blessings, I always felt enlighten and peace of mind to face the challenges.

I am indebted to my father (Mr. Naresh Chandra Gupta) and mother (Mrs. Kasturi Gupta) for their affection, encouragement and support at every stage of my life. I am extremely thankful to my loved one – Somya who always encouraged and supported me with her deepest love and ideas during the past several months. I know how proud they are about my achievements and that makes this PhD degree even more special. I also wish to acknowledge my brothers (Munish and Anish) for their co-operation and understanding. Above all, I would like to thank the Almighty, for His kindness, grace and blessings throughout my career.

I am lucky to have bunch of friends who always kept me cheerful. I would like to thank Satyen, Bharat, Damar, Dr. Sunil, Dr. Sanjiv, Manish, Sudhir, Niranjani, Anbharasi, Liu Gang, Poh Hui, Suhanya, Anitha, Danping, Vivek, Karthiga, Prashant, Ravi, Sivashangari, Dhawal, Prashant Chandrasekharan, Suresh, Sundar, Bibin, Vinayak, Anjaiah, Rama Rao, Vigneshwar, Dr. Shashi Bhusan, Ashish, Ashvani, Harendra, Gyanveer, Saurabh, Dr. Naveen, Dr. Amit Gupta, Shweta, Amit Tonk, Anupam, Nidhi, Shrikant, Goldi, Avinash and Abhishek for their timely assistance, inspiring discussions and criticisms which helped me to a large extent and made my staying in NUS and Singapore more enjoyable and memorable.

I would like to thank the National University of Singapore for providing me financial support in the form of research scholarship and an excellent research environment throughout my candidature.

Lastly, I wish to thank the people who have helped me in one way or another that I might have missed out.

TABLE OF CONTENTS

Dedication ..... **i**
Acknowledgements ..... **ii**
Table of Contents ..... **vi**
Summary ..... **xii**
Nomenclature ..... **xvii**
List of Figures ..... **xix**
List of Schemes and Tables ..... **xxv**
Chapter 1 Introduction **1**
Chapter 2 Literature Review **9**
2.1 Electronic Memory 10
2.2 Types of Electronic Memory 10
2.3 Flash Memory 11
2.3.1 Operation Mechanism for Nanocrystal Based Memory Devices 13
2.3.1.1 Fowler-Nordheim Tunneling 14
2.3.1.2 Channel Hot Electron Injection 15
2.4 Organic Electronics 17
2.4.1 Organic Based Memory Devices 17
2.4.2 Organic and Nanoparticle Based Hybrid Memory Devices 19
2.5 Polyimide Film 24
2.5.1 Polyimide Films for Memory Devices 24
2.5.2 Nanoparticles Embedded Polyimide Films for Memory Devices 25
2.6 Motivation for the Present Study 26
2.7 Device Fabrication Methods 27
2.7.1 Spin Coating Technique 27
2.7.2 Langmuir-Blodgett Films 28
2.7.3 Electrostatic LbL Films 29
2.7.4 Covalent Assembly 30
2.8 Fabrication Methods for Nanoparticle Containing Hybrid Structures 30

2.8.1 Spin Coating Technique Based 30
2.8.2 Assembly Based 31
2.8.2.1 Langmuir-Blodgett Assembly Based 31
2.8.2.2 Electrostatic Assembly Based 33
2.8.2.3 Covalent Assembly Based 34
2.8.2.4 Dendrimers Based 35
2.9 Large Area Memory Devices 40
2.9.1 Nanoparticles on Patterned Surfaces 40
Chapter 3 Copper Nanoparticles Embedded in a Polyimide Film for Nonvolatile Memory Applications 42
3.1 Introduction 43
3.2 Experimental Section 43
3.2.1 Materials 43
3.2.2 Substrate Preparation 44
3.2.3 Preparation of poly (amic acid) 44
3.2.4 Preparation of poly (amic acid) Films 46
3.2.5 Introduction of Copper Precursor 46
3.2.6 Polyimide Conversion through Chemical Imidisation in Benzene 47
3.2.7 Reduction of Copper Precursor 47
3.2.8 MIS Capacitor Fabrication 47
3.2.9 Characterization 48
3.3 Results and Discussions 50
3.3.1 X-Ray Photoelectron Spectroscopy 50
3.3.2 Surface Morphology 52
3.3.3 Field Emission Scanning Electron Microscopy 52
3.3.4 Capacitance–voltage (C–V) and Capacitance–time (C–t) Analysis 54
3.4 Conclusions 61
Chapter 4 Langmuir−Blodgett Assembly of 4-Methylbenzenethiol Functionalized Gold Nanoparticles for Nonvolatile Memory Applications 62
4.1 Introduction 63
4.2 Experimental Section 63

4.2.1 Materials....63
4.2.2 Synthesis of Thiol-Stabilized Gold Nanoparticles....64
4.2.3 Immobilization on Silicon Surface....64
4.2.3.1 Substrate Preparation....64
4.2.3.2 Self-Assembly of Silane....65
4.2.3.3 LB Film Deposition of Gold Nanoparticles....65
4.2.4 MIS Capacitor Fabrication....66
4.2.5 Characterization....66
4.3 Results and Discussions....68
4.3.1 Synthesis of MBT Capped Gold Nanoparticles....68
4.3.1.1 Transmission Electron Microscopy (TEM)....68
4.3.2 LB Assembly of Gold Nanoparticles....70
4.3.2.1 Ellipsometric Characterization....70
4.3.2.2 Surface Morphology....70
4.3.3 C–V Analysis....72
4.4 Conclusions....80
Chapter 5 Covalent Assembly of Functionalized Gold Nanoparticles....81
5.1 Synthesis of Short Chain Thiol Capped Gold Nanoparticles, their Stabilization and Immobilization on Silicon Surface....84
5.1.1 Introduction....85
5.1.2 Experimental Section....85
5.1.2.1 Materials....85
5.1.2.2 Synthesis of Thiol-Stabilized Gold Nanoparticles....86
5.1.2.3 Stabilization of Thiol-Capped Gold Nanoparticles....88
5.1.2.4 Immobilization on Silicon Surface....88
5.1.2.5 Characterization....89
5.1.3 Results and Discussions....92
5.1.3.1 Synthesis and Stabilization of 4-ATP Capped Gold Nanoparticles....92
5.1.3.2 Immobilization of Stabilized Gold Nanoparticles....101
5.1.4 Conclusions....104
5.2 Synthesis of 16-Mercaptohexadecanoic Acid Capped Gold Nanoparticles and their

Immobilization on a Substrate 105
5.2.1 Introduction 106
5.2.2 Experimental Section 106
5.2.2.1 Materials 106
5.2.2.2 Synthesis of Thiol-Stabilized Gold Nanoparticles 107
5.2.2.3 Immobilization on Silicon Surface 108
5.2.2.4 Characterization 110
5.2.3 Results and Discussions 110
5.2.3.1 Synthesis 16-MHDA Capped Gold Nanoparticles 110
5.2.3.2 Immobilization of Acid Terminated Gold Nanoparticles 117
5.2.4 Conclusions 123
5.3 Covalent Assembly of Gold Nanoparticles for Nonvolatile Memory Applications 124
5.3.1 Introduction 125
5.3.2 Experimental Section 125
5.3.2.1 Materials 125
5.3.2.2 Synthesis of Thiol-Stabilized Gold Nanoparticles 126
5.3.2.3 Immobilization on Silicon Surface 127
5.3.2.4 MIS Capacitor Fabrication 128
5.3.2.5 Characterization 128
5.3.3 Results and Discussions 131
5.3.3.1 Synthesis of MUD Capped Gold Nanoparticles 131
5.3.3.2 Immobilization of MUD Capped Gold Nanoparticles 134
5.3.3.3 C-V and C-t Analysis 138
5.3.4 Conclusions 141
Chapter 6 Hybrid Multilayer Assembly of Functionalized Gold Nanoparticles and Thin Polymeric Films 143
6.1 Optimization for Deposition of Covalently Bound Ultrathin Polymer Films: An Example for Improvement to Wear Life 146
6.1.1 Introduction 147
6.1.2 Experimental Section 147

6.1.2.1 Materials 147
6.1.2.2 Immobilization on Silicon Surface 148
6.1.2.3 Characterization 151
6.1.3 Results and Discussions 152
6.1.3.1 Surface Morphology 152
6.1.3.2 Ellipsometric Characterization 154
6.1.3.3 X-ray Photoelectron Spectroscopy (XPS) 154
6.1.3.4 Tribology 156
6.1.4 Conclusions 162
6.2 Multilayer Assembly of Gold Nanoparticles and their Controlled Separation on Silicon Substrate through Covalently Bound Multilayer of Ultrathin Polymer Films 163
6.2.1 Introduction 164
6.2.2 Experimental Section 164
6.2.2.1 Materials 164
6.2.2.2 Multilayer of Gantrez Film Deposition 165
6.2.2.3 Synthesis of Citrate Stabilized Gold Nanoparticles 167
6.2.2.4 Immobilization of Citrate Gold Nanoparticles 167
6.2.2.5 Immobilization of Multilayer of Citrate Gold Nanoparticles 167
6.2.2.6 Characterization 169
6.2.3 Results and Discussions 171
6.2.3.1 Multilayer of Gantrez Film 171
6.2.3.2 Immobilization of Citrate Stabilized Gold Nanoparticles 174
6.2.4 Conclusions 182
Chapter 7 Tailored Assembly of Gold Nanoparticles over Patterned Surface for Nonvolatile Memory Applications 183
7.1 Introduction 184
7.2 Experimental Section 184
7.2.1 Materials 184
7.2.2 Synthesis of Citrate Stabilized Gold Nanoparticles 185
7.2.3 Immobilization on Silicon Surface 185

7.2.3.1 APhS Deposition on Substrate 185
7.2.3.2 ATP Deposition on Patterned Substrate 186
7.2.3.3 Immobilization of Gold Nanoparticles 186
7.2.4 MIS Capacitor Fabrication 186
7.2.5 Characterization 186
7.3 Results and Discussions 188
7.3.1 Synthesis of Citrate Capped Gold Nanoparticles 188
7.3.1.1 Transmission Electron Microscopy (TEM) 188
7.3.2 Immobilization of Citrate Capped Gold Nanoparticles 188
7.3.2.1 Surface Morphology 188
7.3.2.2 FESEM Analysis 190
7.3.3 C–V Analysis 193
7.4 Conclusions 197
Chapter 8 Conclusions 200
Chapter 9 Future Recommendations 205
References 209
Appendix 241

Summary

Today, memory devices with faster access time, easily processable, less power consumption, longer retention time, enhanced stability and importantly low cost are on demand for current electronic industry. Organic based memory devices have attracted considerable attention due to their low cost and easy processing. Self-assembly techniques that allow the controlled growth of nanometer-scale organic molecular films which eventually leads simple processing and device fabrication and present new opportunities to develop electronic devices with dimensions much smaller than those of current technologies. However, processing technology on a nano-scale is immature and continuous development is required.

The metal nanoparticles could be exploited as potential storage elements for nonvolatile memory device applications such as metal/insulator/semiconductor (MIS) memory structures using nanocrystals embedded in a dielectric material. The recent interest in nanofloating gate MIS memory structures starts largely from their potential application in future memory market, since assembled layer of metal nanoparticles functioning as a floating gate can reduce the charge loss problem encountered with the conventional flash memories. This will lead to reduced power consumption, increased write/erase speed and increased device density. Currently, most of the memory devices employ incorporation of metals nanoparticles through thermal evaporation of metal which leads to random distribution of metal nanoparticles inside a dielectric. In addition, there is not any control over ordering, organization and size of the nanoparticles used in such memory devices. Shortcomings of non-uniformity in size and shape of metallic nanoparticles in these

memory devices can be overcome by incorporating pre-synthesized nanoparticles in the devices. The self-assembly of pre-formed nanoparticles using spin-coating technique either suffer from random distribution of the nanoparticles or lack of uniformity when coated on large areas.

The objective of this Ph.D thesis is to improve performance of current memory devices fabricated using spin coating technique through polyimide films to give better thermal stability to memory devices and to develop molecular assembly based thin films of organic and organo-metallic structures for nonvolatile memory applications. Techniques, based on Langmuir-Blodgett deposition and electrostatic assemblies are able to produce multilayer films with controlled thickness, tailored structure or desired functionality. In terms of stability or strength, multilayer films with covalent interlayer bonding are more advantageous over Langmuir-Blodgett and electrostatic bonding, since they are robust enough to withstand elevated temperatures, polar solvent attack, mechanical wear and abrasion.

Nonvolatile organic bistable devices, that utilize solution processed uniformly distributed copper nanoparticles in polyimide matrix, have been fabricated and their unique nonvolatile electrical bistability properties are discussed. Copper acetylacetonate ($Cu(acac)_2$) as a precursor has been used. Polymer memory device was fabricated by spin coating solution containing polyamic acid and the nanoparticle precursors. The precursors were subsequently thermally reduced to form the nanoparticles. The resulting films were then characterized by X-ray photoelectron spectroscopy (XPS), atomic force

and scanning electron microscopies. Capacitance-voltage measurements showed that the embedded Cu nanoparticles functioning as a floating gate in metal-insulator-semiconductor-type capacitor exhibits a hysteresis window of 1.52 V at an applied voltage of 8 V.

The Langmuir-Blodgett technique of molecular assembly has been employed in fabricating a multilayered array of gold nanoparticles functionalized by 4-methylbenzenethiol on Si substrates. The 2 layer, 4 layer and 6 layer structures of functionalized gold nanoparticles (AuNPs) were fabricated. Thickness measurements by ellipsometry showed a linear increase of film thickness with the number of layers, indicating a reproducible deposition process. The capacitance versus voltage characteristics of these devices showed increment in hysteresis window with the number of layers.

Short chain thiol (4-aminothiophenol)-capped AuNPs functionalized with amine-termination have been synthesized, and changes in their morphology by varying the process conditions as well as the dispersion medium were studied. Subsequently, the nanoparticles (which are prone to agglomerate due to amine-amine hydrogen bonding) were stabilized in solution and by anhydride capping. Finally, these stabilized nanoparticles were immobilized on a silicon substrate. The cross-sectional high resolution transmission electron microscopy (HR-TEM) images directly indicated that the particles are anchored to the silicon surface.

16-mercaptohexadecanoic acid capped AuNPs with a narrow size distribution have been synthesized through a single phase synthesis method and subsequently immobilized onto silicon/gold surfaces through covalent molecular assembly. Fourier transform infrared spectroscopy and XPS confirmed the absence of unreacted thiol in the synthesized AuNPs. Presence of AuNPs on silicon surface, after the immobilization process, was confirmed through XPS. Cross-sectional HR-TEM images provided direct evidence that the particles are indeed anchored to the silicon surface.

Gold nanoparticles bearing pendant alcohol functional groups have been synthesized with a narrow size distribution (diameter ~5 nm). Later, these nanoparticles were immobilized on a silicon substrate using a functionalized polymer as a surface modifier. Microscopic and spectroscopic techniques were used to characterize the nanoparticles and their morphology before and after immobilization. In addition, the electrical characterization of covalently bound AuNPs, as a charge trapping layer in nonvolatile memory was also investigated by means of a metal-insulator semiconductor device structure.

The application of covalent molecular assembly in fabricating robust thin film multilayer structures has been demonstrated. An anhydride functionalized polymer was deposited over an amine-terminated silane, which was assembled on a silicon surface through covalent binding. Multilayers of polymers were obtained by using a diamine molecule as a spacer that is covalently bound to adjacent polymer layers. The thickness and surface morphology of the covalently bound polymer layers were characterized with ellipsometry and atomic force microscopy. Later, we present a new synthetic strategy to build

multilayered composite films comprising functionalized polymer and AuNPs. AuNPs are stabilized and immobilized through electrostatic binding between a functionalized polymer and gold nanoparticle (AuNP). The assembly process allows placement of AuNP layers with controlled inter-layer separation using covalently bound spacers. Characterizations, performed by spectroscopic (XPS) and microscopic (Field emission scanning electron microscopy and cross-sectional HR-TEM) methods showed the positioning of the AuNP layers and uniform distribution of the nanoparticles over the surface.

The combination of block copolymer directed synthesis and electrostatic self-assembly of AuNPs was used to achieve the assemblies. This helped to create size-tunable particle arrays of metal nanoparticles down to sub-10 nm dimensions with narrow dispersion, high density and excellent homogeneity over large areas. The nanoparticle assemblies are demonstrated to significantly benefit from a high charge storage capacity, as well as ease of charge-injection. The resulting AuNP assembled structures displayed improved charge storage over patterned gold substrate. Charge storage capacity was also enhanced by increasing the density of AuNPs via increasing the deposition time.

NOMENCLATURE

AFM	Atomic force microscopy
APhS	p-Aminophenyltrimethoxysilane
ATP	Aminothiophenol
AuNPs	Gold nanoparticles
BE	Binding energy
CPS	3-cyanopropyltrichlorosilane
$Cu(acac)_2$	Copper acetylacetonate
C–V	Capacitance–voltage
DADA	1, 12-diaminododecane
DDE	Diaminodiphenyl ether
DMAc	N,N'-dimethylacetamide
DMF	N,N'-dimethylformamide
DRAM	Dynamic random-access memory
eV	Electron volt
FESEM	Field emission scanning electron microscopy
FTIR	Fourier transform infrared spectroscopy
HDD	Hard disk drive
HR-TEM	High resolution transmission electron microscopy
LB	Langmuir-Blodgett
LbL	Layer-by-layer
MBT	Methylbenzenethiol

MHDA	Mercaptohexadecanoic acid
MIS	Metal-insulator-semiconductor
MOSFET	Metal oxide field effect transistor
MUD	11-mercapto-1-undecanol
NPs	Nanoparticles
OBDs	Organic bistable devices
OTS	Octadecyltrichlorosilane
PAA	Poly(amic acid)
PDA	1, 4-phenylene diamine
PI	Polyimide
PMDA	Pyromellitic dianhydride
rpm	Revolutions per minute
SAM	Self-assembled monolayer
SRAM	Static random access memory
TEM	Transmission electron microscopy
TGA	Thermogravimetric analysis
THF	Tetrahydrofuran
TOAB	Tetraoctylammonium bromide
UV	Ultraviolet-visible
VASE	Variable angle spectroscopic ellipsometry
WORM	Write-once read-many times
XPS	X-ray photoelectron spectroscopy

List of Figures

Figure 2.1. (a) Schematic diagram of a nanocrystal memory structure and (b) schematic diagram of a memory cell with nanocrystals as discrete charge storage elements.

Figure 2.2. Schematic band diagram of a nanocrystal (NC) memory structure with SiO_2 as the tunneling dielectric and Al_2O_3 as the control dielectric under (a) write state (positive applied bias), (b) retention state and (c) erase state (negative applied bias).

Figure 3.1. Schematic of MIS device structure.

Figure 3.2. XPS wide scans for copper nanoparticle containing PI film. (A) 1 day after reduction (B) 15 days after reduction.

Figure 3.3. Surface topography for copper nanoparticles embedded PI film. (A) height image, (B) phase image and (C) section analysis.

Figure 3.4. FESEM images for copper nanoparticles embedded PI film. (A), (B) Reduction before chemical imidisation step; (C), (D) Reduction after chemical imidisation step.

Figure 3.5. Normalized C-V characteristics at 100 kHz obtained by biasing the top electrodes at ± 2 V for control sample (without CuNPs) and with CuNPs.

Figure 3.6. Normalized C-V characteristics at 100 kHz obtained by biasing the top electrodes at ± 5 V for control sample (without CuNPs) and with CuNPs.

Figure 3.7. C–V characteristics at 100 kHz under different scan voltage ranges for an MIS capacitor incorporating copper nanoparticles.

Figure 3.8. Charge retention characteristics (normalized capacitance) of the MIS device at 100 kHz after programming at + 5 V.

Figure 4.1. The MIS device configuration for the multilayer of MBT capped gold nanoparticles.

Figure 4.2. TEM image of MBT capped gold nanoparticles.

Figure 4.3. Ellipsometric thickness of MBT capped gold nanoparticles films prepared by LB deposition versus number of layers.

Figure 4.4. Surface topographies of 2 μm × 2 μm regions for different deposition steps (A) OTS surface, (B) 2 layer of nanoparticles, (C) 4 layer of nanoparticles and (D) 6 layer of nanoparticles.

Figure 4.5. A comparison of section analysis at various deposition steps (A) OTS surface, (B) 2 layer of nanoparticles, (C) 4 layer of nanoparticles and (D) 6 layer of nanoparticles.

Figure 4.6. Normalized C-V characteristics at 100 kHz obtained by biasing the top electrodes at ± 5 V for control sample (without nanoparticles) and with 4 Layer of MBT capped AuNPs.

Figure 4.7. Normalized C-V characteristics at 100 kHz obtained by biasing the top electrodes at ± 7 V to compare effect of number of layer of MBT capped AuNPs.

Figure 4.8. Normalized C–V characteristics at 100 kHz under different scan voltage ranges for an MIS capacitor incorporating 4 Layer of MBT capped AuNPs.

Figure 4.9. Normalized C–V characteristics at ± 5 V to compare effect of frequency for 4 Layer of MBT capped AuNPs.

Figure 5.1.1. Schematic for immobilization of anhydride functionalized gold nanoparticles on to a hydroxyl-terminated silicon surface.

Figure 5.1.2. UV-visible absorption spectra of gold nanoparticles synthesized (A) effect of synthesis method (B) effect of dispersion media.

Figure 5.1.3. UV-visible absorption spectra of gold nanoparticles of DMAc dispersion after reaction of various amounts of nanoparticles with 5 mL of 5 mM.

Figure 5.1.4. X-ray photoelectron spectra of 4-ATP capped gold nanoparticles through mixed approach showing the (A) N 1s region and the (B) S 2p region.

Figure 5.1.5. X-ray photoelectron spectra of gold nanoparticles stabilized with PMDA showing the (A) C 1s region and the (B) N 1s region.

Figure 5.1.6. TEM images for gold nanoparticles (A) synthesized gold nanoparticles through mixed approach (B) 0.25 µmoles of gold nanoparticles after reaction with PMDA (C) 0.05 µmoles of gold nanoparticles after reaction with PMDA (D) 0.025 µmoles of gold nanoparticles after reaction with PMDA.

Figure 5.1.7. X-ray photoelectron wide spectra. (A) APhS-modified Si substrate, (B) gold nanoparticles immobilized on Si substrate, (C) Au $4f_{7/2}$ and $4f_{5/2}$ spectra of gold nanoparticles immobilized on Si substrate.

Figure 5.1.8. Cross-sectional HR-TEM image of gold nanoparticles immobilized on Si substrate.

Figure 5.2.1. FTIR spectra for 16-MHDA capped gold nanoparticles synthesized by different methods.

Figure 5.2.2. TEM images for 16-MHDA capped gold nanoparticles synthesized by (A) Method A - carried out at room temperature (B) Method B – carried out at 0 ^{o}C.

Figure 5.2.3. UV-visible absorption spectra of 16-MHDA capped gold nanoparticles synthesized by different methods in DMAc.

Figure 5.2.4. X-ray photoelectron spectra of 16-MHDA capped gold nanoparticles synthesized by Method B – carried out at 0 ^{o}C showing the (a) C 1s region, (b) S 2p region and (c) Au 4f region.

Figure 5.2.5. TEM images for (A) 16-MHDA monolayer deposited gold grid and (B) 16-MHDA capped gold nanoparticles immobilized on gold grid.

Figure 5.2.6. X-ray photoelectron wide spectra. (A) gold nanoparticles immobilized on Si substrate; (B) CPS-COOH modified Si substrate.

Figure 5.2.7. Cross-sectional HR-TEM images for (A) Si substrate without gold nanoparticles; (B) 16-MHDA capped gold nanoparticles immobilized on Si. The inset shows the enlarged view of immobilized gold nanoparticles.

Figure 5.3.1. The MIS device configuration for the immobilized MUD capped gold nanoparticles.

Figure 5.3.2. (a) TEM image of MUD capped gold nanoparticles, (b) size distribution of MUD capped gold nanoparticles.

Figure 5.3.3. X-ray photoelectron spectra of MUD capped gold nanoparticles showing the (a) C 1s region, (b) S 2p region and (c) Au 4f region.

Figure 5.3.4. C1s core-level XPS spectra at various steps of the AuNPs assembly; (a) the gantrez deposited APhS substrate, (b) MUD capped AuNPs immobilized on Si substrate.

Figure 5.3.5. Tapping mode AFM images ($2 \times 2\ \mu m^2$) and z profiles of a gantrez deposited Si surface (A) and similar surface after immobilization of MUD capped gold nanoparticles (B).

Figure 5.3.6. FESEM images for MUD capped AuNPs immobilized on Si surface: after rinsing (a), after 5 min sonication (b).

Figure 5.3.7. FESEM images for MUD capped AuNPs solution spin coated Si surface: before sonication (a), after 5 min sonication (b).

Figure 5.3.8. Normalized C-V characteristics at 100 kHz obtained by biasing the top electrodes at ± 6 V for control sample (without gold nanoparticles) and with gold nanoparticles.

Figure 5.3.9. Normalized C–V characteristics at 100 kHz under different scan voltage ranges for an MIS capacitor incorporating gold nanoparticles.

Figure 5.3.10. Charge retention characteristics (normalized capacitance) of the MIS device at 100 kHz after programming at + 5 V.

Figure 6.1.1. Surface topographies (2×2 μm^2) for different deposition steps: (a) APhS; Gantrez deposition for (b) 0.2% and 1 h deposition time; (c) 0.2% and 3 h deposition time; (d) 0.5% and 1 h deposition time; (e) 0.5% and 3 h deposition time; (f) 1% and 1 h deposition time.

Figure 6.1.2. Comparison of average thickness for gantrez deposition at different processing steps.

Figure 6.1.3. C1s core-level XPS spectra for different deposition steps: (A) gantrez deposition for 0.2% and 3 h deposition time; (B) gantrez deposition for 0.5% and 1 h deposition time.

Figure 6.1.4. C1s core-level XPS spectra for different deposition steps: (A) gantrez deposited surface; (B) PFPE deposited surface.

Figure 6.2.1. Ellipsometric thickness of gantrez film versus number of layers.

Figure 6.2.2. TEM image of gold nanoparticles.

Figure 6.2.3. FESEM images for citrate AuNPs immobilized on amine terminated Si surface. (A) APhS; (B) 1st layer of DADA; (C) 2nd layer of DADA; (D) 3rd layer of DADA.

Figure 6.2.4. Cross-sectional HR-TEM images for (A) citrate stabilized AuNPs on APhS deposited Si surface; (B) citrate stabilized AuNPs on 2nd layer of DADA deposited Si surface.

Figure 6.2.5. FESEM images for (A) citrate stabilized AuNPs on APhS; (B) citrate stabilized AuNPs on APhS after immersion in pH 10 buffer solution; (C) citrate stabilized AuNPs on APhS stabilized by gantrez film; (D) citrate stabilized AuNPs on APhS stabilized by gantrez film after immersion in pH 10 buffer solution.

Figure 6.2.6. Cross-sectional HR-TEM images for: 1st layer of citrate stabilized AuNPs on APhS deposited Si surface (A), (B); 2nd layer of citrate stabilized AuNPs on DADA deposited gantrez polymer film on Si surface (C), (D).

Figure 7.1. The MIS device configuration for the immobilized citrate capped gold nanoparticles.

Figure 7.2. TEM image of gold nanoparticles.

Figure 7.3. Tapping mode AFM images (5×5 μm^2) of patterned gold nanoparticle on Si substrate (A) surface topography (B) section analysis.

Figure 7.4. FESEM images for 100000 magnification (A) patterned gold array substrate, (B) 4-ATP modified patterned gold array substrate, (C) citrate capped AuNPs deposition on above 4-ATP modified substrate for 1 h deposition time, and (D) citrate capped AuNPs deposition on above 4-ATP modified substrate for 6 h deposition time.

Figure 7.5. FESEM images for 25000 magnification (A) patterned gold array substrate, (B) 4-ATP modified patterned gold array substrate, (C) citrate capped AuNPs deposition on above 4-ATP modified substrate for 1 h deposition time, and (D) citrate capped AuNPs deposition on above 4-ATP modified substrate for 6 h deposition time.

Figure 7.6. FESEM images for citrate capped AuNPs deposition for 6 h on 4-ATP unmodified patterned gold array substrate for (A) 100000 magnification, and (B) 25000 magnification.

Figure 7.7. FESEM images for 100000 magnification for citrate capped AuNPs deposition on APhS modified Si substrate for (A) 1 h deposition time, and (B) 6 h deposition time.

Figure 7.8. Normalized C-V characteristics at 100 kHz obtained by biasing the top electrodes at ± 4 V to study effect of citrate capped AuNPs deposition on patterned substrate.

Figure 7.9. Normalized C-V characteristics at 100 kHz under different scan voltage ranges for an MIS capacitor incorporating citrate capped AuNPs deposition for 1 h on patterned substrate.

Figure 7.10. C-V characteristics at 100 kHz obtained by biasing the top electrodes at ± 6 V for an MIS capacitor incorporating citrate capped AuNPs deposition for 6 h on APhS modified Si substrate.

Figure 7.11. Schematic for citrate capped AuNPs deposition on APhS modified Si substrate.

List of Schemes and Tables

Scheme 3.1. Molecular structures of the main materials used.

Scheme 5.1.1. Molecular structures of the main materials used.

Scheme 5.1.2. Schematic for the possible hydrogen bonding among various functionalities.

Scheme 5.1.3. Schematic for the preparation of stabilized gold nanoparticles.

Scheme 5.1.4. Schematic for the proposed mechanism to get well separated anhydride functionalized gold nanoparticles.

Scheme 5.2.1. Immobilization of acid terminated gold nanoparticles on to a hydroxyl-terminated silicon surface.

Scheme 5.2.2. Schematic for the 16-MHDA capped gold nanoparticles synthesized by (a) Method B – carried out at 0 ^{o}C and (b) Method A - carried out at room temperature.

Scheme 5.3.1. Immobilization of MUD capped gold nanoparticles on to a hydroxyl-terminated silicon surface.

Scheme 6.1.1. Immobilization of gantrez on to a hydroxyl-terminated silicon surface.

Scheme 6.1.2. Immobilization of PMDA on to a hydroxyl-terminated silicon surface.

Scheme 6.2.1. Multilayer of gantrez polymer film deposition.

Scheme 6.2.2. 1st layer of citrate AuNPs stabilized by gantrez polymer film.

Scheme 6.2.3. 2nd layer of citrate AuNPs deposition on DADA deposited gantrez polymer film.

Table 2.1. Examples of recently demonstrated two-terminal, programmable-resistance organic nonvolatile memory devices.

Table 6.1.1. Coefficient of friction and wear life values for PFPE deposited various surfaces.

Table 6.2.1. C/Si and N/Si ratios at various deposition steps.

CHAPTER 1

INTRODUCTION

The increasing demand for electronic storage devices, driven by sales of personal computers and mobile electronic devices, palmtop, mobile PC, mp3 player, audio player, digital camera and so on, provides a significant incentive for the continued development of high-performance memory. Although, some data-storage technologies, such as digital video disks (DVDs), offer almost limitless, inexpensive data storage. But, their ability to alter the stored data is limited. For most applications, memory in which the stored data can be readily altered is highly desirable. Currently, there are four technologies (HDD, DRAM, SRAM and flash) for the programmable-memory market. The first technology is the hard disk drive (HDD), which stores data in the local polarization of a paramagnetic disk. This data is accessed and programmed by the head as the disk rotates. Hard disks are nonvolatile, meaning that a stored state is retained even without applying the power. Although, being an inexpensive, the mechanical rotation of hard disk limits operating speed and ability to withstand physical vibrations and shocks (Scott and Bozano, 2007).

The second technology and known as dynamic random-access memory (DRAM) utilizes charge to store data. In DRAM, the charge is stored on a silicon capacitor that is accessed by a transistor. The memory state is read by measuring the charge stored on the capacitor. This stored charge can leak out of the capacitor through the channel of the access transistor very quickly (~100 ms) (Kuhr et al., 2004). Since this charge must constantly be refreshed to retain data, DRAM is a volatile memory technology.

The third technology is static random access memory (SRAM). In this, each memory cell consists of two cross-coupled complementary metal-oxide-semiconductor (CMOS)

inverters that form a flip-flop. The stored memory state is determined by the voltage on these inverters. Although, SRAM does not need to be refreshed, it is volatile because stored data is lost if power is removed.

Last technology is dedicated to the flash memory, which was developed from erasable programmable read only memory (EPROM), the charge on the floating gate of a metal-oxide-semiconductor field-effect transistor (MOSFET) determines the state of a memory cell. The current in the channel of the transistor depends on the amount of charge on the floating gate, so, can be used to read the stored state. Because, the floating gate is embedded in a high-quality silicon dioxide insulating layer, it can take years for the charge to leak out of the floating gate (Streetman and Banerjee, 2000). Therefore, flash memory is nonvolatile. Flash memory is currently the most successful nonvolatile solid state data storage technology, but it is more expensive, in terms of dollars per gigabyte, than HDD (Scott, 2004).

The semiconductor industry has been increasing the memory density for almost three decades, just as predicted by the famous Moore's law, which states that the number of transistors per integrated circuit would double every 18 months. But the validity of Moore's law is coming to its end since the manufacturing processes (lithography, etching, deposition etc.) are being carried out near their respective resolution limits. All traditional memories have the scaling limitation and other serious performance limitations mentioned above.

Slower access time, high power consumption, less retention time and high cost are few of inadequacies of current nonvolatile memory devices. Metal nanoparticles could be exploited as potential storage elements for nonvolatile memory device applications such as metal-insulator-semiconductor (MIS) memory structures using nanocrystals embedded in a dielectric. MIS structure is the charge storage component of a transistor memory. The recent interest in nanofloating gate MIS memory structures largely arises from their potential application in future memory markets since the assembled layer of metal nanoparticles functioning as a floating gate can reduce the charge loss problem encountered with the conventional flash memories which will lead to reduced power consumption, increased write/erase speed and increased device density.

The research on memories comprising nanoparticle is underway and these have not found any application yet. Currently, metals nanoparticles are incorporated in most of the memory devices through thermal evaporating the metal. This may lead to random distribution of metal nanoparticles inside a dielectric; further, there is no control over ordering, organization and size of nanoparticles (Tang et al., 2007). Problems of non-uniformity in size and shape of metallic nanoparticles have been overcome by including pre-synthesized nanoparticles in the memory devices. Spin coating is being used to prepare the films of polymer matrix containing metal nanoparticles for the memory devices. However, there are limitations to obtain thin films, in terms of dilution of the solvent and the spinning rate. Also, many common defects such as comets, striations and wafer edge effects restrict the use of spin coating.

Electronic devices based on crystalline silicon have enjoyed enormous technological success, but face growing challenges in continued scaling to reduce device dimensions. Molecular-scale electronics offer exciting possibilities of making devices that can achieve (a) the ultimate in scaling with high reproducibility, (b) a wide variety of functionality and (c) low-cost. Bottom-up approaches for constructing ordered nano-scale structures in organic molecular assemblies are of interest and therefore, various techniques for preparation of organic ultrathin films have been extensively studied. However, processing the nano-scale technology is immature and continuous developments are required. A key approach for preparing molecular-scale devices can be solution-based self assembly, which has already found widespread use in fabricating electronic devices based on self-assembled monolayers (Tirrell and Katz, 2005; Heath and Ratner, 2003).

The drawbacks of current deposition techniques are that the binding forces between molecular chains are electrostatic or van der Waals in nature, giving rise to insufficient mechanical strength to the obtained films. In particular, Langmuir-Blodgett and electrostatic self-assembly techniques introduce weaker species in the film, which needs special effort to be removed, to avoid adverse impact on film properties. Covalent bonds with higher bond energies (320-1000 KJ/mol) (Morrison and Boyd, 1983) will enable construction of mechanically, thermally and chemically robust ultra thin films by making use of interlayer covalent bond.

Based on the above considerations, this Ph.D project aims to improve performance of current spin coating technique-based organic memories in terms of enhanced stability

through covalent binding and to develop molecular assembly based thin films of organic and organo-metallic hybrid structures for nonvolatile memory applications. Thus, this provides the rationale for building the molecular assembly based nano-composite structures for nonvolatile memory applications. Proposed work has been summarized in the following schematic diagram.

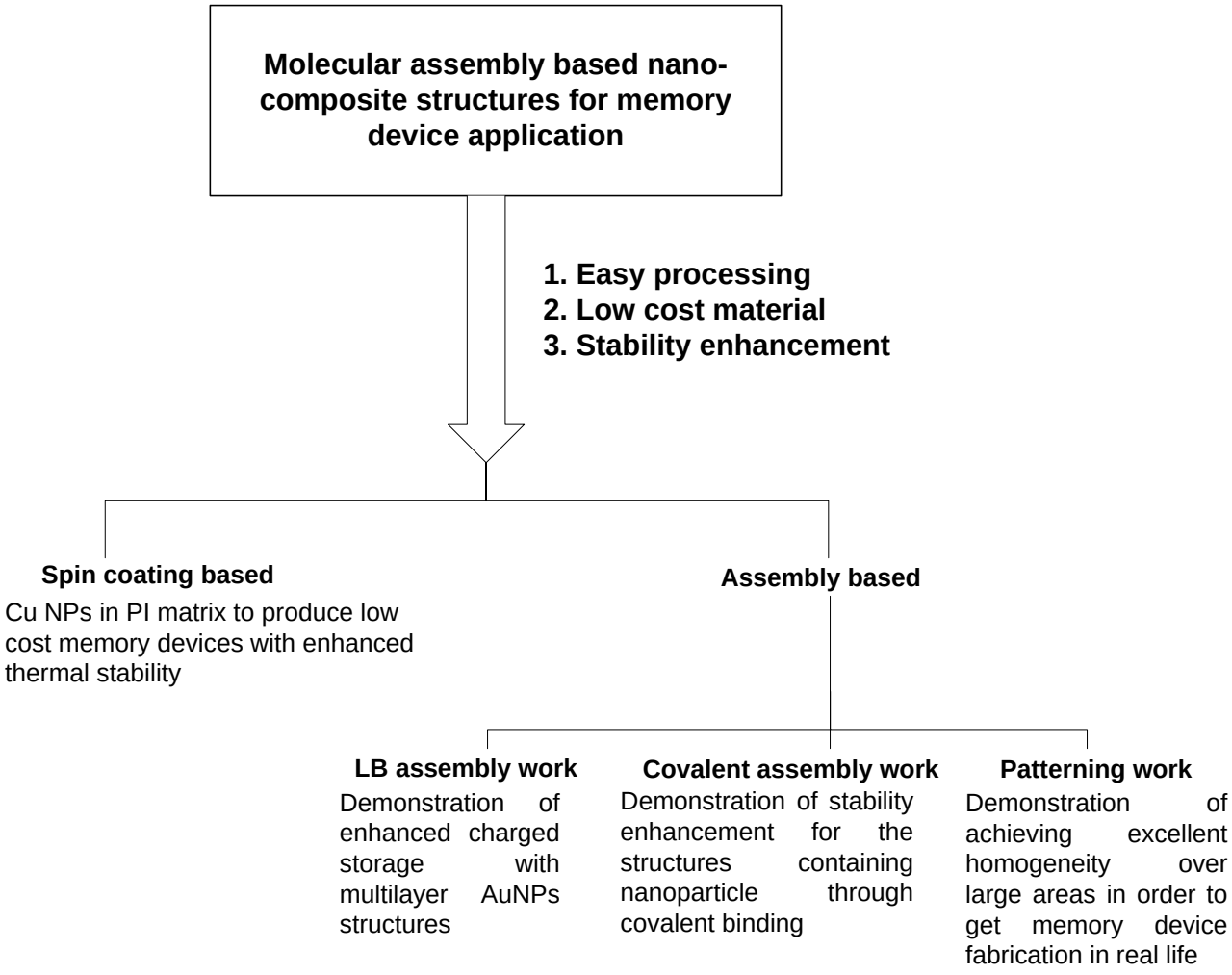

Functionalization of nanoparticles with specific ligands can meet the requirement of the immobilization. Interaction of the functionalized gold nanoparticles with substrate as well as monomer/polymer species has been studied for a hybrid organo-metallic structure. Having functional end groups for capping layers as compared to inert groups can facilitate formation of multilayers with covalent interlayer links.

The thesis begins with a detailed literature review and followed by five parts of work outlined below.

Chapter 3 describes nonvolatile organic memory devices utilizing solution processed, uniformly distributed copper nanoparticles in polyimide matrix functioning as a floating gate in MIS type capacitor. Chapter 4 deals with the use of the Langmuir-Blodgett technique in fabricating a multilayered array of gold nanoparticles (AuNPs) functionalized by 4-methylbenzenethiol, on Si substrates. The electrical characterization of such multilayered AuNPs structures is investigated by means of a MIS device for nonvolatile memory applications.

Chapter 5 deals with the synthesis, stabilization and covalent immobilization of short/long-chain thiol capped gold nanoparticles, and the demonstration of covalently bound AuNPs, as a charge trapping layer in nonvolatile memory by means of a MIS device. Chapter 6 covers optimization of process conditions to obtain covalently bound polymeric film of molecular thicknesses and building the multilayered composite films comprising functionalized polymer and AuNPs. Finally, Chapter 7 shows a novel route

towards fabricating high-density assemblies of AuNPs employing combination of block copolymer template directed in-situ synthesis as well as directed self-assembly of pre-formed nanoparticles on surface for charge storage applications.

The above research work has been carried out in partial fulfillment of the requirements for the Ph.D. degree. The work reported by others in the literature has been duly acknowledged. I would like to mention that the training received by me in the research methodology is of great significance to me and I hope that the research results presented in the thesis will add to the existing knowledge of the materials aspects of memory devices.

CHAPTER 2

LITERATURE REVIEW

2.1 Electronic Memory

Memory is one of the fundamental components of all modern computers and electronic systems (Sharma, 2003). Electronic memory refers to a component, device or recording medium that retains retrievable digital data over a time interval. An electronic memory is fast in response and compact in size, and can be read and written when connected to a central processing unit.

2.2 Types of Electronic Memory

Electronic memories can be divided into two primary categories according to its volatility: volatile and nonvolatile memories. Volatile memory loses the stored data as soon as the system is turned off. It requires a constant power supply to retain the stored information. Non-volatile memory can retain the stored information even when the electrical power supply has been turned off. Non-volatile memory can be further divided in the write-once read-many times (WORM) memory, the hybrid non-volatile and rewritable (flash) memory, and the dynamic random access memory (DRAM). As a non-volatile memory, a WORM memory is capable of holding data permanently and being read repeatedly. It can be written only once, and the stored data cannot be modified. For the flash memory, stored state can be electrically reprogrammed and it has the ability to write, read, erase and retain the stored state. This does not require power to retain the information stored in the cell. Thus, this is a non-volatile, as well as rewritable, memory. DRAM is a random access memory that stores each bit of data in a separate capacitor and thus, requires periodic refreshing to retain data. Because of this refresh requirement, it is

a dynamic memory. Since DRAM loses its data when the power supply is removed, it is in the class of volatile memories (Ling et al., 2008).

2.3 Flash Memory

Recently, portable electronic devices, such as laptop, mobile phones, and digital cameras are being used widely in people's daily lives. There is demand for more efficient and faster memory structures. Electronic nonvolatile memory technology is based on flash memories (Fazio 2004). Future of memory business will be much brighter compared to that of the past and the present. As, total amount of information generated world-wide doubles every year, with the famous Moore's law being used to describe how the number of transistors in an integrated circuit doubles in every two years (Intel, 2005). In reality, the rate of growth has been exceeded Moore's prediction.

Silicon technology has been used to fabricate a flash memory cell and its principle of operation is closely related to the operation of a metal oxide field effect transistor (MOSFET). In a flash cell, a continuous layer of doped poly-silicon film is buried within the insulator of the MOSFET, separated by a thin insulator, called tunneling oxide, from the channel area of the transistor and by a thicker insulator, named control oxide, from the gate (Tsoukalas, 2009). This device operates through application of voltage pulses to the gate, allowing electrons from the silicon channel to cross the tunneling oxide barrier and charge the floating gate.

As the capacity of non-volatile memories increases, the feature sizes of the storage cells need to continue to shrink to accommodate higher bit densities in the future. Conventional floating gate flash memory approaches have increased difficulties around the 32 nm node, primarily due to charge leakage through the gate oxide. Local storage of the electrons may be one of the approaches to solve scale limitation in flash memory technology and the relevant research is ongoing. One important advantage of local storage is the possibility of further scaling thickness of the tunneling oxide, as any defect present in that oxide would allow only local loss of stored information. While in case of a continuous storage medium, any defect between the floating gate and the channel of the transistor will result in complete loss of the charge.

Nanoparticles have been introduced for charge storage by Tiwari et al. (1996) as a method of local charge storage. Nonvolatile memories based on nanoparticle memory structure have many advantages such as low operating voltage without compromising its retention characteristics, high endurance, and fast write/erase speed. Charges are more immune to the leakage caused by localized oxide defects when stored in discrete traps, thus improving the device retention characteristics. With the utilization of discrete storage nodes, a single leakage path due to defect in the oxide can only discharge a single storage node, thus improving the device retention characteristics. Due to a less sensitivity to gate oxide quality, a thinner tunneling oxide can be employed, which allows a faster write/erase speed and lower power operation. Different kinds of nanocrystals, such as Au, Pt, Ag, W, Ni, Al, Ru, Zn, Si, Ge, SiGe, $SrTiO_3$, Al_2O_3, have been prepared and their electrons storage abilities are studied (Yuan et al., 2006; Yim et al., 2006; Yang et al.,

2007; Wang et al., 2004; Samanta et al., 2005; Park et al., 2007; Normand et al., 2001; Liu et al., 2002a,b; Lee et al., 2005; Kim et al., 2007; Kim et al., 2003; Chen et al., 2005).

Silicon and germanium were initially being used as nanoparticle materials because of their compatibility with silicon technology. However, compared to their semiconductor counterparts, metallic nanoparticles are preferred because of their stronger coupling with the conduction channel, higher density of states around the Fermi level, smaller energy disturbance, and larger work function (Liu et al., 2002a; Hou et al., 2007; Lee et al., 2005; Sargentis et al., 2007; Dufourcq et al., 2008). The higher the metal work function, the lower is the leakage tunnelling coefficient of charges from the nanocrystals back to the silicon substrate. This would allow improved data retention for memory devices operating at low voltages. Also, metals have a wide range of available work functions, which can be exploited to improve the relationship between the retention time and the programme/erase speed giving freedom to the device optimization. In addition, noble metals neither oxidize nor react with the surrounding dielectric layers. Three dimensionally confined nanoparticles embedded in insulating layers have been investigated extensively for their promising applications in nonvolatile flash memory devices with nanoscale floating gates (Saitoh et al., 2003; Perego et al., 2004; Kapetanakis et al., 2002; Kim et al., 2002; Kanjilal et al., 2003; Kanoun et al., 2004).

2.3.1 Operation Mechanism for Nanocrystal Based Memory Devices

Figure 2.1a shows a schematic diagram of a nanocrystal floating gate memory device. In this memory structure continuous polysilicon floating gate of the conventional structure

is replaced by an array of nanocrystals. Figure 2.1b shows schematic diagram of a memory cell with nanocrystals as discrete charge storage elements. The operation principle of nanocrystal memory device is very similar to that of conventional floating gate nonvolatile memory devices. Figure 2.2 shows the illustration of band diagram during the operation of the nanocrystal memory device with SiO_2 tunneling dielectric and Al_2O_3 control dielectric. There are two mechanisms for charge injection into the nanocrystals through the tunnel oxide layer: Fowler-Nordheim (F-N) tunneling mechanism, which is usually used in devices with relatively thin tunnel oxides; and channel hot electron (CHE) injection, which is employed for device with relatively thick tunnel oxides. The details of the two mechanisms are given below.

2.3.1.1 Fowler-Nordheim Tunneling

F-N tunneling mechanism is based on the quantum mechanical tunneling mechanism induced by a high electric field. When a large positive voltage is applied to the gate, the band structure will be influenced as shown in Figure 2.2a. Due to the high electric field, electrons in the conduction band of the Si substrate see a triangular energy barrier with a width dependent on the applied field. At a sufficiently high applied field, the width is small enough that the electron can tunnel through the barrier from the silicon conduction band into the oxide conduction band without destroying SiO_2 dielectric properties (Brown et al., 1998). F-N tunneling current is adequate enough for memory devices to inject electrons into the nanocrystals.

2.3.1.2 Channel Hot Electron Injection

Nonvolatile memory can also be programmed by hot-carrier injection mechanism (Guterman et al., 1979). Hot carriers generally refer to the particles which attain the kinetic energy from a high electric field. The hot-electrons get their energy from the drain voltage, and are further accelerated by the lateral electric field along the channel. Once they obtain sufficient energy, these hot electrons will overcome the SiO_2/Si barrier and tunnel into the floating gate to program the cell.

When only reading voltages are applied to the gate, tunneling barriers are sufficiently opaque to prevent electrons from leaking out and therefore information is retained (Figure 2.2b). In this state, leakage of the charge can occur either laterally by conduction between the nanocrystals or to the silicon surface. The lateral charge conduction could be prevented with well-separated nanocrystals that can effectively increase charge confinement and reduce the tunneling probability between the nanocrystals (Liu et al., 2002a). Hence the primary mechanism for charge leakage would be restricted to the quantum mechanical tunneling of charges either directly or through trap levels in the oxide. In order to reprogram nonvolatile memory devices, it first has to be erased. F-N tunneling can also be used to erase a nonvolatile memory device. One of the methods is by applying a large negative voltage at the control gate. The energy band structure will be influenced as shown in Figure 2.2c. The applied voltage causes F-N tunneling of stored electrons from the nanocrystals to the substrate through the thin tunnel oxide.

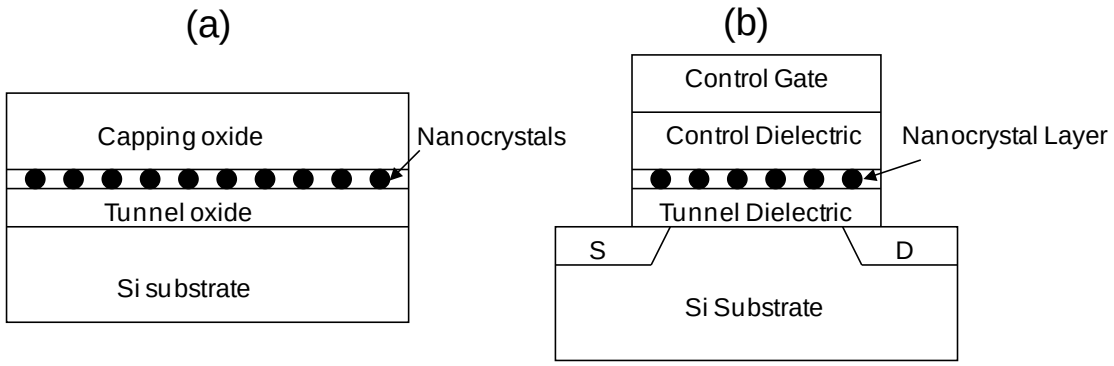

Figure 2.1. (a) Schematic diagram of a nanocrystal memory structure and (b) schematic diagram of a memory cell with nanocrystals as discrete charge storage elements.

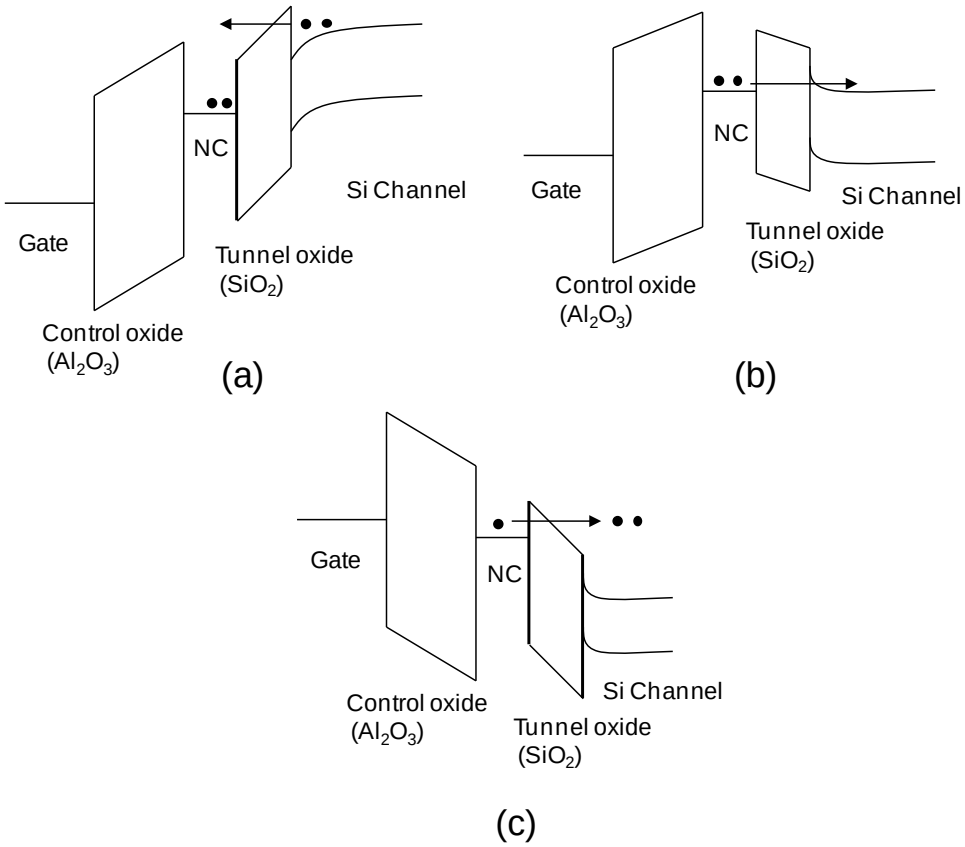

Figure 2.2. Schematic band diagram of a nanocrystal (NC) memory structure with SiO_2 as the tunneling dielectric and Al_2O_3 as the control dielectric under (a) write state (positive applied bias), (b) retention state and (c) erase state (negative applied bias).

2.4 Organic Electronics

Organic electronics has been the focus of a growing body of investigation in the fields of physics and chemistry for more than 50 years. Organic electronics, which could offer cheaper electronics and simpler device architectures compared to those based on silicon, has gained momentum for research. The key attraction of this field has been the ability to modify chemical structure in ways that could directly impact the properties of the materials when deposited in thin film form. Recent advances in devices such as organic field-effect transistors and organic light-emitting diodes (OLEDs), and the commercialization of organic-based devices such as OLED based flat panel displays (Sony, 2008), have shown capability of organic electronics to compete with silicon. There is a growing need to generate inexpensive and fast memory devices that are characterised by high densities and longer data retention times. Scott (2004) suggested that demand for new types of memory devices clearly exists and newcomer memory devices must exceed the existing speed and cost constraints of today's entrenched technologies. Organic electronics has the potential to produce such memory devices, having low-cost and high-performance, due to organic strength of potentially low fabrication costs.

2.4.1 Organic Based Memory Devices

Flash memory effect can also be realized in many polymer materials based on their resistance changes in response to an applied voltage. The ability to tailor the properties of organic materials, low fabrication cost, solution processing and good scalability give organic based memory devices many advantages over their conventional inorganic

counterparts. Moreover, solution processed organic material allows high-volume production and simplified fabrication techniques such as stamping, blade coating, ink-jet printing, and roll-to-roll processing (Muller et al., 2003; Fairley, 2004), and increases the commercial viability of these devices.

Choi et al. (2008) reported the fabrication and operation of novel programmable WORM memory based on nanoscale thin films of a soluble hyperbranched copper phthalocyanine polymer by means of conventional solution spin-coating technique. A variety of promising approaches, including reconfigurable and redox-active molecules (Liu et al., 2003; Bandyopadhyay and Pal, 2003; Chen and Reed, 2002; Luo et al., 2002), write-once mechanisms (Muller et al., 2003a) have recently been demonstrated. A switching effect in Cu-tetracyanoquinodimethane (Cu:TCNQ) charge transfer complex thin films (Oyamada et al., 2003), single-layer memory devices based on pentacene and tris (8-hydroxyquinoline) Aluminum (Tondelier et al., 2004; Mahapatro et al., 2004), memory effect from charge trapping in organic light-emitting devices (Kang et al., 2004), a WORM memory by burning polymer fuses (Muller et al., 2003b), conducting switching between three levels from supramolecular structure structures of Rose Bengal (Bandyopadhyay and Pal, 2004) and polymer memory device based on a novel copolymer of N-vinylcarbazole and Eu-complexed vinylbenzoate (Ling et al., 2005) have also been demonstrated.

2.4.2 Organic and Nanoparticle Based Hybrid Memory Devices

The metal nanoparticle-based polymer memory device is a promising technology in which a polymer matrix containing metal nanoparticles is sandwiched between a cross-point array of electrodes. These devices store data by existing in a high or low conductivity state via application of write or erase voltage across the memory cell, respectively.

Ma et al. (2002a,b,c) used a discontinuous evaporated metal layer in the middle of the polymer layer to trap charge. While, these memory devices have been shown to exhibit rewritable and non-volatile characteristics, are not commercialized yet due to large amounts of uncertainty and associated debate over the exact mechanisms that are responsible for the large change in conductivity between the on and off states of the devices. Some of the main theories that are still discussed in the literature may be broken down to the following categories: charge transfer between nanoparticles and an electron-donating species (such as 8-hydroxyquinoline) (Ouyang et al. 2004), conductive filament formation (Tondelier et al. 2004) and charge trapping leading to space-charge inhibition of injected current (Bozano et al. 2004).

The memory devices that can be classed as nanoparticle-based were proposed by Ma et al. (2002a,b,c, 2003), He et al. (2005) and Pyo et al. (2005). These devices consist of a trilayer structure of organic/metal-nanocluster/organic sandwiched between two aluminium electrodes. An organic semiconducting polymer, 2-Amino-4,5-imidazoledicarbonitrile (AIDCN) was used for the organic layers. The metal nanocluster

layer was formed in these devices by evaporating a thin metal layer in the presence of oxygen or AIDCN, forming discontinuous metal nanoclusters. They proposed that charge can be stored at either side of the nanocluster layer which significantly increases the conductivity of the devices, allowing 'digital bits' of information to be stored. Many combinations of metals (Ma et al., 2002a,b,c) and various layer thicknesses (Pyo et al. 2005) were studied. He et al. (2005) showed that switching mainly occurs in the bottom organic layer, due to the organometallic complex formed by evaporating the top contact, giving rise to an asymmetric device structure. It is also shown in this paper that devices can be made symmetric by deliberately introducing an Al_2O_3 layer under the top electrode.

Subsequently, Tondelier et al. (2004) also studied the same trilayer structure as well as devices without the middle metal-nanocluster layer. They found similar switching behaviour present even in the absence of middle metal layer and concluded that metal nanoparticles were included in the polymer layer due to thermal evaporation of the top electrode, with metallic filaments of nanoparticles forming in the polymer under high electric fields, giving rise to a high-conductivity on state.

Shortcomings of metallic contamination, formation of metal compounds, and non-uniformity in size and shape of metallic nanoparticles in the above mentioned memory devices can be overcome by including readymade nanoparticles in the devices (Tseng et al., 2004; Kato et al., 1987). Paul et al. (2003) demonstrated the first of these devices by incorporating a monolayer of gold nanoparticles via the Langmuir–Blodgett technique

into the insulating layer of metal–insulator–semiconductor (MIS) capacitors. Capacitance–voltage (C–V) characteristics for devices containing nanoparticles showed hysteresis when compared with devices without nanoparticles. This was attributed to injection of electrons onto the nanoparticles from the gate electrode that charges the nanoparticles which allows the data storage. Similar results were also demonstrated in MIS structures more recently by Leong et al. (2007, 2008).

Ouyang et al. (2004) demonstrated metal–insulator–metal (MIM) memory structures which comprised a mixture of gold nanoparticles capped with 1-dodecanethiol (Au-DT) and 8-hydroxyquinoline (8HQ) molecules in a polystyrene matrix, with the change in conductivity in these devices attributed to the transfer of electrons from the 8HQ molecules to the Au-DT. This positive and negative charging of the 8HQ and Au-DT, respectively, leads to a change in the conduction properties of the insulating film. Ouyang et al. (2005a,b) later studied MIM structures including nanoparticles capped with 2-naphthalenethiol embedded in a polystyrene matrix. Here, the proposed mechanism was a transfer of electrons from the capping ligands of the nanoparticles and the nanoparticle core itself. These devices exhibited WORM memory. Bozano et al. (2005) investigated the effect of nanoparticles using different metals, as well as the position of the nanoparticles in the structure and electrode material.

Other memory structures based on gold nanoparticle charge-transfer complexes have also been studied, with poly(3-hexylthiophene) (Prakash et al., 2006), poly(N-vinylcarbazole) (PVK) (Song et al., 2007; Lai and Chen, 2008) and 4-cyano-2,4,4-trimethyl-2-

methylsulphanylthiocarbonylsulphanyl-poly(butyric acid 1-adamantan-1-yl-1-methyl-ethyl ester) (PCm) (Lin et al., 2007), being used as both the electron donor material and the polymer matrix material. Recent articles by Kim et al. (2008), and Lai and Chen (2008) concluded that charge transfer onto the nanoparticles is responsible for the change in conductivity of the devices and carrier transport is via hopping of holes along the PVK polymer chains contrary to popular theory of electron tunneling through the nanoparticles. There are good research articles (Bozano et al., 2005; Yang et al., 2006; Scott and Bozano, 2007; Ling et al., 2008) which have summarized the work on nanoparticle-based organic memories.

Some of the characteristics of the recently demonstrated organic memory devices are given in the Table 2.1, which includes the materials used, memory mechanism and performance characteristics, including program time, program voltage for the device, the retention time of stored states and the ON/OFF ratio.

Unfortunately, owing to the variety of devices studied by different research groups (semiconducting or insulating polymer matrices, different nanoparticle capping ligands, differing metals, etc.), differences in the implementation of electrical testing methods and differences in the manufacturing procedures for different laboratories, it is very difficult to draw unanimous conclusion for a likely mechanism that could be responsible for every single case. However, from the point of view of the proposed theory of nanoparticle charging, where carriers are trapped on the nanoparticles, then experiments based on

Table 2.1. Examples of recently demonstrated two-terminal, programmable-resistance organic nonvolatile memory devices.

Material	Mechanism	Program time (s)	Program voltage (V)	Retention time	ON/OFF ratio	Reference
AIDCN	polarizing embedded metal clusters	$<10^{-8}$	2	> weeks	10^{5}	(Ma et al., 2002c)
Polystyrene w/gold nanoparticles	charge transfer to gold particles	10^{-8}	< 3	years	10^{4}	(Ouyang et al., 2004)
Polystyrene w/C60	charge transfer to C60	-	4-6	> months	10^{4}	(Majumdar et al., 2005)
Polythiophene	charge storage	-	1-2	> hours	10^{5}	Majumdar et al., 2004)
Rose Bengal film	molecular reduction and conformation change	-	4	> hours	10^{3}	(Bandyopadhyay and Pal, 2004)
Molecular SAM	redox leading to localization of orbitals	$<10^{-7}$	0.25-0.5	> 15 min	-	(Reed et al., 2001)
Rotaxanes	oxidation leading to conformation change	-	2-7	> 4 months	4 to 10^{2}	(Chen et al., 2003)
Cu-organic device	movement of Cu+ ions	10^{-3}	2	> months	10^{7}	(Ma et al., 2004)
Cu-TCNQ	charge transfer	-	10	-	10^{4}	(Oyamada et al., 2003)

capacitance measurements of MIS capacitors are much more sensitive to changes in trapped charge than I –V measurements of MIM devices. In conventional semiconductor MIS theory, the amount of trapped charges that are present in the insulating layer can be measured by studying the flatband voltage shifts of experimental capacitors compared to the theoretical ones (Nicollian & Brews 1982).

2.5 Polyimide Film

Polyimides (PIs) are materials frequently used by the microelectronics industry for interfacial modification because of their excellent mechanical properties, high thermal stabilities, and favorable dielectric properties for use as insulating layers. Normally, polyimides are deposited onto substrates in a two-step process by spin casting a thin film from a solution of the poly(amic acid) followed by thermal curing to convert the poly(amic acid) into the imide. The viscosity of polymer solution and rate of rotation, limit the thin film thickness obtainable by spin casting.

2.5.1 Polyimide Films for Memory Devices

Films of polyimides containing electron donor and electron acceptor groups are capable of exhibiting bistable behavior. The memory properties can be tuned by tailoring the molecular structure of PIs. Dynamic random access memory (DRAM), write-once read-many-times (WORM) memory and rewritable flash memory have been demonstrated by selecting PIs with electron donating and/or withdrawing groups of proper strengths, and with suitable arrangements of the donors and acceptors in the structure (Ling et al., 2006, 2007). The Langmuir Blodgett technique has also been used to fabricate memory devices

based on PIs (Takimoto et al., 1992). Hahm et al. (2009) fabricated electrically programmable nonvolatile memory devices based on based on a high performance synthesized polyimide, poly(3,30-bis(diphenylcarbamyloxy)-4,40-biphenylene hexafluoroisopropylidenediphthalimide) having high thermal and dimensional stability. Devices exhibited excellent ON and OFF switching behavior with very low power consumption.

2.5.2 Nanoparticles Embedded Polyimide Films for Memory Devices

A monolayer of Fe_2O_3 nanoparticles embedded in a polyimide (PI) matrix was fabricated by oxidizing a Fe metal film between two PI precursor layers (Lim et al., 2004). Jung et al., (2006) reported nonvolatile electrical bistability properties for chemically self-assembled, uniformly distributed cuprous oxide (Cu_2O) semiconductor nanoparticles in polyimide matrix. 10–30 nm thick Cu films were deposited onto Si or quartz substrates using a thermal evaporator. The PI precursor was spin coated; then the samples were soft baked at 135 °C for 30 min to evaporate the solvent. The thin film stacks were cured at 400 °C for 1 h in N_2 atmosphere in order to polymerize the polyamic acid into PI. The metal oxide particles embedded in PI were produced during imidization of the polyamic acid (Chung et al., 2003). Ni, SnO_2 and Au nanoparticles embedded in the PI matrix were also demonstrated to function as charging and discharging islands in floating gate memory structure (Kim et al., 2005, 2007; Lee et al., 2009). Zhen et al. (2008) fabricated an all-organic memory device based on a copper phthalocyanine (CuPc) thin-film transistor using gold nanocrystals embedded in a polyimide gate dielectric.

2.6 Motivation for the Present Study

So far, expensive processes such as vacuum evaporation or high temperature processing have been mainly used to form nanoclusters for the nanoparticle-based memory devices. Moreover, organic layers are susceptible to damage due to thermal budget (Kolosov et al., 2001) and resulting nanoparticles are non-uniform in size and shape during these processes. For the realization of metallic nanoparticle memory devices, requirements include the formation of high density and uniformly distributed nanoparticles (Liu et al., 2002a; Tsoukalas et al., 2005). A large spatial density enhances the charge storing capability of the floating layer, while a high degree of size uniformity ensures reproducible storage characteristics.

In the case of pre-synthesized nanoparticles used in spin coating based memory devices, spun cast polymer nanoparticle blends where nanotraps are randomly distributed throughout the host matrix result in uncontrolled nature of particle size distribution. Randomly distributed nanoparticles may show non-uniform device performance, since there are different numbers of nanoparticles within each unit device. Solution processing approach has the potential for fabricating low-cost and large-area organic-nanoparticle hybrid memory devices at the room temperature. Assembly based solution processed layer-by-layer deposition technique can easily facilitate fabrication of multistack layer nanoparticle structures, resulting in high density of nanoparticles which is a requirement for high capacity memory devices.

2.7 Device Fabrication Methods

2.7.1 Spin Coating Technique

Spin coating is commonly used technique for flat substrates which involves preparing the material to be coated on by dispersing or dissolving it into a solvent, depositing it onto the surface and spinning up the substrate at a high velocity to thin the fluid on the surface and fling off excess solvent. The thickness of the coating can be usually adjusted by varying the viscosity of the solvent and changing the spin rate. A higher spin rate and less viscous solvent can be used if a thinner film is desired.

However, there are many limitations of spin coating such as requirements of minimum solvent dilution and maximum spin rate to obtain ultra thin films. Also many common defects such as comets, striations and wafer edge effects plague the usefulness of spin coating. Wafer edge effects cause a huge amount of wastage because coating thickness cannot be maintained at the edges of the wafer. Surface tension effects will make it difficult for the solution that is flowing outwards to detach from the edge of the wafer and cause it to have a higher thickness at the rim area.

Currently, spin coating is the widely used method of coating organic thin film layers for memory devices applications. As mentioned earlier, with the rapidly shrinking sizes of many electronic components, we are forced to look at alternative methods to match the advancement in technology due to smaller sizes. Furthermore, spin coating is a physical deposition process and it becomes less feasible when the surface to be coated either

becomes smaller or uneven. It may become necessary to coat an irregularly shaped object with a uniformly thick protective film.

Due to technological developments at the nano-scale, bottom-up approach is preferred against top-down approach to achieve small-sized structures. This implies building up from smallest level to the required size to keep up with current decreasing sizes. Using the idea of building 'upwards' from the smallest level, we begin the construction from the molecular level. Layer-by-layer (LbL) assembly is an important technique that is capable of yielding such ultra thin films. Controlled stepwise growth of multilayer architecture requires efficient means of connecting individual layers.

2.7.2 Langmuir-Blodgett Films

The Langmuir-Blodgett (LB) technique is a well-established method for preparing ultra thin and relatively defect-free organic films of controlled thickness. The appealing feature of LB technique is the intrinsic control of the internal layer structure down to the molecular level and the precise control of resulting film thickness. In this technique, a known amount of amphiphilic material dissolved in a water-immiscible, volatile organic solvent such as chloroform is placed on the surface of a subphase (usually ultra-pure water). After evaporation of the solvent, the monolayer material is compressed with movable barriers to form a monolayer, referred to as a Langmuir monolayer. Next, the Langmuir monolayer is transferred onto a solid support via up-and-down strokes of the latter through the air-water interface. This technique is capable of producing relatively ordered and defect-free multilayer films, but the weak interlayer binding force, which is

simply van der Waals interaction, might result in the film not stable enough against thermal, chemical or mechanical degradation (Ulman, 1991).

2.7.3 Electrostatic LbL Films

The sequential adsorption of polyanions and polycations on charged surfaces has been known as a simple and versatile method for preparation of stable ultra thin multilayer films (Decher, 1997; Bertrand et al., 2000), in which neighboring layers are firmly held together by electrostatic interactions. The films are grown in a layer by layer manner by first immersing a charged substrate into an aqueous solution containing an oppositely charged polyelectrolyte, followed by rinsing and then immersion of the substrate into a second polyelectrolyte of opposite charge to the first. Thickness of individual layers can be controlled by ionic strength of the adsorption solution, higher concentrations of small electrolytes yielding thicker layers (Decher and Schmitt, 1992). Variations of the layer thickness by control of the polyelectrolyte and surface charge density with pH have been demonstrated using weak electrolytes (Yoo et al., 1998). The multilayer films made in this way are not well ordered at the molecular level and characteristically exhibit considerable interpenetration between the adjacent layers (Baur et al., 1999).

The main disadvantage with this method lies in that the resulting films will be pH-sensitive and may degrade in acidic or basic environments since the multilayer architecture is built up on basis of electrostatic interaction. Moreover, for example the polycation introduced as the counterpart of poly(amic acid) for self-assembly often

remains in the final film; it will be a chemical impurity if not removed properly and may cause undesired effects on the film.

2.7.4 Covalent Assembly

Covalent-bonding self-assembly is advantageous over LB technique and electrostatic self-assembly in the sense that each layer in self-assembled film can be covalently linked to its underlying layer and no excess deposition can take place as it is limited by the reactive sites on the layer surface. In this technique, the molecules are transferred to the surface of a solid substrate from the liquid or vapor phase containing self-assembling material by a dipping process and subsequently, a highly organized and densely packed molecular layer forms spontaneously on the substrate. The formation of the self-assembled monolayer is driven by strong interaction between the substrate and a surface-specific functional group of the adsorbent.

2.8 Fabrication Methods for Nanoparticle Containing Hybrid Structures

2.8.1 Spin Coating Technique Based

Andres et al. (1996) prepared an array of metallic nanoparticles by spin casting a dilute solution of the particles prepared by gas phase synthesis. The particles were then interconnected by displacement of the capping dodecanethiol by aryl-bisisocyanide molecules. Taranekar et al. (2008) described the preparation and properties of an

electrochemically crosslinked Au nanoparticle/polyvinylcarbazole (PVK)/polyfluorene (PFC) nano-composite film. Blends of the blue-light emitting PFC, PVK, and the 11-(9H-carbazol-9-yl)-undecane1-thiol-capped Au nanoparticles were prepared as thin films by spin-coating and subsequent crosslinking by cyclic voltammetry. Liu et al. (2003) reported the fabrication of self-assembled gold nanoparticles attached to 3-aminopropyltrimethoxysilane (APTMS) modified fused silica substrates by the spin coating method. Uniformly dispersed gold nanoparticles were obtained on fused silica substrates with high packing density within short fabrication time.

2.8.2 Assembly Based

2.8.2.1 Langmuir-Blodgett Assembly Based

Langmuir monolayers of nanoparticles offer distinct advantages over dropcast thick films in that the inter-particle structure can be well defined by the precise mechanical compression at the air/water interface and hence the inter-particle spacing. Nanoparticles into LB films can be incorporated using a metal salt solution as the subphase in the fabrication of a polymer LB film, followed by metal ion reduction. This method offers considerable possibilities for particle-film synergy, molecular-level control over film thickness and particle size and distribution. The metal ion in the subphase can also help to stabilize the Langmuir monolayer and facilitate high quality film transfer. The metal salt can be reduced to form metal nanoparticles in situ inside the LB stacks by exposure to a reducing gas such as N_2H_4 (Elliott et al., 1995, 1998), CO (Elliot, 1997) and H_2 (Hemakanthi and Dhathathreyan, 1999), or by photoreducing under UV light (Zhang et

al., 2002). Swami et al. (2003) demonstrated that the spontaneous reduction of chloroaurate ions present in the subphase by Langmuir monolayers of HAD (4-hexadecylaniline) leads to the formation of highly oriented, flat gold sheets and ribbon like nanocrystals bound to the monolayer.

Markovich et al. (1999) studied the electrical characteristics of a Langmuir monolayer of alkanethiolate-protected silver nanoparticles. Nanoparticle electronic conductivity properties have also been probed more directly by measuring the current–potential responses of their Langmuir–Blodgett thin films (Kim et al., 1999; Sampaio et al., 2001; Cassagneau et al., 1998). Lee et al. (1997) used a microband electrode to directly measure the I–V response of a monolayer of alkanethiolate-passivated gold nanoparticles at the air/water interface. Chen (2003) has examined the charge-transfer chemistry for the Langmuir monolayers of gold nanoparticles having alkyl spacers of varied chain lengths at the air/water interface. The results demonstrated a transition of the particle monolayer (lateral) conductivity characteristics from that of semiconductors (rectified charging) to that of conductors (linear or ohmic). Langmuir–Blodgett technique was employed to prepare monolayers of dodecanethiol-capped gold nanoparticles resulting in an interconnected array of gold nanoclusters (Bourgoin et al., 1998). Heriot et al. (2006) investigated properties of 4-methylbenzenethiol capped gold nanoparticles at the air–water interface. Pure 4-methylbenzenethiol does not form monolayer films at the air–water interface. However, isotherms of gold nanoparticles capped by 4-methylbenzenethiol reveal a stable monolayer even though their chemical structure is very different to the classical amphiphilic features normally associated with Langmuir

film-forming materials. The isotherm exhibits two-dimensional gas, liquid and solid-like phases with collapse of the monolayer at higher surface pressures. The Langmuir-Blodgett deposition of gold nanoparticles passivated with tri-n-octylphosphine oxide/octadecylamine has been reported for flash memory applications (Paul et al., 2003).

2.8.2.2 Electrostatic Assembly Based Polymer Nanoparticle Multilayered Structures

Hybrid ultrathin films composed of polymers and inorganic nanoparticles hold great promise due to their potential applications in the design of electronic, optical, electrooptical, magnetic devices and sensors (Jin et al., 2001; Sohn and Seo, 2001; Musick et al., 2000; Damle et al., 2000; Rajeshwar et al., 2001; Hammond, 2000; He et al., 1999; Schuetz and Caruso, 2002; Joly et al., 2000; Liu et al., 1998; Trindade, 2001; Cassagneau et al., 1998; Lesser et al., 1999; Fendler, 2001). The electrostatic LbL assembly of nanoparticles and polyelectrolytes is regarded as one of the most simple and versatile method for the construction of ultrathin organized multilayers. Gold nanoparticle (AuNP) composite film was prepared via LbL assembly using dodecylamine-stabilized AuNPs as the main building blocks and hexadecanedithiol or poly (propyleneimine) dendrimer as the linking agent; the dodecylamine ligand was exchanged with thiol or amino dendrimer during film assembly (Joseph et al., 2004). According to Isaacs et al. (2006), these films might lack stability compared with polymer linked nanoparticle assemblies due to much smaller number of linking groups in dendrimer or dithiol than in the polymer linkers.

Multilayer films of AuNPs and a water-soluble poly (vinylimidazole) complex with osmium (4,4'-dimethyl-2, 2'- bipyridine) chloride were deposited on a glass carbon electrode via electrostatic LbL assembly (Qian et al., 2005). Multilayered AuNP thin films on aminosilane functionalized quartz slides were fabricated using LbL assembly with poly(allylamine hydrochloride) (PAH) (Zhang and Srinivasan, 2008). Jiangs et al. (2007) investigated optical and dielectric properties of hybrid ultrathin LbL films of AuNPs and polyelectrolytes under different pH conditions which resulted in surface plasmon resonance signal enhancement under attenuated total reflection spectroscopy conditions.

Lee et al. (2007) described a versatile approach for preparing flash memory devices composed of polyelectrolyte/gold nanoparticle multilayer films using the LbL approach. The memory capacity per unit area was significantly increased by increasing the number of PE/AuNP layers. Jiang et al. (2007) reported a write-read device for LbL films based on conjugated polymers using current-sensing atomic force microscopy. Das et al. (2007) reported electrical bistability for electrostatic assembled multilayers films composed of CdSe quantum dots. Lee et al. (2009) fabricated resistive switching memory device using the LbL approach to assemble titania precursor/poly(allylamine hydrochloride) multilayer films on platinum electrodes.

2.8.2.3 Covalent Assembly Based

Hybrid films constructed through the LbL method, having electrostatic interaction can be altered or even destroyed through variable solution conditions, especially high ionic

strength (Dubas and Schlenoff, 2001; Kovacevic et al., 2002; McAloneyet al., 2003; Izumrudov and Sukhishvili, 2003; Sui and Schlenoff, 2004; Morgan et al., 2007). Fu et al. (2002) have prepared covalently attached hybrid films by the photolysis of LbL self-assembly multilayer films using diazo-resins (DAR) and sulfonate-capped colloidal AuNPs. Covalently bound 3D superstructure on quartz wafer, Si slide and glassy carbon electrode were synthesized using DAR and citrate stabilized AuNPs by LbL self-assembly and UV irradiation; such multilayer films of colloidal AuNPs were excellent uniform and stable (Bai et al., 2006).

Multilayer films of Ag-NPs have been fabricated from Ag-NPs and a bifunctional molecule as the crosslinker (Musick et al., 2000). Later, the stability of such films toward polar solvents was enhanced through covalently attached polymer/Ag-NP film. Covalent binding between polycations of nitro-diazoresin containing polymeric films and hydroxy groups containing Ag-NPs was carried out by UV irradiation (Conghua et al., 2003). A composite thin film consisting of AuNPs and polyimide was fabricated through LbL assembly. Zhang and Srinivasan (2007) synthesized multilayered composite films comprising polyimide and AuNPs. The binding between AuNPs and amino poly(amic acid) (APAA) (bearing amino pendant groups) chains was found to be mainly based on coordination chemistry, which is advantageous over electrostatic interaction or van der Waals force in terms of robustness of the composite structures formed.

2.8.2.4 Dendrimers Based

Dendrimer Encapsulated Metallic Nanoparticles

Dendrimers constitute a unique class of macromolecules that are distinguished from others by their globular shape, resulting from their perfectly branched architecture and monodisperse nature (Tomalia et al., 1985; Frechet, 1994; Newkome et al., 1996). Dendrimers can serve as templating agents and stabilizers in the synthesis of metal nanoparticles. Dendrimer based synthesis offers the possibility of synthesizing nanoparticles with controlled, uniform size on the nanometer scale. By controlling the chemical structure and size of the dendrimers, different-size clusters can be prepared. Previous work has employed poly(amidoamine) (PAMAM) dendrimers because they are well characterized (Zeng and Zimmerman, 1997; Bosman et al., 1999; Juris, 2003; Boas and Heegaard, 2004) and commercially available. The chemistry of PAMAM features interior amide and amine groups that physically coordinate with metal cations or covalently bond with metal precursors through ligand exchange reactions. The branched structure terminates in exterior chemical groups (primary amine, hydroxyl and carboxyl) useful for subsequent functionalization, molecular recognition, and binding to surfaces (Crooks et al., 2001b). The hyperbranched molecular architecture creates interior voids that can accommodate guest molecules or metal nanoparticles. However, the necessity of packing many branches into a limited space results in steric constraints that decrease the conformational flexibility of the PAMAM molecule as the generation number increases.

To prepare PAMAM-stabilized metal nanoparticles, one mixes metal precursor with PAMAM in water or organic solvents. The mixture equilibrates for a certain time, from a few minutes to several days, depending on the metal precursor and the way it interacts

with the dendrimer. Addition of $NaBH_4$ or H_2 gas reduces the metal to zero valence. The metal atoms coalesce to produce the final dendrimer-stabilized nanoparticles. PAMAM dendrimers act as both template and stabilizer for preparing nanoparticles with controlled size and minimal surface passivation. Encapsulation occurs if the reduced metal nanoparticles are trapped within the dendrimer interior, producing dendrimer-encapsulated metal nanoparticles. Various transition metal nanoparticles have been synthesized this way (Crooks et al., 2001a,b; Esumi, 2003; Scott et al., 2003; Oh et al., 2003; Kim et al., 2004; Ye et al., 2004; Gu et al., 2005) .

Zhao et al. (1999) reported loading of fourth-generation polyamidoamine starburst dendrimer with Pt^{2+} which was chemically reduced in situ to yield a dendrimer-encapsulated metal cluster. The clusters were monodisperse and very stable, and when attached to an electrode surface, they acted as efficient electrocatalysts for O_2 reduction. Nanoparticles of platinum were prepared by reduction of their metal salts with $NaBH_4$ in the presence of generations 3, 4 and 5 of poly(amidoamine) dendrimers (Esumi et al., 2000). Manna et al. (2001) and Esumi et al. (2000) reported the synthesis of silver and gold metal nanospherical particles stabilized by the fourth-generation poly(amido amine) (G4 PAMAM) dendrimer.

Nickel nanoparticles were prepared with in the sixth generation PAMAM templates functionalized on their periphery with alkyl groups. The metallic nanoparticles indicate are ferromagnetic and exhibit low hysteresis and suppressed magnetic saturation, both of which are directly correlated to the small size of the particles (Knechet et al., 2006). Lang

et al. (2003) reported the successful preparation of supported metal catalysts using dendrimer-encapsulated Pt nanoparticles as metal precursors. PAMAM dendrimers were first used to template and stabilize Pt nanoparticles prepared in solution. These dendrimer-encapsulated nanoparticles were then deposited onto a commercial high surface area silica support and thermally activated to remove the organic dendrimer. The resulting materials are active oxidation and hydrogenation catalysts.

Acosta et al. (2004) demonstrated that the complex organic-inorganic hybrids can be formed wherein the organic dendrimers can be grown directly off the solid support of SBA-15 and also controlled the porosity by constructing different generations of dendrimers. Similarly Jiang and Gao (2006) anchored catalytically active nanoparticles in porous matrices using dendrimeric components as sequestering agents. The catalysts show highly catalytic activity for the hydrogenation of allyl alcohol. Importantly, the hydrogenation rate and selectivity can be controlled by using different generation dendrimers. Additionally, the catalysts are stable enough to be recycled multiple times and preserved for one month under ambient conditions, while maintaining the catalytic activity.

Nanoparticles in Immobilized Dendrimers

He et al. (1999) reported the electrostatic layer-by-layer assembly of the gold-dendrimer nanocomposite using poly(sodium 4-styrenesulfonate) as the oppositely charged polyelectrolyte leading to formation of nanoscale uniform multilayers of gold-dendrimer nanoclusters. In a similar work, Luo et al. (2003) reported the assembly of ultrathin films

using a Ag-PAMAM dendrimer nano-composite as the polyanion and diazoresin as the polycation, and subsequent conversion of the electrostatic bond between layers to covalent. Pd and Pt nanoparticles prepared within dendrimers have been immobilized on to Au surfaces via covalent amide bond formation between the unquaternized amine groups on the dendrimer periphery and anhydride-activated self-assembled monolayers (Oh et al., 2003). Crespilho et al. (2006) prepared LbL films of PAMAM dendrimer incorporating platinum nanoparticles alternated with poly(vinylsufonic acid) (PVS) using formic acid as reducing agent. Nano sized Pt nanoparticles were grown in the presence of PAMAM molecules and the LbL films were employed as methanol-tolerant cathodes for oxygen electroreduction.

Sun et al. (2002) have shown that sixth generation of PAMAM dendrimers can serve as a convenient mediator for immobilizing small catalytic particles onto flat model surfaces. Immobilization can be achieved either through adsorption of dendrimer-encapsulated particles or through surface synthesis reactions after adsorption of empty dendrimer hosts. Ye and Crooks (2005) fabricated platinum dendrimer-encapsulated nanoparticles within fourth generation, hydroxyl-terminated, (polyamidoamine) dendrimers and immobilized on glassy carbon electrodes using an electro chemical coupling strategy.

Joo et al. (2006) reported application of PAMAM-OH dendrimer for nonvolatile organic resistive memory. The bistability was realized in the PAMAM device by electronically controlling the density of the copper ions within the dendrimer layer. The copper ions were captured at the binding sites such as amine of PAMAM groups resulting in decrease

of the device resistance. The formation of covalently bonded, multilayered, dendrimer-containing ultrathin films and formation of Cu, Au, and Pd–Pt, Fe–Ni nanoparticles within the thin film matrix using supercritical carbon dioxide ($SCCO_2$) as a processing medium has been investigated (Puniredd and Srinivasan, 2007a,b; Puniredd et al., 2008). Puniredd et al. (2009) demonstrated that the dendrimer encapsulated Pt nanoparticles can be effectively employed for the construction of metal-insulator-semiconductor (MIS) devices by covalent molecular assembly in $SCCO_2$. Significant charge storage capability of the nanoparticle memory devices were demonstrated under low operation voltage, with sufficient retention time obtained.

2.9 Large Area Memory Devices

2.9.1 Nanoparticles on Patterned Surfaces

The demand for methods to create sub-micron and nanoscale features is increasing in several different fields: optics, photonics, sensors, bio-chips, genomics, proteomics, organic electronics etc. Being able to place nano-objects at the desired position is of highest interest for the possible integration of these building blocks into devices (Ozin et al., 2005). Integration of nanoparticles with high accuracy inside circuits is a promising route for the development of photonic devices, high-density patterned media, and catalysis (Antonietti and Ozin, 2004). The possibility to form regular arrays of metallic nanostructures on semiconductor surfaces opens a large spectrum of applications in electronic (Schnippering et al., 2007; Bratton et al., 2006), photonic (Langhammer et al., 2006) and biosensing (Alivisatos, 2004).

Nanoparticle based memory devices will have added advantage after controlling trap density and the distribution in the memory devices. For significant commercial applications, these devices can be integrated into large arrays. The synthesis of metallic nanostructures and the control of their spatial arrangement at the nanoscale by means of block copolymer (BCP) self-assembly has been shown to be very attractive and powerful alternative (Boontongkong and Cohen, 2002; Aizawa and Buriak, 2005; Krishnamoorthy et al., 2006; Kim et al., 2010). The synthesis of nanoparticles in BCP micelles solves the problem of particle size control and stabilization compared to classical stabilization systems that employ surfactants (Daniel and Astruc, 2004; Jun et al., 2001; Turkevich et al., 1951) or microemulsions (Brust et al., 1994; Wang et al., 2006). Recently, the production of ordered arrays of nanoparticles (Boontongkong and Cohen, 2002; Hinderling et al., 2004) and linear patterns (Chai et al., 2007) made of various metals (Pt, Au, Pd) have been demonstrated, by taking advantage of different affinities of the metallic precursors with amphiphilic BCPs (Forster and Antonietti, 1998; Sohn et al., 2003). Guarini et al. (2003) fabricated a silicon nanocrystal floating-gate memory using block copolymer self-assembly. Recently, Leong et al. (2008) fabricated two-terminal devices using gold nanoparticles synthesized within a block copolymer (polystyrene-block-poly(4-vinylpyridine) over a pentacene layer. The devices demonstrated charge storage because of charge exchange between the nanoparticles and pentacene. The block copolymer acted as the insulating material and the nanoparticles served as floating gate charge storage centers.

CHAPTER 3

COPPER NANOPARTICLES EMBEDDED IN A POLYIMIDE FILM FOR NONVOLATILE MEMORY APPLICATIONS

3.1 Introduction

Memory devices utilizing metal nanoparticles embedded in polyimide (PI) layer have been reported where nanoparticles were formed through reaction of metal film during curing of the PI precursor at a high temperature (Kim et al., 2005, 2007; Lee et al., 2009). However, high temperature processing results in diffusion of metal atoms into the thin dielectric tunnelling oxide and causes the discharging paths from nanoparticles to the substrate (Tan et al., 2005). This chapter describes the formation and characterization of a simple, solution processable and low-cost hybrid metallic copper nanoparticles (CuNPs)/PI film system and its application for nonvolatile memory devices. Nanoparticles containing PI film was fabricated by spin coating a solution of the nanoparticle precursor (copper acetylacetonate) and polyimide precursor (polyamic acid) to form a thin film and both precursors were converted to CuNPs and polyimide, respectively, by thermal treatment. The resulting films were characterized by X-ray photoelectron spectroscopy, atomic force and scanning electron microscopies. AFM and FESEM images revealed that the embedded nanoparticles are fairly tightly distributed in terms of size with an average diameter of 7 nm. Capacitance-voltage measurements at 300 K showed that the embedded CuNPs functioning as a floating gate in metal-insulator-semiconductor-type capacitor exhibited a hysteresis window of 1.52 V at an applied voltage of 8 V.

3.2 Experimental Section

3.2.1 Materials

4,4'-Diaminodiphenyl Ether (DDE) (>98%, Fluka), Pyromellitic dianhydride (PMDA) (97%, Aldrich), Copper acetylacetonate ($Cu(acac)_2$) (Aldrich), tetrahydrofuran (THF) (≥ 99 %, Merck) and N, N-dimethylacetamide (DMAc) (≥ 99 %, Merck) were used directly without further purification. Their molecular structures are shown in Scheme 3.1. Silicon wafers <100> (Chartered Semiconductor, Singapore) were 0.6 mm thick, p-doped, polished on both side and having 4 nm thermally grown oxide layer.

3.2.2 Substrate Preparation

Silicon wafers were cut into 1.5 cm * 1.5 cm pieces, cleaned by successive sonication in methanol and acetone for 30 min each, and later treated with "piranha solution" (7/3 (v/v) mixture of concentrated sulfuric acid and 30 % hydrogen peroxide) at 75 °C for 45 min (*Caution: Piranha solution reacts violently with organic matter*). They were then copiously rinsed with deionized water, blown dry with nitrogen, and dried at 100 °C under vacuum for 30 min.

3.2.3 Preparation of poly (amic acid)

A 50 mL round bottom flask equipped with a magnetic stirrer was used for this purpose, and the flask was fitted with a tube for delivering nitrogen gas. 0.5 g (0.0025 mol) bis (4-aminophenyl) ether was dissolved in 8 mL of DMAc. Then, 0.545 g (0.0025 mol) solid PMDA was added to this solution with an additional 2 mL of DMAc. Nitrogen gas was introduced into the flask to provide a dry, inert ambient environment. Then, the system was maintained under slightly positive nitrogen pressure and the mixture was stirred for

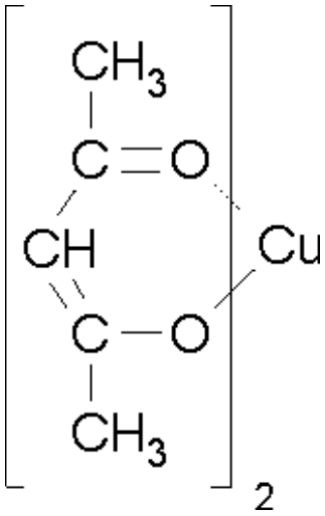

Cu (acac) 2

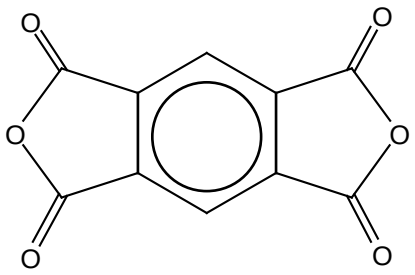

PMDA

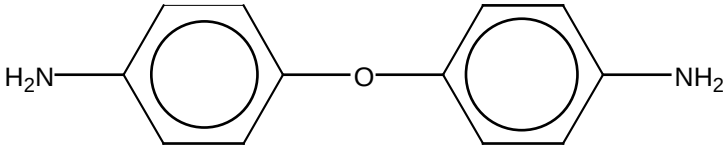

DDE

Scheme 3.1. Molecular structures of the main materials used.

4 h at room temperature to obtain a yellow, viscous solution. If not used immediately, the poly (amic acid) (PAA) would then be stored at -10°C until needed, because the source materials of PAA are moisture-sensitive.

3.2.4 Preparation of poly (amic acid) Films

Silicon substrate was placed on the vacuum chuck of a spin-coater (SCS, USA). A small volume of PAA was poured onto the centre of the substrate. Then the chuck was spun at 2000 rpm for 30 s. The concentration of PAA was adjusted such that resulting film thickness was around 45-50 nm. The film-laden substrate was further dried for 1 h at 80 °C under the vacuum to remove most of DMAc. The samples were then placed in a desiccator, if not used immediately.

3.2.5 Introduction of Copper Precursor

Synthesis of surface-metalized polyimide films via in situ reduction of metal complexes in a poly(amic acid) precursor is widely reported in the literature (Southward et al., 1998, 1999; Rubira et al., 1998). A similar approach used to synthesize films from a blended solution was employed in this experiment. $Cu(acac)_2$ (10 wt%) was added to DMAc solutions of PAA. All the synthesis and mixing procedures were performed under nitrogen atmosphere. The solution was then stirred for 2 h until the solute completely dissolved and a viscous, green solution without suspended material was formed. The solution was spin-coated on clean dry silicon substrate at 2000 rpm for 30 s, dried in a vacuum oven at 30 °C for 1 h and continuously heated at 80 °C for another 1 h to remove

most of the solvent (DMAc). PAA and copper precursor ratio was adjusted to give 5 wt % of precursor amount and film thickness of ~ 50 nm.

3.2.6 Polyimide Conversion through Chemical Imidisation in Benzene

Chemical imidisation was accomplished using a three-solvent mixture. The base-solvent was benzene, while the dehydrating agent was acetic anhydride and the catalyst used was pyridine. The volumetric ratio of benzene: acetic anhydride: pyridine was 1000: 143: 107. During chemical imidisation, the substrates containing dried poly (amic acid) films were immersed in the liquid mixture at a room temperature. After 24 h, the substrate was rinsed copiously with benzene and dried at 80 °C under the vacuum for 1 h to remove benzene.

3.2.7 Reduction of Copper Precursor

The precursor-laden films were heated at 250 ^{o}C for 2 h in presence of hydrogen and nitrogen (1:3 by volume) to decompose the acetylacetonate complex to metallic copper nanoparticles. Precursor containing PAA films were also converted to PI apart from formation of copper nanoparticles through this process.

3.2.8 MIS Capacitor Fabrication

A metal-insulator-silicon (MIS) capacitor device was fabricated. Following the formation of copper nanoparticles, gold top electrodes (0.3 mm diameter size) are then sputter-deposited using shadow mask technique subsequently. After removing the oxide, Pt film

was deposited as the back side contact. The MIS device configuration is shown in Figure 3.1.

3.2.9 Characterization

(1). X-Ray Photoelectron Spectroscopy (XPS)

XPS measurements were made on a Kratos Analytical AXIS HSi spectrometer with a monochromatized AlKα X-ray source (1486.6 eV photons) at a constant dwell time of 100 ms and a pass-energy of 40 eV. The X-ray source was run at a reduced power of 150 W. The pressure in the analysis chamber was maintained at 7.5 $\times 10^{-9}$ Torr or lower during each measurement. All binding energies (BEs) were referenced to the C1s hydrocarbon peak at 284.6 eV. In curve fitting, the full width at half-maximum (FWHM) for the Gaussian peaks was maintained constant for all components in a particular spectrum.

(2). Atomic Force Microscopy (AFM)

The surface morphology of the films was examined by AFM (Atomic Force Microscopy NanoScope IIIa, Digital Instruments). All images were collected in air using the tapping mode and a monolithic silicon tip. The drive frequency was 330 $\pm$ 50 kHz, and the voltage was between 3.0 and 4.0 V. The drive amplitude was about 300 mV and the scan rate was 1.0~1.5 Hz.

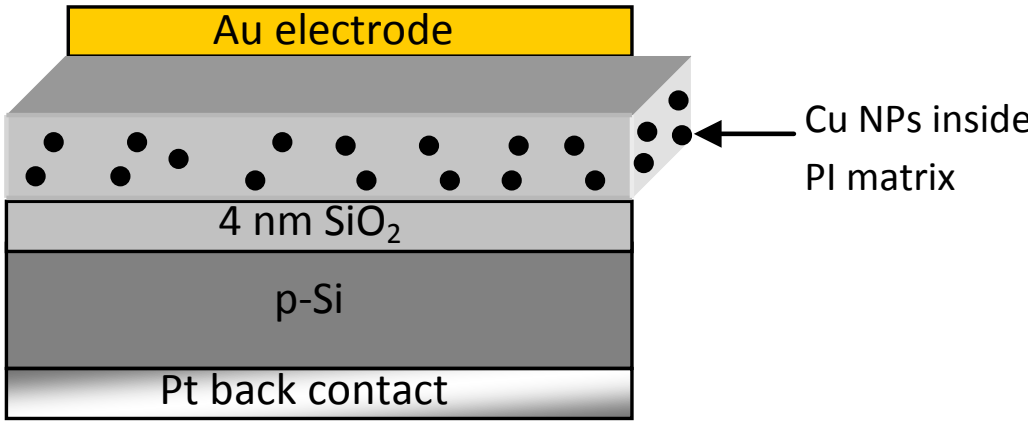

Figure 3.1. Schematic of MIS device structure.

(3). Field Emission Scanning Electron Microscopy (FESEM)

The surface morphology of the nanoparticle containing films was examined by FESEM (JSM-6700F, JEOL Japan).

(4). Capacitance–voltage (C–V) and Capacitance–time (C–t) Measurement

The memory behavior of the MIS device is investigated by means of capacitance-voltage (C-V) and capacitance decay (C-t) measurements. All measurements were performed using HP4284A Precision LCR meter at frequency of 100 kHz.

3.3 Results and Discussion

3.3.1 X-Ray Photoelectron Spectroscopy

The surface chemical state of the Cu-PI composite film was investigated by a surface spectroscopic technique. The XPS data for Cu 2p after reduction process is shown in Figure 3.2A. The spectra of XPS are restricted to the energy range of 925-980 eV, in the immediate vicinity of the Cu 2_P levels, localised at 932.6 eV ($2p_{3/2}$) and 953 eV ($2p_{1/2}$) binding energies for metallic copper (Chastain, 1992). The binding energy for Cu^{2+} in copper oxide is 933.6 eV ($2_{P3/2}$) from the XPS handbook (Chastain, 1992). The binding energy for Cu^{+} is 932.5 eV ($2_{P3/2}$), very close to that for the metallic copper (932.6 eV, $2_{P3/2}$). Since the position of absorption peak ($2_{P3/2}$) was at the binding energy of 932.6 eV and none of the satellite structure associated with Cu^{2+} was observed in the spectra, it is

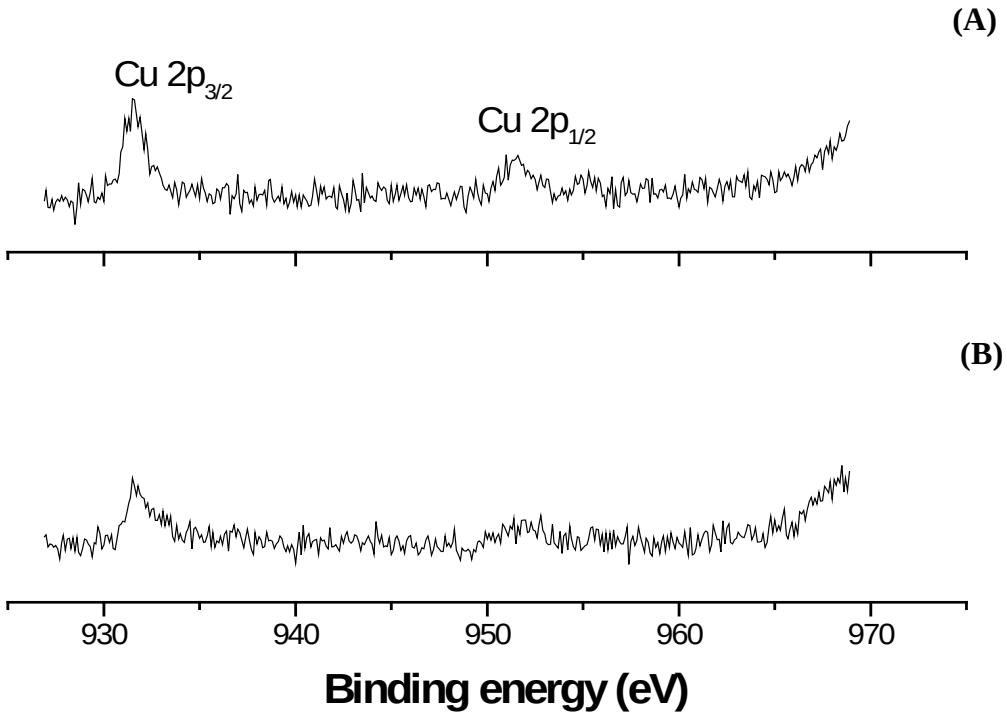

Figure 3.2. XPS wide scans for copper nanoparticle containing PI film. (A) 1 day after reduction (B) 15 days after reduction.

suggested that no Cu^{2+} species were present in the film. Differential charging of Cu clusters on the polyimide film makes it impossible to distinguish Cu^{+} from Cu^{0} at the interface using XPS. Hence, the Cu 2p spectra on the surface are present here in either the +1 or 0 valence states due to the +1 valence state not being ruled out unambiguously on the basis of these data (Pertsin and Pashunin, 1991). The stability of the metallic form of the CuNPs against oxidation in the ambient environment even after 15 days is observed from the XPS scans in Figure 3.2B.

3.3.2 Surface Morphology

Figure 3.3 shows AFM images for copper nanoparticles embedded PI film. The height (Figure 3.3A) and phase (Figure 3.3B) images show presence of nanoparticles on the surface with some height fluctuations. Figure 3.3C presents the surface height profiles along the lines drawn in the flattened images. The vertical distance between the highest and the lowest positions (on average), as marked by arrows in both the image and the height profiling curve, be associated with the dimension of CuNPs. The nanoparticle layer average height, measured at voids in the layer, is ~7 nm. The nanoparticle distribution obtained from AFM was homogeneous in different areas of the sample, displaying uniform distribution of nanoparticles over the substrate.

3.3.3 Field Emission Scanning Electron Microscopy

The films were imaged as is and not sputtered-coated with a conductive layer of platinum, because they contain sufficient copper present to avoid charging the samples by

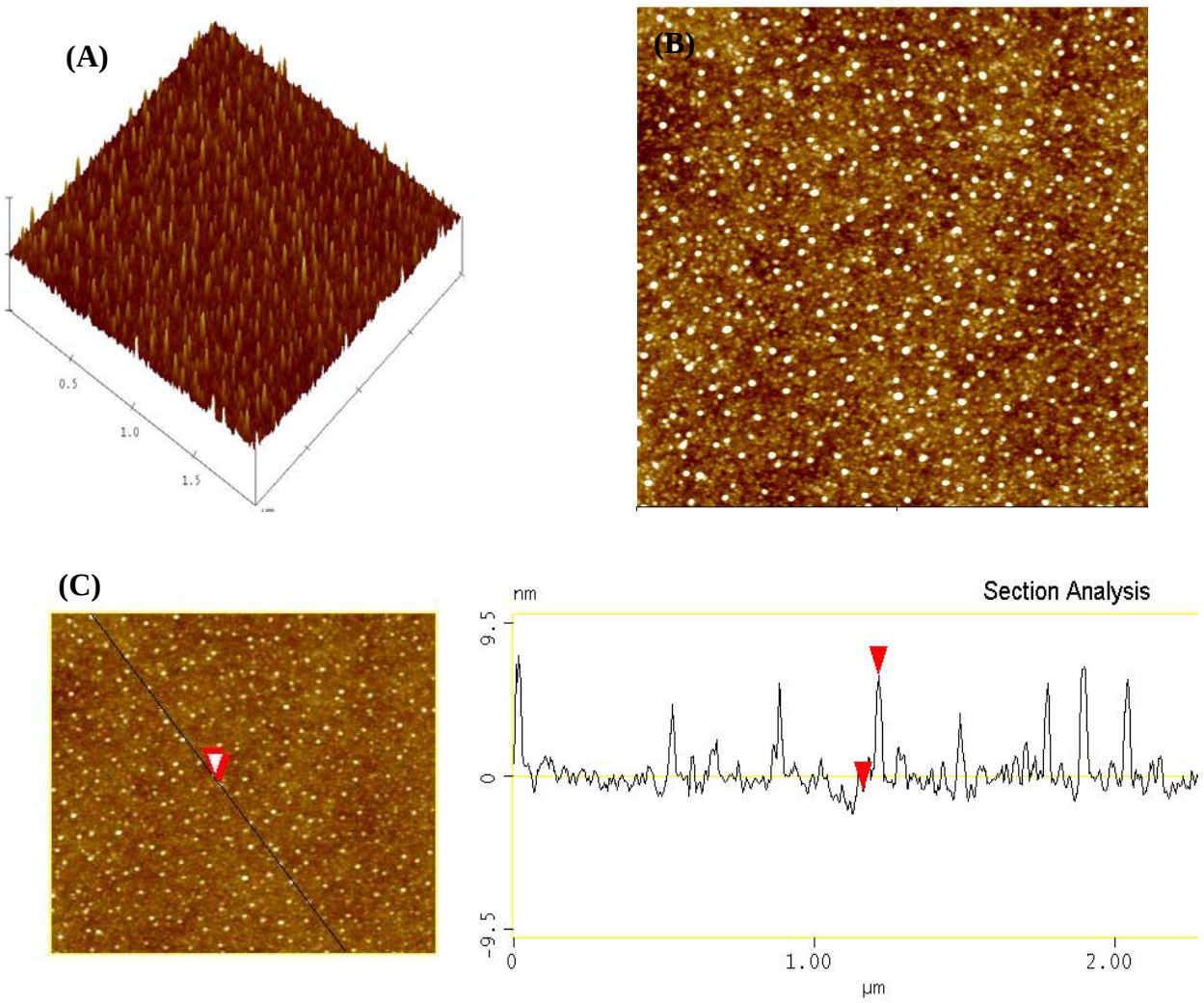

Figure 3.3. Surface topography for copper nanoparticles embedded PI film. (A) height image, (B) phase image and (C) section analysis.

the electron beam. Figure 3.4A and Figure 3.4B are the FESEM images for the sample in which reduction of copper precursor as well as imidisation of PAA film was carried out simultaneously. These images show the presence of the copper nanoparticles as highly dispersed, uniform in size and well separated, showing no evidence of aggregation of nanoparticles during the processing step. The nanoparticles density is calculated to be $1*10^{10}$ cm^{-2}. However, aggregation and non-uniformity is observed for the sample where copper precursor containing PAA film is firstly chemically imidised, and later precursor is reduced to form CuNPs (Figure 3.4C and Figure 3.4D). This may be due to immobilization of precursor molecules in PI films after chemical imidisation of PAA films, while precursor molecules can move inside PAA film to give uniform sized distribution of CuNPs, during the reduction as well as imidisation step.

3.3.4 Capacitance–voltage (C–V) and Capacitance–time (C–t) Analysis

Normalized C-V hysteresis curves of the MIS memory device containing embedded copper nanoparticles at ± 2 V biasing voltage are shown in Figure 3.5. A clear shift in flatband voltage resulting from the electron and hole charging/discharging was observed. The capacitance hysteresis is from demonstration of the Coulomb blockade effect which suppresses the additional injection of carriers into the CuNPs, leading to flatband voltage shift (Lambe et al., 1969; Amman et al., 1993). The observed counter-clockwise hysteresis for the MIS device with nanoparticles is generally attributed to charging and discharging of electrons from the substrate (Leong et al., 2007). The device without

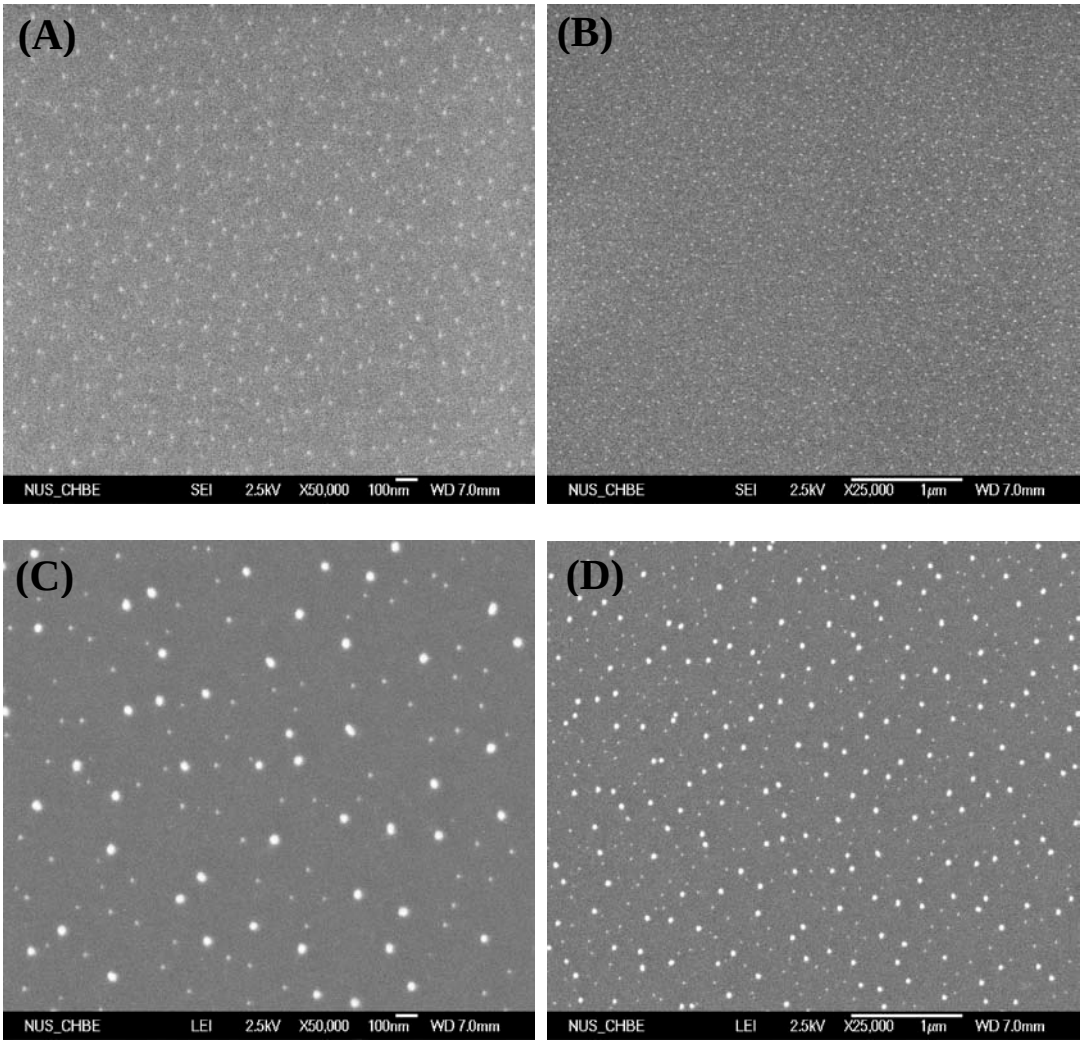

Figure 3.4. FESEM images for copper nanoparticles embedded PI film. (A), (B) Reduction before chemical imidisation step; (C), (D) Reduction after chemical imidisation step.

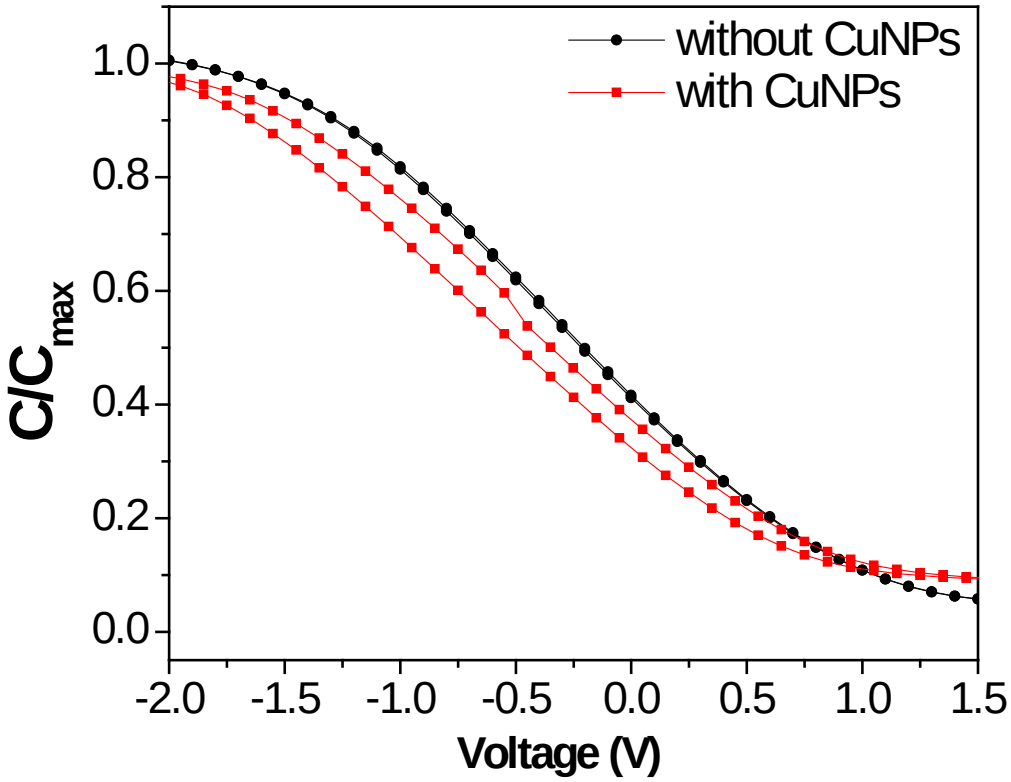

Figure 3.5. Normalized C-V characteristics at 100 kHz obtained by biasing the top electrodes at ± 2 V for control sample (without CuNPs) and with CuNPs.

CuNPs shows a negligible memory window. However, clear hysteresis window of 0.16 V was observed from the sample with CuNPs. Both MIS devices were fabricated using the same procedure, except for the addition of the CuNPs. The observed hysteresis effect, therefore, could be related to the charging of the nanoparticles and nanoparticle-related traps. Normalized C-V hysteresis curves obtained at ± 5 V biasing voltage are shown in Figure 3.6. Hysteresis window of 0.69 V for the sample with CuNPs was observed. However, a small hysteresis window of 0.3 V was observed from the PI film sample. This may be due to existence of some trapped sites in the dielectric film. As shown in Figure 3.7, the hysteresis window of the C-V curve for the sample with CuNPs increases from 0.69 V to 1.52 V with increasing maximum operating bias from 5 V to 8 V, indicating that more electrons are being trapped into the nanoparticles as the sweeping bias increased (Nicolean and Brews, 1992).

Capacitance decay (C-t) measurement was conducted to evaluate the charge retention properties of the device. A charging bias of +5 V was applied to the device for 1 min to facilitate electron injection into the nanoparticles. Subsequently, the capacitance was monitored as a function of time under the flat-band condition of the device. The C-t measurement result is shown in Figure 3.8. The device having embedded CuNPs in PI film shows good retention characteristics up to 20,000 s. However, stored charge discharges in a few seconds for the device with only PI film, which confirms presence of trapped sites in the dielectric film. The observed behavior for the device having embedded CuNPs indicates good suppression of charge losses via vertical and lateral

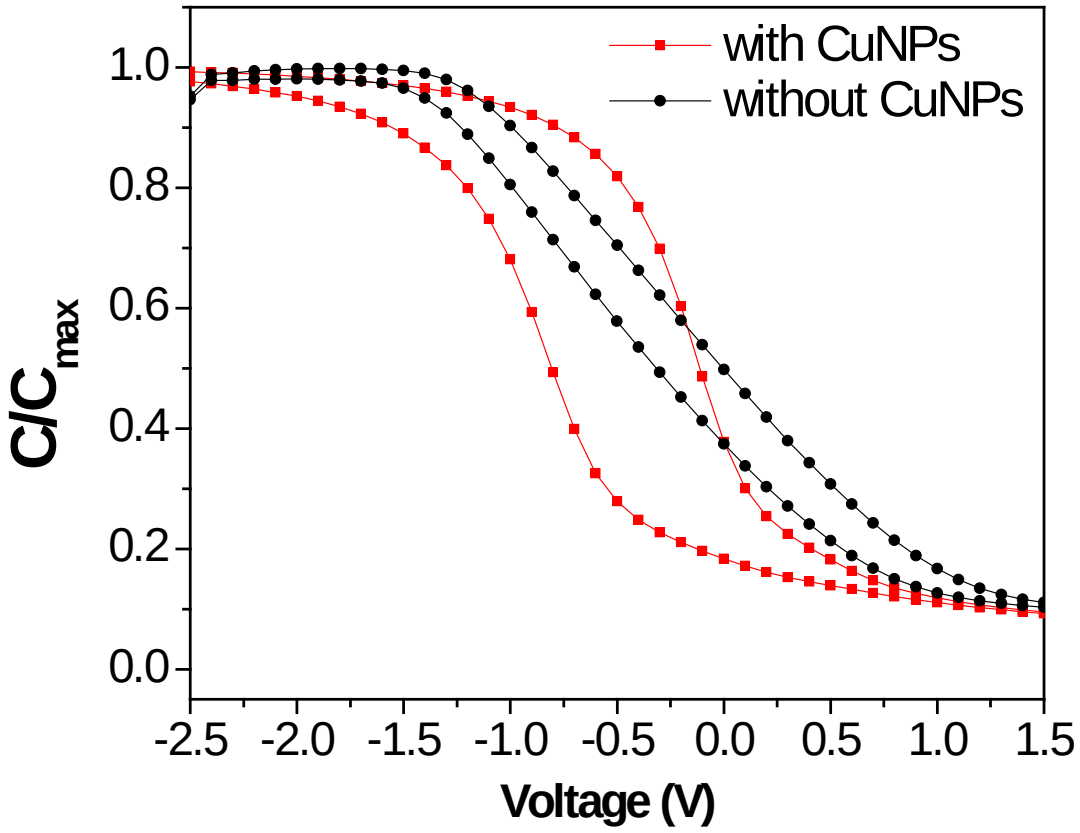

Figure 3.6. Normalized C-V characteristics at 100 kHz obtained by biasing the top electrodes at ± 5 V for control sample (without CuNPs) and with CuNPs.

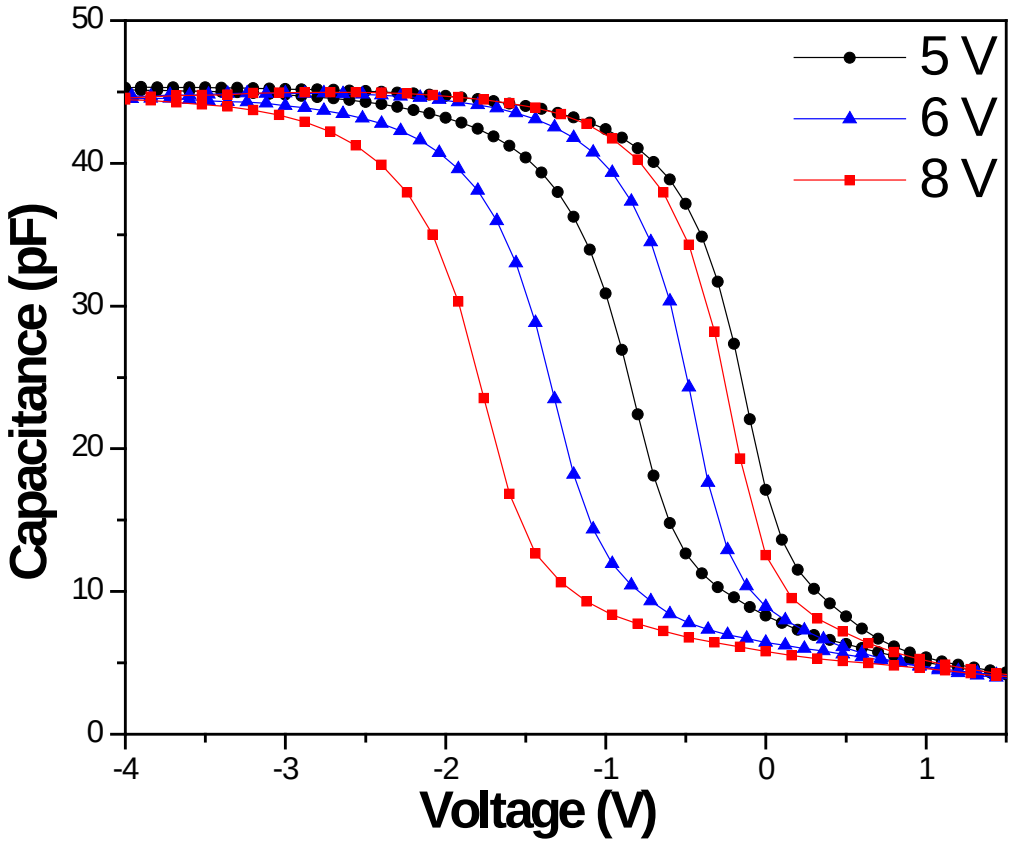

Figure 3.7. C–V characteristics at 100 kHz under different scan voltage ranges for an MIS capacitor incorporating copper nanoparticles.

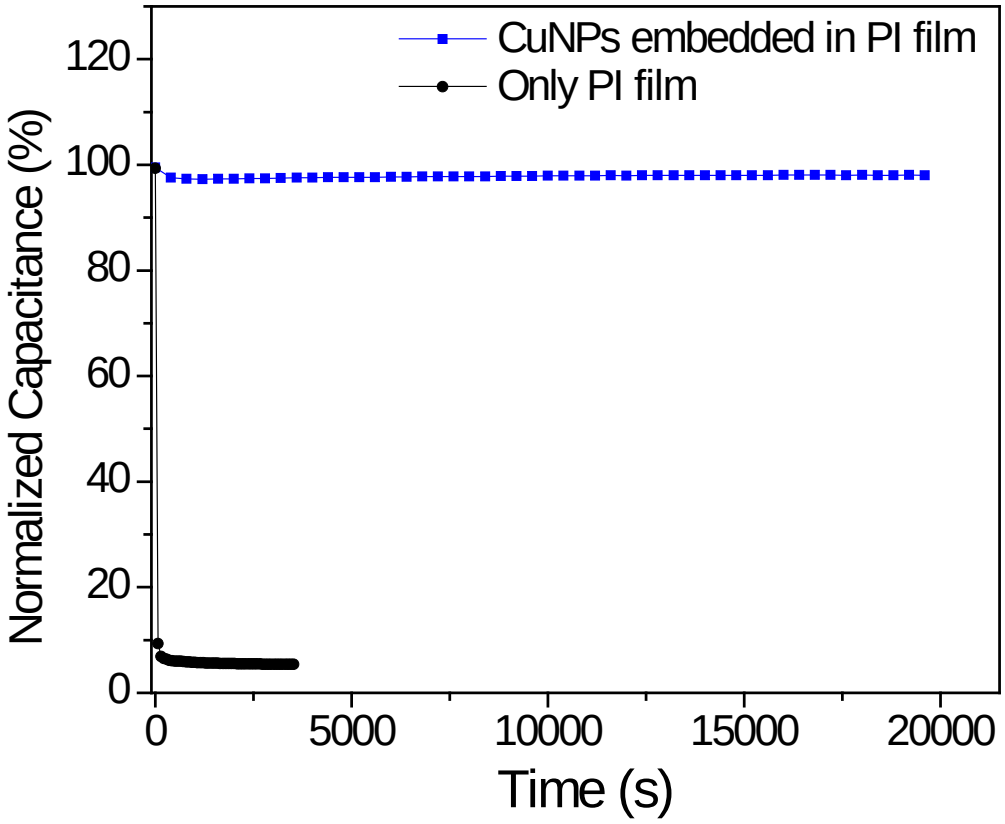

Figure 3.8. Charge retention characteristics (normalized capacitance) of the MIS device at 100 kHz after programming at +5 V.

charge diffusion (Kim et al., 2003), which could be an early indicator for a good, well dispersed nanoparticle distribution.

3.4 Conclusions

This chapter demonstrates solution-processable method to fabricate thermally stable memory device structure containing uniform sized and mutually separated metallic CuNPs embedded in a PI matrix. XPS showed formation of metallic Cu after reduction step and their stability against oxidation. Detailed structural characterizations have been performed for embedded CuNPs in PI film. FESEM and AFM images show the surface morphology of the embedded nanoparticles. Embedded CuNPs are uniform in size and well separated. Good performances in terms of large memory window and long data retention were observed. This approach, by virtue of its simplicity in processing and low-cost, can be potentially utilized in next generation of nonvolatile memory devices.

CHAPTER 4

LANGMUIR–BLODGETT ASSEMBLY OF 4-METHYLBENZENETHIOL FUNCTIONALIZED GOLD NANOPARTICLES FOR NONVOLATILE MEMORY APPLICATIONS

4.1 Introduction

In this chapter, the Langmuir-Blodgett (LB) technique of molecular assembly has been employed in fabricating a multilayered array of gold nanoparticles (AuNPs) functionalized by 4-methylbenzenethiol on Si substrates. The 2 layer, 4 layer and 6 layer structures of functionalized AuNPs have been fabricated. Thickness measurements by ellipsometry show a linear increase of film thickness with the number of layers. Characterization of the multilayer structures has been carried out by atomic force microscopy (AFM). The electrical characterization of such multilayered AuNPs structures is investigated by means of a metal-insulator-semiconductor (MIS) device for nonvolatile memory applications. The effect of increasing the number of gold nanoparticle layers on memory performance has also been investigated.

4.2 Experimental Section

4.2.1 Materials

Octadecyltrichlorosilane (OTS) (90 %, Sigma-Aldrich), hydrogen tetrachloroaurate (III) trihydrate ($HAuCl_4.3H_2O$) (≥ 99.9 %, Aldrich; *corrosive, handle with care*), 4-methylbenzenethiol (MBT) (98 %, Aldrich), tetraoctylammonium bromide (TOAB) (98 %, Aldrich), sodium borohydride ($NaBH_4$) (98 %, Lancaster), acetone (≥ 99 %, Merck), hexane (99.9 %, Fisher-Scientific), methanol (≥ 99 %, Merck), chloroform (≥ 99 %, Merck) were all used as received. Silicon wafers <100> (Chartered Semiconductor, Singapore) were 0.6 mm thick, p-doped, polished on both side and having 4 nm thermally grown oxide layer.

4.2.2 Synthesis of Thiol-Stabilized Gold Nanoparticles

Synthesis of AuNPs was carried out as mentioned earlier (Johnson et al., 1997). Briefly, the preparation procedure was as follows: 9 mL of 30 mM $HAuCl_4$ aqueous solution was added to 24 mL of 50 mM TOAB in toluene in 100 mL of conical flask and stirred vigorously. After 30 min of stirring, solution separated into two layers. 0.1 g of MBT was added to the flask with stirring continued. Finally, freshly prepared 7.5 mL of 0.4 M aqueous solution of $NaBH_4$ was added to the flask in a drop-wise fashion. On addition of $NaBH_4$, the red organic phase immediately changed colour to black. The solution was rapidly stirred for 3 h, and then the black organic phase was separated from the aqueous phase. The solvents were concentrated to 2 mL by rotary evaporator. The nanoparticles were washed with ethanol and centrifuged two times at 8000 rpm. Finally, the nanoparticle precipitate was dried under nitrogen environment overnight at room temperature.

4.2.3 Immobilization on Silicon Surface

4.2.3.1 Substrate Preparation

Silicon wafers were cut into 4 cm * 1.5 cm pieces, cleaned by successive sonication in methanol and acetone for 30 min each, and later treated with “piranha solution” (7/3 (v/v) mixture of concentrated sulfuric acid and 30 % hydrogen peroxide) at 75 °C for 45 min (*Caution: Piranha solution reacts violently with organic matter*). They were then copiously rinsed with deionized water, blown dry with nitrogen, and dried at 100 °C

under vacuum for 30 min. This cleaning procedure creates a surface rich in hydroxyl groups at the oxide surface to facilitate the subsequent silanization process (Madeley and Richmond, 1972; Zhuravlev, 1987).

4.2.3.2 Self-Assembly of Silane

The hydroxyl covered substrates were rinsed with hexane and then immersed in a 0.5 mM OTS solution in hexane for 1 h. Subsequently, the wafers were removed from the solution, rinsed and sonicated for 10 min with hexane, rinsed again with hexane and then with chloroform, finally blown dry with nitrogen. The samples were stored in a desiccator under vacuum.

4.2.3.3 LB Film Deposition of Gold Nanoparticles

The investigation of pressure–area isotherm of the Langmuir film and deposition of LB film was done at 25 $^{\circ}$C on an alternate layer Langmuir–Blodgett trough (NIMA Technology, model 622) equipped with Wilhelmy-type film balance. Prior to use, the trough barriers were cleaned thoroughly with chloroform and rinsed three times with water. Deionized water was used as the sub-phase. With the barriers fully open, 500 µL of 0.5 mg mL^{-1} gold nanoparticle solution (chloroform solvent) was spread slowly on the water surface by a microsyringe. The solvent was allowed to evaporate for 5 min. The barriers were then compressed at a speed of 50 cm^2/min. For deposition, the nanoparticle layer was held for 15 min at a surface pressure of 10 mN/m and transferred by the vertical Y-type deposition method over OTS modified substrate at a speed of 20 mm/min.

Nanoparticles were deposited onto the substrate during both immersion and withdrawal strokes. A holding time of 100 s was imposed between dipping cycles to remove the residual water. Finally, the nanoparticles deposited substrates were dried under vacuum at room temperature to remove residual solvent and water.

4.2.4 MIS Capacitor Fabrication

A metal-insulator-silicon (MIS) capacitor device was fabricated. Following the incorporation of multilayer of AuNPs, a pulsed laser deposition (PLD) method was used to deposit 10 nm thick Al_2O_3 control oxide. Gold top electrodes (0.3 mm diameter size) are then sputter-deposited using shadow mask technique subsequently. After removing the oxide, Pt film was deposited as the back side contact. The MIS device configuration is shown in Figure 4.1.

4.2.5 Characterization

Characterization by TEM was performed as described in chapter 5, section 5.1.2.5.

Ellipsometry

Thickness characterization was performed by ellipsometry (Wvase 32, J.A.Woollam.Co., Inc.,) Scanning spectra were acquired over the wavelength range of 600-1000 nm at three different incidence angles, 65^o, 70^o and 75^o. The modeling for the thin film measurement used silicon (Si.MAT) as the base layer with 0.6 mm thickness, silicon dioxide

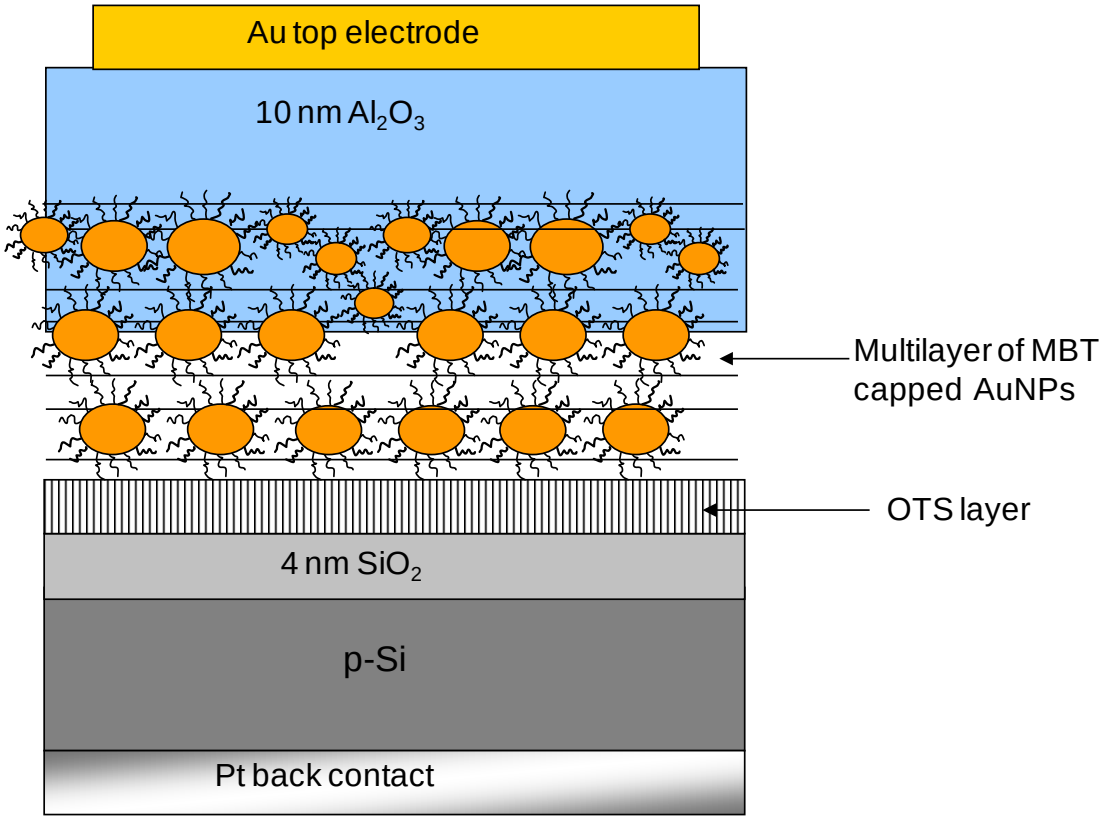

Figure 4.1. The MIS device configuration for the multilayer of MBT capped gold nanoparticles.

(SiO_2.MAT) as the next layer with a thickness of 4 nm and the Cauchy package (CAUCHY.MAT) for the film material. Taking multiple readings and using the average value of the most consistent readings minimized errors in the thickness measurements. The thickness of the film was measured by recording ellipsometric angles Ψ and Δ, which describes the polarization state of the light beam reflected from the sample surface and is related to the ratio of reflection coefficients for p- and s- polarized light. A 3-layer model was established and fitted with the experimental data, Ψ and Δ. The mean-squared error (MSE) values were less than 5 after fitting, indicating reliability of the model and the measurement.

Characterization by AFM and capacitance–voltage (C–V) and capacitance–time (C–t) measurements were performed as described in chapter 3, section 3.2.9.

4.3 Results and Discussions

4.3.1 Synthesis of MBT Capped Gold Nanoparticles

4.3.1.1 Transmission Electron Microscopy (TEM)

A few drops of the solution containing nanoparticles dispersed in chloroform were placed on carbon coated TEM grids, and grids were imaged after solvent evaporation. Figure 4.2 shows the TEM micrograph of synthesized MBT capped AuNPs. The image shows that the NPs are approximately spherical, with an average Au core diameter of 2.6 ± 0.6 nm.

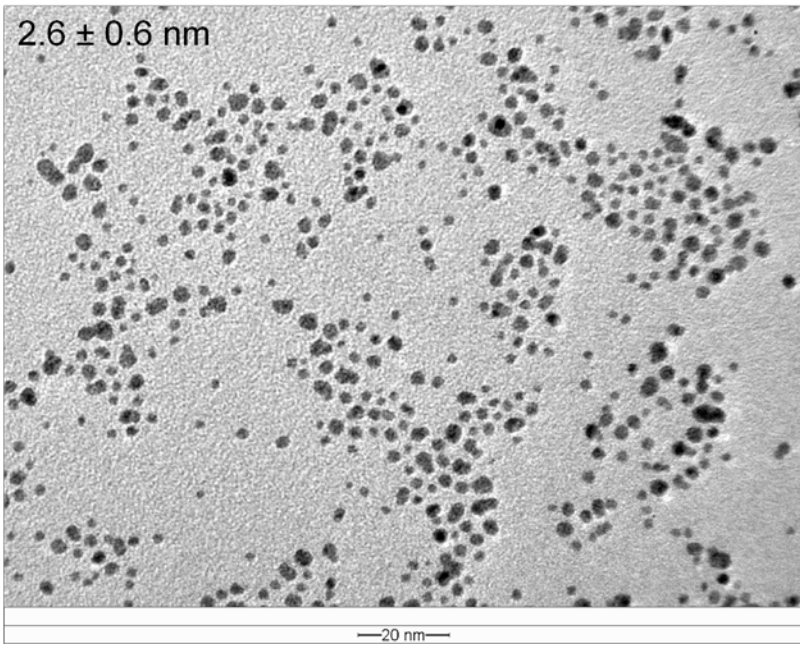

Figure 4.2. TEM image of MBT capped gold nanoparticles.

4.3.2 LB Assembly of Gold Nanoparticles

4.3.2.1 Ellipsometric Characterization

The thickness of the nanoparticle films versus number of layers is shown in Figure 4.3. The films formed from LB technique, exhibit linear increase in thickness with number of layers. Average thickness of about 4.8 nm, 9.2 nm and 13.7 nm were obtained for the 2 layer, 4 layer and 6 layer of MBT capped AuNPs, respectively. The average thickness increase, obtained after each dip is found to be 2.4 nm. The thickness for monolayer of nanoparticle, obtained from ellipsometry, is in reasonable agreement with that measured by TEM. The slight differences in the thickness calculated by the ellipsometry and that expected value may be due to the film coverage being less than a complete monolayer.

4.3.2.2 Surface Morphology

The changes of topography for nanoparticle layers were studied using tapping mode AFM. The scan size was 2 μm for all the images. As shown in Figure 4.4, different deposition steps result in different surface features, confirming presence of different species. Figure 4.4A shows the flat topography for AFM image of OTS deposited Si substrate. Figure 4.4B shows the AFM image for the 2 layer nanoparticle deposited Si substrate by LB deposition. The nanoparticles form monolayer domains and defects were found within these islands. However, no obvious 3D aggregation was observed throughout the film. Also, surface coverage improved with increase in number of

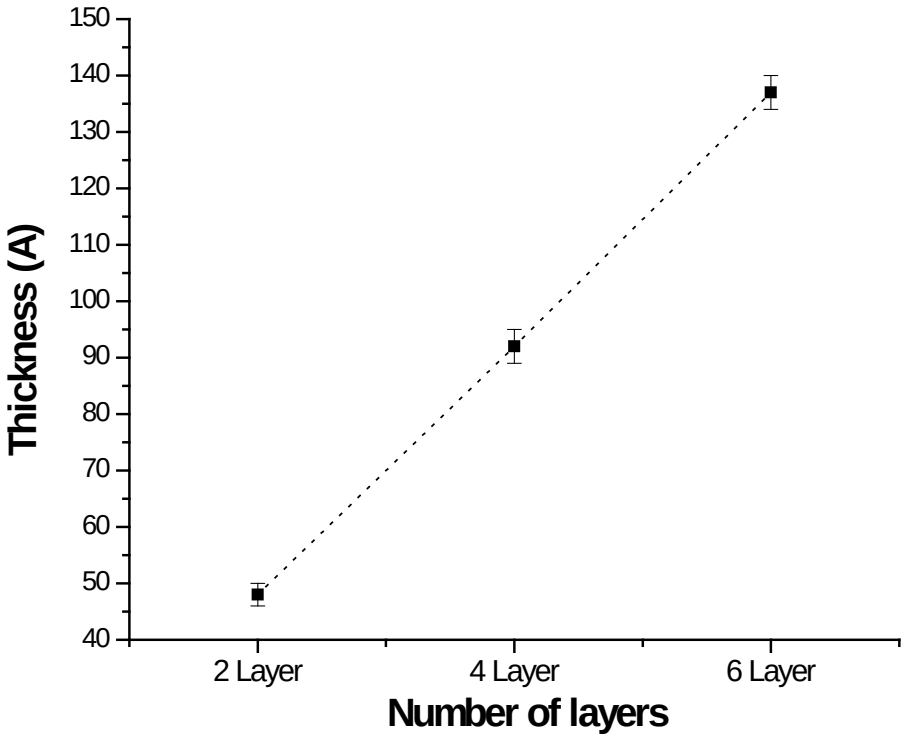

Figure 4.3. Ellipsometric thickness of MBT capped gold nanoparticles films prepared by LB deposition versus number of layers.

deposited nanoparticle layers (Figure 4.4C for 4 layer of nanoparticles and Figure 4.4D for 6 layer nanoparticles). Figure 4.5 presents the surface height profiles along the lines drawn in the flattened images. The vertical distance between the highest and the lowest positions (on average), as marked by arrows in both the image and the height profiling curve, can be associated with the dimension of the constituent molecules for a particular layer. The nanoparticle layer average height, measured at voids, for all the layers was in agreement with the ellipsometry values. The root-mean-square (RMS) roughness determined from the AFM images showed that the gold nanoparticles tend to increase the roughness of the surface compared to OTS deposited surface. RMS values were 0.31 nm, 1.48 nm, 1.85 nm and 2.06 nm for OTS, 2 layers, 4 layers and 6 layers of the nanoparticles deposited surface, respectively. RMS value increased with the number of nanoparticle layers. The nanoparticles distribution obtained from AFM was homogeneous in different areas of the sample, displaying uniform deposition of nanoparticles over the substrate.

4.3.3 C-V Analysis

Normalized C-V hysteresis curves of the MIS memory device containing the multilayer of MBT capped AuNPs, are shown in Figure 4.7. Counterclockwise C-V hysteresis curves with large width were obtained. The observed counter-clockwise hysteresis for the MIS device with nanoparticles is generally attributed to charging and discharging of electrons from the substrate (Leong et al., 2007). We investigated the role of AuNPs as charge-storage elements in the multilayered devices. As shown in Figure 4.6, a device

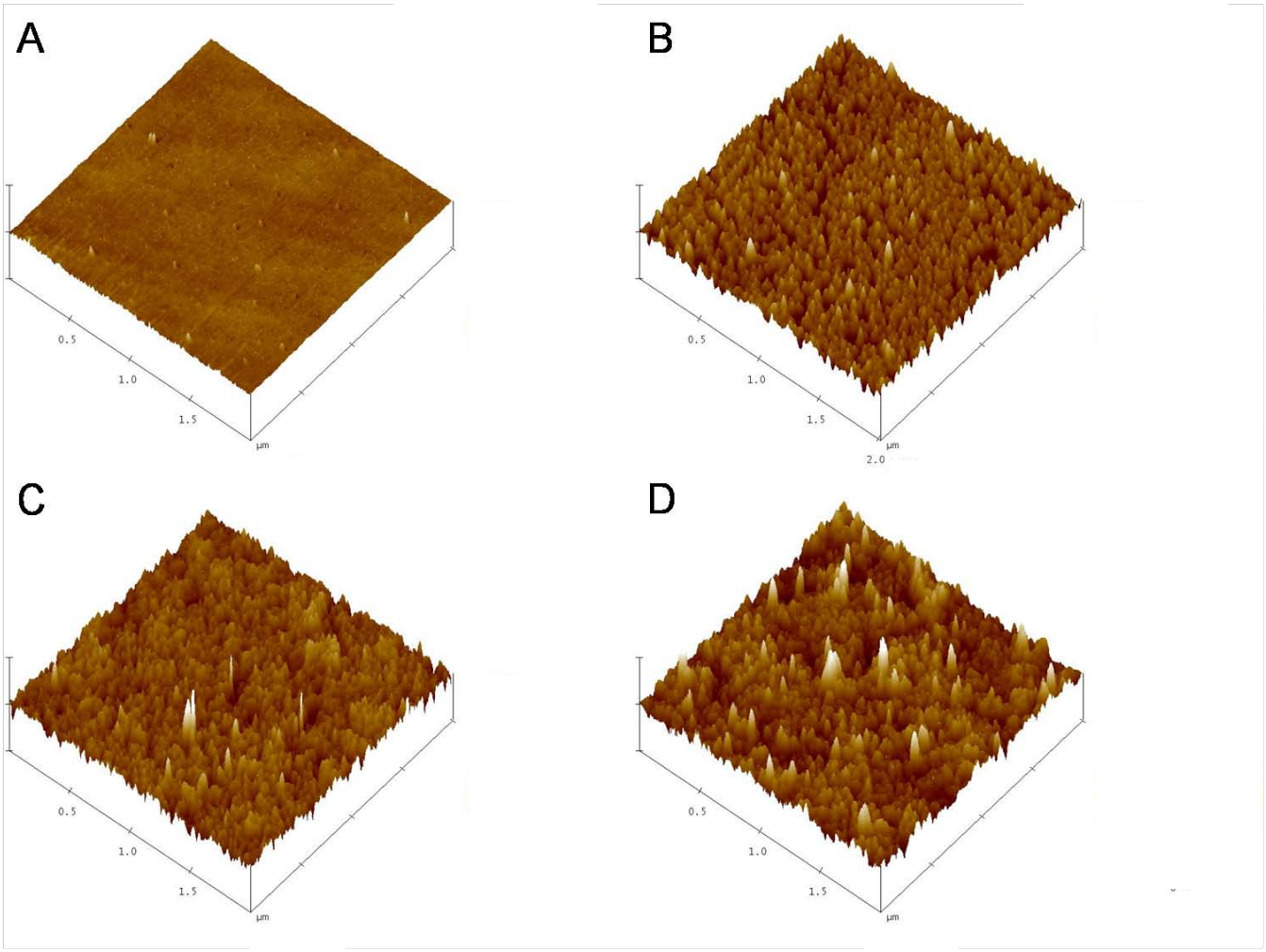

Figure 4.4. Surface topographies of 2 µm × 2 µm regions for different deposition steps (A) OTS surface, (B) 2 layer of nanoparticles, (C) 4 layer of nanoparticles and (D) 6 layer of nanoparticles.

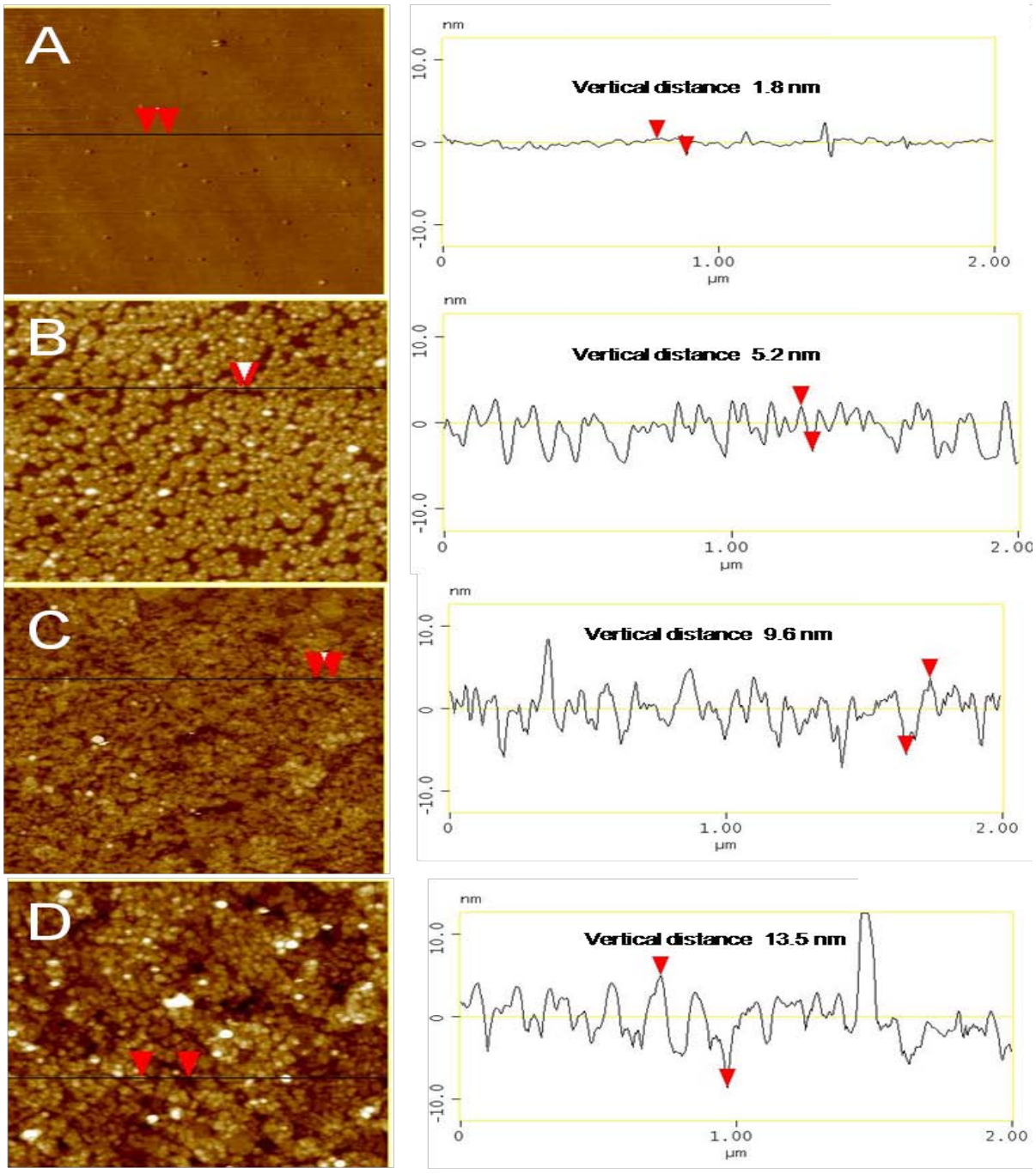

Figure 4.5. A comparison of section analysis at various deposition steps (A) OTS surface, (B) 2 layer of nanoparticles, (C) 4 layer of nanoparticles and (D) 6 layer of nanoparticles.

without AuNPs displayed a small memory effect (memory window of less than 0.25 V) at 5 V biasing. In contrast, device having 4 layers of nanoparticles displayed a memory window of about 0.96 V under the same conditions. These results show that AuNPs have a significant role as charge-storage elements. The observed hysteresis effect, therefore, could be related to the charging of the nanoparticles and nanoparticle-related traps. Figure 4.7 shows dependence of memory window and stored charge density, measured from C-V curves, over number of nanoparticle layers. The memory window increased from 0.84 V for 2 layers of nanoparticles to 2.2 V for 6 layers of nanoparticles at 7 V biasing. The enhancement in memory window is due to increased number density of AuNPs as charge-storage elements with increase in number of nanoparticle layers. As shown in Figure 4.8, the hysteresis window of the C-V curve for the device having 4 layers of nanoparticles increases from 0.53 to 1.52 V with increasing maximum operating bias from 4 to 7 V, indicating that more electrons are being trapped into the nanoparticles as the sweeping bias increased (Sargentis et al., 2008). Figure 4.9 shows the C-V characteristics at various measuring frequencies (100 KHz and 1 MHz) for the device having 4 layers of nanoparticles and it is observed that C-V hysteresis window is independent of the applied frequency. This observed frequency-independent behavior indicates that the traps which may exist at the interfaces between nanoparticle layers and the thermal oxide do not make any contribution to the charging process (Nicollian and Brews, 1982).

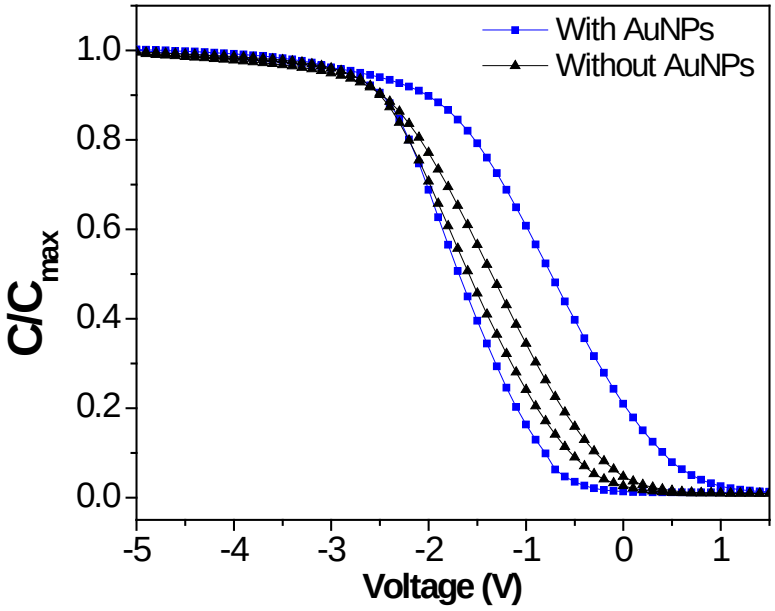

Figure 4.6. Normalized C-V characteristics at 100 kHz obtained by biasing the top electrodes at ± 5 V for control sample (without nanoparticles) and with 4 Layer of MBT capped AuNPs.

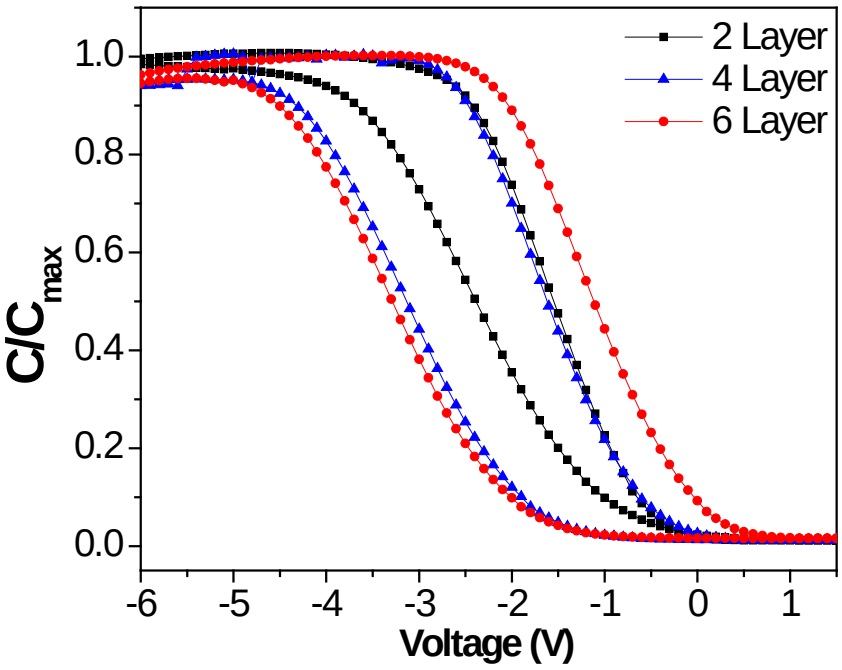

Figure 4.7. Normalized C-V characteristics at 100 kHz obtained by biasing the top electrodes at ± 7 V to compare effect of number of layer of MBT capped AuNPs.

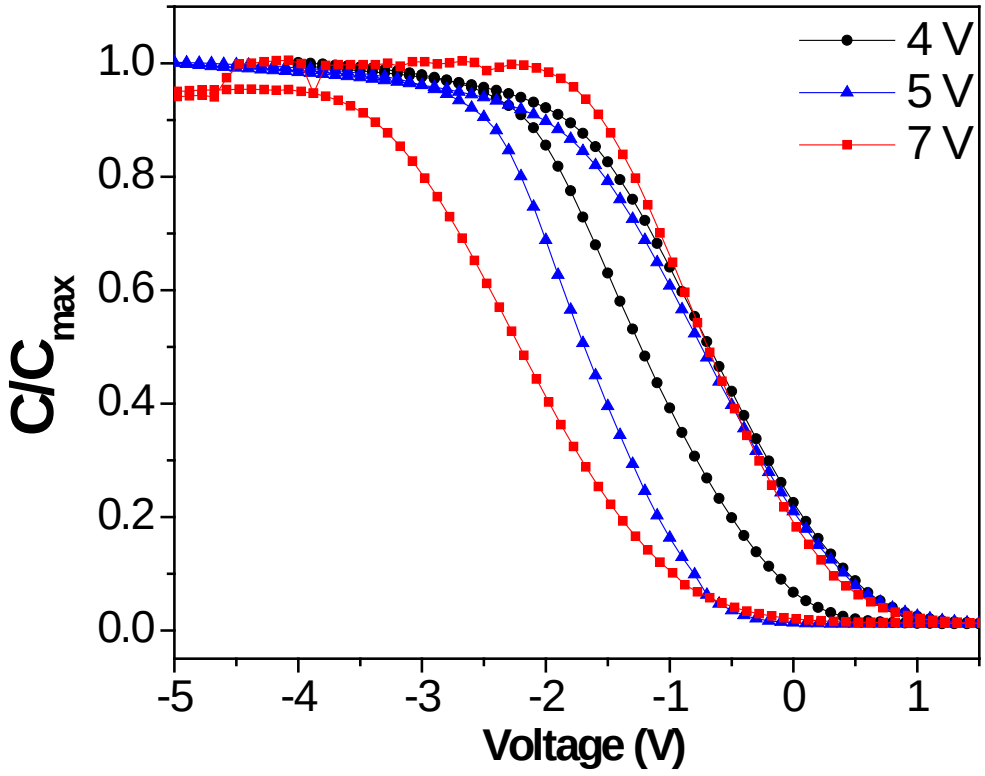

Figure 4.8. Normalized C–V characteristics at 100 kHz under different scan voltage ranges for an MIS capacitor incorporating 4 Layer of MBT capped AuNPs.

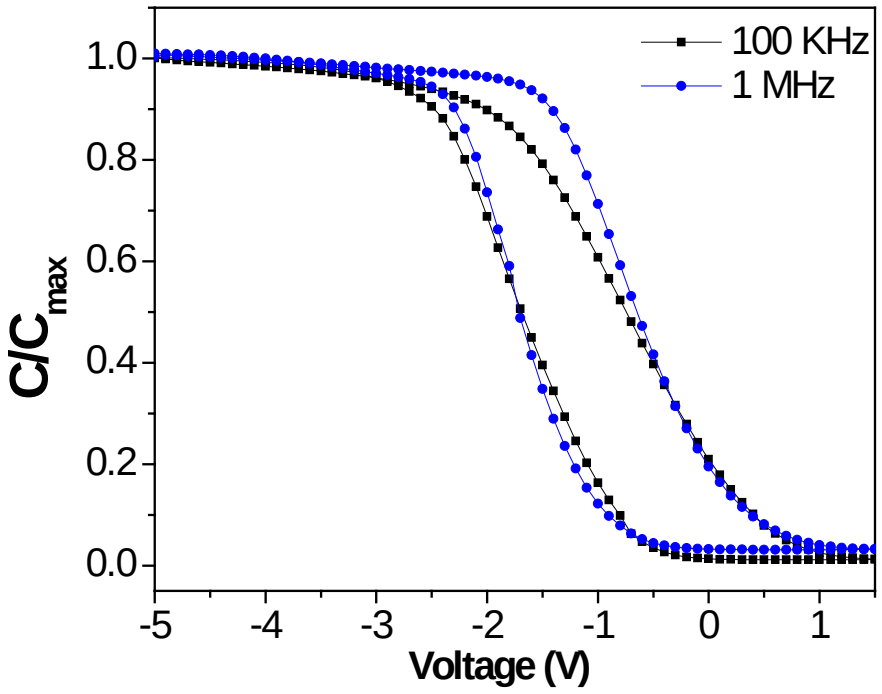

Figure 4.9. Normalized C–V characteristics at ± 5 V to compare effect of frequency for 4 Layer of MBT capped AuNPs.

4.4 Conclusions

This chapter demonstrates a convenient LB assembly approach to form multilayers of functionalized AuNPs. Ellipsometry showed a linear increase in film thickness with the number of nanoparticle layers. AFM images showed improvement in the substrate coverage with the number of nanoparticle layers. The capacitance versus voltage characteristics of these devices showed increase in the hysteresis window with number of layers due to increase in the nanoparticle density with number of layers. A high nanoparticle density on surface translates into high charge storage capacity. The importance of this work resides in the fact that we can significantly increase the memory capacity per unit area by increasing the number of AuNPs layers.

CHAPTER 5

COVALENT ASSEMBLY OF FUNCTIONALIZED GOLD NANOPARTICLES

Bottom-up fabrication of metal nanoparticles into two and three dimensional nano-architectures have recently been of interest due to better flexibility and versatility in terms of material design for developing nano-devices for future technical applications. Two-dimensional assemblies of monodisperse metal particles with controlled size in the nanometer range have potential applications in solid state electronic devices. Despite the continuous progress in this field, the stability of nanostructures containing organic thin films has emerged as one of the critical issues in electronic devices. A key factor in addressing this issue will be assembling the nanoparticles covalently on to a desired surface in order to provide the required stability.

Covalent molecular assembly is advantageous in the sense that each layer in the assembled film can be covalently linked to its underlying layer and no excess deposition can take place as it is limited by the reactive sites on the layer surface. Films with covalent interlayer bonding are more advantageous to withstand elevated temperature, polar solvent attack, mechanical wear and abrasion due to their robustness. Having functional end groups for capping layers as compared to inert groups can facilitate formation of multilayers. In terms of stability or strength, multilayer films with covalent interlayer bonding are even more advantageous because of their increased robustness.

The first section in Chapter 5, describes synthesis, stabilization and assembly of short chain thiol (4-aminothiophenol)-capped gold nanoparticles. Section 5.2 illustrates the synthesis of 16-mercaptohexadecanoic acid capped gold nanoparticles through a single phase synthesis method and subsequently, their immobilization on to silicon/gold

surfaces through covalent molecular assembly. Section 5.3 deals with the synthesis of alcohol thiol capped gold nanoparticles and their immobilization using covalent molecular assembly. In addition, the electrical characterization of covalently bound gold nanoparticles as a charge trapping layer in non-volatile memory, is also investigated by means of a metal-insulator-semiconductor (MIS) device.

CHAPTER 5.1

SYNTHESIS OF SHORT CHAIN THIOL CAPPED GOLD NANOPARTICLES, THEIR STABILIZATION AND IMMOBILIZATION ON SILICON SURFACE

5.1.1 Introduction

Tethering between nanoparticles and a supporting substrate, especially in the form of covalent bonding, is a highly useful way of ensuring development of robust systems for various applications. This requires bestowing specific functionalities on nanoparticle surfaces that can also prevent aggregation between nanoparticles. In this chapter, the synthesis of short chain thiol (4-aminothiophenol)-capped gold nanoparticles through a single phase method, and their covalent immobilization on a silicon surface is described. The nanoparticles (which are prone to agglomerate due to amine-amine hydrogen bonding) were stabilized in solution by anhydride capping. This technique resulted in formation of stabilized suspensions. The anhydride functional groups also help to covalently immobilize the nanoparticles on silicon surfaces. Finally, these stabilized nanoparticles were immobilized on a silicon substrate. X-ray photoelectron spectroscopy (XPS) confirmed the absence of non-reacted thiol groups in the synthesized nanoparticles and presence of nanoparticles on the silicon surface, after the immobilization process. Transmission electron microscope (TEM) and UV-Vis spectroscopy have been used to study particle morphology. Cross-sectional HR-TEM images show direct evidence that the particles are anchored to the silicon surface.

5.1.2 Experimental Section

5.1.2.1 Materials

Pyromellitic dianhydride (PMDA), *p*-aminophenyltrimethoxysilane (APhS) and 4-aminothiophenol (4-ATP) (97 %) were purchased from Aldrich, Gelest and Aldrich, respectively, and used as received. Their molecular structures are shown in Scheme 5.1.1. Hydrogen tetrachloroaurate (III) trihydrate ($HAuCl_4.3H_2O$) (≥ 99.9 %, Aldrich; *corrosive, handle with care*), sodium borohydride ($NaBH_4$) (98 %, Lancaster), methanol (≥ 99.5 %, Merck), toluene ((≥ 99 %, Merck) and N, N-dimethylacetamide (DMAc) (≥ 99 %, Merck) were used as received. Silicon wafers <100> (Engage Electronics Pte Ltd., Singapore) were 0.6 mm thick, p-doped, polished on one side and with a natural oxide layer.

5.1.2.2 Synthesis of Thiol-Stabilized Gold Nanoparticles

4-ATP was dissolved in methanol to obtain a 20 mM solution. 5 mL of this solution was added to 10 mL of 10 mM methanolic solution of $HAuCl_4$. The mixture was vigorously stirred for 20 min. Subsequently, 5 mL of freshly prepared 0.3 M aqueous $NaBH_4$ was added dropwise to the mixture with stirring. The reaction mixture turned dark brown, indicating the formation of gold nanoparticles. The stirring was continued for 1 h. Two approaches were used to isolate functionalised nanoparticles from the methanolic solution. In the first method (method M), the solution was diluted with an equal volume of water and centrifugation was done to remove unreacted surfactants and other byproducts. In the second method (method S), the solution was centrifuged successively with methanol and water. Finally, the purified precipitate obtained by both methods was

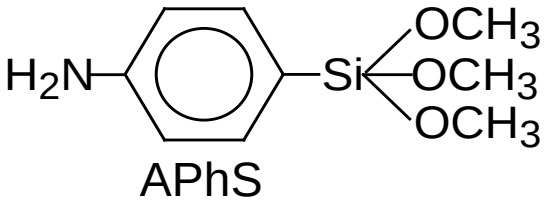

APhS

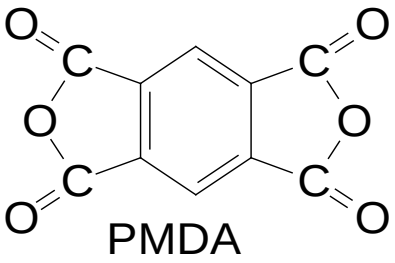

PMDA

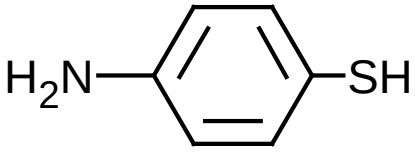

4-ATP

Scheme 5.1.1. Molecular structures of the main materials used.

purged under nitrogen to yield a dry powder and the samples were dispersed in DMAc and methanol.

5.1.2.3 Stabilization of Thiol-Capped Gold Nanoparticles

The amine terminated nanoparticles were stabilized through reaction with PMDA in DMAc. Various amounts of 50 µM amine - capped nanoparticles (calculated based on the original amount of gold salt used in the preparation of the nanoparticles; it is assumed that all the utilized gold in the salt was consumed in the reaction) were mixed with 5 mL of 5 mM PMDA solution in DMAc and reaction continued for 2 h with stirring at 100 rpm. Nanoparticle amounts of 0.25 µmoles, 0.05 µmoles and 0.025 µmoles were used.

5.1.2.4 Immobilization on Silicon Surface

Substrate Preparation

Silicon wafers were cut into 4 cm * 2 cm pieces, cleaned by successive sonication in methanol and acetone for 30 min each, and later treated with “piranha solution” (7/3 (v/v) mixture of concentrated sulfuric acid and 30 % hydrogen peroxide) at 75 °C for 45 min (*Caution: Piranha solution reacts violently with organic matter*). They were then copiously rinsed with deionized water, blown dry with nitrogen, and dried at 100 °C under vacuum for 30 min. This cleaning procedure creates a surface rich in hydroxyl groups at the oxide surface to facilitate the subsequent silanization process (Madeley and Richmond, 1972; Zhuravlev, 1987).

Self-Assembly of Aminosilane

Assembly of aminosilane was performed as described elsewhere (Zhang and Srinivasan, 2004), wherein the hydroxyl covered substrates were rinsed with toluene and then immersed in a 3 mM APhS solution in toluene for 2 h. Subsequently, the wafers were removed from the solution, rinsed and sonicated for 10 min with toluene, rinsed again with toluene and then with methanol, finally blown dry with nitrogen. The samples were stored in a desiccator under vacuum.

Immobilization of Gold Nanoparticles

The above amine-terminated silicon surfaces were immersed in a stirred solution of DMAc, containing anhydride-stabilized gold nanoparticles for 2 h. The substrates were then rinsed with DMAc and sonicated for 5 min in DMAc to remove any loosely bound nanoparticle. Rinsing was repeated with DMAc and then methanol and the substrates were blown dry with nitrogen. Schematic of various deposition steps are shown in Figure 5.1.1.

5.1.2.5 Characterization

(1). UV-Visible Spectroscopy

UV-visible absorption spectra were recorded on a Shimadzu UV-3101 PC scanning spectrophotometer operating at a resolution of 1 nm. Solution spectra were obtained by measuring the absorption of dilute solutions in a quartz cell with a path length of 1 cm; the solvents used were DMAc and methanol.

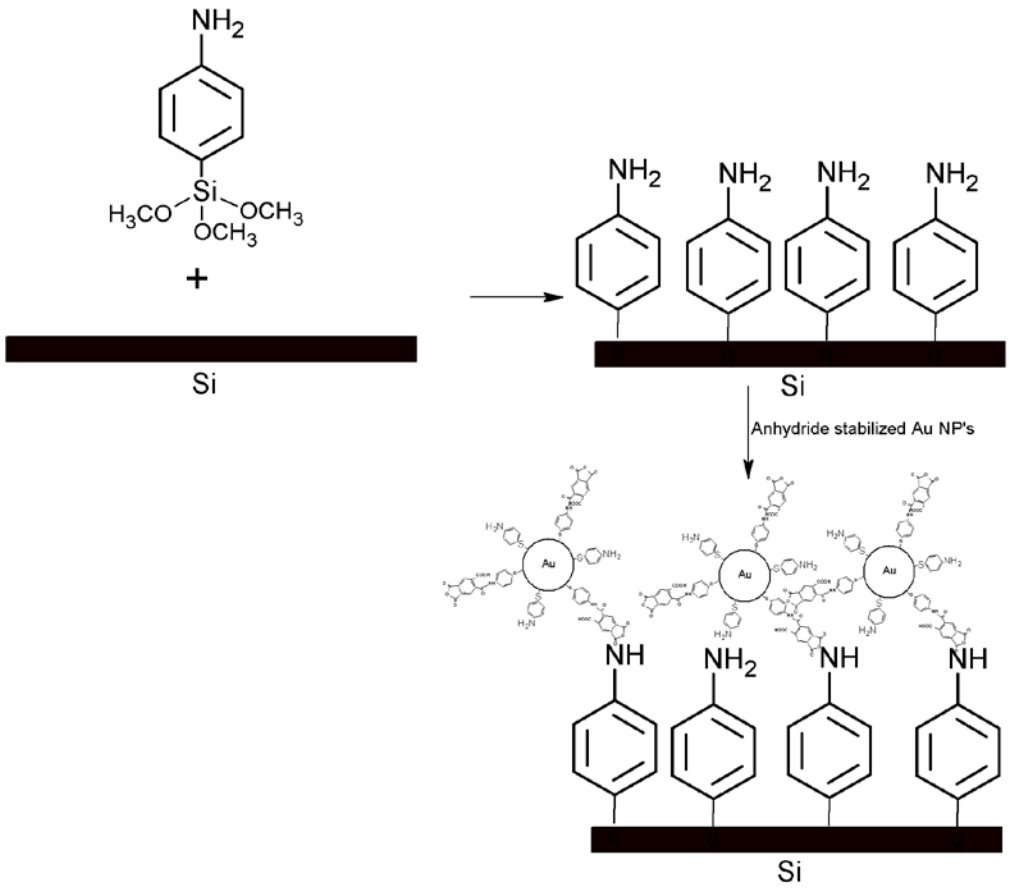

Figure 5.1.1. Schematic for immobilization of anhydride functionalized gold nanoparticles on to a hydroxyl-terminated silicon surface.

(2). X-Ray Photoelectron Spectroscopy (XPS)

XPS measurements were made on a Kratos Analytical AXIS HSi spectrometer with a monochromatized AlKα X-ray source (1486.6 eV photons) at a constant dwell time of 100 ms and a pass-energy of 40 eV. The X-ray source was run at a reduced power of 150 W. The pressure in the analysis chamber was maintained at 7.5×10^{-9} Torr or lower during each measurement. All binding energies (BEs) were referenced to the C1s hydrocarbon peak at 284.6 eV. In curve fitting, the full width at half-maximum (FWHM) for the Gaussian peaks was maintained constant for all components in a particular spectrum.

(3). Transmission Electron Microscope (TEM)

Transmission Electron Microscope (TEM) images of the nanoparticles were obtained with a JEM-2010 TEM (JEOL) operated at 200 kV. Samples for transmission electron microscopy were prepared by placing a drop of the nanoparticle-containing solution on 3-mm formvar/carbon-coated copper grids (Electron Microscopy Sciences). Excess solution was removed by an absorbent paper and the sample was dried overnight in air before scanning. The size distribution of particles was determined by taking the sizes of 100 particles.

(4). High Resolution Transmission Electron Microscope (HR-TEM)

High Resolution Transmission Electron Microscopy (HR-TEM) images were taken using a JEM-3010 TEM (JEOL) equipped with an EDS (energy dispersive spectroscopy) detector. To obtain the cross-sectional TEM images, two Si substrate samples were stuck

together face-to-face using epoxy, followed by thermal curing. The embedded samples were cut into 2 * 3 mm^2 pieces using a Leica ULTRACUT UCT Ultramicrotome. The sample was further ground down to ~ 70 µm and placed on a Cu grid. Finally, the samples were ion milled to the required size.

5.1.3 Results and Discussions

5.1.3.1 Synthesis and Stabilization of 4-ATP Capped Gold Nanoparticles

UV/Visible Spectroscopy

Figure 5.1.2A compares the UV-visible spectra for the gold nanoparticles prepared using sequential (S) and mixed (M) approaches after dispersion in DMAc. It is well known that the position and magnitude of the absorption bands are strongly dependent on the size of particles, the refractive index of the solvent used and the degree of aggregation of the nanoparticles (Mulvaney, 1996). The broadening of the absorption band is due to size shrinkage of nanoparticles and this is caused by the transfer of the excitation energy into adsorbate levels located above the Fermi level (Link and Sayed, 1999). The characteristic surface plasmon absorbance was observed at 571 nm for the solution obtained by the mixed solvent approach (method M). In comparison, the peak was observed at 592 nm for the solution prepared by the sequential approach (method S). Peak shift to shorter wavelength suggests the formation of separated nanoparticles in Method M in comparison to that formed by Method S. This may be due to the dilution of the MeOH

content in the solvent used in Method S, leading to a reduction in hydrogen bonding between methanol and amine-terminated nanoparticles. This may also have been promoted by the formation of hydrogen bonds between MeOH and water at the molecular level, thereby reducing the availability of MeOH to bind with the amines (Guo et al., 2003). A scenario for possible hydrogen bond formation among the various functionalities is shown in Scheme 5.1.2. Thus, there is a possibility that by altering the polarity of the solvent in the processing step, the particle size can be better controlled. Additional evidence of the role of polar solvent molecules in the state of aggregation of the nanoparticles was obtained by observing the spectral features in protic and aprotic media. Figure 5.1.2B compares the UV-visible spectra for the nanoparticles prepared by Method M dispersed separately in a protic medium (MeOH) and an aprotic medium (DMAc). The characteristic surface plasmon absorbance peak shifts to 608 nm after dispersion in MeOH, whereas the peak position is observed at 571 nm for the nanoparticles dispersed in DMAc; this indicates the aggregation of the nanoparticles dispersed in the alcohol medium.

To further reduce the aggregation, masking of the amines that populate the surface of the nanoparticles may be helpful. Accordingly, a dianhydride capping agent was employed to reduce the amine density on the particle surface and further separate the amines from neighboring particles. Schemes 5.1.3 and 5.1.4 show the preparation sequence and the ensuing scenario. The amines on the gold surface were stabilized through reaction with PMDA using DMAc as the medium. Figure 5.1.3 compares the UV-visible spectra for

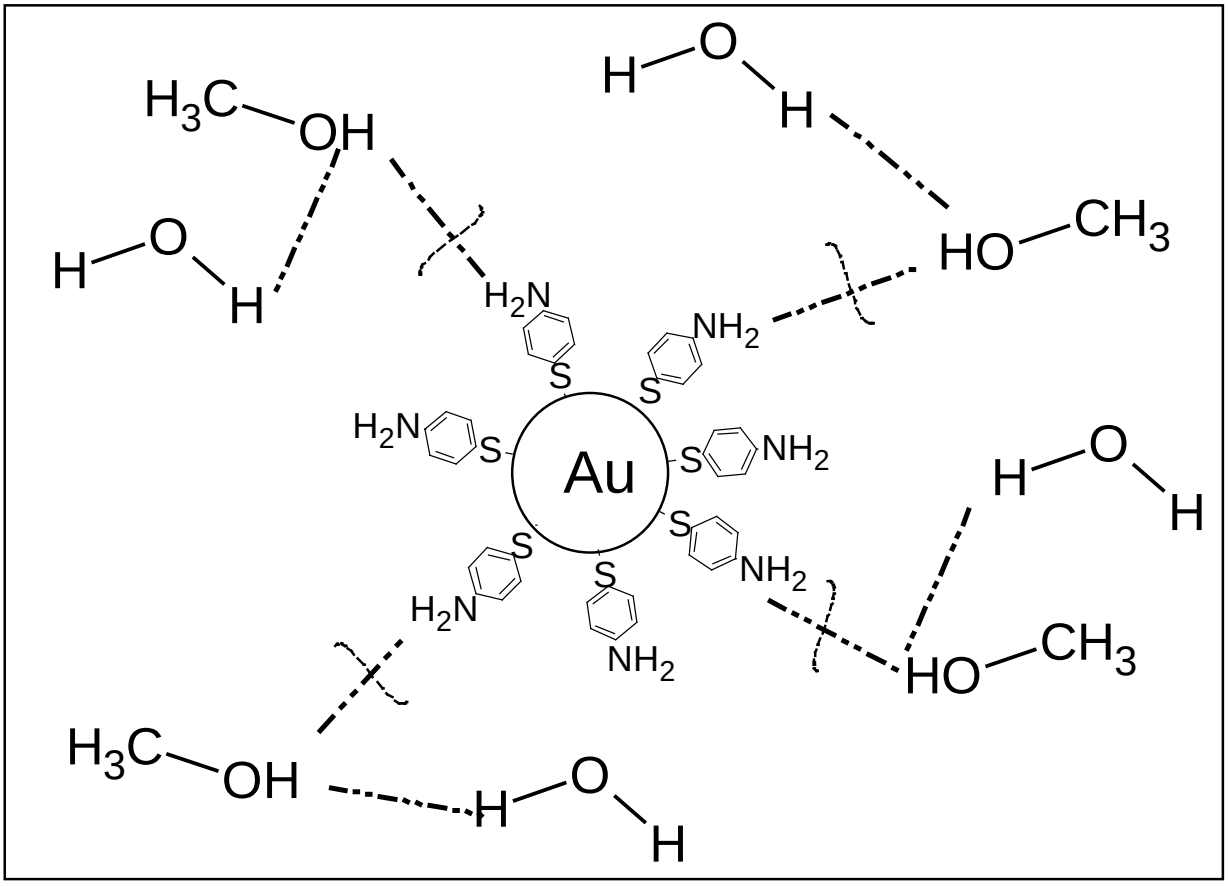

Scheme 5.1.2. Schematic for the possible hydrogen bonding among various functionalities.

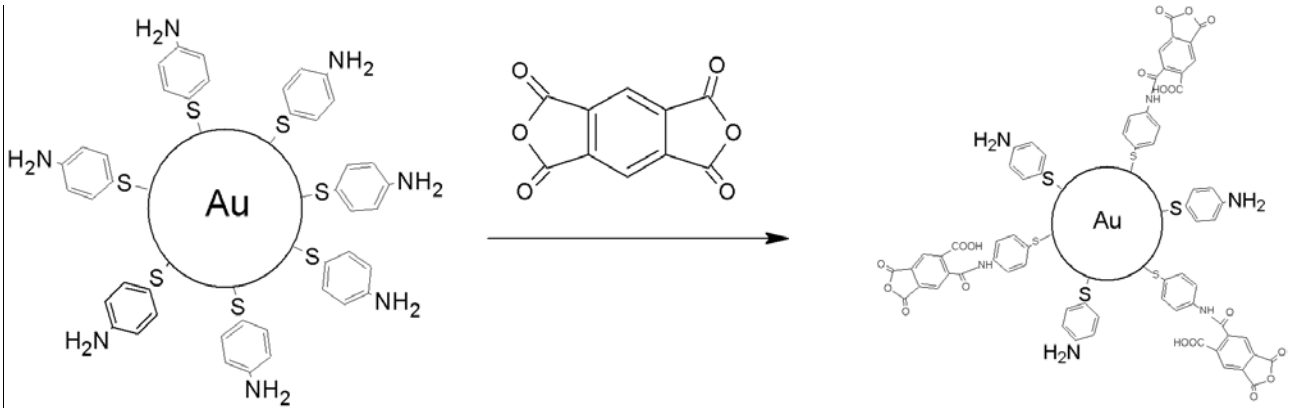

Scheme 5.1.3. Schematic for the preparation of stabilized gold nanoparticles.

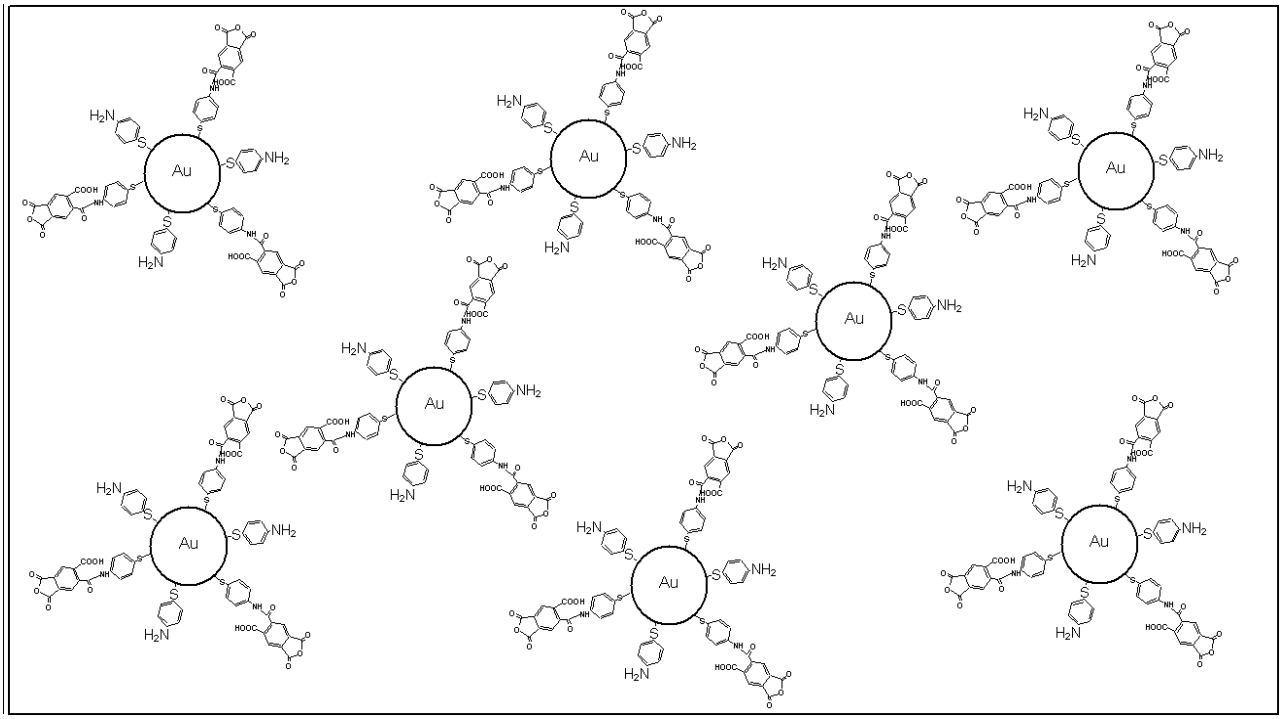

Scheme 5.1.4. Schematic for the proposed mechanism to get well separated anhydride functionalized gold nanoparticles.

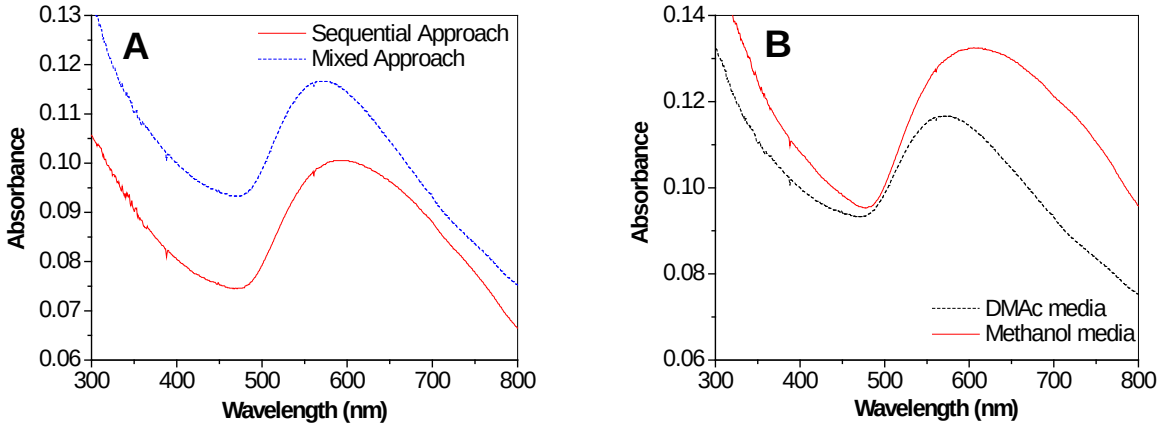

Figure 5.1.2. UV-visible absorption spectra of gold nanoparticles synthesized (A) effect of synthesis method (B) effect of dispersion media.

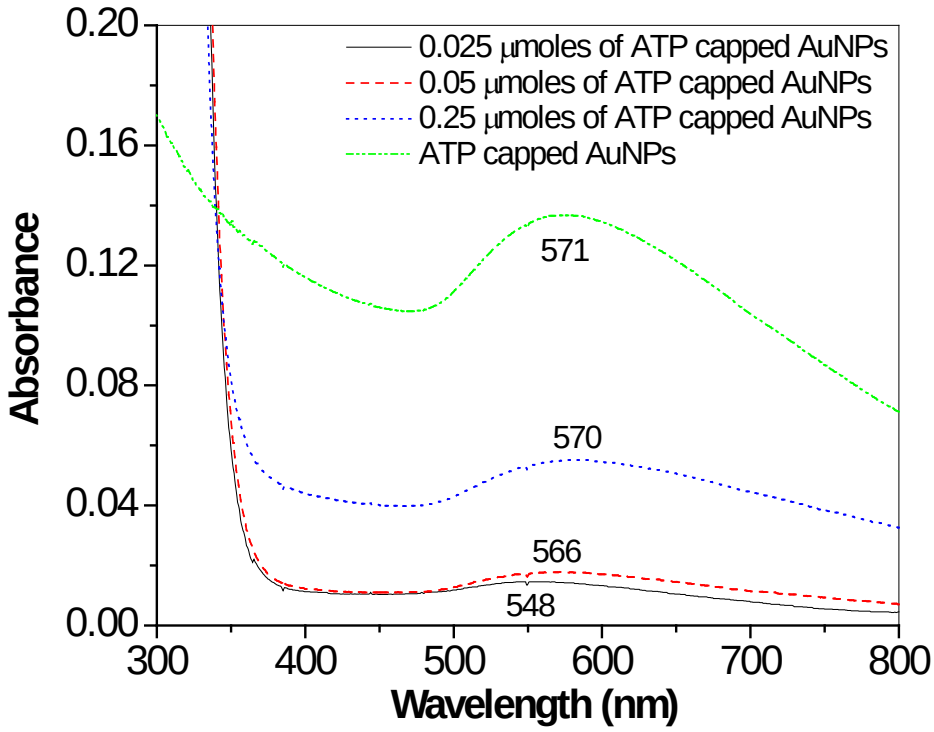

Figure 5.1.3. UV-visible absorption spectra of gold nanoparticles of DMAc dispersion after reaction of various amounts of nanoparticles with 5 mL of 5 mM. PMDA.

different concentrations of the nanoparticles in DMAc. Blue shifts in the peak positions are observed as the amount of nanoparticles relative to that of PMDA (which is held constant as described in experimental section) is reduced. The position of the absorption peak shifts from 571 nm in the case of the amine-capped nanoparticles prior to reaction with PMDA to 548 nm after reaction with PMDA. This shift clearly shows that the extent of aggregation can be controlled by adjusting the nanoparticle content in the reaction mixture relative to that of PMDA.

X-ray Photoelectron Spectroscopy (XPS)

Figure 5.1.4A shows the XPS spectra of the amine-capped nanoparticles formed by Method M obtained for the N 1s region, which consists of a single peak at 398.7 eV indicating the presence of primary amines. Figure 5.1.4B is the spectrum for the S 2p region, with thiolate peaks observed at 163.2 eV and 164.3 eV corresponding to S $2p_{3/2}$ and S $2p_{1/2}$ peaks, confirming the absence of unreacted or oxidized thiol species (Castner, 1996; Majumdar et al., 2003).

The samples for XPS analysis for nanoparticles stabilized with PMDA were prepared by placing drops of a solution of nanoparticles on to a clean Si substrate and allowing the solvent to evaporate under vacuum drying. Figure 5.1.5A shows the spectrum for the C1s region, which consists of peaks at 286 eV, 287.6 eV and 288.7 eV assignable to C-N, amide (-CO-NH-) and the anhydride (-CO-O-CO-), respectively. This indicates that the

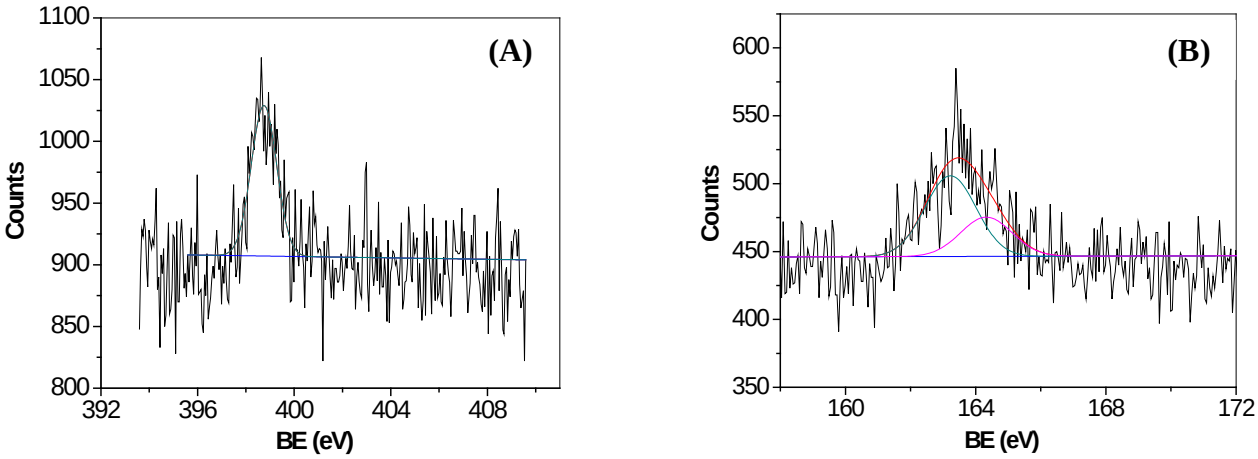

Figure 5.1.4. X-ray photoelectron spectra of 4-ATP capped gold nanoparticles through mixed approach showing the (A) N 1s region and the (B) S 2p region.

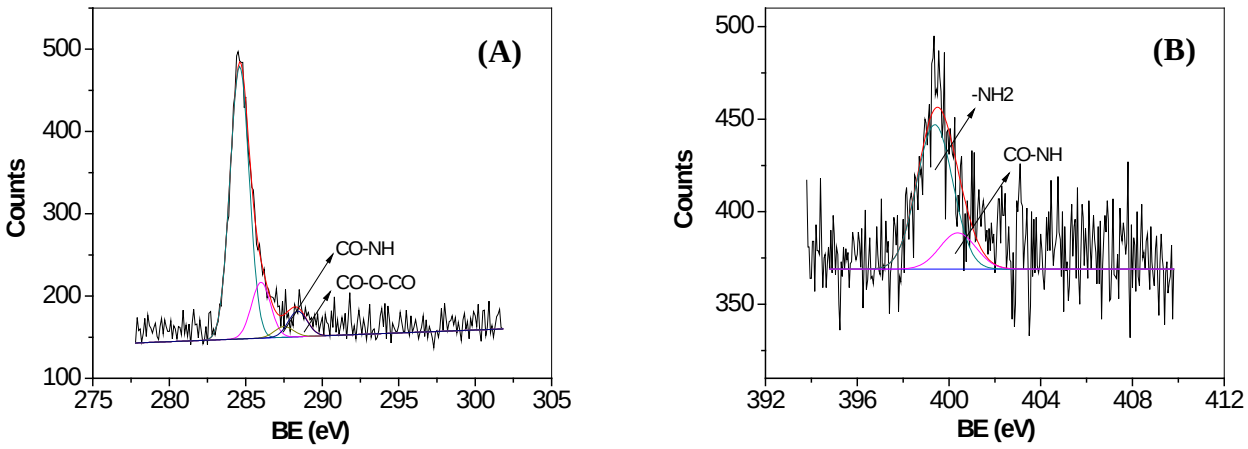

Figure 5.1.5. X-ray photoelectron spectra of gold nanoparticles stabilized with PMDA showing the (A) C 1s region and the (B) N 1s region.

amines of the nanoparticles have reacted with PMDA resulting in formation of the amide bond; it can also be inferred that the anhydride now acts as the end-capping group and assists in the segregation. While there is the likelihood that anhydrides from unreacted PMDA in solution may also show up in C1s spectrum, the presence of the amides provides clear evidence that PMDA is indeed bound to the amine. The N1s region [Figure 5.1.5B] reveals one extra peak at 400.2 eV apart from primary amine peak, which is attributed to the amide group, which further confirms occurrence of this reaction. Presence of primary amine suggests that all amines from the ATP capping on gold nanoparticles do not bind to PMDA, possibly due to steric hindrance among the PMDA molecules.

Transmission Electron Microscopy (TEM)

Samples for TEM were prepared by placing a drop of the nanoparticle-containing solution on copper grids followed by drying overnight. Figure 5.1.6A shows the TEM images of nanoparticles synthesized by the Method M with an average diameter of 3.8 ± 1.1 nm. The micrograph indicates the formation of spherical aggregates due to hydrogen bonding among amine capped nanoparticles. Figures 5.1.6B to 5.1.6D show the TEM images of nanoparticles after reaction with PMDA. The micrographs show the variation in spatial distribution and the state of aggregation of the nanoparticles with the concentration of nanoparticles. Well dispersed nanoparticles were obtained for the lowest concentration of nanoparticles used (viz., 0.025 µmoles) with an average diameter of 2.7 ± 0.5 nm (Figure 5.1.6D). All the nanoparticle solutions were prepared so as to have the same nanoparticle concentration in order to neutralise the effect of dilution on the

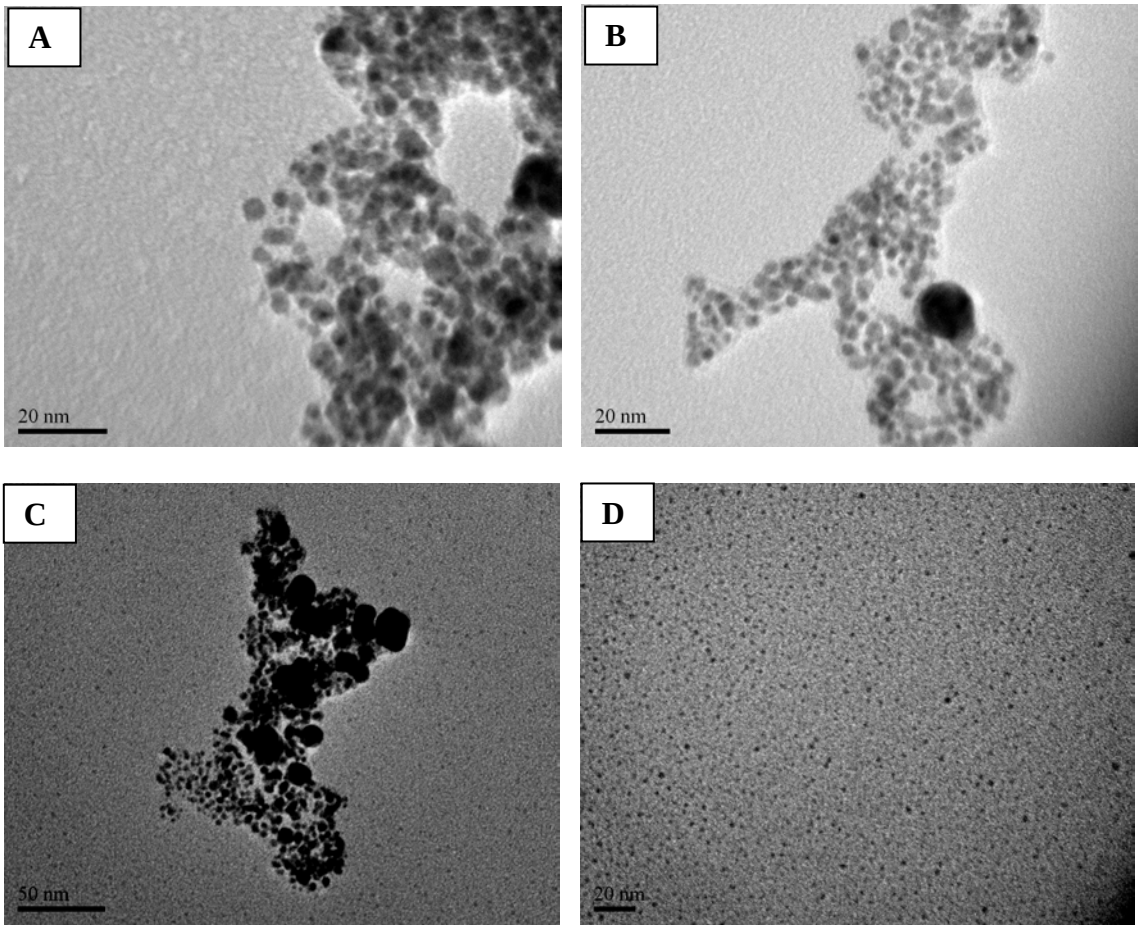

Figure 5.1.6. TEM images for gold nanoparticles (A) synthesized gold nanoparticles through mixed approach (B) 0.25 µmoles of gold nanoparticles after reaction with PMDA (C) 0.05 µmoles of gold nanoparticles after reaction with PMDA (D) 0.025 µmoles of gold nanoparticles after reaction with PMDA.

morphology of the nanoparticles. This confirms that the surface coverage of PMDA makes the aggregation diminish and the particles are sterically far enough apart.

5.1.3.2 Immobilization of Stabilized Gold Nanoparticles

In order to confirm the activity of the anhydride-stabilized nanoparticles, an amine-functionalized silicon surface was immersed in a DMAc solution containing the anhydride terminated nanoparticles so as to immobilise the latter on the substrate. In the wide scan XPS spectra of the nanoparticle-covered surface shown in Figure 5.1.7, the Au 4f peak was observed around 84.4 eV which was absent in APhS (amine – derivatised surface) functionalized film. Figure 5.1.7C shows Au 4f spectrum for gold nanoparticles immobilized on Si substrate de-convoluted at Au $4f_{7/2}$ and Au $4f_{5/2}$. Both Au $4f_{7/2}$ and Au $4f_{5/2}$ bands at 83.9 eV and 87.7 eV, respectively were observed. The slight shift to higher binding energy when compared to that for bulk nanoparticles is probably due to a shift in the Fermi level as the particle size is decreased. These shifts have also been reported previously (Evans, 1977; Nakamoto et al., 2002; Johnson et al., 1998). The detection of the presence of the nanoparticles after the substrates were subjected to a 5 min sonication in DMAc suggests that the nanoparticles are indeed covalently bound to the amine-derivatised silicon surface and not adsorbed on it. The immobilized nanoparticles were also directly observed with cross - sectional HR-TEM. Figure 5.1.8 shows the image of anhydride terminated nanoparticles bound to the silicon surface. The size of the immobilized nanoparticles was observed to be 3.2 ± 0.5 nm, which is similar to that observed in TEM images. While there is no evidence of increase in aggregation during

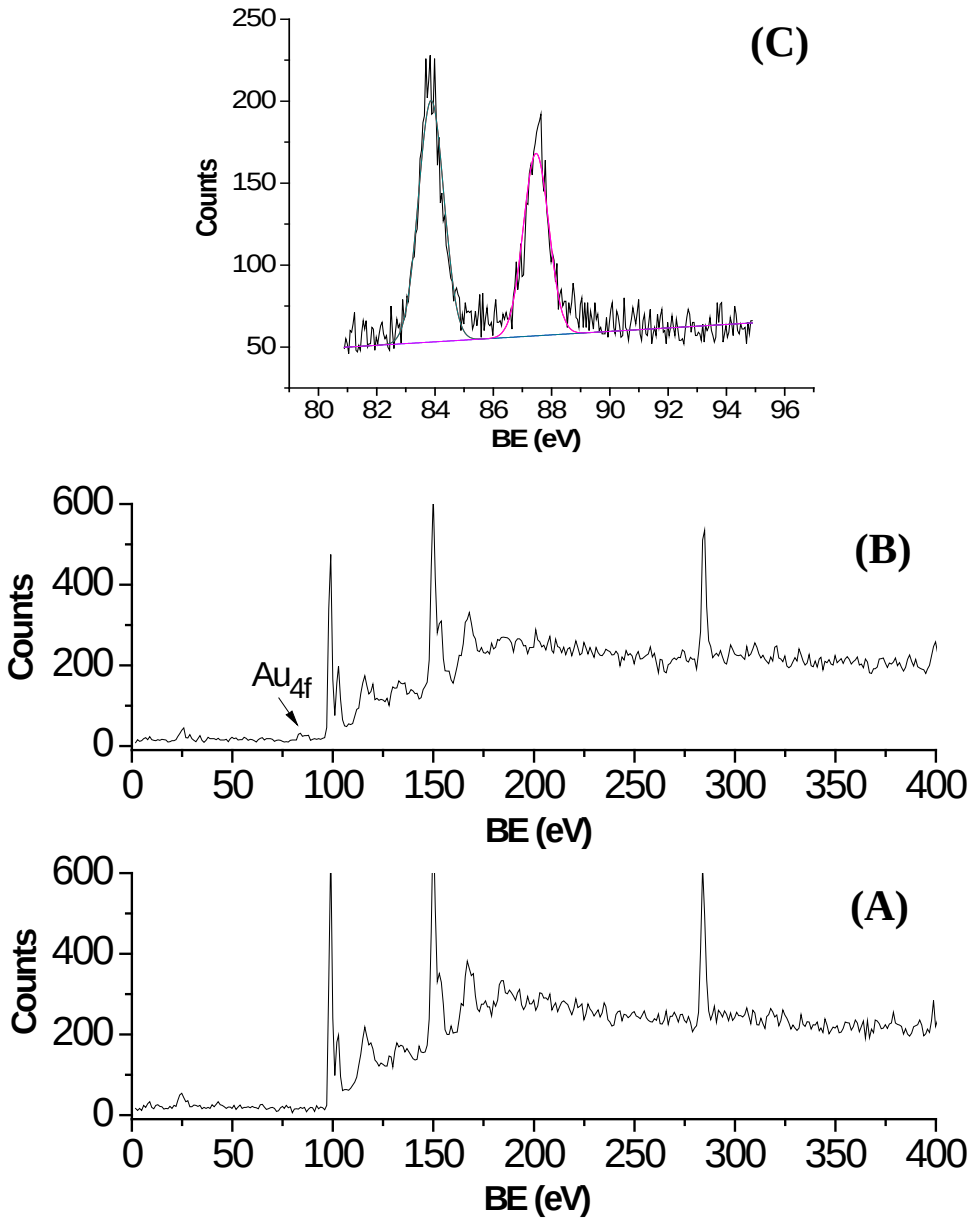

Figure 5.1.7. X-ray photoelectron wide spectra. (A) APhS-modified Si substrate, (B) gold nanoparticles immobilized on Si substrate, (C) Au $4f_{7/2}$ and $4f_{5/2}$ spectra of gold nanoparticles immobilized on Si substrate.

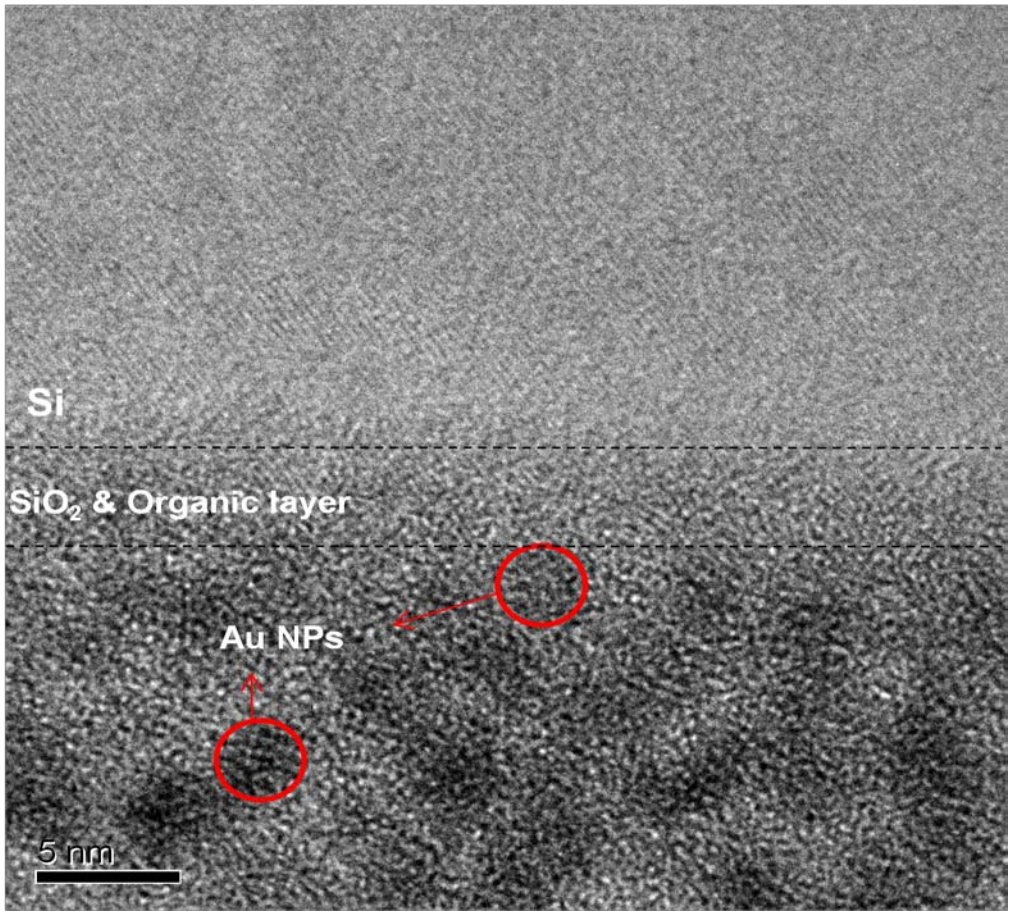

Figure 5.1.8. Cross-sectional HR-TEM image of gold nanoparticles immobilized on Si substrate.

immobilization, the nanoparticles are observed to be present as a multilayered stack. This may be due to binding of the anhydride functionality available at one nanoparticle with the amine functionality from another nanoparticle during the immobilization process.

5.1.4 Conclusions

This chapter has demonstrated the potential of covalent binding in the bottoms up approach for constructing nano-scale structures. Amine-functionalized gold nanoparticles were synthesized using a medium that reduced the aggregation. Subsequently, the nanoparticles were stabilized using a dianhydride (PMDA) as a capping agent. The formation of PMDA capping is confirmed by XPS, and the nanoparticle morphology can be controlled by the relative amount of gold nanoparticles and PMDA. Detailed structural observations of covalently immobilized gold nanoparticles on amine terminated silicon surface were performed. XPS and cross–sectional HR-TEM analysis confirmed that the gold nanoparticles were covalently attached to the silicon surface.

CHAPTER 5.2

SYNTHESIS OF 16-MERCAPTOHEXADECANOIC ACID CAPPED GOLD NANOPARTICLES AND THEIR IMMOBILIZATION ON A SUBSTRATE

5.2.1 Introduction

Controlled assembly of nanoparticles into ordered architectures on substrates is a promising path to develop miniaturized electronic and optical devices. Among the important issues to be addressed in this area include immobilization of the nanoparticles on substrates in order to ensure that the system is robust. In this chapter, synthesis of 16-mercaptohexadecanoic acid capped gold nanoparticles (AuNPs) through a single phase method is described along with their morphological changes at different process conditions, and their immobilization on to silicon and gold surfaces. Fourier transform infrared spectroscopy, X-ray photoelectron spectroscopy, transmission electron microscope and UV-Visible spectroscopy were employed to investigate particle morphology and surface modification of the nanoparticles, and their immobilization on silicon surface. Fourier transform infrared spectroscopy and X-ray photoelectron spectroscopy confirmed the absence of unreacted thiol in the synthesized AuNPs. Presence of AuNPs on Si surface after the immobilization process was confirmed through X-ray photoelectron spectroscopy. Cross-sectional high resolution transmission electron microscope images provide direct evidence that the nanoparticles are indeed anchored to the silicon surface.

5.2.2 Experimental Section

5.2.2.1 Materials

Hydrogen tetrachloroaurate (III) trihydrate ($HAuCl_4.3H_2O$) (≥ 99.9 %, Aldrich; *corrosive, handle with care*), 16-mercaptohexadecanoic acid (16-MHDA) (90 %, Aldrich), sodium borohydride ($NaBH_4$) (98 %, Lancaster), 3-cyanopropyltrichlorosilane (98 %, Lancaster), methanol (≥ 99.5 %, Merck), chloroform (≥ 99 %, Merck), N, N-dimethylacetamide (DMAc) (≥ 99 %, Merck) and thionyl chloride ($SOCl_2$) (≥ 99 %, Merck; toxic) were all used as received. Silicon wafers <100> (Engage Electronics Pte Ltd., Singapore) were 0.6 mm thick, p-doped, polished on one side and with a natural oxide layer.

5.2.2.2 Synthesis of Thiol-Stabilized Gold Nanoparticles

16-MHDA capped AuNPs were synthesized by employing two methods: one carried out at room temperature and the other at 0 ^oC.

Method A – Carried Out at Room Temperature

The nanoparticle synthesis was carried out by a procedure similar to that described (Brust et al., 1995). 20 mL of 0.053 M $HAuCl_4.3H_2O$ in methanol solution was added to a flask at room temperature, followed by 20 mL of 0.095 M 16-MHDA solution in methanol. 10 mL of acetic acid was added to the mixture to prevent deprotonation, followed by addition of 10 mL of a 0.891 M $NaBH_4$ solution with vigorous stirring. A change of color of the solution from yellow to black was observed. The stirring was continued for 3 h to achieve thermodynamic equilibrium at room temperature. The solvent was removed by high speed centrifugation at 8000 rpm. The product was washed three times with diethyl

ether and water to remove excess surfactants, centrifuged at 8000 rpm for 30 min to remove solvents and finally dried in a vacuum oven at room temperature.

Method B – Carried Out at 0^{o}C

5 mL of 0.05 M 16-MHDA solution in methanol was added to 20 mL of 5 mM $HAuCl_4.3H_2O$ in methanol with vigorous stirring, in a flask surrounded by an ice-water mixture at 0^{o}C. After 10 min, 40 mL of freshly prepared 0.39 M aqueous sodium borohydride was added to the mixture with stirring. The reaction mixture turned brown indicating the formation of AuNPs. The stirring was continued for 1 h. The solvent was removed by high speed centrifugation at 8000 rpm. The precipitate was washed twice with a 20% (v/v) water/methanol solution to remove excess surfactants. Subsequently, the product was washed with pure methanol to remove unbound thiols, centrifuged at 8000 rpm for 30 min to remove solvents and finally dried in a vacuum oven at room temperature.

5.2.2.3 Immobilization on Silicon Surface

Preparation of Acid Functionalized Surface

3-cyanopropyltrichlorosilane (CPS) functionalized silicon surface was prepared as described elsewhere (Puniredd and Srinivasan, 2006), wherein the hydroxyl covered substrates were rinsed with chloroform and immersed in 3 mM of CPS solution in chloroform at room temperature for 12 h under nitrogen purge. This was followed by sonication to remove any physically bound silane species. The cyano functional groups at

the free end of the immobilized silane were hydrolyzed to carboxylic acid by treatment with a solution of 1:1 (v/v) of concentrated sulfuric acid and deionized water at 100 °C for 2 h. The substrates were then rinsed in deionized water and dried in a vacuum at 100 °C for 1 h. Acid terminated TEM gold grids (SPI, USA) were obtained by immersing the grids in 1 mM ethanol solution of 16-MHDA for 1 h followed by sonication in ethanol for 5 minutes.

Acid Chloride Formation

Acid to acid chloride conversion was performed in a gaseous phase (Duevel and Corn, 1992). The carboxylic acid-derivatised substrates were placed in a reaction vessel that was purged with N_2. 50 µL $SOCl_2$ was then injected into the reaction vessel and the vessel was left standing for 30 min. The vessel was then purged with nitrogen for another 30 min to remove any HCl and other byproducts of the reaction.

Immobilization of Gold Nanoparticles

Acid terminated nanoparticles were covalently bound to the acid chloride-derivatised surface through ester formation (Inanaga et al., 1979; Kim et al., 1995). The acid chloride-containing surfaces formed as shown above were immersed in a 100 µg/mL solution of 16-MHDA capped nanoparticles in DMAc in a three-necked flask containing a magnetic stirrer-bar, fitted with a reflux condenser and a nitrogen inlet. The contents of the flask were held at 75 ^{o}C for 2 h with stirring after the addition of 50 µL of pyridine which acted as catalyst and proton scavenger. Subsequently, the substrates were rinsed

with DMAc followed by sonication for 5 min in DMAc to remove any physically bound nanoparticles and rinsed again with DMAc as well as acetone, and were finally blown dry with nitrogen. Details of various deposition steps are shown in Scheme 5.2.1.

5.2.2.4 Characterization

Characterization by XPS, UV-Visible absorption, TEM and HR-TEM were performed as described in chapter 5, section 5.1.2.5.

(1). Fourier Transform Infrared Spectroscopy (FTIR)

Fourier Transform Infrared Spectroscopy (FTIR) was carried out using a Bio-Rad FTIR 3500 system in the transmission mode. The spectra, for the thiol stabilized Au nanoparticles were obtained by forming thin transparent KBr pellets containing the materials of interest. Before the measurement the FT-IR system was purged with dry air for 20 min, and the spectra were background corrected using a pure KBr pellet as reference. Each sample was subjected to multiple scans (256 times) at a resolution of 4 cm^{-1}.

5.2.3 Results and Discussions

5.2.3.1 Synthesis of 16-MHDA Capped Gold Nanoparticles

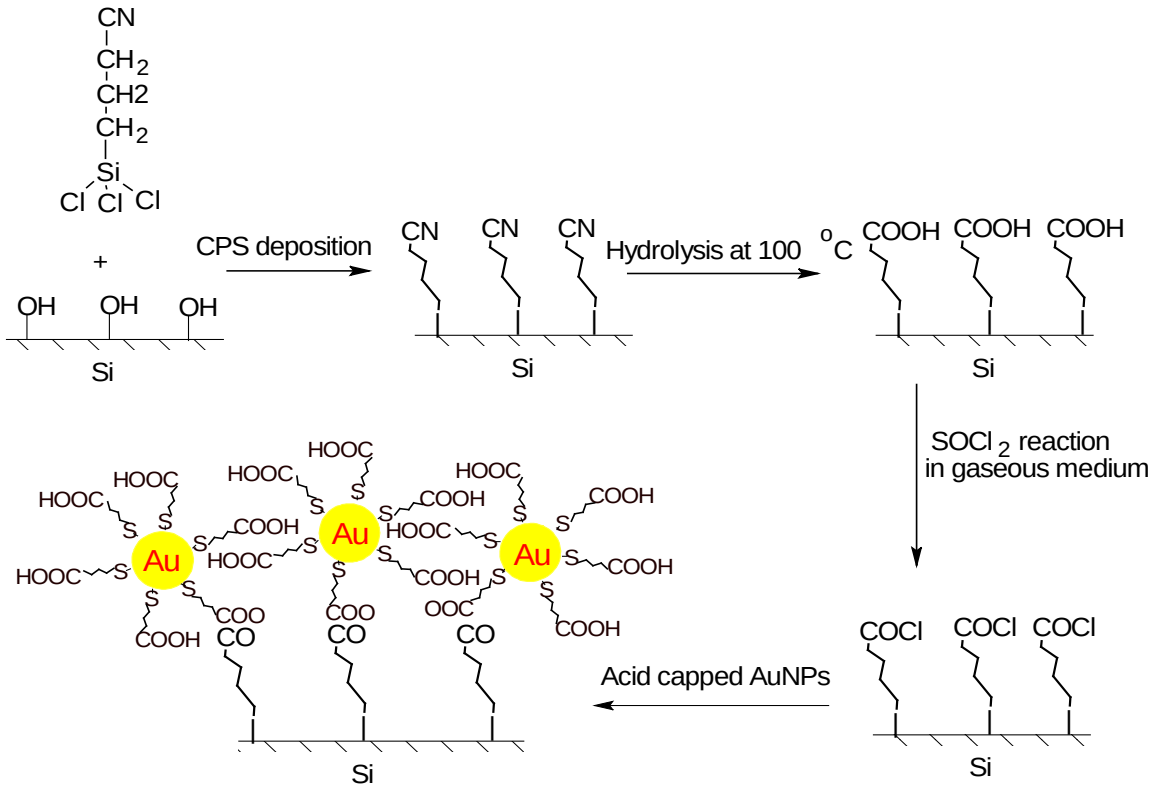

Scheme 5.2.1. Immobilization of acid terminated gold nanoparticles on to a hydroxyl-terminated silicon surface.

Fourier Transform Infrared Spectroscopy (FTIR)

FTIR spectra yield information regarding the stabilizing ligands surrounding the core of the nanoparticles. Figure 5.2.1 represents spectra of 16-MHDA capped AuNPs synthesized by Method A and Method B. Nanoparticles synthesized using Method B show no evidence of the S-H stretch (~2560 cm^{-1}), indicating the formation of an Au-thiolate bond due to cleavage of S-H bond upon S-Au chemisorption; this is typically observed during the formation of a thiol monolayer on gold (Hasan et al., 2002). However, for Method A, the occurrence of the S-H stretch suggests that excess thiol is present in these derivatives which are capable of forming H-bonds with acid terminated nanoparticles. Therefore, we infer that method B is more advantageous in view of the absence of unbound thiols. This inference is in agreement with earlier observation that room temperature synthesis methods do result in excess, unbound thiols (Johnson et al., 1998). Both spectra show the presence of acid functionality via the O-H and C=O stretching peaks at ~3500 cm^{-1} and 1690 cm^{-1}, respectively.

Transmission Electron Microscopy (TEM)

A few drops of the solution containing nanoparticles dispersed in DMAc were placed on carbon coated TEM grids and grids were imaged after solvent evaporation. Figures 5.2.2A and 5.2.2B show the TEM micrographs of 16-MHDA capped AuNPs synthesized by Method A and Method B, respectively. Method B yields well-separated and uniform-sized nanoparticles as shown earlier for 11-mercaptoundecanoic acid (Shi et al., 2004).

.

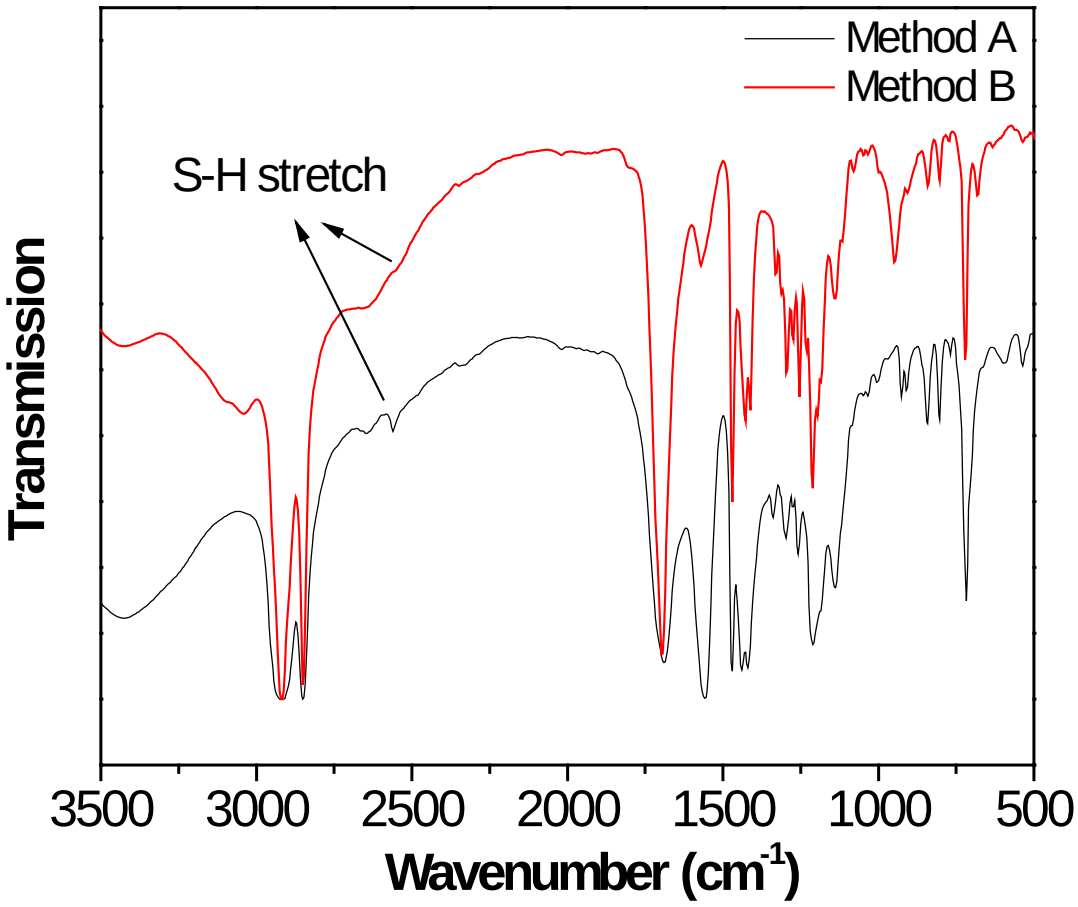

Figure 5.2.1. FTIR spectra for 16-MHDA capped gold nanoparticles synthesized by different methods.

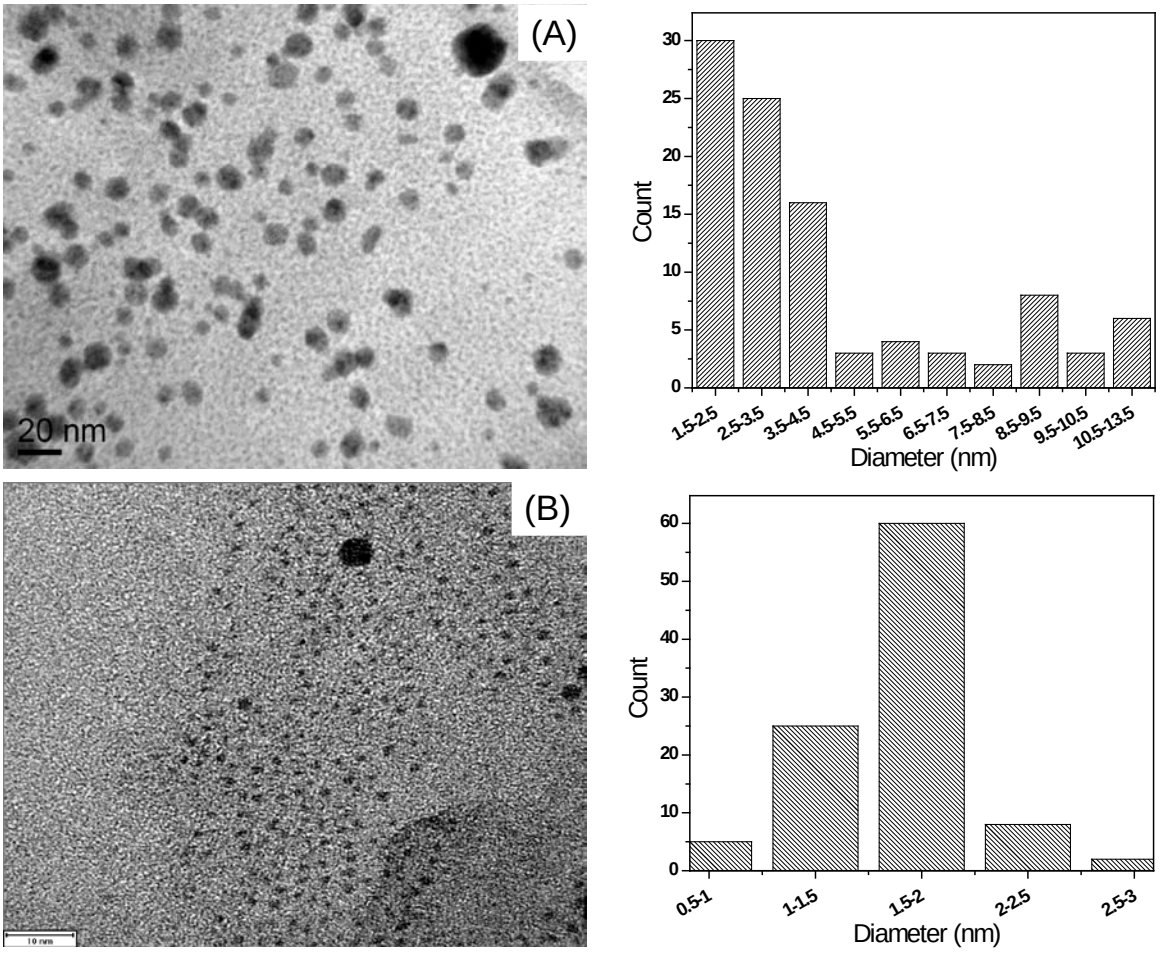

Figure 5.2.2. TEM images for 16-MHDA capped gold nanoparticles synthesized by (A) Method A - carried out at room temperature (B) Method B – carried out at 0 ^{o}C.

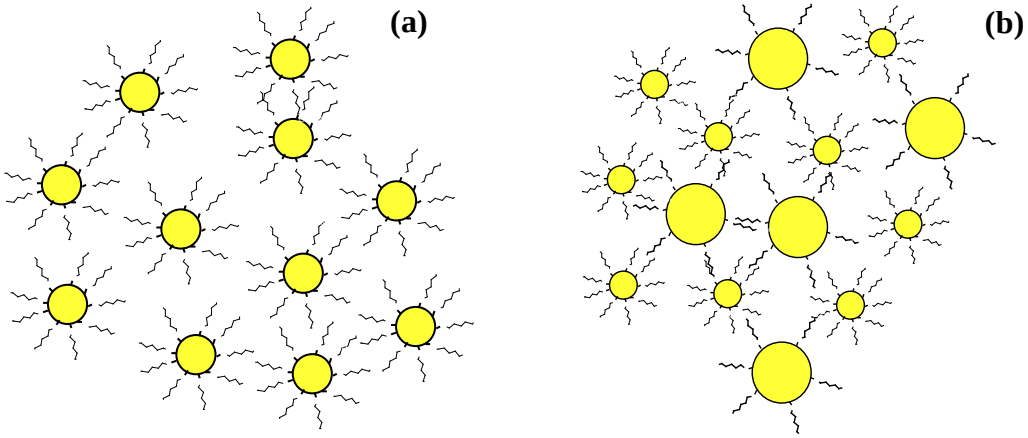

Scheme 5.2.2. Schematic for the 16-MHDA capped gold nanoparticles synthesized by (a) Method B – carried out at 0 ^{o}C and (b) Method A - carried out at room temperature.

From a histogram of frequency versus particle size, a mean particle size of 1.6 ± 0.2 nm was calculated. However, some aggregation of nanoparticles is observed for method A. Since the size of nanoparticles is determined through equilibrium between adsorption and desorption of thiol molecules on the nanoparticle surface, it is envisaged that the desorption rate of thiol molecules is diminished at low temperatures which reduces the exposed surface of the gold particles, and hence the growth of particles, and thus, results in formation of small uniform sized nanoparticles (Murray et al., 2000). Scheme 5.2.2 shows the schematic for 16-MHDA capped AuNPs obtained by different methods.

UV/Visible Spectroscopy

For electronic energy spectra, the position and magnitude of the absorption bands are strongly dependent on the size of particles, the refractive index of solvent used and the degree of aggregation (Balasubramanian et al., 2002; Mulvaney, 1996; Underwood and Mulvaney, 1994). In particular, the maximum of the surface plasmon band moves to longer wavelengths with increasing particle size and an increase in peak width at half maximum is related to increasing particle dispersity. Figure 5.2.3 compares the UV-visible spectra for the AuNPs synthesized by both methods. The broadening of the absorption band is due to size shrinkage of nanoparticles and this is caused by the transfer of the excitation energy into adsorbate levels located above the Fermi level (Link and Sayed, 1999). A characteristic surface plasmon absorbance at 560 nm in DMAc for nanoparticles synthesized by Method B was observed which confirms the presence of

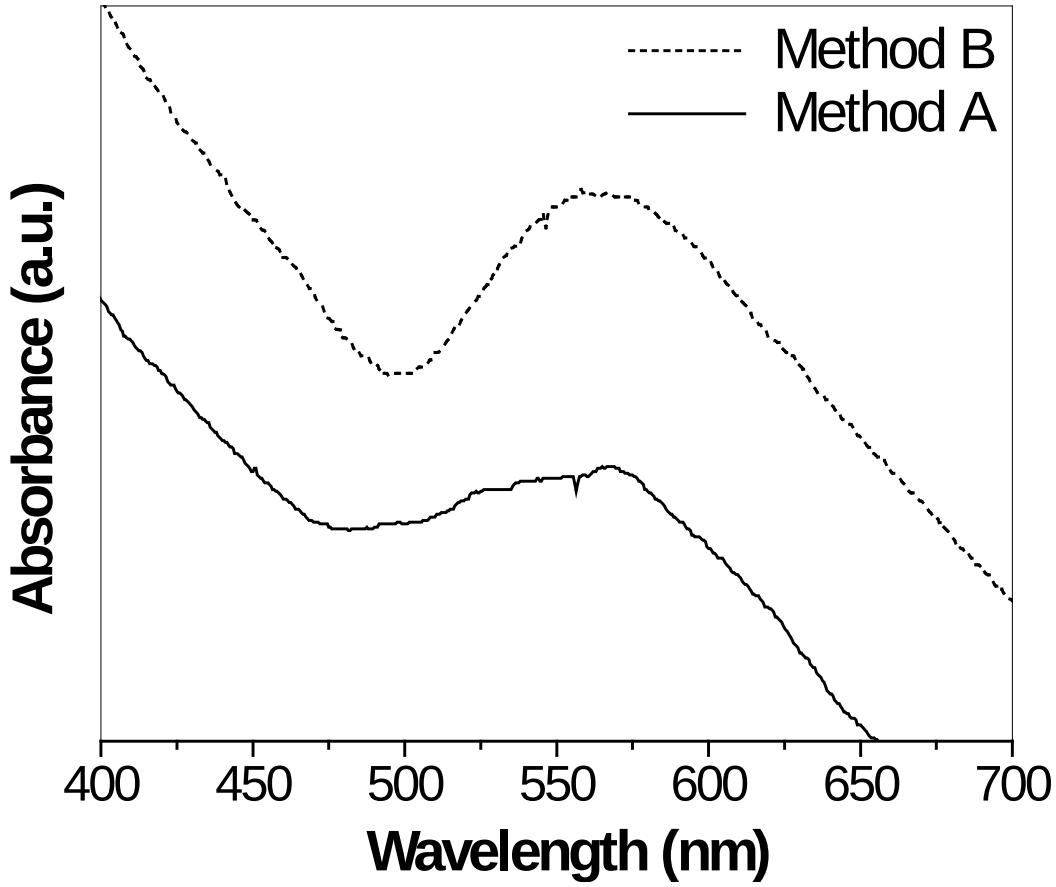

Figure 5.2.3. UV-visible absorption spectra of 16-MHDA capped gold nanoparticles synthesized by different methods in DMAc.

uniform sized and well dispersed nanoparticles as consistent with TEM images. For AuNPs synthesized by Method A, this band is broad with an increase in peak width at half maximum indicating poly-dispersed particle morphology as evidenced through TEM images, in agreement with experimental results (Shi et al., 2004).

X-ray Photoelectron Spectroscopy (XPS)

Figure 5.2.4 shows the XPS spectra for 16-MHDA capped AuNPs synthesized by Method B. Figure 5.2.4a shows the C1s region for the sample with the C-O component at 286.4 eV and the COO- component at 288.8 eV confirming the presence of the acid functionality. Figure 5.2.4b represents the S2p region, with thiolate peaks observed at 163.3 eV and 164.4 eV confirming the absence of unreacted thiol species (Castner, 1996). No evidence of oxidation of the sulfur was observed for which extra sulfur peaks would occur at 168.1 eV and 169.0 eV corresponding to sulfones/sulfates. The Au $4f_{7/2}$ and Au $4f_{5/2}$ bands occur at 84.3 eV and 87.9 eV, respectively (Figure 5.2.4c). There is slight shift to higher binding energy when compared to that for bulk nanoparticles, which is probably due to a shift in the Fermi level as the particle size is decreased. These shifts have also been reported elsewhere (Evans, 1977; Johnson et al., 1998; Nakamoto et al., 2002).

5.2.3.2 Immobilization of Acid Terminated Gold Nanoparticles

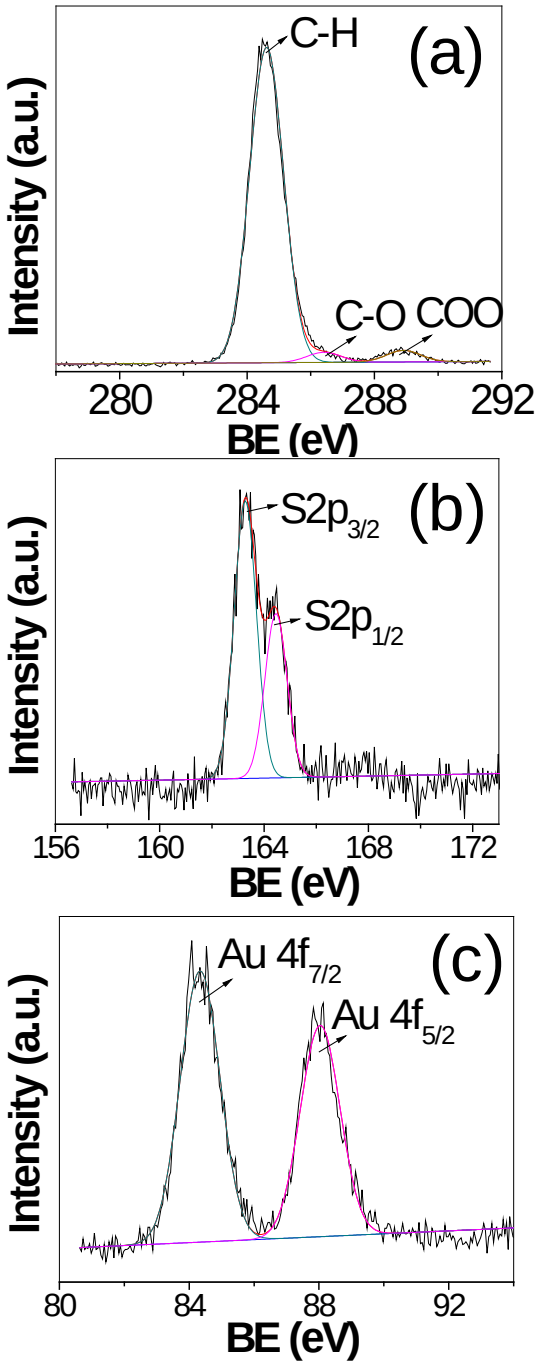

Figure 5.2.4. X-ray photoelectron spectra of 16-MHDA capped gold nanoparticles synthesized by Method B – carried out at 0 ^{o}C showing the (a) C 1s region, (b) S 2p region and (c) Au 4f region.

Figures 5.2.5A and 5.2.5B represent the TEM images of 16-MHDA deposited on a gold grid and 16-MHDA capped AuNPs immobilized on gold grid, respectively. Figure 5.2.5B shows presence of well-separated nanoparticles, indicating that there is no aggregation of nanoparticles during the immobilization step.

Subsequent to the confirmation that immobilization does not cause aggregation; nanoparticles were immobilized on silicon substrates. In the wide scan XPS spectra (Figure 5.2.6), the Au 4f peak observed around 84.4 eV shows the presence of gold (Figure 5.2.6A), which was absent in the CPS-COOH functionalized film immobilized on the silicon substrate (Figure 5.2.6B). It is important to note that these characterizations were performed subsequent to sonicating the substrate-bound nanoparticle systems in DMAc for 5 min, thereby ensuring that the particles were indeed firmly attached to the substrates. Apart from XPS, nanoparticles immobilized on to silicon surfaces were also directly observed with cross - sectional HR-TEM. Figures 5.2.7A and 5.2.7B show cross-sectional images for the silicon substrate without nanoparticles and for 16-MHDA capped AuNPs immobilized on to the silicon substrate, respectively. The inset shows the enlarged view of immobilized nanoparticles wherein a uniform nanoparticle layer can be seen. The size of immobilized nanoparticles was observed to be 1.9 ± 0.3 nm, which is similar to the sizes of particles as observed in TEM images. Thus, there is no aggregation of nanoparticles during the immobilization process on silicon substrate as well.

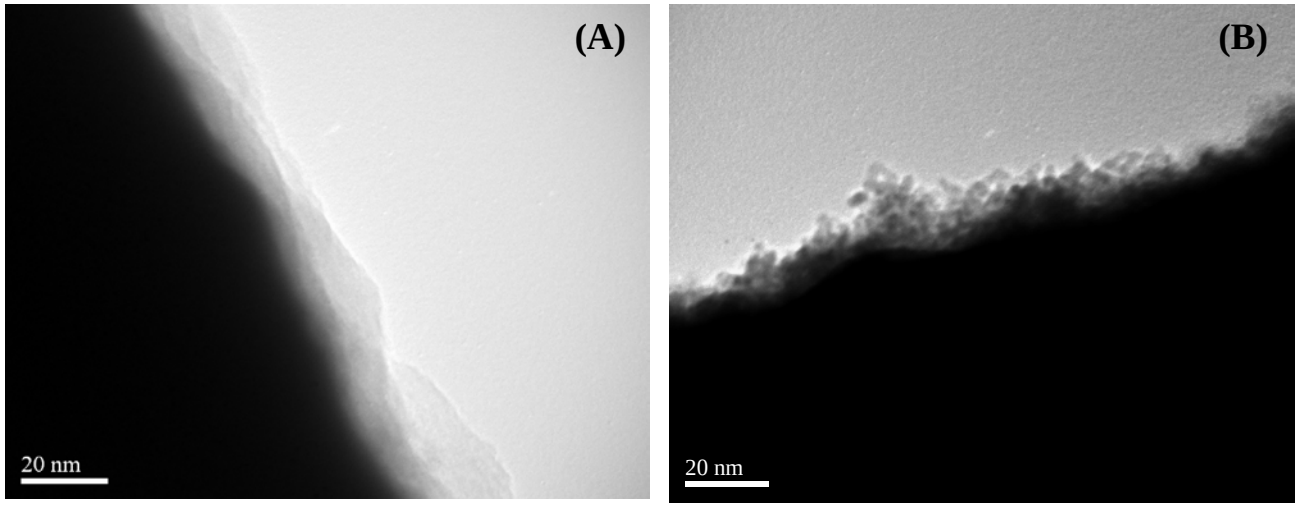

Figure 5.2.5. TEM images for (A) 16-MHDA monolayer deposited gold grid and (B) 16-MHDA capped gold nanoparticles immobilized on gold grid.

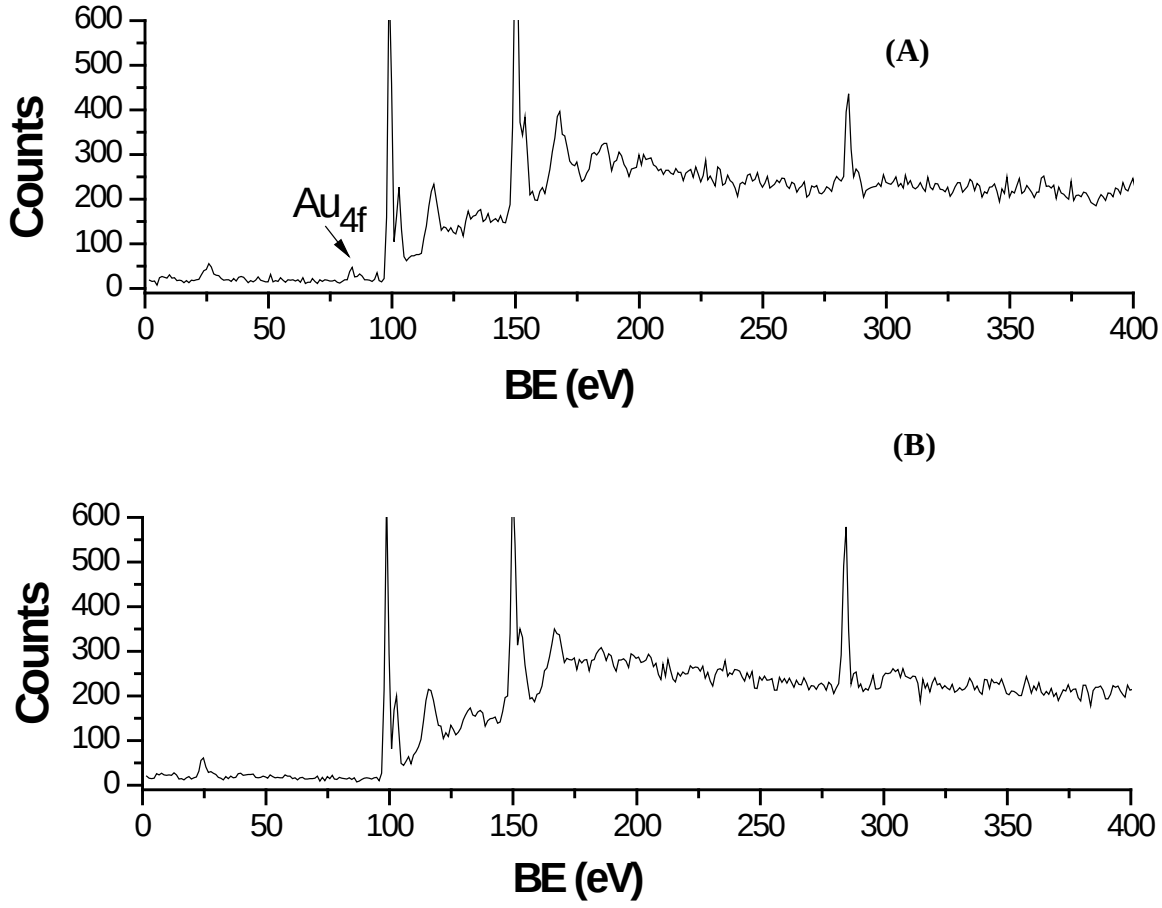

Figure 5.2.6. X-ray photoelectron wide spectra. (A) gold nanoparticles immobilized on Si substrate; (B) CPS-COOH modified Si substrate.

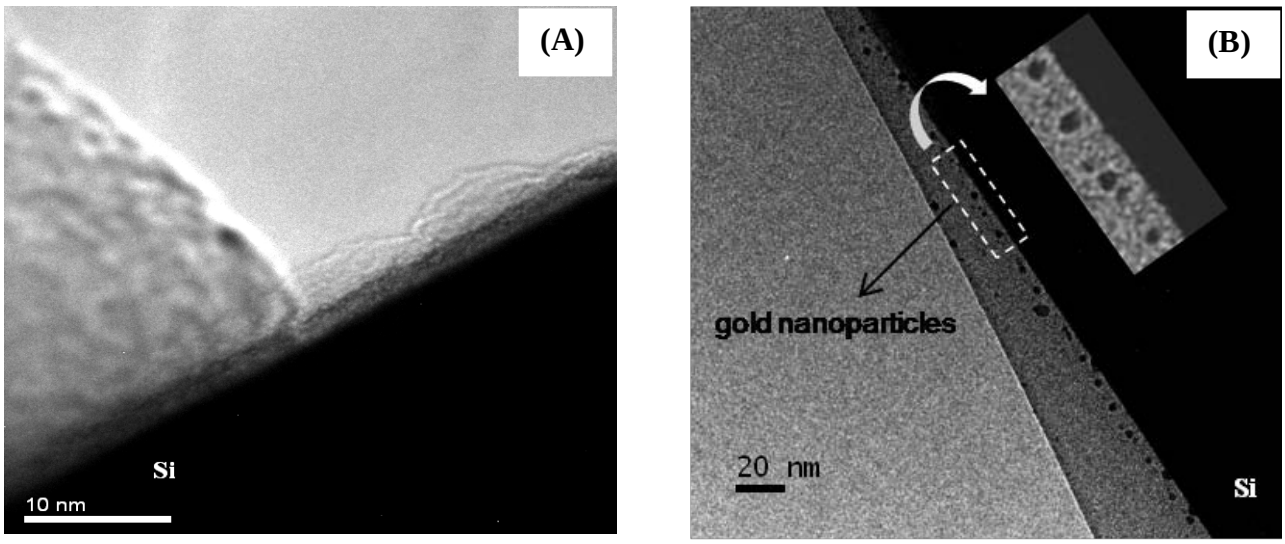

Figure 5.2.7. Cross-sectional HR-TEM images for (A) Si substrate without gold nanoparticles; (B) 16-MHDA capped gold nanoparticles immobilized on Si. The inset shows the enlarged view of immobilized gold nanoparticles.

5.2.4 Conclusions

The work described in this chapter demonstrates the surface functionalization capability of AuNPs prepared with 16-MHDA, a bifunctional ligand acting as a surfactant. Uniform sized, thiol stabilized gold nanoparticles can be obtained using a cold synthesis method in accordance with previous literature which reduces the possibility of leaving unreacted thiols hydrogen-bonded to each other. Detailed structural characterizations have been performed for covalently immobilized gold nanoparticles on silicon and gold surfaces. Using XPS and cross – sectional HR-TEM analysis, covalent attachment of AuNPs onto the silicon substrate has been confirmed. The presence of different terminal functionalities on the surface of nanoparticles may provide a handle for further binding to create purpose-built nanostructures. The present synthetic route to covalently immobilized gold nanoparticles system will be a step towards realization for the nanoparticle-based electronic devices and related applications.

CHAPTER 5.3

COVALENT ASSEMBLY OF GOLD NANOPARTICLES FOR NONVOLATILE MEMORY APPLICATIONS

5.3.1 Introduction

This chapter reports a versatile approach for enhancing the stability of nonvolatile memory devices through covalent assembly of functionalized gold nanoparticles (AuNPs). 11-mercapto-1-undecanol functionalized AuNPs with a narrow size distribution and particle size of about 5 nm were synthesized. Then, the AuNPs were immobilized on a silicon substrate using a functionalized polymer as a surface modifier. Microscopic and spectroscopic techniques were used to characterize the AuNPs and their morphology before and after immobilization. Finally, a metal-insulator-semiconductor (MIS) type memory device with such covalently anchored AuNPs as a charge trapping layer was fabricated. The MIS structure showed well defined counterclockwise C-V hysteresis curves indicating a good memory effect. The flat band voltage shift was 1.64 V at a swapping voltage between ±7 V. Furthermore, the MIS structure showed a good retention characteristic up to 20,000 s.

5.3.2 Experimental Section

5.3.2.1 Materials

p-Aminophenyltrimethoxysilane (APhS) (90 %, Gelest), hydrogen tetrachloroaurate (III) trihydrate ($HAuCl_4.3H_2O$) (≥ 99.9 %, Aldrich; *corrosive, handle with care*), 11-mercapto-1-undecanol (MUD) (≥ 97 %, Fluka), tetraoctylammonium bromide (TOAB) (98 %, Aldrich), sodium borohydride ($NaBH_4$) (98 %, Lancaster), poly(methyl vinyl ether-*alt*-maleic anhydride (Gantrez) (M_n~ 311000, M_w~ 1080000) (Aldrich), acetone (≥

99 %, Merck), i-propyl alcohol (≥ 99 %, Merck), tetrahydrofuran (THF) (≥ 99 %, Merck) and N, N-dimethylformamide (DMF) (≥ 99 %, Fisher Scientific), were all used as received. Silicon wafers <100> (Chartered Semiconductor, Singapore) were 0.6 mm thick, p-doped, polished on both side and having 4 nm thermally grown oxide layer.

5.3.2.2 Synthesis of Thiol-Stabilized Gold Nanoparticles

Synthesis of gold nanoparticles was carried out as mentioned earlier (Wanunu et al., 2005). Briefly, the preparation procedure was as follows: a solution of $HAuCl_4$ (0.2 g) in 20 mL of H_2O was added into a stirred solution of TOAB (0.6 g) in 40 mL of toluene. After 5 min, the biphasic solution was separated and the organic phase was placed in a 125-mL conical flask and stirred vigorously at 250 rpm. A solution of $NaBH_4$ (0.2 g) in 15 mL of H_2O was added dropwise over a period of 10 min, resulting in red colored solution. After the solution was stirred for 1.5 h, the two phases were separated and the organic phase was vigorously washed with 0.1 M HCl (15 mL), 0.1 M NaOH (15 mL), H_2O (45 mL) and saturated brine (20 mL).

Exchange of the TOAB capping layer with MH was performed as follows: To a stirred solution of MUD (0.15 g) in 17 mL of DMF, a solution of TOAB-capped AuNPs in toluene (34 mL) was added dropwise under N_2 atmosphere. The stirring was continued for 2 h, after which the solvents were concentrated to 0.5 mL in a rotary evaporator, and *i*-propyl alcohol was added and evaporated to near dryness. The NPs were flocculated through addition of *i*-propyl alcohol (0.5 mL) followed by acetone (30 mL). Excess MH

and TOAB were removed by centrifugation of the suspension and removal of the solvent, followed by addition of *i*-propyl alcohol (0.5 mL) and acetone (30 mL). This process was repeated four times to ensure complete removal of excess MUD and TOAB. Finally, the nanoparticle precipitate was dried under nitrogen environment overnight at room temperature.

5.3.2.3 Immobilization on Silicon Surface

Self-Assembly of Aminosilane

Silicon substrates were modified into amine terminated surface as described in Chapter 5.1, section 5.1.2.4.

Deposition of Gantrez Polymer Film

The above-treated substrates were immersed in a 0.5 % (w/v) THF solution of gantrez for 1 h under nitrogen environment. The substrates were removed from the solution, rinsed rigorously and sonicated for 5 min with THF, rinsed again with THF, finally blown dry with nitrogen.

Immobilization of Gold Nanoparticles

The above anhydride-terminated silicon surfaces were immersed in a 100 µg/mL solution of MUD capped AuNPs in DMF in a three-necked flask containing a magnetic stirrer-bar, fitted with a reflux condenser and a nitrogen inlet. The contents of the flask were held at

90 ^{o}C for 1 h with stirring. Subsequently, the substrates were rinsed with DMF followed by sonication for 5 min in DMF to remove any physically bound nanoparticles and rinsed again with DMF as well as acetone, and were finally blown dry with nitrogen. Details of various deposition steps are shown in Scheme 5.3.1.

5.3.2.4 MIS Capacitor Fabrication

A metal-insulator-silicon (MIS) capacitor device was fabricated. Following the incorporation of AuNPs, a pulsed laser deposition (PLD) method was used to deposit 10 nm thick Al_2O_3 control oxide. Au top electrodes (0.3 mm diameter size) are then sputter-deposited using shadow mask technique subsequently. After removing the oxide, Pt film was deposited as the back side contact. The MIS device configuration is shown in Figure 5.3.1.

5.3.2.5 Characterization

Characterization by XPS and TEM were performed as described in chapter 5, section 5.1.2.5. Characterization by AFM, FESEM and capacitance–voltage (C–V) and capacitance–time (C–t) measurement were performed as described in chapter 3, section 3.2.9.

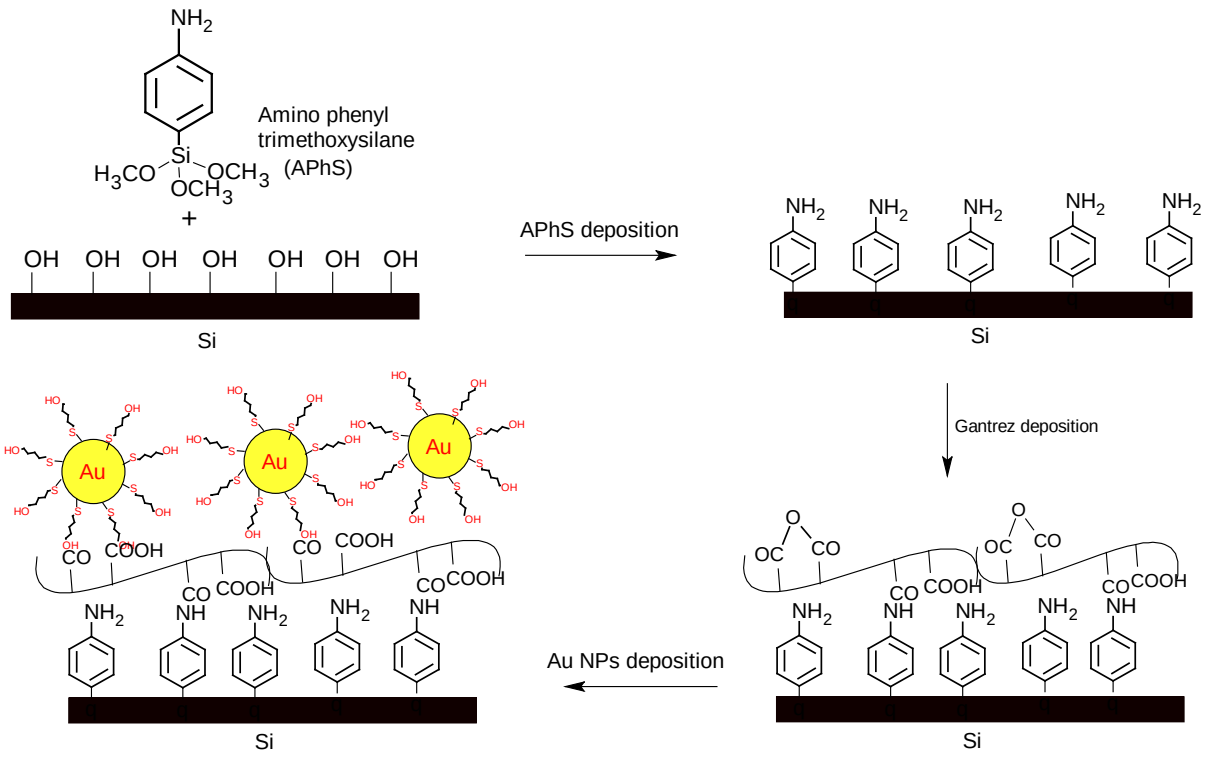

Scheme 5.3.1. Immobilization of MUD capped gold nanoparticles on to a hydroxyl-terminated silicon surface.

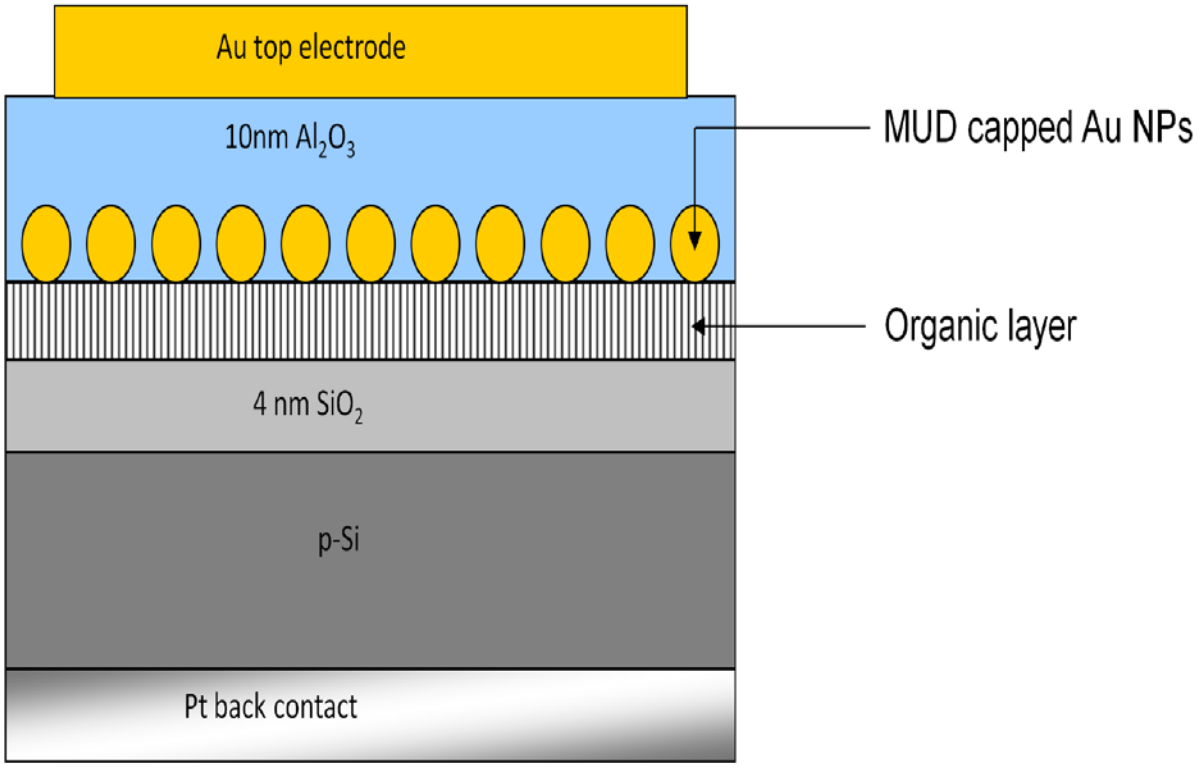

Figure 5.3.1. The MIS device configuration for the immobilized MUD capped gold nanoparticles.

5.3.3 Results and Discussions

5.3.3.1 Synthesis of MUD Capped Gold Nanoparticles

Transmission Electron Microscopy (TEM)

A few drops of the solution containing nanoparticles dispersed in DMF were placed on carbon coated TEM grids and grids were imaged after solvent evaporation. Figure 5.3.2a shows the TEM micrograph of synthesized MUD capped gold nanoparticles, and Figure 5.3.2b shows the size distribution for the AuNPs. The image shows that the NPs are approximately spherical, with an average Au core diameter of 5 ± 0.5 nm.

X-ray Photoelectron Spectroscopy (XPS)

Figure 5.3.3 shows the XPS spectra for synthesized MUD capped gold nanoparticles. Figure 5.3.3a shows the C1s region for the sample with the C-O component at 286.2 eV, confirming the presence of alcohol functionality. Figure 5.3.3b represents the S2p region, with peak observed at 163.3 eV and 164.4 eV corresponding to the thiolates which confirms the absence of unreacted thiol species (Castner, 1996). No evidence of oxidation of the sulfur was observed for which extra sulfur peaks would occur at 168.1 eV and 169.0 eV corresponding to sulfones/sulfates. The Au $4f_{7/2}$ and Au $4f_{5/2}$ bands occur at 84.3 eV and 87.9 eV, respectively (Figure 5.3.3c). There is slight shift to higher binding energy when compared to that for bulk nanoparticles, which is probably due to a shift in

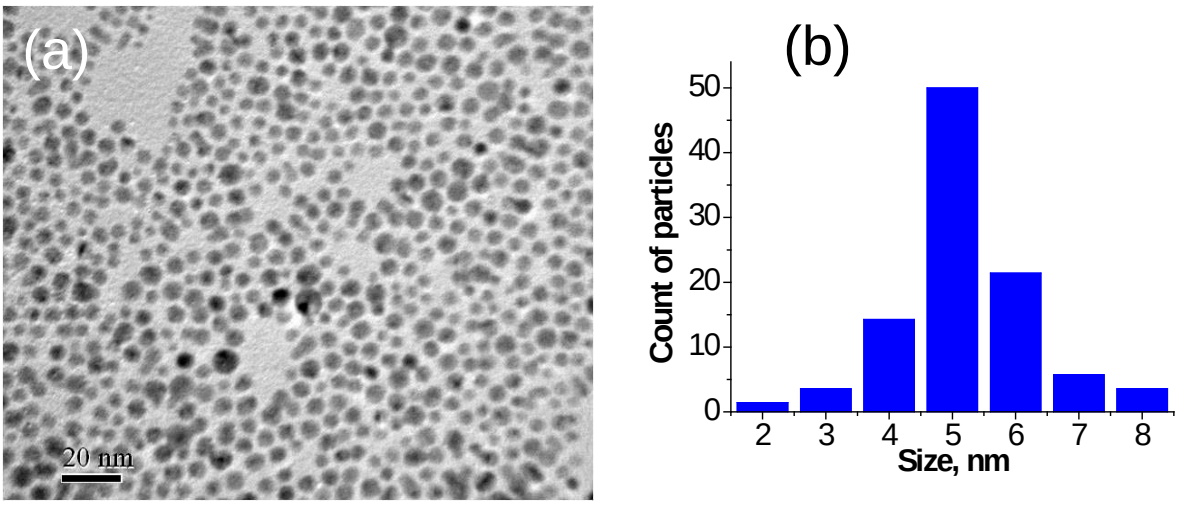

Figure 5.3.2. (a) TEM image of MUD capped gold nanoparticles, (b) size distribution of MUD capped gold nanoparticles.

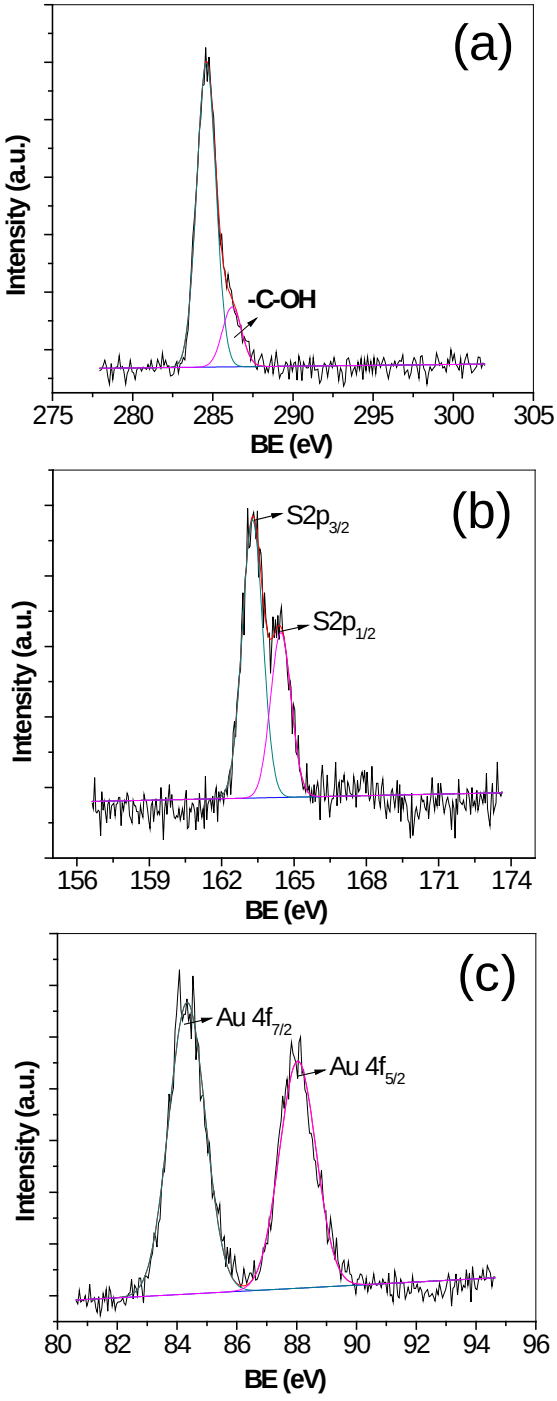

Figure 5.3.3. X-ray photoelectron spectra of MUD capped gold nanoparticles showing the (a) C 1s region, (b) S 2p region and (c) Au 4f region.

the Fermi level as the particle size is decreased. These shifts have also been reported elsewhere (Evans, 1977; Johnson et al., 1998; Nakamoto et al., 2002).

5.3.3.2 Immobilization of MUD Capped Gold Nanoparticles

X-ray Photoelectron Spectroscopy (XPS)

(a) Deposition of Gantrez

Successful reaction between amino moieties and anhydrides of gantrez is confirmed by presence of the C1s peak components for amide formation at 287.5 eV (-CO-NH-) and presence of anhydrides at 288.9 eV (-CO-O-CO-) as shown in Figure 5.3.4a.

(b) Deposition of MUD Capped AuNPs

When MUD capped AuNPs is deposited, these are anchored to the substrate with one of their terminal alcohol groups reacted with the anhydride on the gantrez, forming esters. C1s spectrum [Figure 5.3.4b] contains peak components for acid (-COOH) at 288.5 eV and ester (-COOR) at 288.2 eV. Also, the presence of C-O component at 286.2 eV confirms the presence of alcohol functionality at the substrate, which is due to MUD capped AuNPs.

Surface Morphology

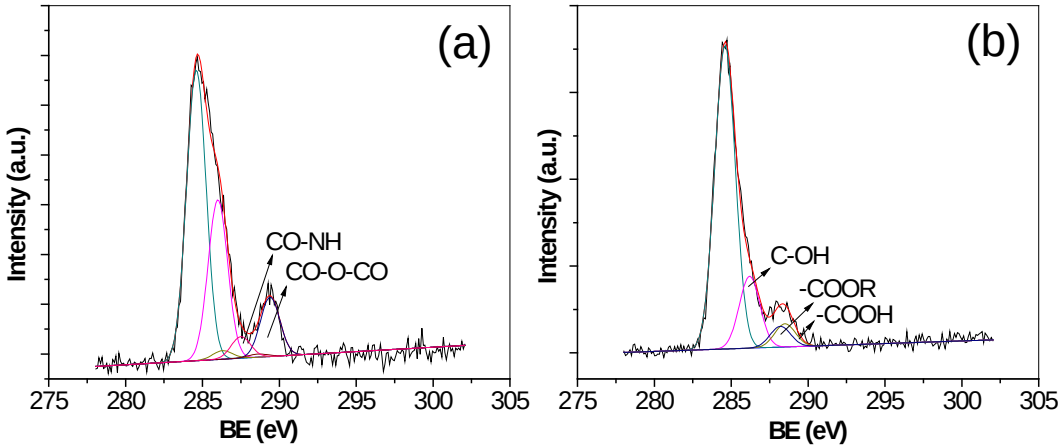

Figure 5.3.4. C1s core-level XPS spectra at various steps of the AuNPs assembly; (a) the gantrez deposited APhS substrate, (b) MUD capped AuNPs immobilized on Si substrate.

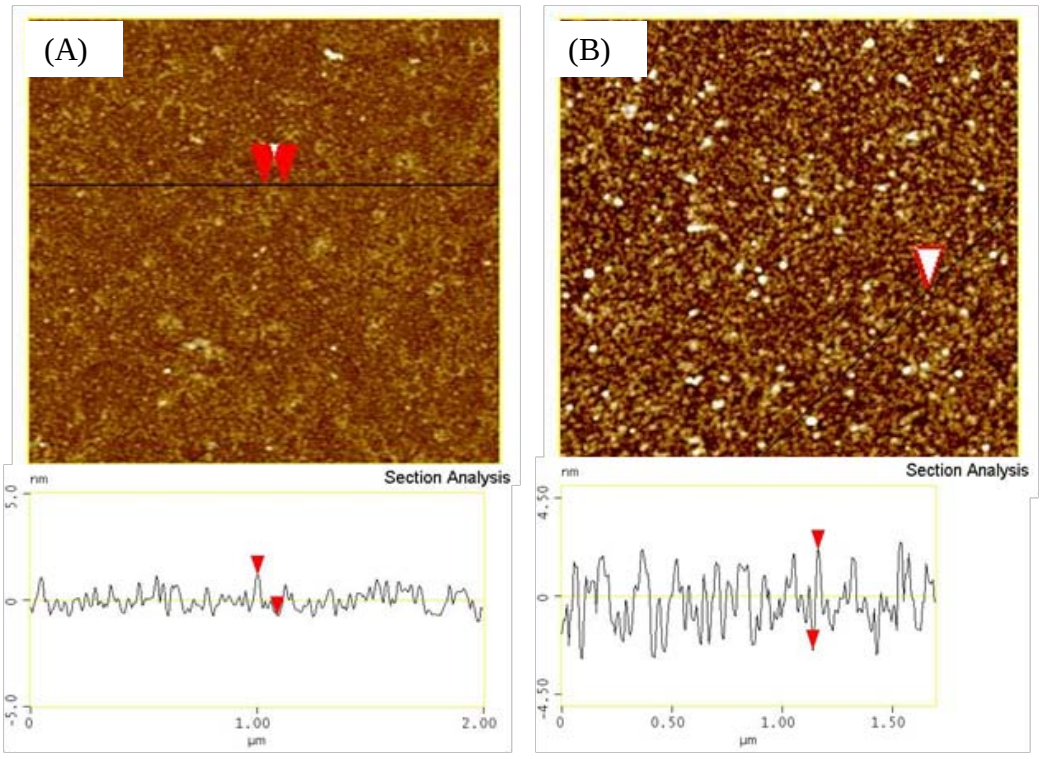

Figure 5.3.5. Tapping mode AFM images (2×2 µm^2) and z profiles of a gantrez deposited Si surface (A) and similar surface after immobilization of MUD capped gold nanoparticles (B).

Figure 5.3.5 shows AFM images of a gantrez deposited Si substrate and immobilized AuNPs on Si substrate. The root-mean-square (RMS) roughness for the gantrez deposited image is 0.4 nm, confirming smooth surface after deposition of gantrez film; whereas that in the immobilized nanoparticle image is 1.4 nm. The image shows a single layer of nanoparticles, with some height fluctuations. The nanoparticle layer average height, measured at voids in the layer, is 4.5-5 nm, in agreement with the nanoparticle size distribution (Figure 5.3.2). This indicates that the film was composed of one layer of MUD capped AuNPs. The nanoparticle distribution obtained from AFM was homogeneous in different areas of the sample, confirming uniform deposition of nanoparticles over the substrate.

FESEM Analysis

The FESEM image [Figure 5.3.6a] shows the presence of AuNPs as highly dispersed and well separated, showing no evidence of aggregation during the immobilization step. The films were imaged as is and not sputtered-coated with a conductive layer of platinum, because they contain sufficient gold present to avoid charging the samples by the electron beam. Stability of these anchored AuNPs was checked by performing sonication of the substrate-bound nanoparticle systems in DMF for 5 min. Figure 5.3.6b shows FESEM image after the sonication step. There is no loss of particles because of sonication, thereby ensuring that the particles were indeed firmly attached to the substrates. The nanoparticle density, after the sonication step is calculated to be $5*10^{11}$ cm^{-2}. To further explore the need of anchoring for the nanoparticles, same nanoparticle solution was spin

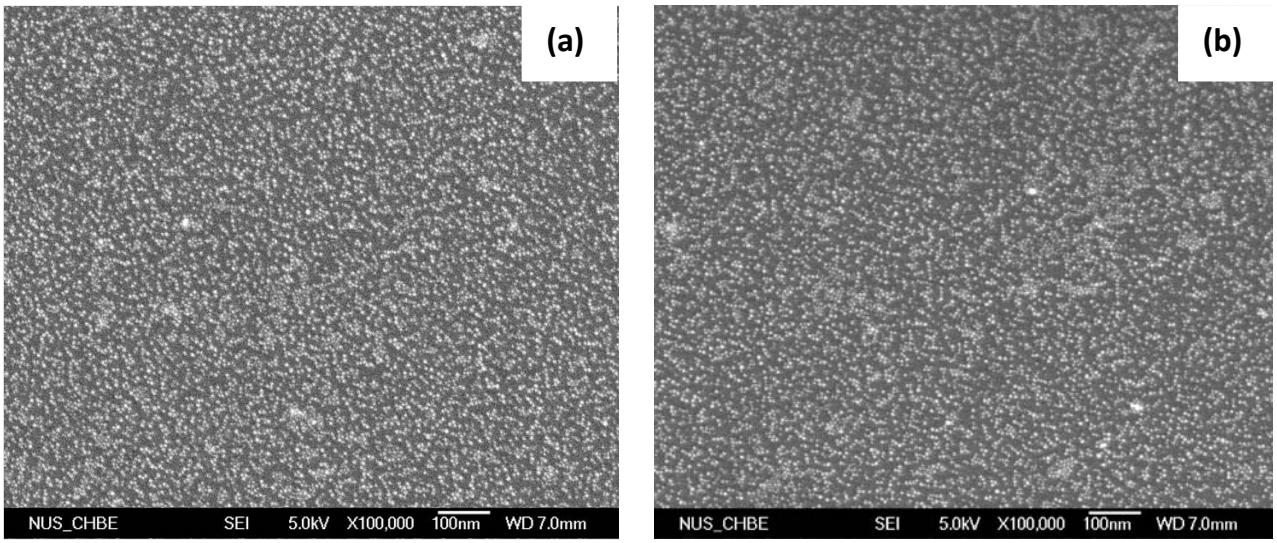

Figure 5.3.6. FESEM images for MUD capped AuNPs immobilized on Si surface: after rinsing (a), after 5 min sonication (b).

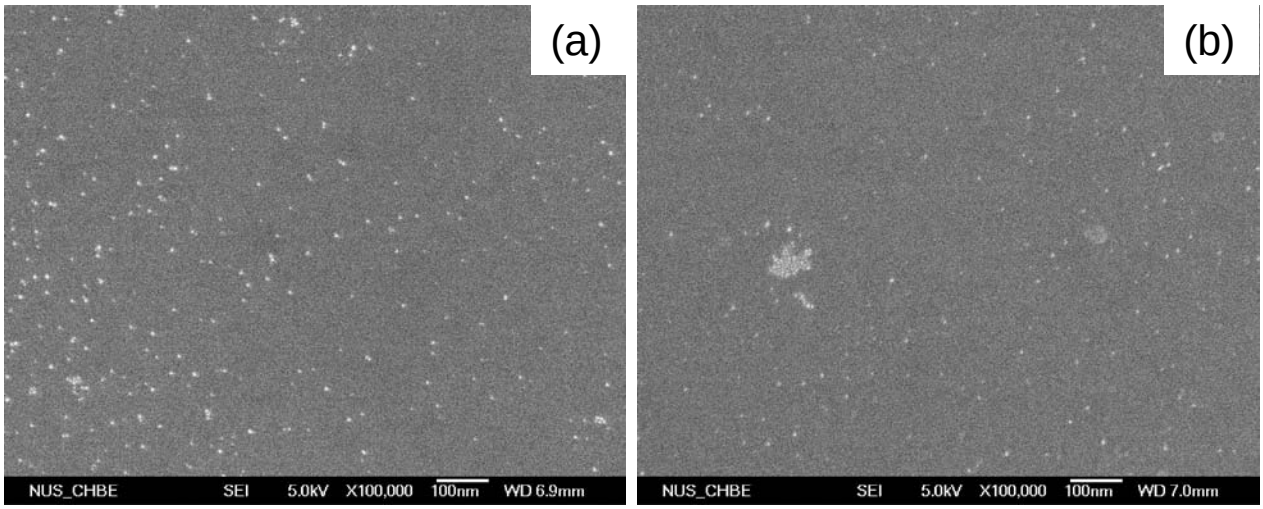

Figure 5.3.7. FESEM images for MUD capped AuNPs solution spin coated Si surface: before sonication (a), after 5 min sonication (b).

coated on a gantrez-modified surface and carried out the sonication step. Figure 5.3.7a shows FESEM image after spin coating the nanoparticle solution. Density of nanoparticles is less as compared to that obtained from the immobilization step. Also, distribution of nanoparticles is not uniform over the surface. After the sonication step, there is loss as well as aggregation of nanoparticles at the surface as shown in Figure 5.3.7b. This further enforces the need of binding of nanoparticles to get stable device structures for nanoparticle-based electronic devices.

5.3.3.3 C-V and C-t Analysis

Normalized C-V hysteresis curves of the MIS memory device containing covalently bound AuNPs are shown in Figure 5.3.8. Counterclockwise C-V hysteresis curves with large width were obtained. The observed counter-clockwise hysteresis for the MIS device with nanoparticles is generally attributed to charging and discharging of electrons from the substrate (Leong et al., 2007). The device without AuNPs shows a negligible memory window at 6/-6 V for its program/erase voltage. However, clear hysteresis window of 1.1 V was observed from the sample with AuNPs. Both MIS devices are fabricated using the same procedure, except for the addition of the AuNPs. The observed hysteresis effect, therefore, could be related to the charging of the nanoparticles and nanoparticle-related traps. As shown in Figure 5.3.9, the hysteresis window of the C-V curve increases from 0.49 to 1.64 V with increasing maximum operating bias from 5 to 7 V, indicating that more electrons are being trapped in the nanoparticles as the sweeping bias is increased (Nicolean and Brews, 1992). The value of observed memory window is similar to the

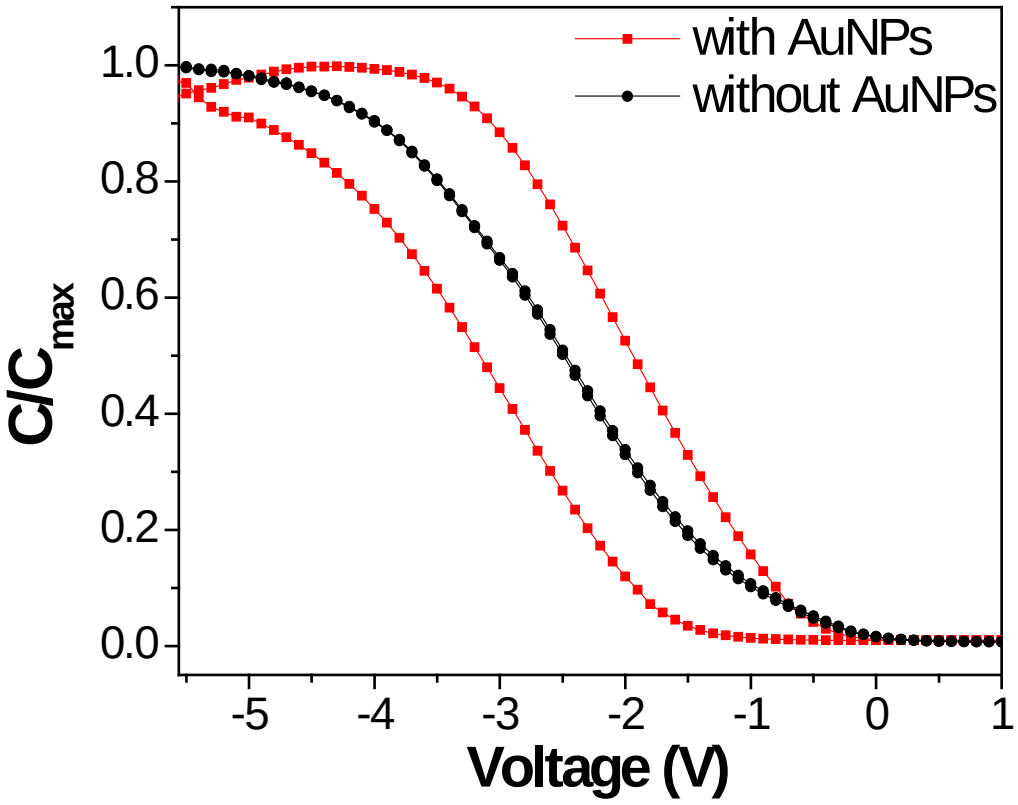

Figure 5.3.8. Normalized C-V characteristics at 100 kHz obtained by biasing the top electrodes at ±6 V for control sample (without gold nanoparticles) and with gold nanoparticles.

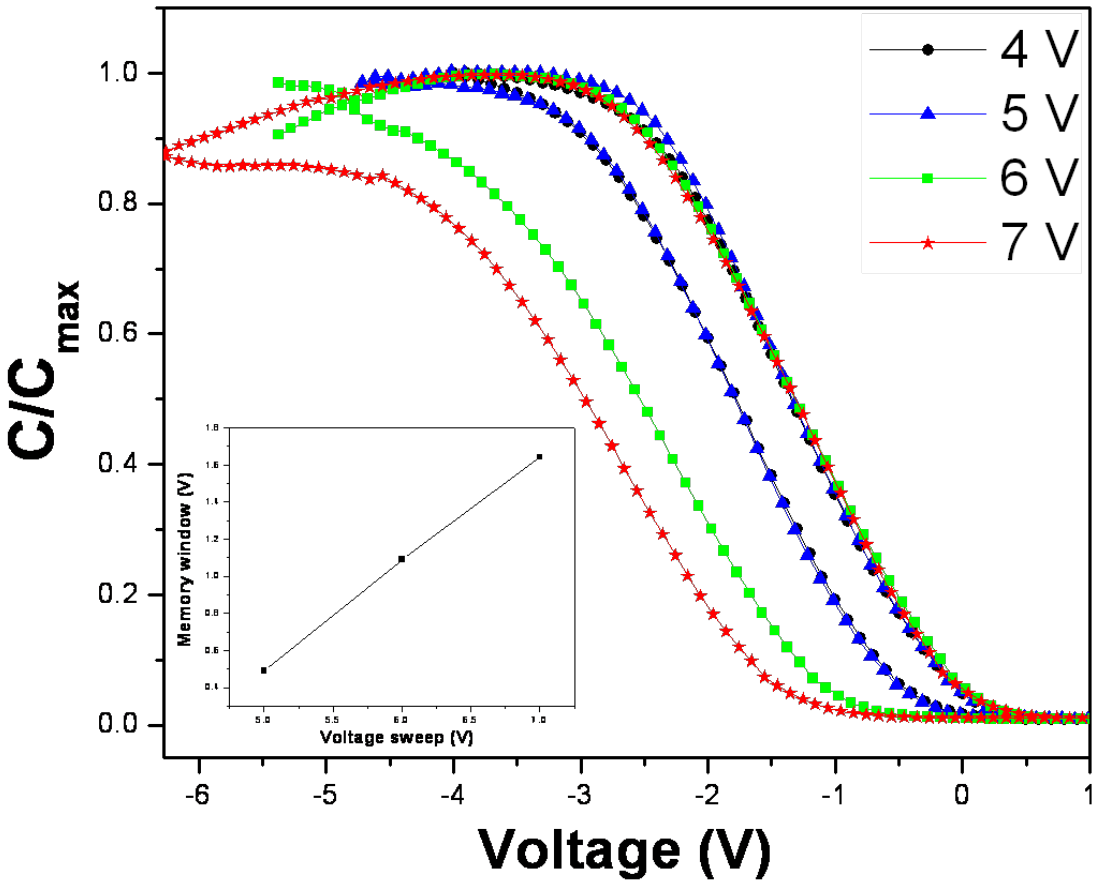

Figure 5.3.9. Normalized C–V characteristics at 100 kHz under different scan voltage ranges for an MIS capacitor incorporating gold nanoparticles.

previously reported value (1.5 V at ± 7 V) for electron-beam evaporated AuNPs (Sargentis et al., 2008). Thus, memory devices fabricated from solution processable covalently assembled nanoparticles will be an alternative to expensive electron-beam evaporation technique due to their low cost and ease of fabrication.

Capacitance decay (C-t) measurement was conducted to evaluate the charge retention properties of the device. A charging bias of +5 V was applied to the device for 1 min to facilitate electron injection into the nanoparticles. Subsequently, the capacitance was monitored as a function of time under the flat-band condition of the device at -3 V. The C-t measurement result is shown in Figure 5.3.10. The immobilized AuNPs device shows good retention characteristics up to 20,000 s. The observed behavior indicates good suppression of charge losses via vertical and lateral charge diffusion (Kim et al., 2003), which could be an early indicator for a good, well dispersed nanoparticle distribution.

5.3.4 Conclusions

The work described in this chapter demonstrates the surface functionalization capability of AuNPs prepared with 11-mercapto-1-undecanol, a bifunctional ligand acting as a surfactant. Detailed structural characterizations have been performed for covalently immobilized AuNPs on silicon surface. Covalent bound AuNPs show charge storage capacity similar to as electron-beam evaporated AuNPs and having advantages of ease of processing and low cost as compared to expensive electron-beam evaporation set up.

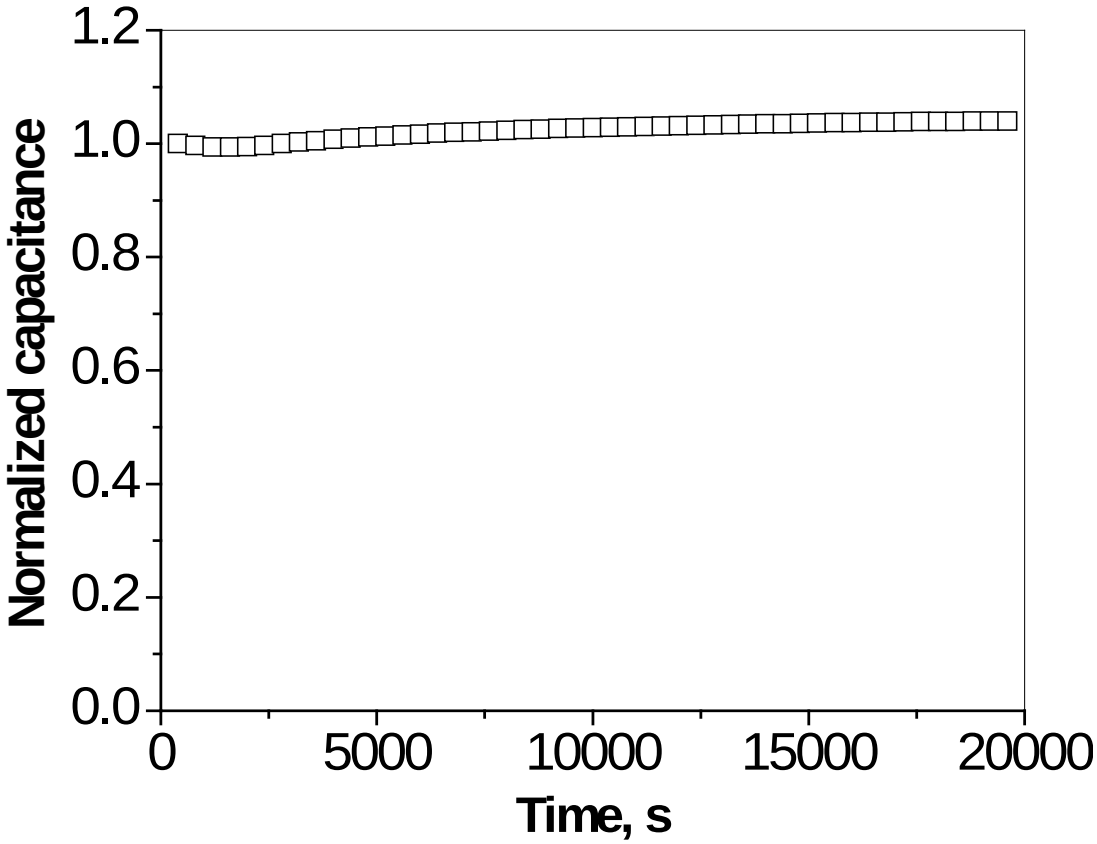

Figure 5.3.10. Charge retention characteristics (normalized capacitance) of the MIS device at 100 kHz after programming at +5 V.

CHAPTER 6

HYBRID MULTILAYER ASSEMBLY OF FUNCTIONALIZED GOLD NANOPARTICLES AND THIN POLYMERIC FILMS

Polymer ultrathin films have received tremendous interest during the past few decades due to their diverse applications in adhesion, corrosion, passivation, sensors, photonics, electronics and membrane technology. Despite the progress in research in recent years, controlled growth of stable polymer multilayer films at the nano-scale level is still a challenge. Layer-by-layer (LbL) growth offers better control over the thickness of ultrathin polymer layers so that the macroscopic defects such as bubbles or pinholes are minimized. Langmuir–Blodgett and electrostatic deposition are well-established techniques to produce such multilayer films. However, the films fabricated thus may not be able to withstand elevated temperatures, polar solvent attack, mechanical wear and abrasion etc. due to the relatively weak interlayer binding forces. Covalent molecular assembly is a promising technique for protecting polymeric films in such harsh environments.

Multilayer films containing inorganic/organic components on substrates of different size, shape and functionality can be prepared by LbL self-assembly technique. Two dimensional assemblies of polymer/gold nanoparticle composites with controlled thickness present considerable interest in various applications involving electrical, optical, catalytic, sensing and magnetic storage devices. While various LbL assembly approaches including hydrogen bonding, gold-thiol bonding and electrostatic interactions have been used to assemble nanoparticles at polymer surfaces, issues about the stability of these systems over a wide range of environmental conditions such as solvent, temperature etc. limits their applicability.

The first section in Chapter 6 shows the optimization of the process conditions to achieve reproducible molecular thicknesses for the polymer film. Subsequently, tribological properties of such ultrathin polymeric films have been demonstrated. Section 6.2 illustrates the synthesis of multilayered composite films comprising functionalized polymer and gold nanoparticles, having controlled separation between two nanoparticle layers as well as between substrate and nanoparticle layer. Although electrical characterizations have not been carried out for such polymer/gold nanoparticle composite structures, study of charge storage capability for such immobilized gold nanoparticles and effect of their density as well as separation between nanoparticle layer and substrate on the charge storage capacity can be part of the future work.

CHAPTER 6.1

OPTIMIZATION FOR DEPOSITION OF COVALENTLY BOUND ULTRATHIN POLYMER FILMS: AN EXAMPLE FOR IMPROVEMENT TO WEAR LIFE

6.1.1 Introduction

In this chapter, the application of covalent molecular assembly in fabricating robust thin film structures has been demonstrated. An anhydride functionalized polymer has been deposited over an amine-terminated silicon surface through covalent binding. The process conditions to achieve reproducible molecular thicknesses for the polymer film have been optimized. X-ray photoelectron spectroscopy, atomic force microscopy and ellipsometry were employed to study the interfacial chemistry, morphology and thickness of the assembled film. The films show excellent stability and strength against sonication, which can be attributed to the covalent interlayer linkage. Later, the applicability of such polymeric film as an intermediate layer between Si and PFPE, to improve the tribological properties of PFPE films has been demonstrated. This shows their potential use as lubricants in several technological applications, such as information storage devices and micro-electro-mechanical systems (MEMS). Requirements for the effective lubrication are strong adhesion of the molecules to the substrate, reduced friction, and high resistance to wear.

6.1.2 Experimental Section

6.1.2.1 Materials

p-Aminophenyltrimethoxysilane (APhS) (90 %, Gelest), poly(methyl vinyl ether-*alt*-maleic anhydride (gantrez) (M_n~ 311000, M_w~ 1080000) (Aldrich), pyromellitic dianhydride (PMDA) (Aldrich), toluene (≥ 99 %, Merck), acetone (≥ 99 %, Merck),

tetrahydrofuran (THF) (≥ 99 %, Merck), methanol (≥ 99 %, Merck), N, N-dimethylacetamide (DMAc) (≥ 99 %, Merck), PFPE Zdol 4000 (molecular weight 4,000 g/mol, with OH terminal groups at both ends); chemical formula $OH–CH_2–CF_2–(O–CF_2–CF_2)_p–(O–CF_2)_q–O–CF_2–CH_2–OH$, where the p/q ratio is 2/3 and hydrofluoropolyether solvent (H-Galden ZV) from Ausimont Inc. were all used as received. Silicon wafers <100> (Engage Electronics Pte Ltd., Singapore) were 0.6 mm thick, p-doped, polished on one side and with a natural oxide layer.

6.1.2.2 Immobilization on Silicon Surface

APhS Deposition on Substrate

Deposition of APhS on Si substrates was performed as described in chapter 5, section 5.1.2.4.

Deposition of Gantrez Polymer Film

The above-treated substrates were immersed in a THF solution of gantrez under nitrogen environment. Concentration of gantrez was used 0.2%, 0.5% and 1% (w/v) for deposition and deposition time was used 1 h and 3 h. The substrates were removed from the solution, rinsed vigorously and sonicated for 5 min with THF, rinsed again with THF, finally blown dry with nitrogen. Details of various deposition steps are shown in Scheme 6.1.1.

PMDA deposition

The above APhS treated substrates were immersed in 0.5% (w/v) PMDA solution in DMAc for 45 min and the substrates were subsequently rinsed copiously with DMAc and subsequently, rinsed vigorously with methanol and blown dry with nitrogen. Details of various deposition steps are shown in Scheme 6.1.2.

Preparation of PFPE coated samples

PFPE was coated onto SAM/polymer modified 2 * 2 cm^2 Si substrates using a custom-built dip-coating machine. Prior to dip coating a solution of PFPE in H-Galden solvent was prepared. The concentration of PFPE in the solution was 0.5 wt%. The SAM/polymer modified Si substrates were dipped into the PFPE solution and held for 1 min and then withdrawn at a constant speed of 2.1 mms^{-1}. Similarly, bare Si after piranha treatment was also coated with PFPE. The PFPE coated samples were baked at 100°C for 1 h in vacuum. The heat treatment procedure of the PFPE film on Si surface resulted reduction in the coefficient of friction after baking due to improved density of the polymer film through evaporation of lower molecular weight fractions (Ruhe et al., 1994). All samples were then stored in desiccator until further tribological characterization.

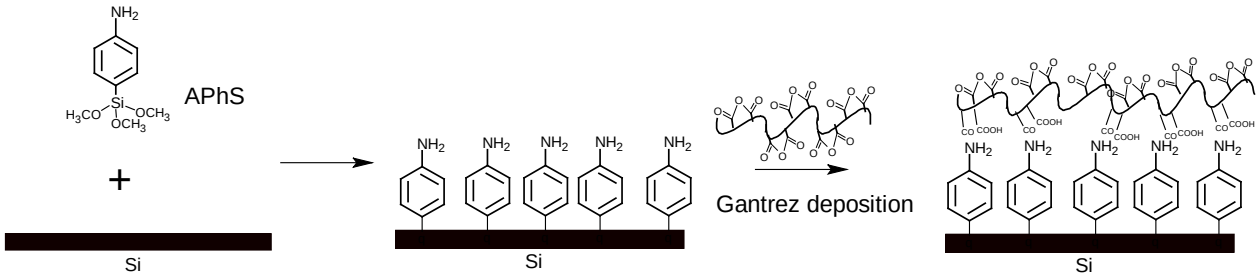

Scheme 6.1.1. Immobilization of gantrez on to a hydroxyl-terminated silicon surface.

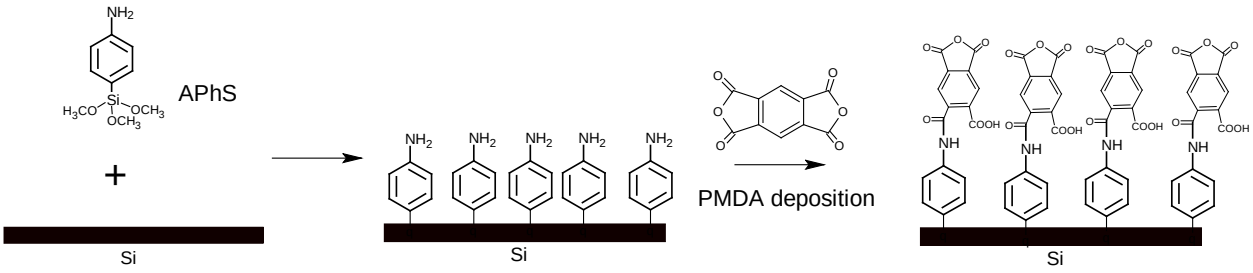

Scheme 6.1.2. Immobilization of PMDA on to a hydroxyl-terminated silicon surface.

6.1.2.3 Characterization

Characterization by AFM was performed as described in chapter 3, section 3.2.9. Characterization by ellipsometry was performed as described in chapter 4, section 4.2.5. Characterization by XPS was performed as described in chapter 5, section 5.1.2.5.

Tribology

Friction and wear tests were carried out on UMT-2 (Universal Micro Tribometer, CETR, USA) using ball-on-disk mode. A Si_3N_4 ball of 4 mm diameter was used as the counterface. The rotating speed of the spindle was 200 rpm giving a sliding speed of 0.067 ms^{-1} at a track radius of 3.2 mm. The roughness of the ball used was 20 nm as provided by the supplier. The ball was cleaned ultrasonically with acetone before the test. Every ball was viewed under the optical microscope to ensure that it was free from contaminants or manufacturing defects. A new ball was employed for each test. The normal load used was 50 g. All experiments were performed in air at room temperature (23°C) and at a relative humidity of approximately 70 %. The tribometer constantly measures normal load and friction force and gives the coefficient of friction as real-time ratio. The wear-life was defined as the number of cycles after which coefficient of friction exceeded a value of 0.3 or a visible wear scar appeared on the substrate, whichever happened earlier. This strategy was adopted to define the wear-life, because of the reason that in some tests, even when a clear visible wear track appeared, the coefficient of friction was less than 0.3. This method of evaluation of wear-life is consistent with the literature for similar kinds of tests (Eapen et al., 2002; Ruhe et al.,

1993). The wear-life data have been obtained on at least five different samples utilizing at least two different tracks on each sample and an average of the three best results is reported.

6.1.3 Results and Discussions

6.1.3.1 Surface Morphology

The changes of topography for gantrez deposited surfaces were studied using tapping mode AFM. The scan size was 2 µm for all the images. As shown in Figure 6.1.1, varying concentration of gantrez as well as deposition time result in different surface features; confirming presence of different species. Figure 6.1.1a shows the flat topography for AFM image of APhS deposited Si substrate. Figure 6.1.1b shows the AFM image for gantrez deposition for concentration of 0.2% (w/v) and 1 h deposition time. Similarly, Figure 6.1.1(c-f) shows the AFM image for gantrez deposition for concentration of [0.2%, 3 h], [0.5%, 1 h], [0.5%, 3 h] and [1%, 1 h] respectively. [0.2%, 1 h] gives non-uniform surface coverage with root-mean-square (RMS) roughness of 0.29 nm as compared to 0.25 nm for APhS surface. However, surface coverage improves for 0.2% concentration with increased deposition time of 3 h. Also, roughness decreases to 0.24 nm giving smoother surface. Gantrez deposition for 1 h with 0.5% concentration gives very smooth surface having roughness of 0.18 nm and roughness increases to 0.26 nm for 3 h deposition time. Non-uniform and aggregated surface with much higher

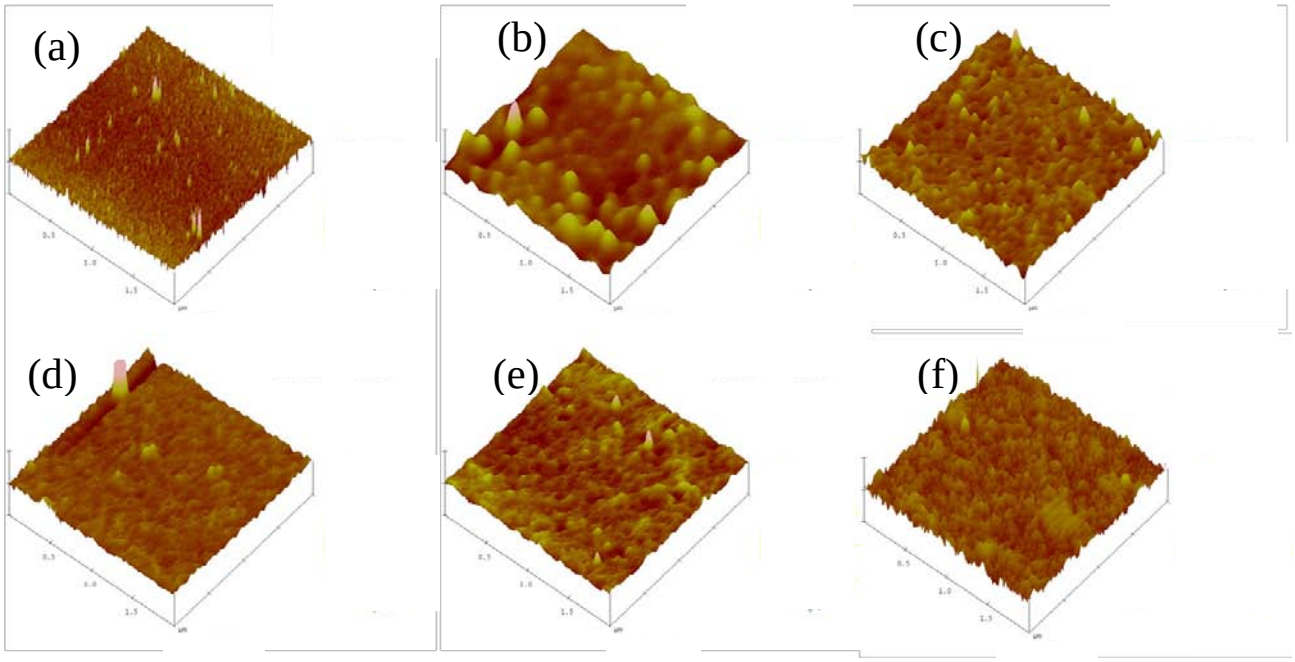

Figure 6.1.1. Surface topographies (2 × 2 μm^2) for different deposition steps: (a) APhS; Gantrez deposition for (b) 0.2% and 1 h deposition time; (c) 0.2% and 3 h deposition time; (d) 0.5% and 1 h deposition time; (e) 0.5% and 3 h deposition time; (f) 1% and 1 h deposition time.

roughness value of 0.68 nm is obtained for 1% gantrez concentration and 1 h deposition time. This may be due to coiling of polymer at such higher concentration.

6.1.3.2 Ellipsometric Characterization

The thickness of the individual film at various deposition steps is shown in Figure 6.1.2. [0.2%, 3 h] and [0.5%, 1 h] gave thickness of 15 ± 0.3 A for gantrez film deposited on APhS surface having 9.7 ± 0.5 A thickness. The observed thickness value is similar to molecular thickness of gantrez polymer film, thus indicating deposition of gantrez without aggregation under above conditions. However, the thickness results were not consistent for gantrez deposition conditions [0.5%, 3 h] and [1%, 1 h]; this may be due to coiling of polymer for higher deposition time or higher concentration. Stability of the deposited gantrez layer was checked by sonicating the polymer deposited substrate for 15 min in THF solvent. No change in the film thickness was observed after sonication, thus, confirming strong binding of the polymer to the APhS surface.

6.1.3.3 X-ray Photoelectron Spectroscopy (XPS)

Successful reaction between amine moieties of APhS and anhydrides of gantrez is confirmed by presence of the C1s peak components for amide formation at 287.5 eV (-CO-NH-) and presence of anhydrides at 288.9 eV (-CO-O-CO-) as shown in Figure 6.1.3. C1s core-level XPS spectra for gantrez films deposited at conditions of [0.2%, 3 h] and [0.5%, 1 h] have been compared since these conditions yield films of molecular thicknesses. Figure 6.1.3A is the C1s core-level XPS spectra for [0.2%, 3 h] gantrez deposition giving $\frac{C_{anhydride}}{C_{amide}}$ of 2.05 as compared to 5.88 for [0.5%, 1 h] gantrez

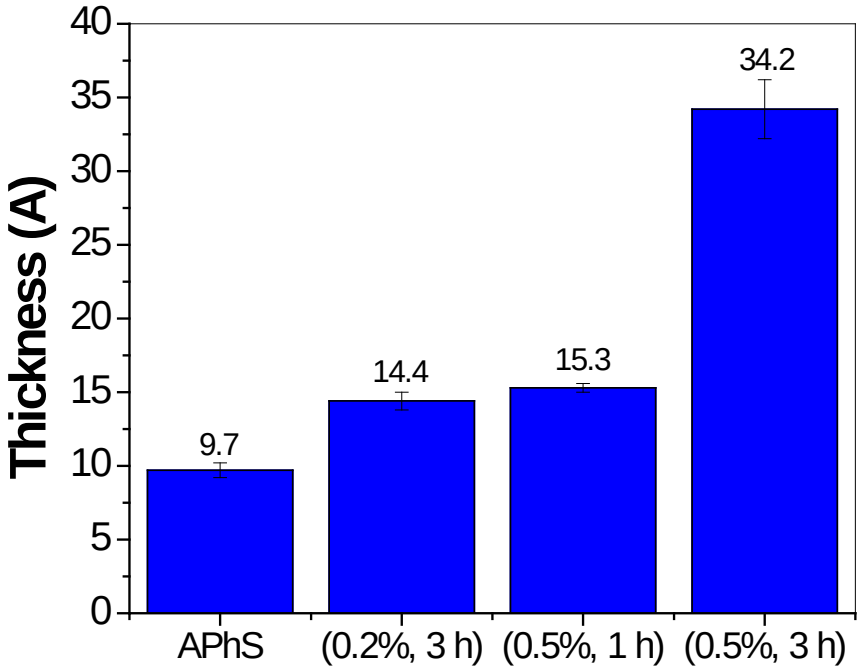

Figure 6.1.2. Comparison of average thickness for gantrez deposition at different processing steps.

deposition condition (Figure 6.1.3B). Amount of anhydrides available is reduced for gantrez deposition for longer duration. Thus, we can tune the available anhydride amount through varying the deposition time.

Figure 6.1.4A is the C1s core-level XPS spectra for [0.5%, 1 h] gantrez deposited surface and Figure 6.1.4B is the C1s core-level XPS spectra for PFPE deposited on above gantrez surface. PFPE is expected to be anchored to the substrate with one of its terminal alcohol groups reacted with the anhydride on the gantrez, forming esters. C1s spectrum [Figure 6.1.4(B)] contains peak components at 288.6 eV for acid (-COOH) and ester (-COOR), thus confirming binding of PFPE to gantrez surface. Also, presence of peak at 293 eV for C-F component confirms presence of PFPE molecules over gantrez surface.

6.1.3.4 Tribology

Si is the primary material in many micro-components, such as MEMS. Si is generally not considered a good tribological material because it experiences high friction, adhesion and wear during sliding (Tsurkuk, 2001a). Hence, there is a great search for organic or inorganic coatings and lubricants for the improvement of tribological properties of Si surface (Ruhe et al., 1993; Bhushan et al., 1995). Several types of ultra-thin films have been proposed, which have considerably enhanced the tribological properties of Si in terms of reduction in coefficient of friction and wear (Zhang and Lan, 2002; Ren et al., 2004; Nakano et al., 2008). However, despite low coefficient of friction, the wear resistance achieved by these monomolecular layers is not sufficient to provide long life to the high velocity moving MEMS components (De Boer and Mayer, 2001).

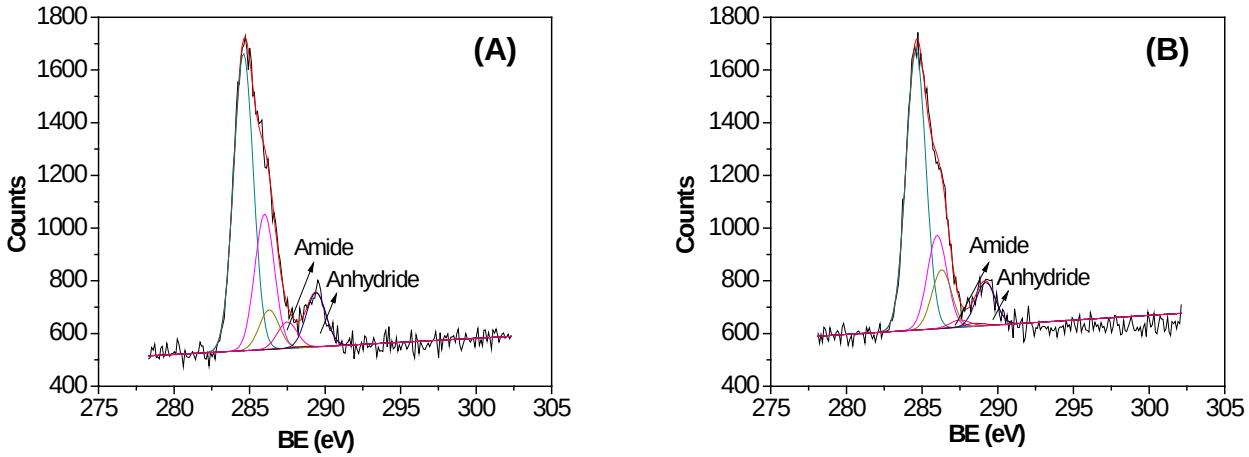

Figure 6.1.3. C1s core-level XPS spectra for different deposition steps: (A) gantrez deposition for 0.2% and 3 h deposition time; (B) gantrez deposition for 0.5% and 1 h deposition time.

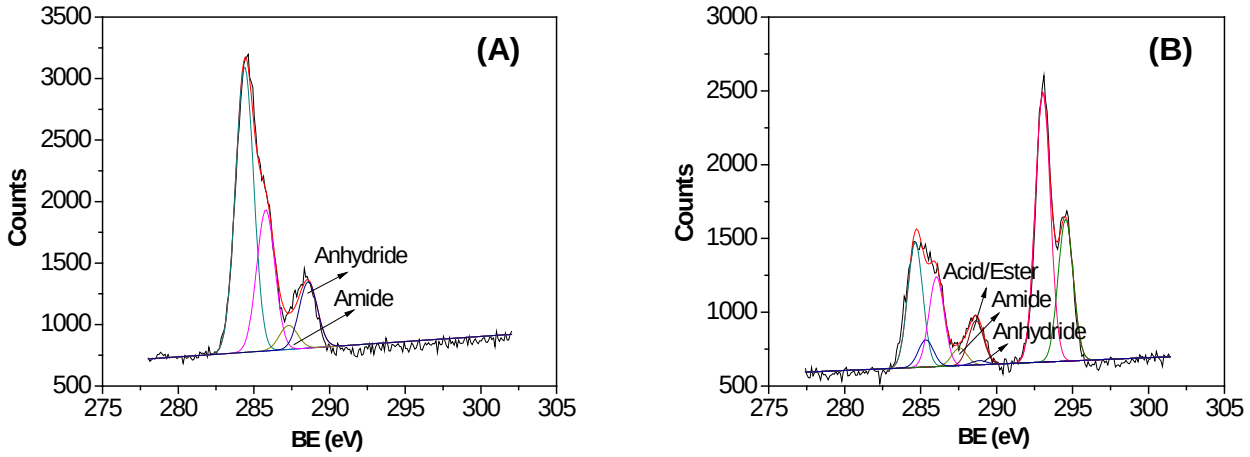

Figure 6.1.4. C1s core-level XPS spectra for different deposition steps: (A) gantrez deposited surface; (B) PFPE deposited surface.

The polymer coatings onto the Si surface can provide good wear durability because of their inherent properties such as low surface energy, molecular flexibility, high toughness coupled with good strength and damping characteristics and their lower shear strength (Tsurkuk, 2001b). PFPE is selected as the top layer because of its properties such as low surface tension, chemical and thermal stability, low vapor pressure, high adhesion to the substrate and good lubricity (Liu and Bhushan, 2003). PFPE coating onto silane based self-assembled monolayer (SAM) surfaces resulted in increased wear resistance and low coefficient of friction (Satyanarayana and Sinha, 2005). The tribological properties of a Si/epoxy SAM/PFPE dual-layer film were investigated to ascertain the chemical and physical interactions between PFPE and SAM molecules and their influence on the tribological properties (Satyanarayana et al., 2007). Polymer composite films, consisting of ultra-high molecular weight polyethylene (UHMWPE) as the first layer and PFPE as the second top layer on Si showed better tribological properties compared to PFPE coating on SAM deposited Si surface. The chemical bonding between the UHMWPE and PFPE molecules can be ruled out due to unavailability of any reactive chemical groups at the UHMWPE polymer surface. Also, UHMWPE film thickness was high enough to restrict its tribological application for micro-components made out of Si (Satyanarayana et al., 2006).

The idea of using molecular thick gantrez film as an intermediate layer is similar to the use of SAMs as intermediate layers between Si and PFPE molecules as studied earlier (Satyanarayana and Sinha, 2005; Satyanarayana et al., 2007), except that in the present

study, a polymer film having reactive chemical groups is used as an intermediate layer. This will be a tri layer (SAM/polymer/PFPE) system to study compared to previously studied dual layer (SAM/PFPE or polymer/PFPE) system. Also, tribological studies have been performed at much higher load of 50 g compared to previously used 5 g load.

Table 6.1.1 shows that Si/APhS/gantrez/PFPE illustrates very low coefficient of friction (0.18) and high wear life (>100,000 cycles) when tested against 4 mm diameter Si_3N_4 ball at a normal load of 50 g (0.5 N) and a sliding speed of 0.042 m/sec (200 rpm). Without any modification, bare Si has shown a coefficient of friction of 0.7 and failed within 100 cycles under same conditions of sliding test, which is in agreement with the literature data (Satyanarayana and Sinha, 2005; Ren et al., 2004). Therefore, the Si/APhS/gantrez/PFPE film has reduced the coefficient of friction by ~3.5 times and improved the wear durability by more than 1000 times, when compared with bare Si. This is a remarkable improvement in terms of tribological properties when compared with those of PFPE coated SAMs as studied earlier (Satyanarayana and Sinha, 2005; Satyanarayana et al., 2007). The better tribological properties of Si/APhS/gantrez/PFPE should have originated from several factors such as self-lubrication properties of PFPE molecules, good anchoring between PFPE and gantrez molecules, the damping and the toughness provided by gantrez molecules.

Further, Si/APhS/PFPE has shown similar wear behavior as Si/APhS/gantrez/PFPE with a slightly higher coefficient of friction (0.23) than that observed for Si/APhS/gantrez/PFPE (0.18). The improved tribological properties as observed in the

Table 6.1.1. Coefficient of friction and wear life values for PFPE deposited various surfaces

Serial No.	Sample Description	Repetitions	Coefficient of Friction	Wear Life (cycles)
1	Bare Silicon	3	0.7	<100
2	Gantrez	3	0.18	100000
3	APhS	3	0.23	100000
4	PMDA	2	0.70	<100

case of Si/APhS/PFPE must have been resulted from hydrogen bonding between APhS and PFPE molecules providing good anchoring between them and also good rigidity from the benzene rings of APhS molecules compared to earlier used APTMS (3-aminopropyltrimethoxysilane) molecules. It has to be noted that the data reported in Table 6.1.1 was obtained from sliding tests at a normal load of 50 g (0.5 N). But when the sliding tests were carried out at a normal load of 60 g (0.6 N) both Si/APhS/PFPE and Si/APhS/gantrez/PFPE films have failed within short duration after the start of the test. Further tests need to be done at normal loads between 50 g to 60 g to compare the performance of Si/APhS/PFPE and Si/APhS/gantrez/PFPE.

To further understand the explicit role of gantrez molecules (as an intermediate layer between Si and PFPE) on the tribology of Si/APhS/gantrez/PFPE, a monolayer of PMDA has been used as an intermediate layer between Si and PFPE and the tribological properties were investigated. PMDA also contain anhydride chemical groups similar to gantrez but the difference being PMDA is a monomer whereas gantrez is a polymer. Therefore, through this study we can elucidate the effect of monomer or polymer molecules used as an intermediate layer between Si and PFPE on the tribological properties. PMDA was chemisorbed onto Si using APhS SAM layer as the reactive surface to form amide bonds between APhS and PMDA.

Si/APhS/PMDA/PFPE has shown a coefficient of friction of 0.70 and a wear life of <100 cycles (Table 6.1.1) at a normal load of 50 g (0.5 N) and a sliding speed of 0.042

m/sec (200 rpm). These tribological properties are very inferior when compared to those of Si/APhS/gantrez/PFPE. Therefore, these results suggest that a polymer layer when used as an intermediate layer between Si and PFPE leads to better tribological performance as previously shown (Satyanarayana et al., 2006).

6.1.4 Conclusions

This chapter demonstrates the fabrication of gantrez polymer films of molecular thicknesses. AFM, ellipsometry and XPS characterization have been carried out to optimize process conditions for gantrez deposition on APhS surface. Tribological properties of PFPE films having gantrez film as an intermediate layer between Si and PFPE have been demonstrated. Gantrez molecules being polymer in nature provides sufficient damping, toughness and load-bearing capacity to external loads after PFPE coating. Anhydride groups available at gantrez film anchor to PFPE molecules (which have –OH terminal groups) as confirmed by XPS. The bonding of PFPE molecules to gantrez layer eventually lead to improved tribological properties due to the difficulty of the removal of such chemisorbed molecules.

CHAPTER 6.2

MULTILAYER ASSEMBLY OF GOLD NANOPARTICLES AND THEIR CONTROLLED SEPARATION ON SILICON SUBSTRATE THROUGH COVALENTLY BOUND MULTILAYER OF ULTRATHIN POLYMER FILMS

6.2.1 Introduction

In this chapter, we present a new synthetic strategy to build multilayered composite films comprising functionalized polymer and gold nanoparticles (AuNPs). AuNPs are stabilized and immobilized through electrostatic binding between a functionalized polymer and gold nanoparticle. The assembly process allows placement of gold nanoparticle layers with controlled inter-layer separation by use of covalently bound spacers. Multilayers of polymers were obtained by using a diamine molecule as a spacer that is covalently bound to adjacent polymer layers. The thickness of the covalently bound polymer layers were characterized with ellipsometry. Characterizations performed by spectroscopic (X-ray photoelectron spectroscopy - XPS) and microscopic techniques [Field emission scanning electron microscopy (FESEM) and cross-sectional high resolution transmission electron microscopy (HR-TEM)] show the positioning of the gold nanoparticle layers and uniform distribution of the nanoparticles over the surface. Such gold nanoparticle-polymer composite films can find diverse applications varying from sensors to memory devices.

6.2.2 Experimental Section

6.2.2.1 Materials

p-Aminophenyltrimethoxysilane (APhS) (90 %, Gelest), poly(methyl vinyl ether-*alt*-maleic anhydride) (Gantrez) (M_n~ 311000, M_w~ 1080000) (Aldrich), 1, 4-phenylene diamine (PDA) (97 %, Sigma-Aldrich), 1, 12-diaminododecane (DADA) (98 %,

Aldrich), toluene (≥ 99 %, Merck), acetone (≥ 99 %, Merck), tetrahydrofuran (THF) (≥ 99 %, Merck), methanol (≥ 99 %, Merck), N, N'-dimethylacetamide (DMAc) (≥ 99 %, Merck), were all used as received. Silicon wafers <100> (Engage Electronics Pte Ltd., Singapore) were 0.6 mm thick, p-doped, polished on one side and with a natural oxide layer.

6.2.2.2 Multilayer of Gantrez Film Deposition

APhS Deposition on Substrate

Deposition of APhS on Si substrates was performed as described in chapter 5, section 5.1.2.4.1 and 5.1.2.4.2.

Deposition of Gantrez Polymer Film

The above-treated substrates were immersed in a 0.5% (w/v) gantrez in THF solution under nitrogen environment for 1 h while solution being stirred. The substrates were removed from the solution, rinsed vigorously and sonicated for 5 min with THF, rinsed again with THF, finally blown dry with nitrogen. The as-prepared gantrez deposited substrates were immersed sequentially in 10 mM DADA in DMAc solution for 1.5 h and 0.5% (w/v) gantrez in THF solution for 1 h. After each deposition substrates were rinsed copiously, sonicated for 5 min, rinsed again with respective solvents, finally blown dry with nitrogen. Details of various deposition steps are shown in Scheme 6.2.1.

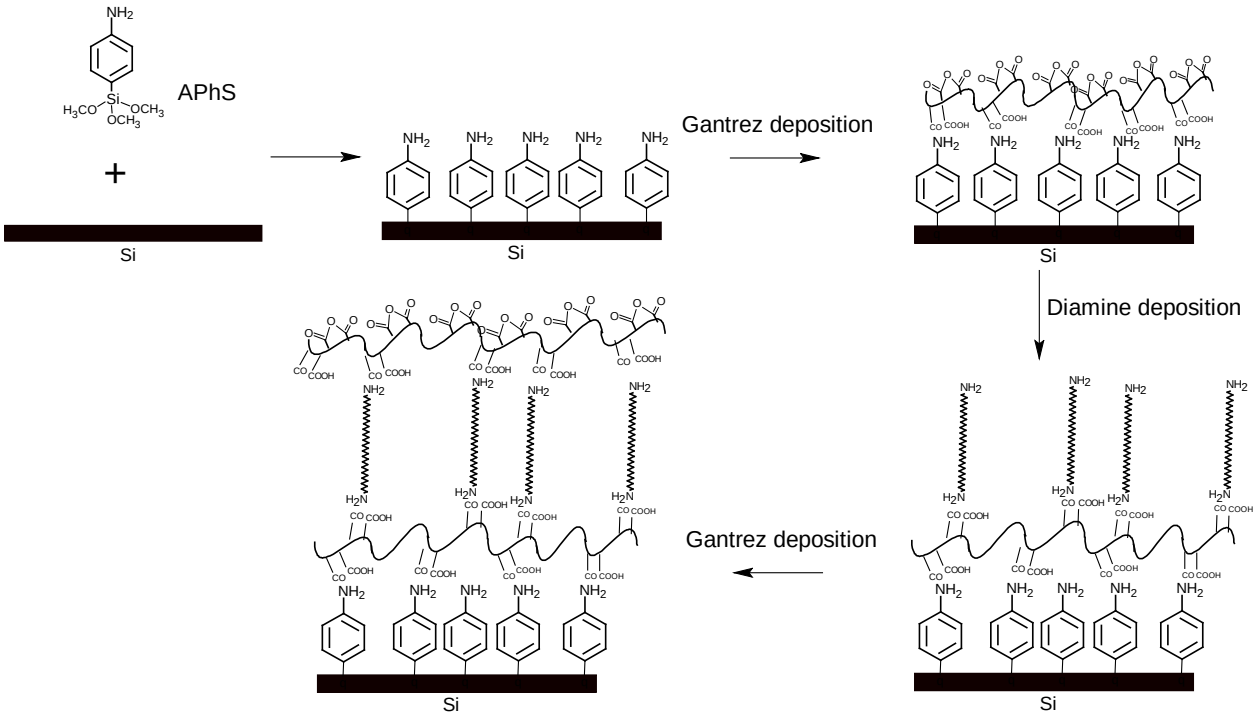

Scheme 6.2.1. Multilayer of gantrez polymer film deposition.

6.2.2.3 Synthesis of Citrate Stabilized Gold Nanoparticles

Gold nanoparticles were prepared according to the method reported by Grabar et al. (1995). Specifically, 0.012g of $HAuCl_4.3H_2O$ was dissolved in 30 mL of deionized (DI) water giving a 1 mM solution, which was then refluxed at ca. 115 ˚C for 10 min. 6 mL of 38.8 mM sodium citrate also dissolved in DI water was added to the refluxing solution. The color of the mixture evolved gradually from grey to purple and finally to wine red. Refluxing was continued for another 10 min and then was stopped to let the resulting solution cool to room temperature.

6.2.2.4 Immobilization of Citrate Gold Nanoparticles

The above amino-functionalized silicon substrates obtained from APhS or DADA deposition, were immersed in the freshly prepared AuNPs solution for 1 h; rinsed thoroughly with DI water and then baked at 110 ˚C for 5 min to remove residual moisture.

6.2.2.5 Immobilization of Multilayer of Citrate Gold Nanoparticles

Stabilization of 1st Layer of Citrate Gold Nanoparticles

The above 1st layer citrate AuNPs immobilized on APhS substrates were immersed in 50 mM PDA in DMAc solution for 1 h. Subsequently, substrates were rinsed copiously in DMAc, rinsed again with acetone and finally blown dry with nitrogen. The above-treated substrates were immersed in a 0.5% (w/v) gantrez in THF solution under nitrogen

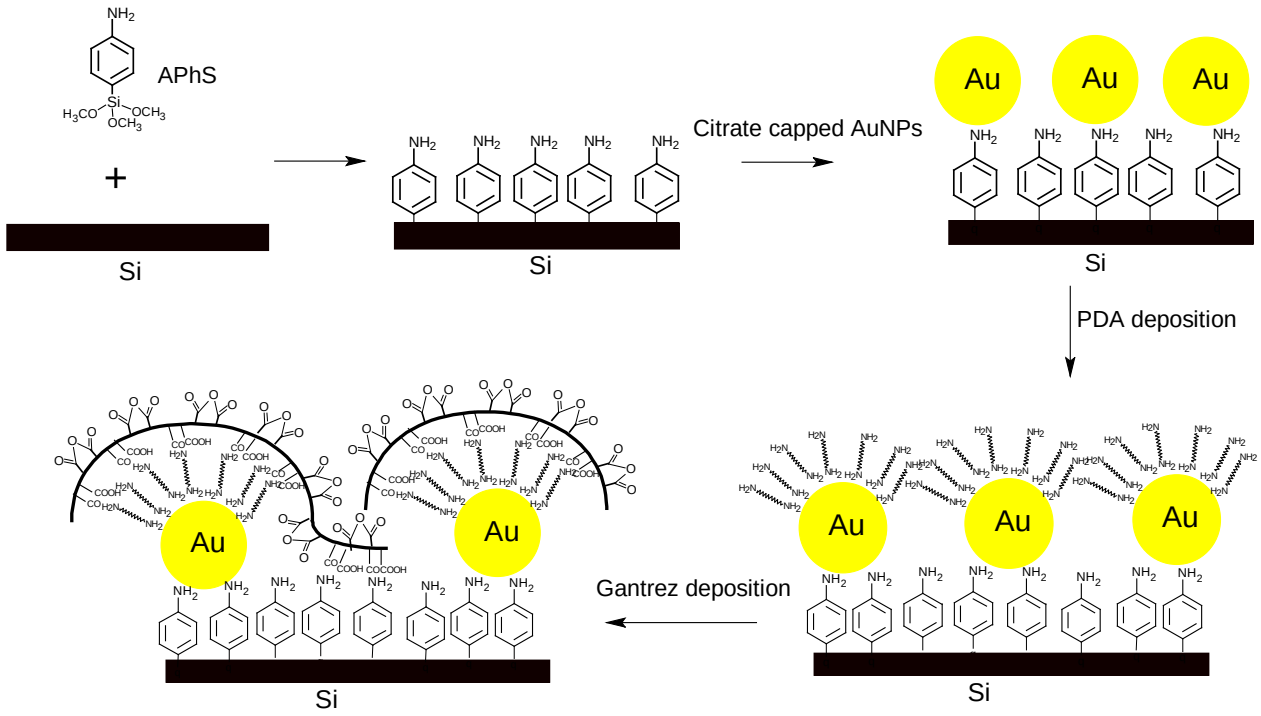

Scheme 6.2.2. 1st layer of citrate AuNPs stabilized by gantrez polymer film.

environment for 1 h. The substrates were removed from the solution, rinsed rigorously and sonicated for 5 min with THF, rinsed again with THF, finally blown dry with nitrogen. Details of various deposition steps are shown in Scheme 6.2.2.

Immobilization of 2nd Layer of Citrate Gold Nanoparticles

The above-gantrez deposited substrates were immersed in 10 mM DADA in DMAc solution for 1 h. Subsequently, the substrates were rinsed copiously, sonicated for 5 min, rinsed again with DMAc, finally rinsed with acetone and blown dry with nitrogen. DADA deposited silicon substrates were immersed in the freshly prepared AuNPs solution for 1 h; rinsed thoroughly with DI water and then baked at 110 ˚C for 5 min to remove residual moisture. Details of various deposition steps are shown in Scheme 6.2.3.

6.2.2.6 Characterization

Characterization by ellipsometry was performed as described in chapter 4, section 4.2.5. Characterization by XPS, TEM and HR-TEM were performed as described in chapter 5, section 5.1.2.5. Characterization by FESEM was performed as described in chapter 3, section 3.2.9.

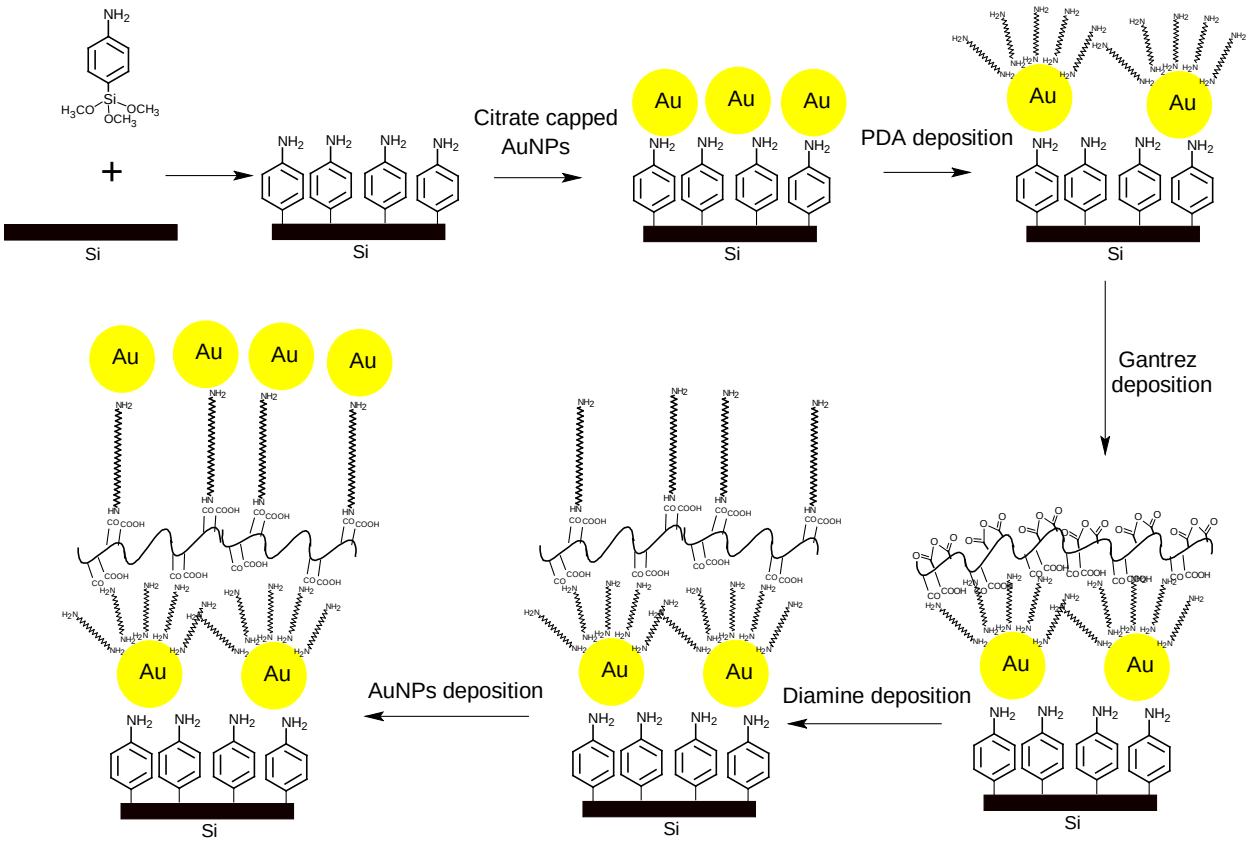

Scheme 6.2.3. 2nd layer of citrate AuNPs deposition on DADA deposited gantrez polymer film.

6.2.3 Results and Discussions

6.2.3.1 Multilayer of Gantrez film

Ellipsometric Characterization

Spectroscopic ellipsometry showed steady increase in the film average thickness after deposition of each gantrez layer. The thickness of the gantrez films versus the number of layers is shown in Figure 6.2.1. The films formed from alternate deposition of gantrez and DADA exhibit linear increase in thickness with number of layers. Average total thickness of about 25 A, 47 A, 71 A and 93 A were obtained for 1, 2, 3 and 4 layer of gantrez film deposition, respectively with APhS monolayer having thickness of about 9 A.

X-ray Photoelectron Spectroscopy (XPS)

Successful covalent binding between amino moieties of APhS and anhydrides of gantrez is demonstrated as described in chapter 6.1, section 6.1.3.3 through presence of the C1s peak components for amide formation at 287.5 eV (-CO-NH-) and anhydrides at 288.9 eV (-CO-O-CO-). Multilayer of gantrez deposition is demonstrated through calculating C/Si and N/Si ratios at various deposition steps as shown in Table 6.2.1. C/Si ratio increases with each gantrez deposition and N/Si ratio increases with each DADA deposition. Thus, confirming successful deposition of multilayer of gantrez films.

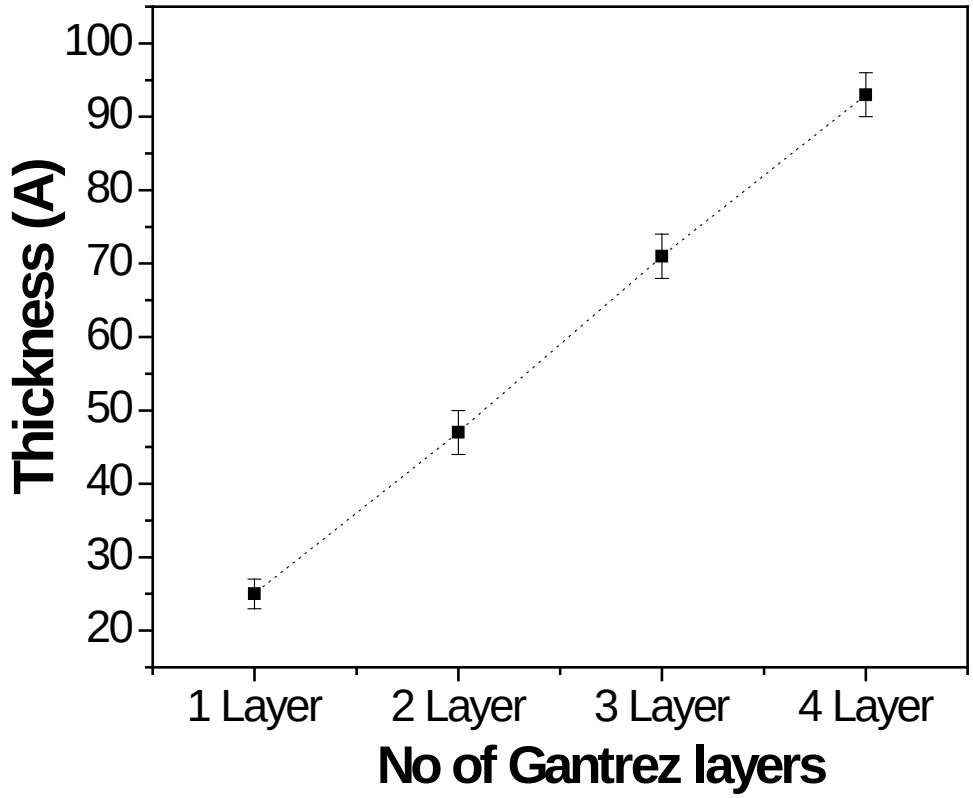

Figure 6.2.1. Ellipsometric thickness of gantrez film versus number of layers.

Table 6.2.1. C/Si and N/Si ratios at various deposition steps.

Serial No.	Deposition steps	C/Si ratio	N/Si ratio
1	1st layer of gantrez deposition	1.93	0.08
2	DADA deposition on 1st layer of gantrez deposited surface	1.62	0.16
3	2nd layer of gantrez deposition	3.69	0.14
4	DADA deposition on 2nd layer of gantrez deposited surface	3.68	0.32

6.2.3.2 Immobilization of Citrate Stabilized Gold Nanoparticles

(A) Synthesis of Citrate Stabilized AuNPs

Transmission Electron Microscopy (TEM)

An aqueous solution of AuNPs was prepared by reducing $HAuCl_4.3H_2O$, a precursor for AuNPs, with sodium citrate; after reduction, the citrate ions in the solution may help to prevent particle aggregation. A few drops of the solution containing nanoparticles were placed on carbon coated TEM grids and grids were imaged after solvent evaporation. The AuNPs obtained had an average diameter of 10 ± 1 nm based on the particle size shown in the TEM picture (Figure 6.2.2).

(B) Controlled Separation of Citrate Stabilized AuNPs from Si Substrate

FESEM Analysis

The FESEM images for immobilized citrate stabilized AuNPs on various DADA terminated surfaces are shown in Figure 6.2.3. The highest density of nanoparticles was achieved for APhS surface. Later, nanoparticle density decreased with DADA layers. This might be due to reduction in amine moieties available for AuNPs binding due to coiling of gantrez polymeric film compared to uncoiled gantrez polymer. However, this could be a way to control the density of AuNPs over a substrate.

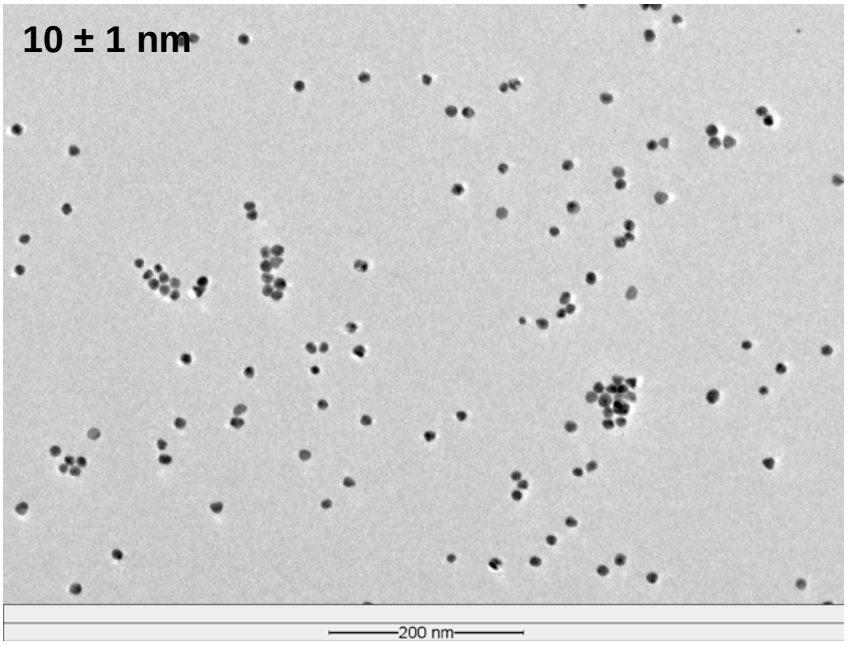

Figure 6.2.2. TEM image of gold nanoparticles.

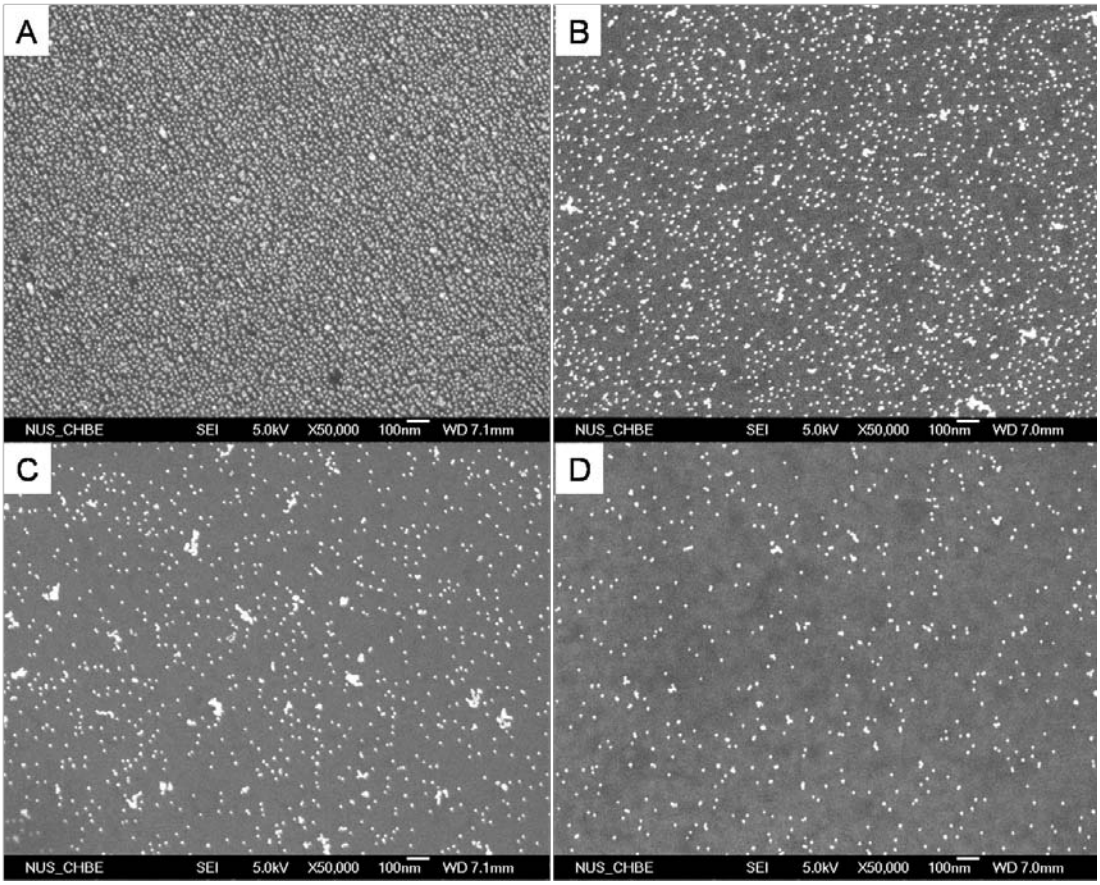

Figure 6.2.3. FESEM images for citrate AuNPs immobilized on amine terminated Si surface. (A) APhS; (B) 1st layer of DADA; (C) 2nd layer of DADA; (D) 3rd layer of DADA.

HR-TEM Analysis

Immobilized AuNPs on to silicon surfaces were directly observed with cross - sectional HR-TEM. Figures 6.2.4A and 6.2.4B show cross-sectional images for the AuNPs on APhS surface and AuNPs on 2^{nd} layer of DADA deposited Si surface, respectively. AuNPs are separated from Si substrate by 1 nm for APhS surface which is similar to APhS layer thickness. Also, AuNPs are separated from Si substrate for DADA layer deposited on 2^{nd} layer of gantrez surface by 5 nm which is similar to the thickness as observed in ellipsometric data. Thus, we can control the separation between immobilized AuNPs and Si substrate surface through multilayer deposition of gantrez and DADA films.

(C) Stabilization of Immobilized Citrate Stabilized AuNPs Layer

FESEM Analysis

Stability of immobilized AuNPs was examined by immersing immobilized AuNPs substrates in a pH 10-buffered solution (0.025 M Na_2CO_3/0.025 M $NaHCO_3$ in 1 M Na_2SO_4) for 30 min followed by a DI water rinse. FESEM images for the immobilized AuNPs after immersing in pH 10-buffered solution are shown in Figure 6.2.5. The number density of AuNPs immobilized on APhS surface (Figure 6.2.5A) decreased after immersion in buffered solution (Figure 6.2.5B). This loss of nanoparticles might be due to deprotonation of amines on APhS at pH 10, and electrostatic bonds linking the AuNPs

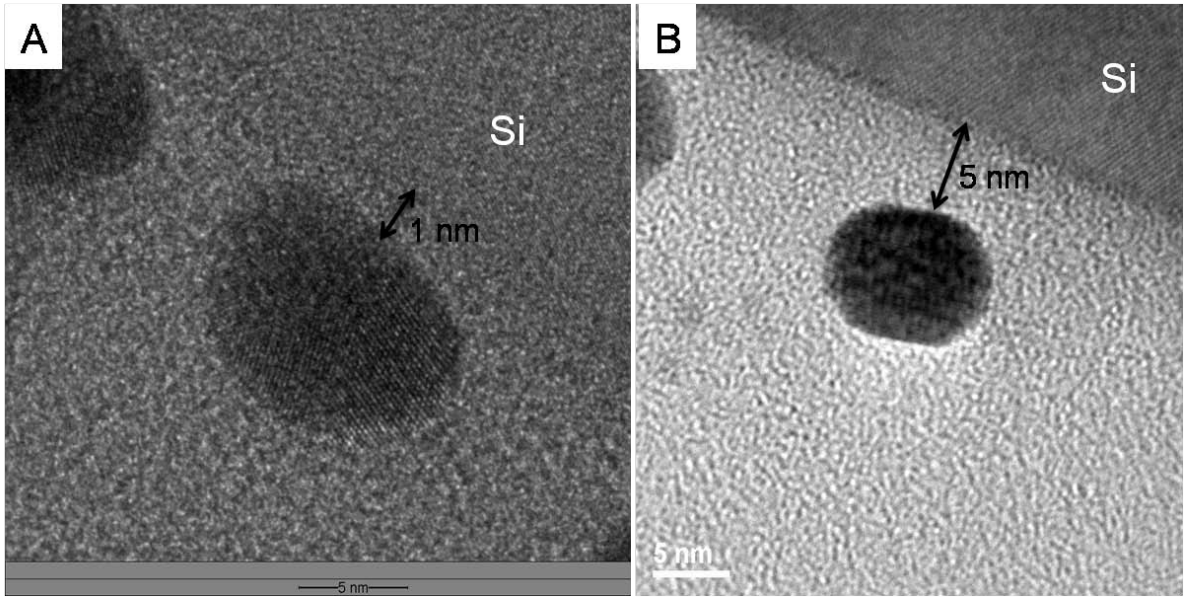

Figure 6.2.4. Cross-sectional HR-TEM images for (A) citrate stabilized AuNPs on APhS deposited Si surface; (B) citrate stabilized AuNPs on 2nd layer of DADA deposited Si surface.

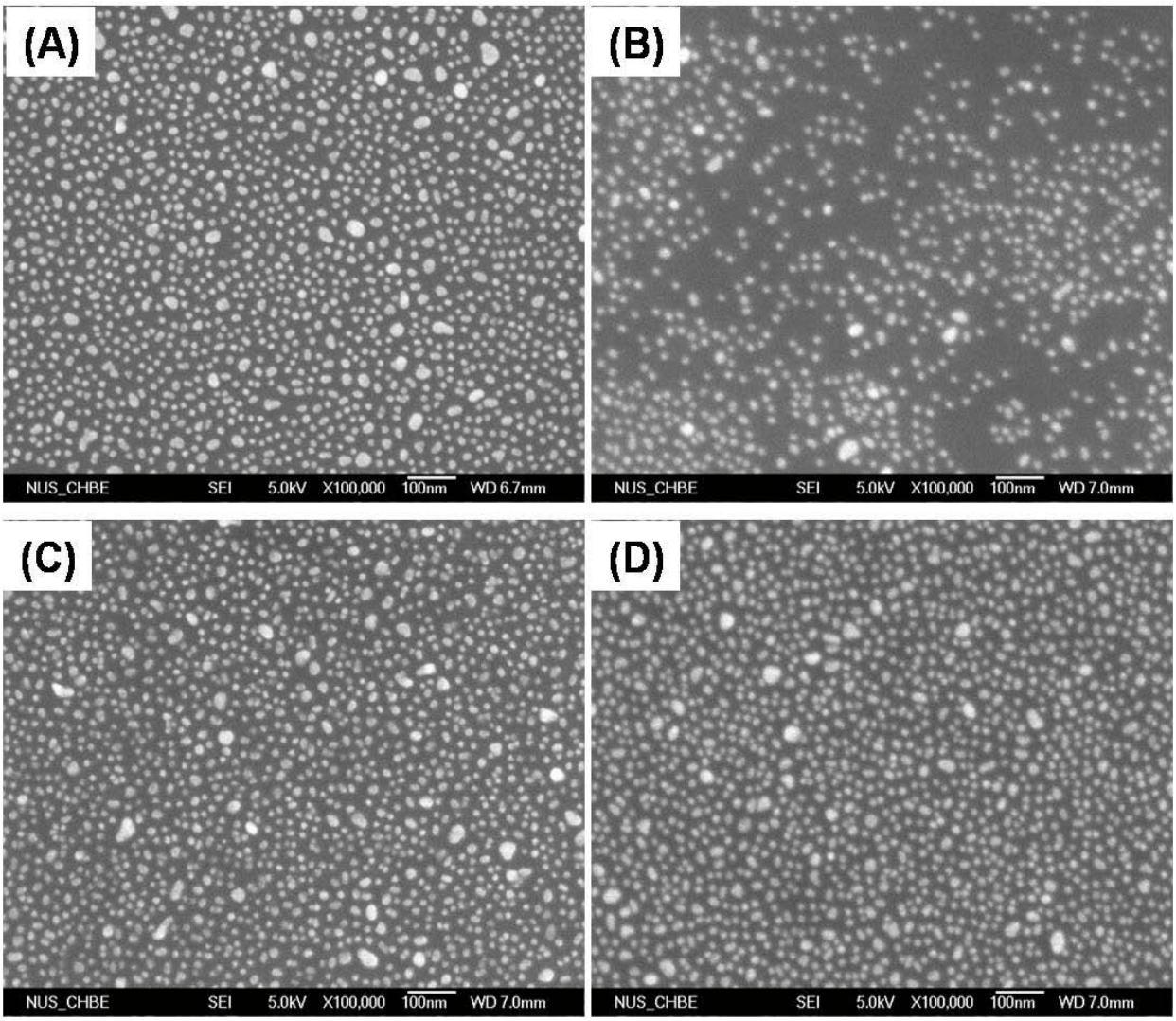

Figure 6.2.5. FESEM images for (A) citrate stabilized AuNPs on APhS; (B) citrate stabilized AuNPs on APhS after immersion in pH 10 buffer solution; (C) citrate stabilized AuNPs on APhS stabilized by gantrez film; (D) citrate stabilized AuNPs on APhS stabilized by gantrez film after immersion in pH 10 buffer solution.

and amines are no longer present after immersion in the buffered solution. However, there was no change in the nanoparticle density after immersion in pH 10-buffered solution for the nanoparticles capping with gantrez layer (Figure 6.2.5C and Figure 6.2.5D). Thus, the layer of immobilized AuNPs was stabilized against immersion in polar media through capping nanoparticles with gantrez polymeric films. This also opens up a possibility for immobilization of another layer of AuNPs through functionalization of gantrez film.

(D) Immobilization of 2nd Layer of Citrate Gold Nanoparticles

HR-TEM Analysis

After stabilizing 1st layer of AuNPs; 2nd layer of AuNPs was deposited on to DADA functionalized gantrez film. 1st and 2nd layers of immobilized AuNPs on to silicon surfaces were directly observed with cross - sectional HR-TEM. Figures 6.2.6A and 6.2.6B show cross-sectional images for the 1st layer of immobilized AuNPs on APhS surface. Figures 6.2.6C and 6.2.6D show cross-sectional images for the 2nd layer of AuNPs immobilized on DADA deposited gantrez surface. Cross-sectional images show that there is increase in the density of AuNPs after immobilization of another layer of AuNPs. Also, there is no aggregation observed for the 2nd layer of nanoparticles during the immobilization process. We can also control separation between two nanoparticle layers, as described earlier through multilayer of gantrez polymeric films.

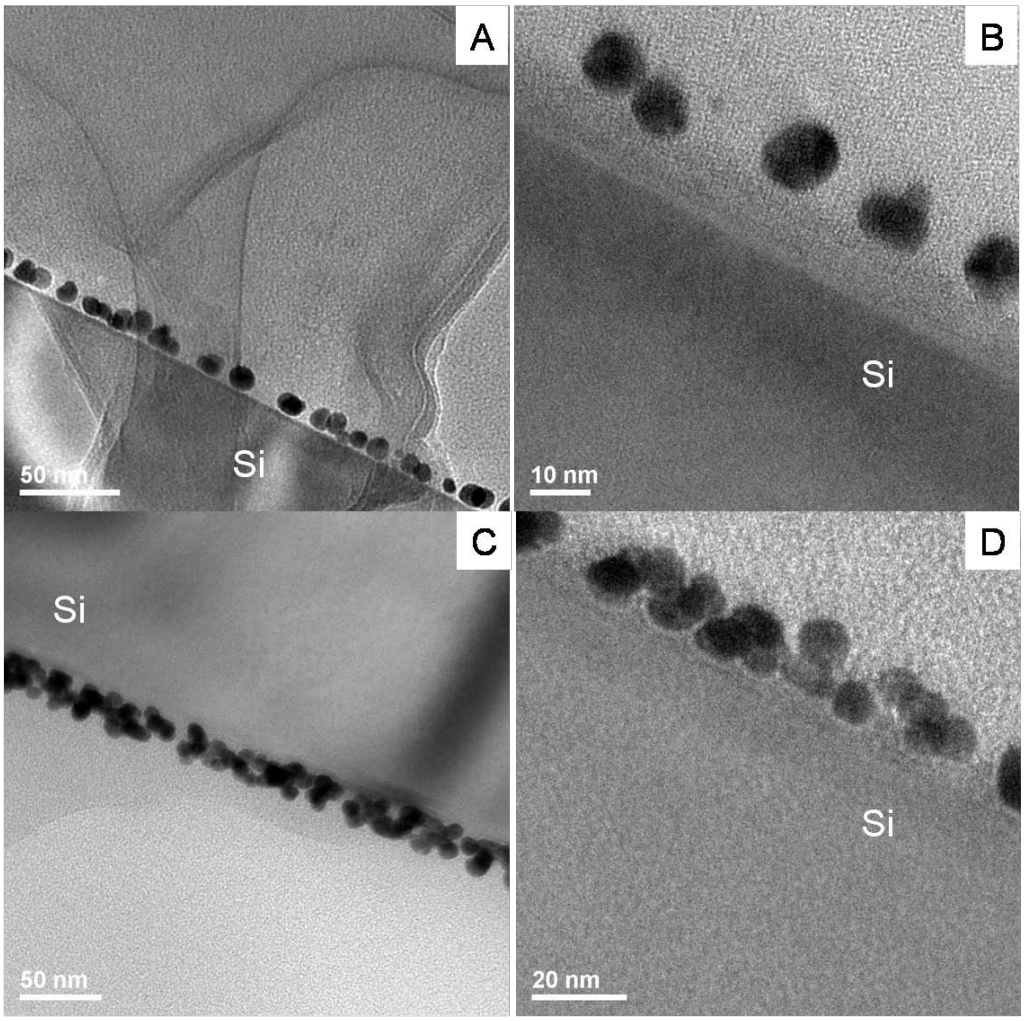

Figure 6.2.6. Cross-sectional HR-TEM images for: 1st layer of citrate stabilized AuNPs on APhS deposited Si surface (A), (B); 2nd layer of citrate stabilized AuNPs on DADA deposited gantrez polymer film on Si surface (C), (D).

6.2.4 Conclusions

This chapter demonstrates the feasibility of fabricating multilayered stack of gantrez polymer film from molecular layers. Ellipsometry and XPS characterization have been carried out to show multilayer deposition of gantrez films. Separation between immobilized AuNPs and Si substrate has been controlled through these multilayered-gantrez films as confirmed by cross – sectional HR-TEM analysis. Subsequently, the first layer of immobilized AuNPs was stabilized against attack of polar media through gantrez film capping as shown by FESEM images. Also, AuNPs density was increased through immobilization of 2^{nd} layer of AuNPs as confirmed by cross – sectional HR-TEM analysis. The importance of this work resides in the fact that we can tune the distance between AuNPs layer and the substrate as well as increase the density of AuNPs per unit area by increasing the number of nanoparticle layers.

CHAPTER 7

Tailored Assembly of Gold Nanoparticles over Patterned Surface for Nonvolatile Memory Applications

7.1 Introduction

The performance of nanoparticle memory devices critically depends on nanoparticle size, density, and their size/spatial distribution (Tsoukalas et al., 2005; Jang et al., 2009; Lombardo et al., 2004). A high nanoparticle density on surface translates into high charge storage capacity of the floating layer. However, the uniformity in the particle density across the device area is critical in ensuring reliability and reproducibility in charge storage characteristics. Hence, there is currently a need for well-controlled and scalable means of preparing high-density nanoparticle assemblies over large areas suitable for high-performance memory devices. This chapter describes a novel route towards fabricating high-density assemblies of gold nanoparticles (AuNPs) employing combination of block copolymers template directed in-situ synthesis as well as directed self-assembly of citrate stabilized AuNPs on surface. Gold nanoparticle arrays were modified using 4-aminothiophenol as surface modifier. Subsequently, citrate stabilized AuNPs were immobilized over these modified surfaces. The resulting structures were characterized by atomic force and scanning electron microscopies. In addition, the electrical characterization of AuNPs as a charge trapping layer in nonvolatile memory was also investigated by means of a metal-insulator-semiconductor (MIS) device.

7.2 Experimental Section

7.2.1 Materials

p-aminophenyltrimethoxysilane (APhS) and 4-aminothiophenol (4-ATP) (97 %) were purchased from Gelest and Aldrich, respectively, and used as received. Hydrogen tetrachloroaurate (III) trihydrate ($HAuCl_4.3H_2O$) (≥ 99.9 %, Aldrich; *corrosive, handle with care*), sodium citrate (meeting USP testing specifications, Sigma), ethanol (≥ 99.5 %, Merck), toluene (≥ 99 %, Merck) and methanol (≥ 99.5 %, Merck) were used as received. Silicon wafers <100> (Chartered Semiconductor, Singapore) were 0.6 mm thick, p-doped, polished on both side and having 4 nm thermally grown oxide layer.

7.2.2 Synthesis of Citrate Stabilized Gold Nanoparticles

Gold nanoparticles were prepared according to the method reported by Grabar et al. (1995). Specifically, 0.012g of $HAuCl_4.3H_2O$ was dissolved in 30 mL of deionized (DI) water giving a 1 mM solution, which was then refluxed at ca. 115 ˚C for 10 min. 6 mL of 38.8 mM sodium citrate also dissolved in DI water was added to the refluxing solution. The color of the mixture evolved gradually from grey to purple and finally to wine red. Refluxing was continued for another 10 min and then was stopped to let the resulting solution cool to room temperature.

7.2.3 Immobilization on Silicon Surface

7.2.3.1 APhS Deposition on Substrate

Deposition of APhS on Si substrates was performed as described in chapter 5, section 5.1.2.4.1 and 5.1.2.4.2.

7.2.3.2 ATP Deposition on Patterned Substrate

Si substrates having gold nanoparticle arrays (27 nm diameter and 60 nm center-to-center spacing; obtained in collaboration) were rinsed with ethanol and then immersed in a 1 mM 4-ATP solution in ethanol for 3 h. Subsequently, the samples were removed from the solution, rinsed and soaked for 5 min with ethanol to remove unbound 4-ATP molecules, rinsed again with ethanol, finally blown dry with nitrogen. The samples were stored in a desiccator under vacuum.

7.2.3.3 Immobilization of Gold Nanoparticles

The treated silicon substrates were immersed in the freshly prepared AuNPs solution for 1 h and 6 h deposition time; rinsed thoroughly with DI water and then baked at 110 ˚C for 5 min to remove residual moisture.

7.2.4 MIS Capacitor Fabrication

MIS device structures were fabricated after immobilization of citrate capped AuNPs through 10 nm thick Al_2O_3 control oxide deposition by a pulsed laser method and Au top electrodes (0.3 mm diameter size) sputter-deposition using a shadow mask technique. After removal of the native oxide by sand paper rub, a film of Pt was sputter-deposited as the back side contact. The MIS device configuration is shown in Figure 7.1.

7.2.5 Characterization

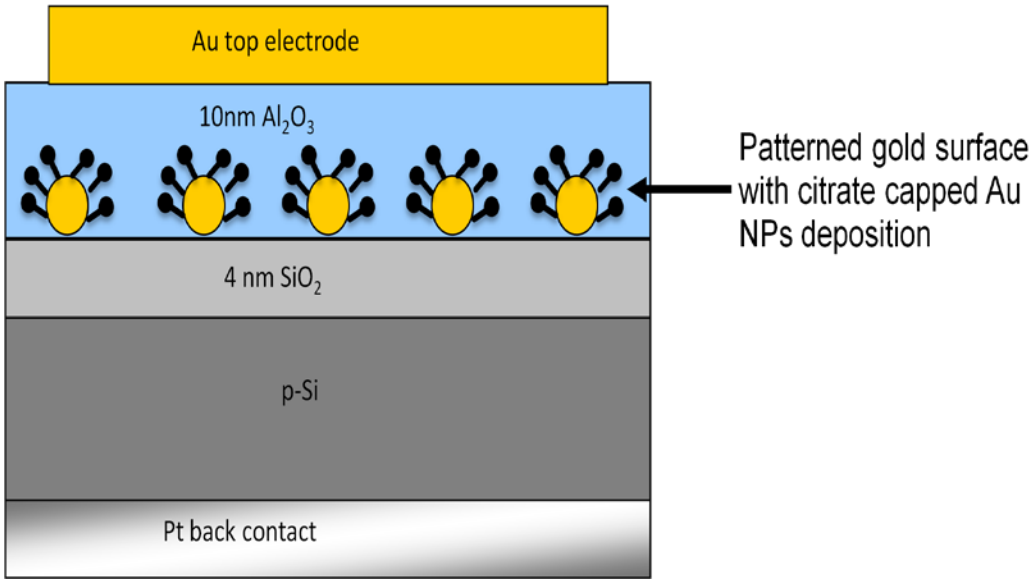

Figure 7.1. The MIS device configuration for the immobilized citrate capped gold nanoparticles.

Characterization by TEM was performed as described in chapter 5, section 5.1.2.5. Characterization by AFM, FESEM and Capacitance–voltage (C–V) measurements were performed as described in chapter 3, section 3.2.9.

7.3 Results and Discussions

7.3.1 Synthesis of Citrate Capped Gold Nanoparticles

7.3.1.1 Transmission Electron Microscopy (TEM)

An aqueous solution of AuNPs was prepared by reducing $HAuCl_4.3H_2O$, a precursor for AuNPs, with sodium citrate; after reduction, the citrate ions in the solution may help to prevent particle aggregation. A few drops of the solution containing nanoparticles were placed on carbon coated TEM grids and grids were imaged after solvent evaporation. The AuNPs obtained had an average diameter of 10 ± 1 nm based on the particle size shown in the TEM picture (Figure 7.2).

7.3.2 Immobilization of Citrate Capped Gold Nanoparticles

7.3.2.1 Surface Morphology

Figure 7.3 shows AFM images of gold arrays on Si substrate. The surface revealed sharper features for patterned gold nanoparticles surface (Figure 7.3A). The patterned surface has long-range uniformity over a wide area over the substrate. Figure 7.3B presents the surface height profiles along the line drawn in the flattened image. The

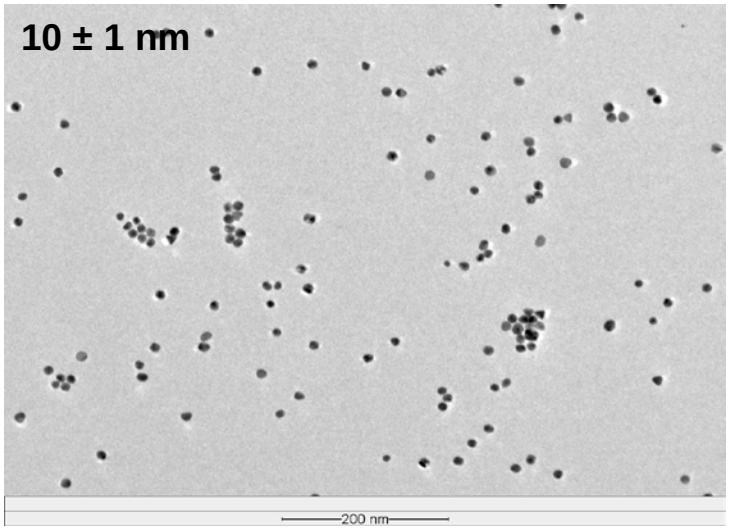

Figure 7.2. TEM image of gold nanoparticles.

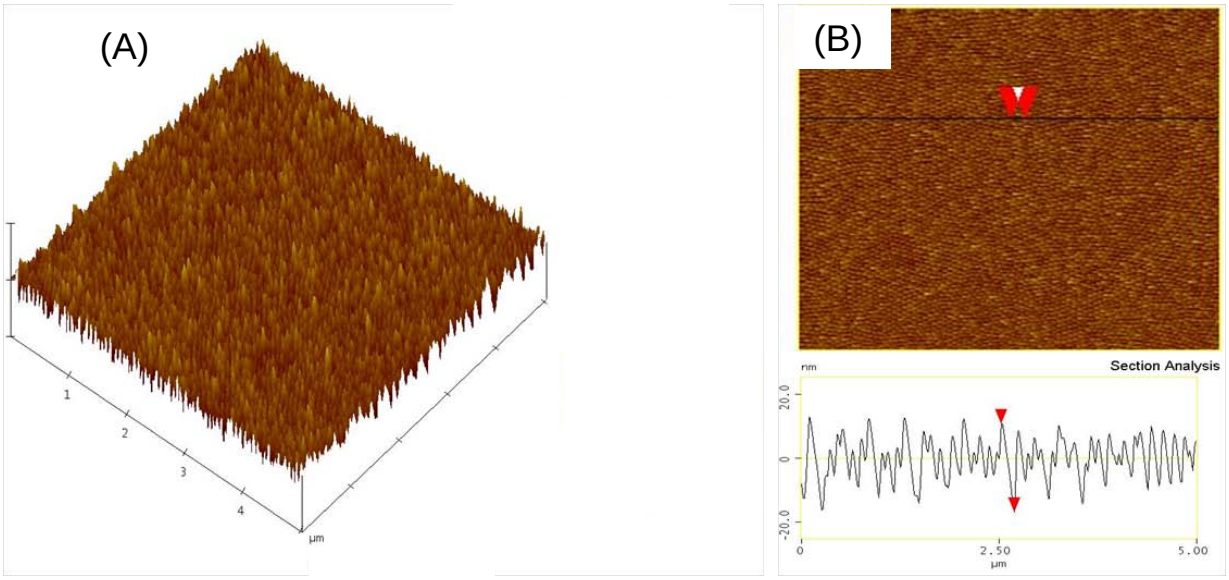

Figure 7.3. Tapping mode AFM images (5 × 5 μm^2) of patterned gold array on Si substrate (A) surface topography (B) section analysis.

vertical distance between highest and lowest positions (on average), as marked by arrows in both the image and the height profiling curve, can be associated with the dimension and shape of the constituent molecules for a particular layer. The section profile shows that the height of the nanoparticle is almost similar to the mean diameter of the nanoparticles (27 nm).

7.3.2.2 FESEM Analysis

The FESEM image for patterned gold array substrate (Figure 7.4A) is almost similar to the AFM image, although there is a difference in the breadth of the nanoparticle which appears much larger in the AFM image than the true values. This discrepancy can be attributed to the AFM tip surface convolution effects (Grabar et al., 1997). Center-to-center spacing between the nanoparticles is ~ 60 nm. The patterned gold arrays have long-range lateral order with a uniform size over a wide area similar to AFM images. FESEM images, after immobilization of citrate stabilized AuNPs, are shown in Figure 7.4C and Figure 7.4D for 1 h and 6 h deposition time, respectively. AuNPs are deposited only over amine terminated patterned nanoparticle surface due to amine-gold electrostatic attraction. The nanoparticle density after 1 h deposition time is calculated to be $1.6*10^{11}$ cm^{-2}. However, density increases to $3.2*10^{11}$ cm^{-2} for 6 h deposition time. There was no observable increase in particle densities for incubation durations beyond 6 h indicating a saturated coverage. An average of 12-14 nanoparticles per patterned gold array was observed after 6 h. FESEM images at low magnification show that the citrate AuNPs deposition over patterned gold array surface has long-range lateral order over a wide area

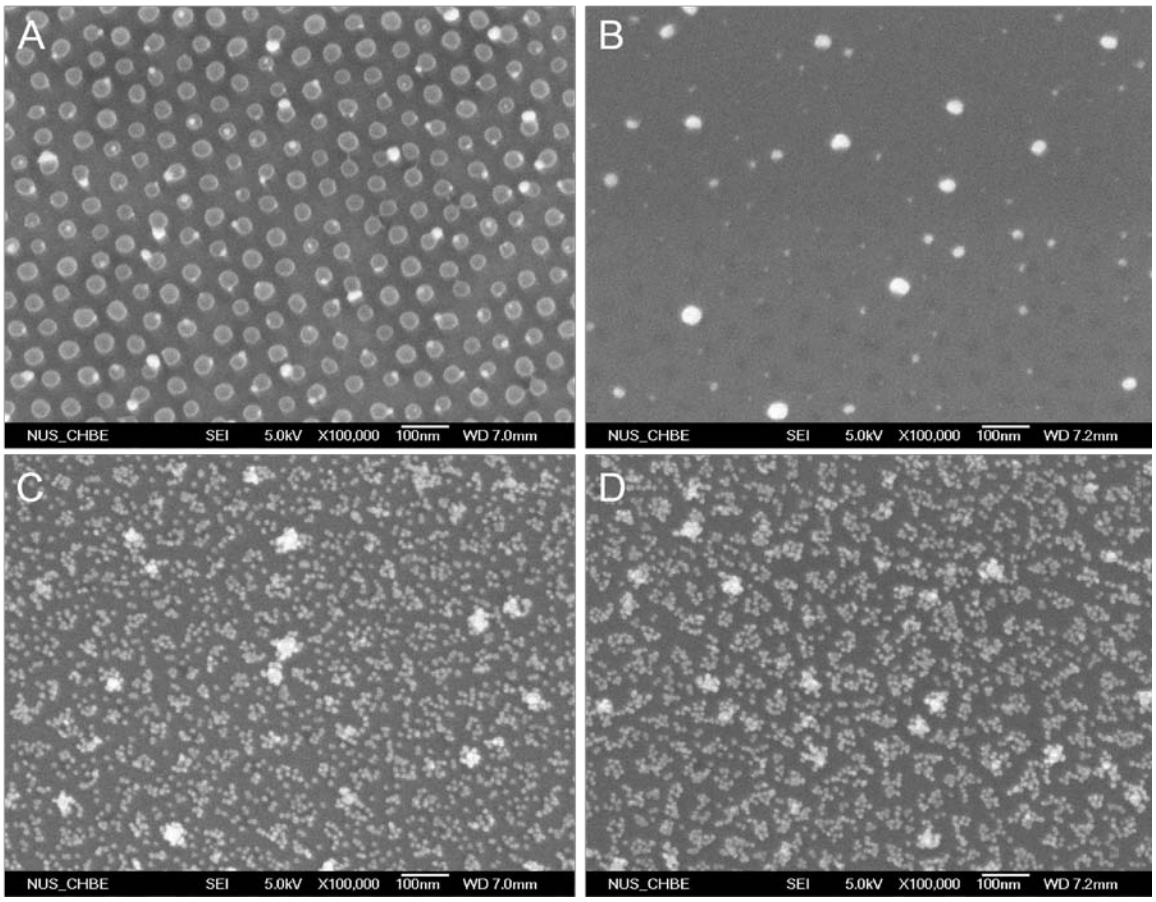

Figure 7.4. FESEM images for 100000 magnification (A) patterned gold array substrate, (B) 4-ATP modified patterned gold array substrate, (C) citrate capped AuNPs deposition on above 4-ATP modified substrate for 1 h deposition time, and (D) citrate capped AuNPs deposition on above 4-ATP modified substrate for 6 h deposition time.

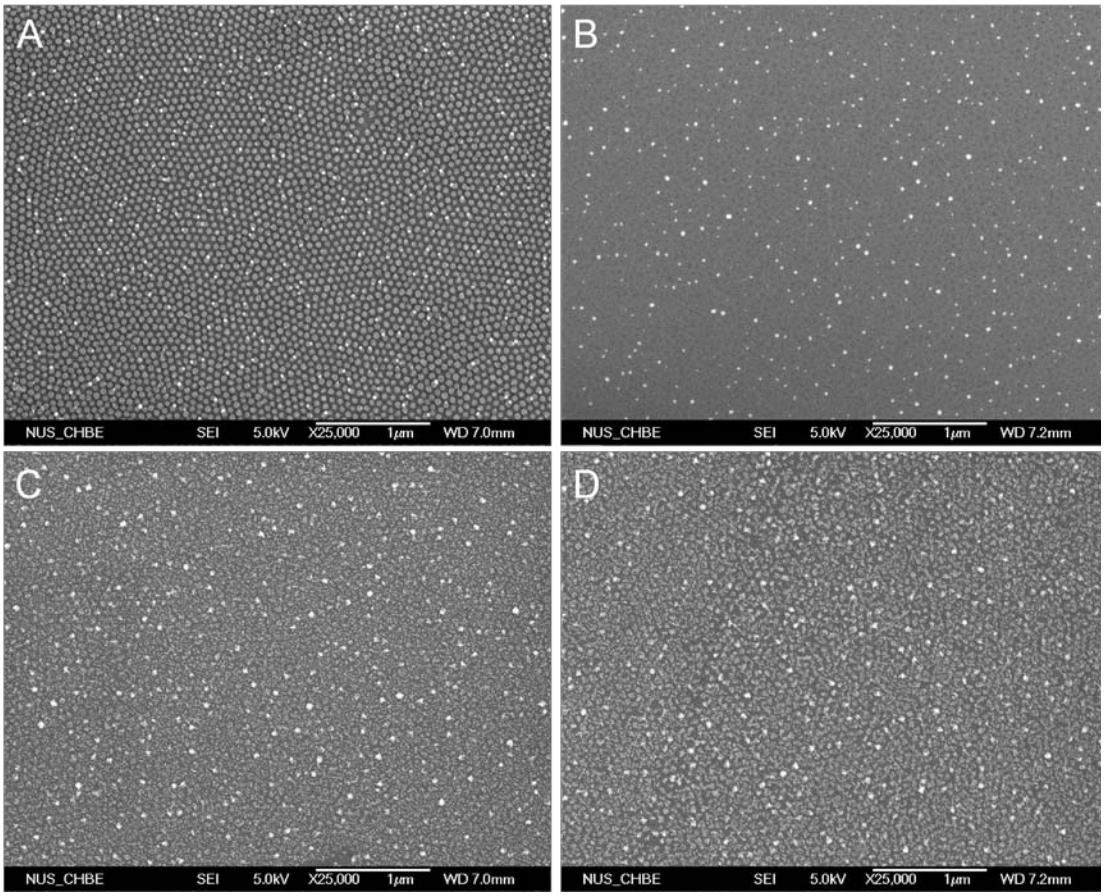

Figure 7.5. FESEM images for 25000 magnification (A) patterned gold array substrate, (B) 4-ATP modified patterned gold array substrate, (C) citrate capped AuNPs deposition on above 4-ATP modified substrate for 1 h deposition time, and (D) citrate capped AuNPs deposition on above 4-ATP modified substrate for 6 h deposition time.

(Figure 7.5). Citrate capped AuNPs were also deposited for 6 h on 4-ATP unmodified patterned gold array substrate. There is no deposition of citrate capped AuNPs on such patterned surfaces (Figure 7.6), which indicates the need of 4-ATP modification for immobilizing AuNPs on patterned gold surfaces. Citrate capped AuNPs were also immobilized over flat APhS deposited Si substrate. Figure 7.7A and Figure 7.7B are FESEM images after immobilization of citrate stabilized AuNPs over flat Si surface for 1 h and 6 h deposition time, respectively. However, density ($1.5*10^{11}$ cm^{-2}) does not change for 1 h and 6 h deposition time as observed for patterned gold surface.

7.3.3 C-V Analysis

Normalized C-V hysteresis curves of the MIS memory device containing immobilized citrate stabilized AuNPs on patterned surface are shown in Figure 7.8. Counterclockwise C-V hysteresis curves are observed that is generally attributed to charging and discharging of electrons from the substrate (Leong et al., 2007). The device with patterned gold array shows a small memory window of 0.26 V at 4/-4 V for its program/erase voltage. Hysteresis window increases to 0.68 V for citrated stabilized AuNPs immobilized patterned surface for 1 h deposition time. There is further increase in hysteresis window to 0.99 V for 6 h deposition time due to increase in density of nanoparticles. The observed hysteresis effect, therefore, could be related to the charging of the nanoparticles and nanoparticle-related traps. As shown in Figure 7.9, the hysteresis window for citrated stabilized AuNPs immobilized patterned surface for 1 h deposition

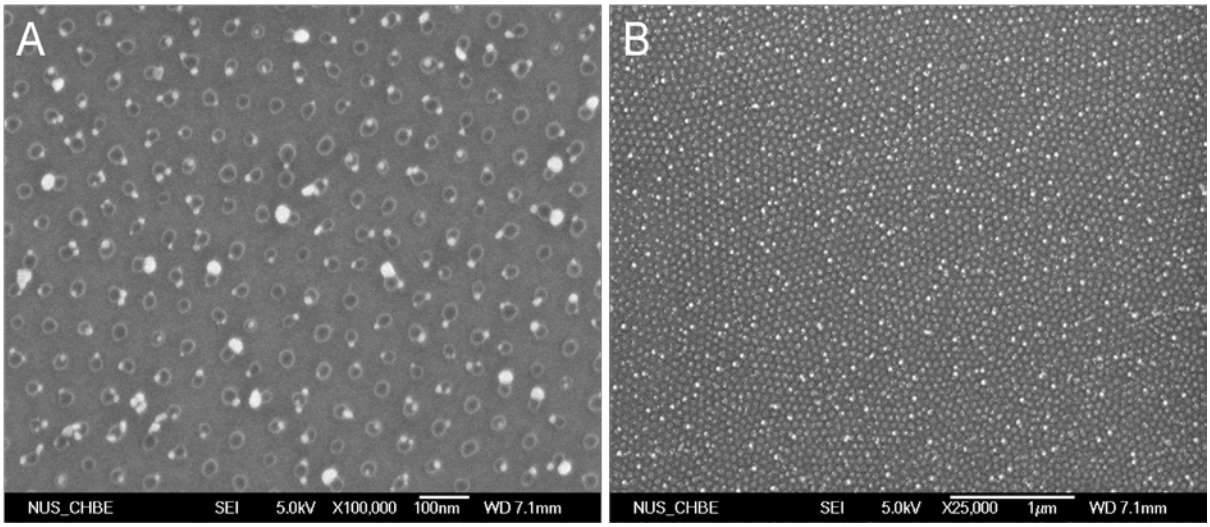

Figure 7.6. FESEM images for citrate capped AuNPs deposition for 6 h on 4-ATP unmodified patterned gold array substrate for (A) 100000 magnification, and (B) 25000 magnification.

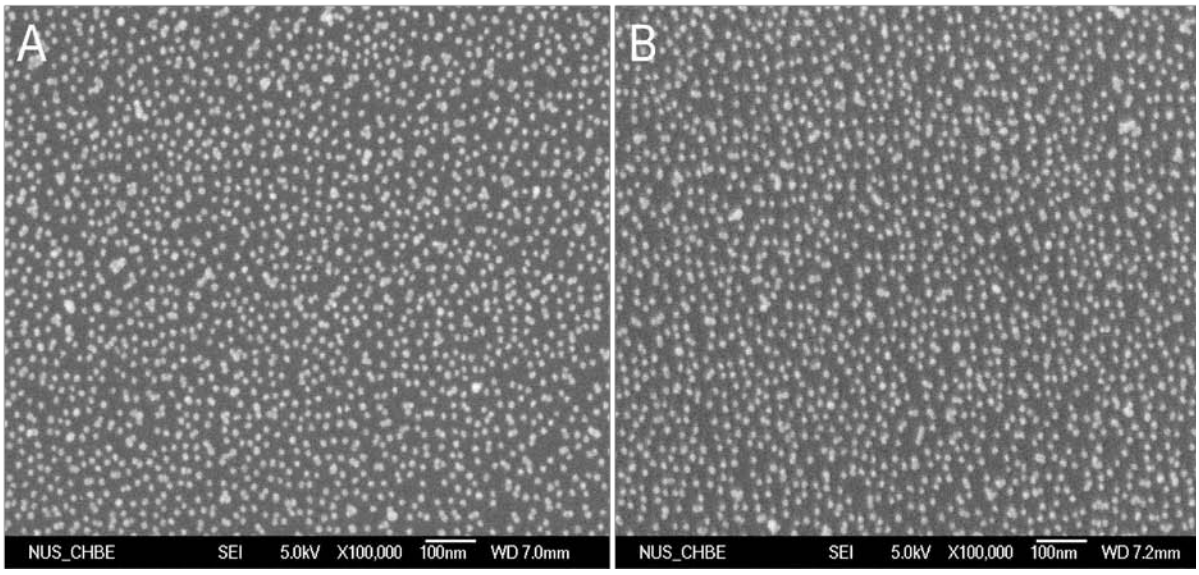

Figure 7.7. FESEM images for 100000 magnification for citrate capped AuNPs deposition on APhS modified Si substrate for (A) 1 h deposition time, and (B) 6 h deposition time.

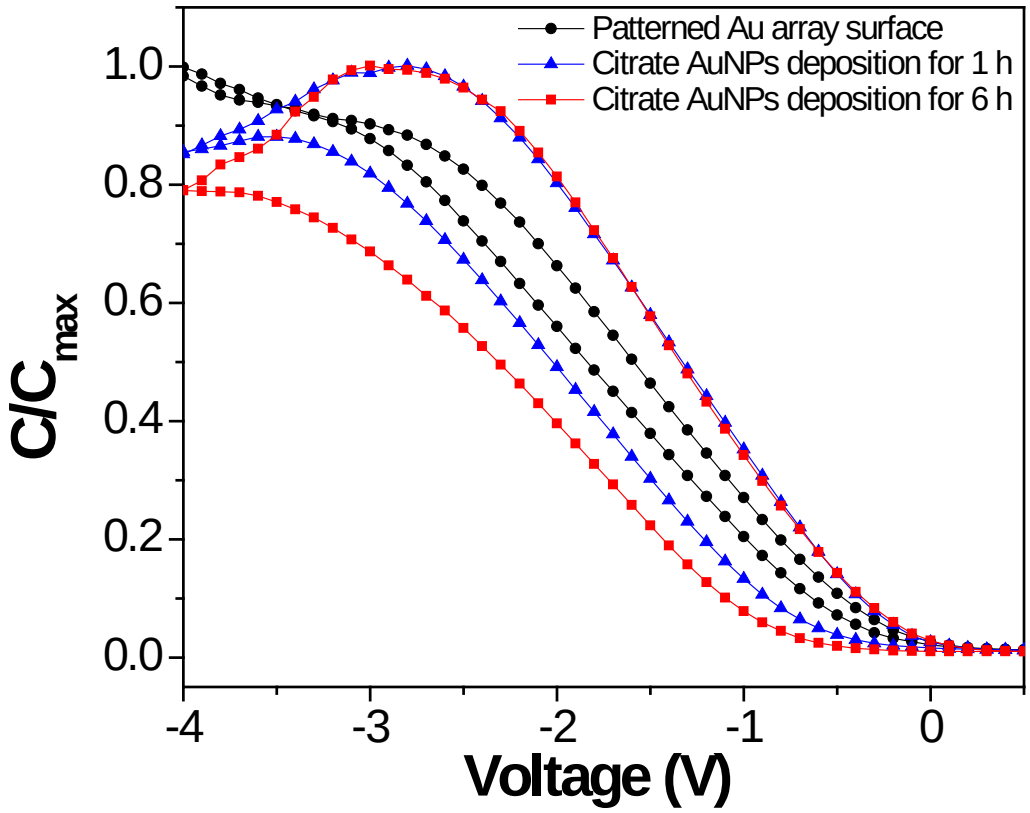

Figure 7.8. Normalized C-V characteristics at 100 kHz obtained by biasing the top electrodes at ±4 V to study effect of citrate capped AuNPs deposition on patterned substrate.

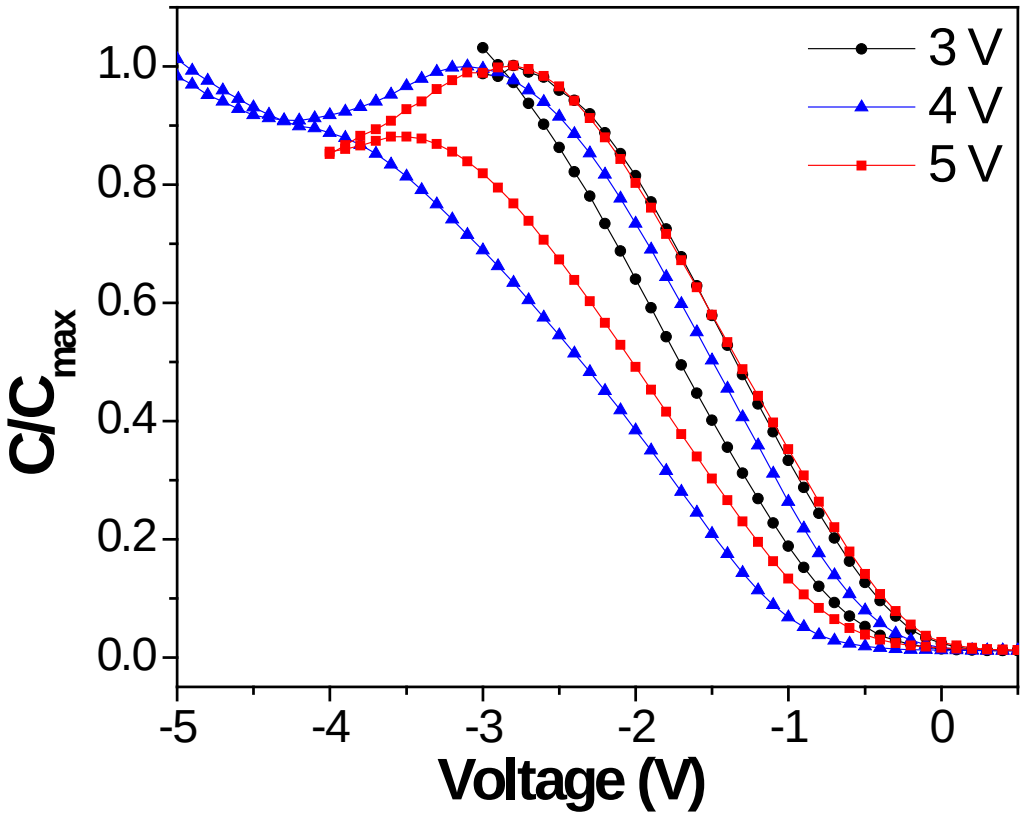

Figure 7.9. Normalized C-V characteristics at 100 kHz under different scan voltage ranges for an MIS capacitor incorporating citrate capped AuNPs deposition for 1 h on patterned substrate.

time increases from 0.39 to 0.89 V with increasing maximum operating bias from 3 to 5 V, indicating that more electrons are being trapped into the nanoparticles as the sweeping bias increased (Nicolean and Brews, 1992). C-V hysteresis curve of the MIS memory device containing immobilized citrate stabilized AuNPs over flat APhS deposited Si substrate is shown in Figure 7.10. Hysteresis window is not observed for such immobilized AuNPs structures having similar nanoparticle density. The lack of hysteresis observed in this case is indicative of a higher energy barrier for electron injection from the substrate to the AuNPs presumably due to electrostatic repulsions from citrate ion shell around gold nanoparticle surface (Figure 7.11). However, the fact that a high hysteresis is still observed in case of AuNPs on gold arrays show that the gold arrays play a vital role in reducing the barrier towards electron injection to AuNPs.

7.4 Conclusions

This chapter demonstrates the surface functionalization capability of patterned gold array surface with citrate stabilized AuNPs using 4-ATP as surface modifier. Detailed structural characterizations have been performed for immobilized AuNPs. FESEM images show the surface morphology of the immobilized nanoparticles. Charge storage capability for such immobilized AuNPs structures has been demonstrated. Charge storage capacity for the patterned gold surface improves after immobilization of citrate AuNPs. Moreover, we demonstrate the ability to tune the memory window by controlling the density of immobilized AuNPs. Our work acts as a proof-of-concept, demonstrating the

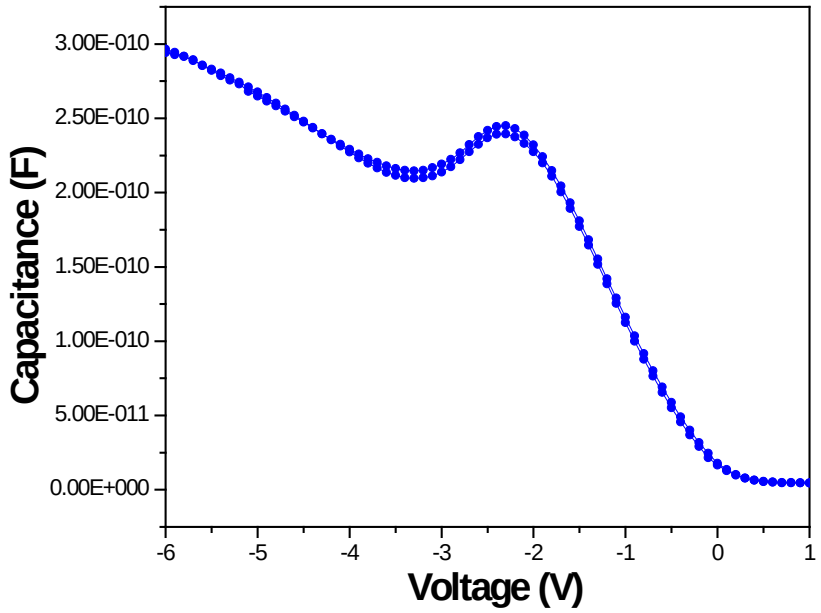

Figure 7.10. C-V characteristics at 100 kHz obtained by biasing the top electrodes at ±6 V for an MIS capacitor incorporating citrate capped AuNPs deposition for 6 h on APhS modified Si substrate.

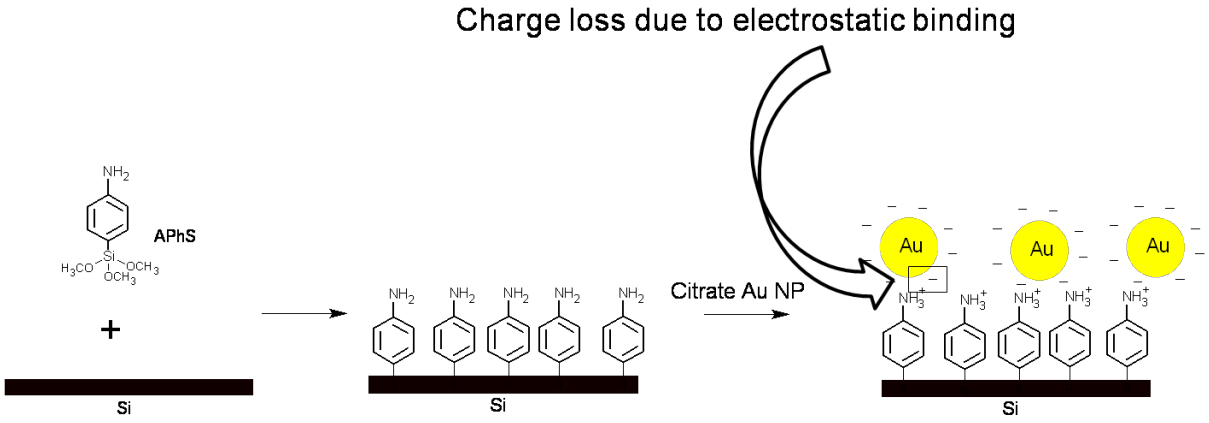

Figure 7.11. Schematic for citrate capped AuNPs deposition on APhS modified Si substrate.

vast potential of these nanoscaled arrays of nanoparticles. This approach, by virtue of its simplicity in design and processing, can realize low cost integrated memory devices.

CHAPTER 8

CONCLUSIONS

Low cost, easy processing, less power consumption and stability are some of the requirements for the memory devices in current electronic industry. The metal nanoparticles for the metal/insulator/semiconductor (MIS) memory device structures were exploited as potential storage elements in this thesis work. Solution processable assembly based organic-metallic hybrid structures as well as patterned nanoparticle structures were fabricated and their charge storage capabilities were investigated. Memory devices will be of low cost by utilizing such structures, because of their easy processing and possessing ability of fabrication over large scale. Stability of the memory devices was enhanced through assembling nanoparticles by covalent binding. Also, thermal stability of the memory devices was improved by using polyimide films as matrix.

The formation and characterization of a simple, solution processable and low-cost hybrid metallic copper nanoparticles (CuNPs)/PI film system and its application for fabricating a nonvolatile memory device structure was demonstrated. Detailed structural characterizations had been performed for embedded CuNPs in PI film. FESEM and AFM images showed the surface morphology of the embedded nanoparticles. Embedded CuNPs were uniform in size and well separated. Capacitance-voltage measurements showed that the embedded CuNPs functioned as a floating gate in MIS type capacitor and exhibited a large hysteresis window of 1.52 V. C-t measurements conducted after applying a charging bias of 5 V showed that the charge was retained beyond 20,000 s.

Langmuir-Blodgett assembly approach to form multilayers of gold nanoparticles (AuNPs) were demonstrated. Linear increase in the film thickness with the number of nanoparticle layers was observed by Ellipsometry. AFM images showed improvement in the substrate coverage with the number of nanoparticle layers. Memory devices, fabricated using these multilayered AuNPs structures, showed increase in hysteresis window with the number of nanoparticle layers. A hysteresis window of 2.2 V was observed for 6 layers of nanoparticles at 7 V biasing.

Short chain thiol (4-aminothiophenol)-capped AuNPs were synthesized. Subsequently, the nanoparticles were stabilized using PMDA as a capping agent. The formation of PMDA capping was confirmed by XPS. The nanoparticle morphology was controlled by the relative amount of AuNPs and PMDA. Detailed structural characterizations of covalently immobilized AuNPs on amine terminated silicon surface were performed. XPS and cross–sectional HR-TEM analysis confirmed the covalent attachment of AuNPs to the silicon surface.

16-mercaptohexadecanoic acid functionalized AuNPs of uniform size were synthesized using a cold synthesis method. Fourier transform infrared spectroscopy, XPS, transmission electron microscope and UV-Visible spectroscopy were employed to investigate particle morphology and surface modification of the nanoparticles. Detailed structural characterizations were performed for covalent immobilization of such AuNPs onto silicon and gold surfaces. XPS and cross – sectional HR-TEM confirmed direct

attachment of AuNPs onto the silicon substrate without occurrence of aggregation during the immobilization step.

Gold nanoparticles were covalently immobilized onto silicon substrate using a gantrez polymer as a surface modifier. XPS confirmed covalent attachment of functionalized AuNPs onto the silicon substrate. FESEM and AFM images showed the surface morphology of the immobilized nanoparticles. Immobilized nanoparticles were well separated and stable against sonication as compared to spin coated nanoparticles. In addition, the charge storage capability of such covalently bound AuNPs was also demonstrated by means of a MIS device structure. A hysteresis window of 1.64 V at 7 V biasing and good retention time up to 20,000 s were observed.

Fabrication of molecular thick gantrez polymer film was investigated. AFM, ellipsometry and XPS characterization were carried out to optimize the process conditions for the gantrez deposition on APhS modified silicon surface. The covalent bound films showed excellent stability and strength against sonication. Later, tribological properties of PFPE films having gantrez film as an intermediate layer between Si and PFPE were demonstrated. Anhydride groups available at gantrez film anchored to PFPE molecules having –OH terminal groups and eventually lead to improved tribological properties.

Multilayers of gantrez polymer films having covalent interlayer linkages were demonstrated. Ellipsometry and XPS characterization were carried out to show multilayer deposition of gantrez films. Separation between immobilized AuNPs and substrate

surface was controlled by such multilayered-gantrez polymeric films, as shown by cross – sectional HR-TEM images. AuNPs density was increased through immobilization of the 2nd layer of AuNPs, after stabilizing 1st layer of immobilized AuNPs through gantrez film capping, as shown by FESEM images. Cross – sectional HR-TEM analysis was carried out to show direct evidence of increase in AuNPs density for the 2nd layer of immobilized AuNPs, without occurrence of aggregation.

A novel route towards fabrication of gold nanoparticle clusters as a means of significantly enhancing charge-storage capacity of nonvolatile memory device was demonstrated. Detailed structural characterizations were performed for immobilized AuNPs. Charge storage capability for such immobilized AuNPs structures was demonstrated by means of a MIS device structure. The resulting patterned gold nanoparticle assemblies showed better charge storage capacity over un-patterned gold counterparts with comparable particle densities. A memory window of 1 V was achieved at low biasing voltage of 4 V through high-density of nanoparticles.

CHAPTER 9

FUTURE RECOMMENDATIONS

Solid supports containing separated nanoparticles have attracted a great deal of attention largely due to their unique physical and chemical properties which are suitable for a wide range of industrial applications. In particular, nanoparticles of uniform and controllable size immobilized on appropriate support find uses in areas as diverse as catalysis, microelectronics, magnetic, electrochemistry, tribology, and optics. This thesis work has demonstrated the technique of immobilizing nanoparticles on solid substrate and the application of this work has been showed in nonvolatile memory. Some more applications are identified and stated below.

Charge storage capability for the citrate stabilized gold nanoparticles (AuNPs) which were immobilized through functionalized gantrez polymeric films, can be studied. Effect of the density of AuNPs through multilayers of AuNPs as well as the effect of separation distance between AuNPs layer and substrate, on charge storage capacity, can also be investigated. Our approach to get multilayered composite films comprising functionalized polymer and gold nanoparticles can enable the preparation of films from various inorganic/organic components with controlled thickness at the molecular level and on substrates of different size, shape and functionality. Such nano-structured materials will enable development of low cost, easily usable, disposable and light weight sensors with enhanced performance in terms of detection limit and selectivity and can find applications in the environmental, defence, biomedical, agricultural, and industrial arenas. Also, nano-scale polymeric coatings developed using solution processable methods, can provide specific protective reactive coatings for protection against chemical warfare agents.

Development of simple and reliable protocols for the immobilization of catalytically active metal nanoparticles is an important aspect in the field of catalysis. Agglomeration of the nanoparticles is a key challenge for the catalysis application, which can be overcome through surface functionalization/stabilization of these nanoparticles. Homogeneous catalysis has some drawbacks such as difficulties in quantitative separation (purity of the product), recovery, and regeneration of the catalyst. Porous materials such as activated carbon, silica, and zeolites have many advantages as supports because of their high surface areas, shape/size selectivity and easy separation from reaction mixtures for heterogeneous catalysis. A possible strategy to overcome aggregation problem for metal nanoparticles could be through the immobilization of functionalized metal nanoparticles over these solid supports with inter layer covalent bonds.

In order to utilize the characteristics of metal nanoparticles, it is ideal to assemble them on a substrate in a controlled manner, rather than randomly. The proper 2D arrangement of nanoparticles is expected to exhibit new magnetic properties due to an exchange interaction of electron spin mediated by the substrate. Moreover, a regular pattern is technologically crucial to define the coordinate of the nanoparticle positions for magnetic data storage with nano-structured magnets. So there is a need to develop a simple and economical approach for patterning surfaces that have nano-scale feature sizes, which allows long-range ordering over large areas. Our work on the surface functionalization of patterned gold arrays with citrate stabilized AuNPs can be applied to achieve array of magnetic nanoparticle over a substrate for magnetic memory applications.

Recently, small sized thiol-capped AuNPs have shown permanent magnetism and hysteresis up to room temperature. This is due to occurrence of charge transfer between gold–sulfur bonds through loss of *d*-electrons from AuNPs after capping with strongly interacting thiols. This charge is localized, which gives rise to a magnetic moment. Our combined work on covalent immobilization of thiol capped AuNPs and surface functionalization of patterned surface can result in thiol functionalized AuNPs over a patterned surface. These structures can find application in the production of devices having both the electrical and the magnetic memory and thus, result in enhanced capacity for the memory devices.

In addition to the above, we can also study the effect of using other metallic nanoparticles (Pt, Pd), having higher work function than Au, on charge storage capacity for the construction of nonvolatile memory devices.

REFERENCES

Acosta, E. J., Carr, C. S., Simanek, E. E. and Shantz, D. F. Engineering nanospaces: Iterative synthesis of melamine-based dendrimers on amine-functionalized SBA-15 leading to complex hybrids with controllable chemistry and porosity, Adv. Mater., 16, pp.985-989. 2004.

Aizawa, M. and Buriak, J. M. Block copolymer-templated chemistry on Si, Ge, InP, and GaAs surfaces, J. Am. Chem. Soc., 127, pp.8932-8933. 2005.

Alivisatos, P. The use of nanocrystals in biological detection, Nat. Biotechnol., 22, pp.47-52. 2004.

Amman, M., Field, S. B., and Jaklevic, R. C. Coulomb-blockade spectroscopy of gold particles imaged with scanning tunneling microscopy, Phys. Rev. B, 48, pp.12104-12109. 1993.

Andres, R. P., Bielefeld, J. D., Henderson, J. I., Janes, D. B., Kolagunta, V. R., Kubiak, C. P., Mahoney, W. J. and Osifchin, R. G. Self-assembly of a two-dimensional superlattice of molecularly linked metal clusters, Science, 273, pp.1690-1693. 1996.

Antonietti, M. and Ozin, G. A. Promises and problems of mesoscale materials chemistry or why meso?, Chem. Eur. J., 10, pp.29-41. 2004.

Bai, Y., Zhao, S., Zhang, K. and Sun, C. Covalently attached multilayer assemblies of citrate-capped colloidal gold nanoparticles and diazo-resins, Colloids Surf., A, 281, pp.105-112. 2006.

Balasubramanian, R., Kim, B., Tripp, S. L., Wang, X., Lieberman, M. and Wei, A. Dispersion and stability studies of resorcinarene-encapsulated gold nanoparticles, Langmuir, 18, pp.3676-3681. 2002.

Bandhopadhyay, A. and Pal, A. J. Large conductance switching and memory effects in organic molecules for data-storage applications, Appl. Phys. Lett., 82, pp.1215. 2003.

Bandyopadhyay, A. and Pal, A. J. Multilevel conductivity and conductance switching in supramolecular structures of an organic molecule, Appl. Phys. Lett., 84, pp.999. 2004.

Baur, J. W., Rubner, M. F., Reynolds, J. R. and Kim, S. Förster energy transfer studies of polyelectrolyte heterostructures containing conjugated polymers: A means to estimate layer interpenetration, Langmuir, 15, pp.6460-6469. 1999.

Bertrand, P., Jonas, A., Laschewsky, A. and Legras, R. Ultrathin polymer coatings by complexation of polyelectrolytes at interfaces: Suitable materials, structure and properties, Macromol. Rapid Commun., 21, pp.319-348. 2000.

Bharat, H. L. B. Nanotribological characterization of molecularly thick lubricant films for applications to MEMS/NEMS by AFM, Ultramicroscopy, 97, pp.537. 2003.

Bhushan, B., Kulkarni, A. V., Koinkar, V. N., Boehm, M., Odoni, L., Martelet, C. and Belin, M. Microtribological characterization of self-assembled and langmuir-blodgett monolayers by atomic and friction force microscopy, Langmuir, 11, pp.3189-3198. 1995.

Boas, U. and Heegaard, P. M. H. Dendrimers in drug research, Chem. Soc. Rev., 33, pp.43-63. 2004.

Boontongkong, Y. and Cohen, R. E. Cavitated block copolymer micellar thin films: Lateral arrays of open nanoreactors, Macromolecules, 35, pp.3647-3652. 2002.

Bosman, A. W., Janssen, H. M. and Meijer, E. W. About dendrimers: Structure, physical properties, and applications, Chem. Rev., 99, pp.1665-1688. 1999.

Bourgoin, J. P., Kergueris, C., Lefevre, E. and Palacin, S. Langmuir-Blodgett films of thiol-capped gold nanoclusters: Fabrication and electrical properties, Thin Solid Films, 327, pp.515-519. 1998.

Bozano, L. D., Kean, B. W., Deline, V. R., Salem, J. R. and Scott, J. C. Mechanism for bistability in organic memory elements, Appl. Phys. Lett., 84, pp.607-609. 2004.

Bozano, L. D., Kean, B. W., Beinhoff, M., Carter, K. R., Rice, P. M. and Scott, J. C. Organic materials and thin-film structures for cross-point memory cells based on trapping in metallic nanoparticles, Adv. Funct. Mater., 15, pp.1933-1939. 2005.

Bratton, D., Yang, D., Dai, J. and Ober, C. K. Recent progress in high resolution lithography, Polymers for Advanced Technologies, 17, pp.94-103. 2006.

Brown, W. D. and Brewer, J. E. Nonvolatile semiconductor memory technology, IEEE Press. 1998.

Brust, M., Walker, M., Bethell, D., Schiffrin, D. J. and Whyman, R. Synthesis of thiol-derivatised gold nanoparticles in a two-phase liquid–liquid system, J. Chem. Soc., Chem. Commun., 7, pp.801-802. 1994.

Brust, M., Fink, J., Bethell, D., Schiffrin, D. J. and Kiely, C. Synthesis and reactions of functionalised gold nanoparticles, J. Chem. Soc., Chem. Commun. , 16, pp.1655-1656 1995.

Cassagneau, T., Mallouk, T. E. and Fendler, J. H. Layer-by-layer assembly of thin film zener diodes from conducting polymers and CdSe nanoparticles, J. Am. Chem. Soc., 120, pp.7848-7859. 1998.

Castner, D. G., Hinds, K. and Grainger, D. W. X-ray photoelectron spectroscopy sulfur 2p study of organic thiol and disulfide binding interactions with gold surfaces, Langmuir, 12, pp.5083-5086. 1996.

Chai, J., Wang, D., Fan, X. and Buriak, J. M. Assembly of aligned linear metallic patterns on silicon, Nat. Nanotechnol., 2, pp.500-506. 2007.

Chastain, J., Handbook of X-ray Photoelectron Spectroscopy. USA: Perkin-elmer, Physical electronic division. 1992.

Chen, J. and Reed, M. A. Electronic transport of molecular systems, Chem. Phys., 281, pp.127-145. 2002.

Chen, S. Langmuir monolayers of gold nanoparticles: From ohmic to rectifying charge transfer, Anal. Chim. Acta., 496, pp.29-37. 2003.

Chen, Y., Jung, G. Y., Ohlberg, D. A. A., Li, X., Stewart, D. R., Jeppesen, J. O., Nielsen, K. A., Stoddart, J. F. and Williams, R. S. Nanoscale molecular-switch crossbar circuits, Nanotechnology, 14, pp.462-468. 2003.

Chen, J. H., Yoo, W. J., Chan, D. S. H. and Tang, L. J. Self-assembly of Al_2O_3 nanodots on SiO_2 using two-step controlled annealing technique for long retention nonvolatile memories, Appl. Phys. Lett., 86, pp.1-3. 2005.

Choi, S., Hong, S. H., Cho, S. H., Park, S., Park, S. M., Kim, O. and Ree, M. High-performance programmable memory devices based on hyperbranched copper phthalocyanine polymer thin films, Adv. Mater., 20, pp.1766-1771. 2008.

Chung, Y., Park, H. P., Jeon, H. J., Yoon, C. S., Lim, S. K. and Kim, Y. H. Synthesis of oxide nanoparticles embedded in polyimide, J. Vac. Sci. Technol., B, 21, pp.L9-L11. 2003.

Clement Wann, H. and Hu, C. High-endurance ultra-thin tunnel oxide in MONOS device structure for dynamic memory application, IEEE Electron Device Lett., 16, pp.491-493. 1995.

Colle, M., Buchel, M. and de Leeuw, D. M. Switching and filamentary conduction in non-volatile organic memories, Org. Electron., 7, pp.305-312. 2006.

Conghua Lu , S. B., Dongbai Zhang , Lan Huang , Jiming Ma , Chuanqiou Luo and Weixiao Cao. Stable multilayer ultrathin film containing covalently attached colloidal Ag nanoparticles, Nanotechnology 14, pp.680-683. 2003.

Crespilho, F. N., Huguenin, F., Zucolotto, V., Olivi, P., Nart, F. C. and Oliveira, J. O. N. Dendrimers as nanoreactors to produce platinum nanoparticles embedded in layer-by-layer films for methanol-tolerant cathodes, Electrochem. Commun., 8, pp.348-352. 2006.

Crooks, R. M., Lemon, B. I., Sun, L., Yeung, L. K. and Zhao, M. Dendrimer-encapsulated metals and semiconductors: Synthesis, characterization, and applications, Top. Curr. Chem., 212, pp.81-135. 2001a.

Crooks, R. M., Zhao, M., Sun, L., Chechik, V. and Yeung, L. K. Dendrimer-encapsulated metal nanoparticles: Synthesis, characterization, and applications to catalysis, Acc. Chem. Res., 34, pp.181-190. 2001b.

Damle, C., Gole, A. and Sastry, M. Multilayer Langmuir-Blodgett assemblies of hydrophobized CdS nanoparticles by organization at the air-water interface, J. Mater. Chem., 10, pp.1389-1393. 2000.

Daniel, M. C. and Astruc, D. Gold nanoparticles: Assembly, supramolecular chemistry, quantum-size-related properties, and applications toward biology, catalysis, and nanotechnology, Chem. Rev., 104, pp.293-346. 2004.

Das, B. C., Batabyal, S. K. and Pal, A. J. A bit per particle: Electrostatic assembly of CdSe quantum dots as memory elements, Adv. Mater., 19, pp.4172-4176. 2007.

De Blauwe, J. Nanocrystal nonvolatile memory devices, IEEE Trans. Nanotechnol., 1, pp.72-77. 2002.

De Boer, M. P. and Mayer, T. M. Tribology of MEMS, MRS Bulletin, 26, pp.302-304. 2001.

Decher, G. and Schmitt, J. Fine-tuning of the film thickness of ultrathin multilayer films composed of consecutively alternating layers of anionic and cationic polyelectrolytes, J. Prog. Colloid Polym. Sci., 89, pp.160-164. 1992.

Decher, G. Fuzzy nanoassemblies: Toward layered polymeric multicomposites, Science, 277, pp.1232-1237. 1997.

Dubas, S. T. and Schlenoff, J. B. Polyelectrolyte multilayers containing a weak polyacid: Construction and deconstruction, Macromolecules, 34, pp.3736-3740. 2001.

Duevel, R. V. and Corn, R. M. Amide and ester surface attachment reactions for alkanethiol monolayers at gold surfaces as studied by polarization modulation fourier transform infrared spectroscopy, Anal. Chem., 64, pp.337-342. 1992.

Dufourcq, J., Bodnar, S., Gay, G., Lafond, D., Mur, P., Molas, G., Nieto, J. P., Vandroux, L., Jodin, L., Gustavo, F. and Baron, T. High density platinum nanocrystals for non-volatile memory applications, Appl. Phys. Lett., 92, pp.073102. 2008.

Eapen, K., Patton, S. and Zabinski, J. Lubrication of microelectromechanical systems (MEMS) using bound and mobile phases of fomblin Zdol, Tribol. Lett., 12, pp.35-41. 2002.

Elliot, D. J., Furlong, D. N., Gengenbach, T. R., Grieser, F., Urquhart, R. S., Hoffman, C. L. and Rabolt, J. F. Reactions of complex-ions of platinum and palladium in Langmuir-Blodgett-films of dimethyldioctadecylammonium chlorometallates, Colloids Surf., A, 103, pp.207-219. 1995.

Elliot, D. J., Furlong, D. N., Grieser, F., Mulvaney, P. and Giersig, M. Preparation and spectral characteristics of gold particles in Langmuir-Blodgett films, Colloids Surf., A, 130, pp.141-150. 1997.

Elliot, D. J., Furlong, D. N. and Grieser, F. Fabrication of nano-sized particles of metallic copper and copper sulfide in Langmuir-Blodgett films, Colloids Surf., A, 141, pp.9-17. 1998.

Esumi, K., Suzuki, A., Yamahira, A. and Torigoe, K. Role of poly(amidoamine) dendrimers for preparing nanoparticles of gold, platinum, and silver, Langmuir, 16, pp.2604-2608. 2000.

Esumi, K. Dendrimers for nanoparticle synthesis and dispersion stabilization, Top. Curr. Chem., 227, pp.31-52. 2003.

Evans, S. Handbook of X-ray and Ultraviolet Photoelectron Spectroscopy. London. 1977.

Fairley, P. Hybrids' rising sun, Tech. Rev., 107, pp.34-42. 2004.

Fazio, A. Flash memory scaling, MRS Bulletin, 29, pp.814-817. 2004.

Fendler, J. H. Chemical self-assembly for electronic applications, Chem. Mater., 13, pp.3196-3210. 2001.

Forster, S. and Antonietti, M. Amphiphilic block copolymers in structure-controlled nanomaterial hybrids, Adv. Mater., 10, pp.195-217. 1998.

Frechet, J. Functional polymers and dendrimers: Reactivity, molecular architecture, and interfacial energy, Science, 263, pp.1710-1715. 1994.

Fu, Y., Xu, H., Bai, S. L., Qiu, D. L., Sun, J. Q., Wang, Z. Q. and Zhang, X. Fabrication of a stable polyelectrolyte/Au nanoparticles multilayer film, Macromol. Rapid Commun., 23, pp.256-259. 2002.

Grabar, K. C., Griffith Freeman, R., Hommer, M. B. and Natan, M. J. Preparation and characterization of Au colloid monolayers, Anal. Chem., 67, pp.735-743. 1995.

Grabar, K. C., Brown, K. R., Keating, C. D., Stranick, S. J., Tang, S. L. and Natan, M. J. Nanoscale characterization of gold colloid monolayers: A comparison of four techniques, Anal. Chem., 69, pp.471-477. 1997.

Gu, Y., Xie, H., Gao, J., Liu, D., Williams, C. T., Murphy, C. J. and Ploehn, H. J. AFM characterization of dendrimer-stabilized platinum nanoparticles, Langmuir, 21, pp.3122-3131. 2005.

Guarini, K., Black, C. T., Zhang, Y., Babich, I. V., Sikorski, E. M. and Gignac, L. M. Low voltage, scalable nanocrystal FLASH memory fabricated by templated self assembly, Proc. of Electron Devices Meeting, IEDM '03 Technical Digest, IEEE International, pp.541-544. 2003.

Guo, J., Luo, Y., Augustsson, A., Kashtanov, S., Rubensson, J., Shuh, D. K., Agren, H. and Nordgren, J. Molecular structure of alcohol-water mixtures, Phys. Rev. Lett., 91, pp.1574011-1574014. 2003.

Guterman, D. C., Rimawi, I. H., Chiu, Te-Long, Halvorson, R. D. and McElroy, D. J. An electrically alterable nonvolatile memory cell using a floating gate structure, IEEE Tran. Electron Devices, 26, pp.576-586. 1979.

Hahm, S. G., Choi, S., Hong, S. H., Lee, T. J., Park, S., Kim, D. M., Kim, J. C., Kwon, W., Kim, K., Kim, M. J., Kim, O. and Ree, M. Electrically bistable nonvolatile switching devices fabricated with a high performance polyimide bearing diphenylcarbamyl moieties, J. Mater. Chem., 19, pp.2207-2214. 2009.

Hammond, P. T. Recent explorations in electrostatic multilayer thin film assembly, Curr. Opin. Colloid Interface Sci., 4, pp.430-442. 1999.

Hasan, M., Bethell, D. and Brust, M. The fate of sulfur-bound hydrogen on formation of self-assembled thiol monolayers on gold: 1H NMR spectroscopic evidence from solutions of gold clusters, J. Am. Chem. Soc., 124, pp.1132-1133. 2002.

He, J.-A., Valluzzi, R., Yang, K., Dolukhanyan, T., Sung, C., Kumar, J., Tripathy, S. K., Samuelson, L., Balogh, L. and Tomalia, D. A. Electrostatic multilayer deposition of a gold−dendrimer nanocomposite, Chem. Mater., 11, pp.3268-3274. 1999.

He, J., Ma, L., Wu, J. and Yang, Y. Three-terminal organic memory devices, J. Appl. Phys., 97, pp.1-6. 2005.

Heath, J. R. and Ratner, M. A. Molecular electronics, Phys. Today, 56, pp.43-49. 2003.

Hemakanthi, G. and Dhathathreyan, A. Formation of size-quantized copper immobilized in Langmuir-Blodgett films of 2,4-dihydroxybenzilidine-4'-(hexadecylamino) benzylamine, Langmuir, 15, pp.3317-3320. 1999.

Heriot, S. Y., Pedrosa, J. M., Camacho, L. and Richardson, T. H. Langmuir monolayer properties of 4-methylbenzenethiol capped gold nanoparticles, Mater. Sci. Eng., C, 26, pp.154-162. 2006.

Hinderling, C., Keles, Y., Stöckli, T., Knapp, H. F., Arcos, T. d. l., Oelhafen, P., Korczagin, I., Hempenius, M. A., Vancso, G. J., Pugin, R. and Heinzelmann, H.

Organometallic block copolymers as catalyst precursors for templated carbon nanotube growth, Adv. Mater., 16, pp.876-879. 2004.

Hou, T. H., Ganguly, U. and Kan, E. C. Fermi-level pinning in nanocrystal memories, IEEE Electron Device Lett., 28, pp.103-106. 2007.

Inanaga, J., Hirata, K., Saeki, H., Katsuki, T. and Yamaguchi, M. Bull. Chem. Soc. Jpn., 52, pp.1989. 1979.

Intel. 2005 Moore's law 40th anniversary.
See http://www.intel.com/cd/corporate/techtrends/emea/eng/209729.htm.

Isaacs, S. R., Choo, H., Ko, W. B. and Shon, Y. S. Chemical, thermal, and ultrasonic stability of hybrid nanoparticles and nanoparticle multilayer films, Chem. Mater., 18, pp.107-114. 2006.

Izumrudov, V. and Sukhishvili, S. A. Ionization-controlled stability of polyelectrolyte multilayers in salt solutions, Langmuir, 19, pp.5188-5191. 2003.

Jang, J., Choi, C., Lee, J.-S., Min, K.-S., Lee, J., Kim, D. M. and Kim, D. H. Design of gate stacks for improved program/erase speed, retention and process margin aiming next generation metal nanocrystal memories, Semicond. Sci. Technol., 24, pp.115009. 2009.

Jiang, Y. and Gao, Q. Heterogeneous hydrogenation catalyses over recyclable Pd(0) nanoparticle catalysts stabilized by PAMAM-SBA-15 organic-inorganic hybrid composites, J. Am. Chem. Soc., 128, pp.716-717. 2006.

Jiang, G., Baba, A. and Advincula, R. Nanopatterning and fabrication of memory devices from layer-by-layer poly(3,4-ethylenedioxythiophene)-poly(styrene sulfonate) ultrathin films, Langmuir, 23, pp.817-825. 2007.

Jiangs, G., Baba, A., Ikarashi, H., Risheng, X., Locklin, J., Kashif, K. R., Shinbo, K., Kato, K., Kaneko, F. and Advincula, R. Signal enhancement and tuning of surface plasmon resonance in Au nanoparticle/polyelectrolyte ultrathin films, J. Phys. Chem. C, 111, pp.18687-18694. 2007.

Jin, Y. D., Kang, X. F., Song, Y. H., Zhang, B. L., Cheng, G. J. and Dong, S. J. Controlled nucleation and growth of surface-confined gold nanoparticles on a (3-aminopropyl)trimethoxysilane-modified class slide: A strategy for SPR substrates, Anal. Chem., 73, pp.2843-2849. 2001.

Johnson, S. R., Evans, S. D., Mahon, S. W. and Ulman, A. Alkanethiol molecules containing an aromatic moiety self-assembled onto gold clusters, Langmuir, 13, pp.51-57. 1997.

Johnson, S. R., Evans, S. D. and Brydson, R. Influence of a terminal functionality on the physical properties of surfactant-stabilized gold nanoparticles, Langmuir, 14, pp.6639-6647. 1998.

Joly, S., Kane, R., Radzilowski, L., Wang, T., Wu, A., Cohen, R. E., Thomas, E. L. and Rubner, M. F. Multilayer nanoreactors for metallic and semiconducting particles, Langmuir, 16, pp.1354-1359. 2000.

Joo, W. J., Choi, T. L., Lee, S. K., Chung, Y., Jung, M. S. and Kim, J. M. Electronically controlled nonvolatile memory device using PAMAM dendrimer, Org. Electron., 7, pp.600-606. 2006.

Joseph, Y., Krasteva, N., Besnard, I., Guse, B., Rosenberger, M., Wild, U., Knop-Gericke, A., Schlogl, R., Krustev, R., Yasuda, A. and Vossmeyer, T. Gold-nanoparticle/organic linker films: Self-assembly, electronic and structural characterisation, composition and vapour sensitivity, Faraday Discuss., 125, pp.77-97. 2004.

Jun, Y. W., Lee, S. M., Kang, N. J. and Cheon, J. Controlled synthesis of multi-armed CdS nanorod architectures using monosurfactant system, J. Am. Chem. Soc., 123, pp.5150-5151. 2001.

Jung, J. H., Kim, J.-H., Kim, T. W., Song, M. S., Kim, Y.-H. and Jin, S. Nonvolatile organic bistable devices fabricated utilizing Cu_2O nanocrystals embedded in a polyimide layer, Appl. Phys. Lett., 89, pp.122110-3. 2006.

Juris, A. Recent developments in photo- and redox-active dendrimers, Annu. Rep. Prog. Chem. Sect. C, 99, pp.177-241. 2003.

Kang, S. H., Crisp, T., Kymissis, I. and Bulovic, V. Memory effect from charge trapping in layered organic structures, Appl. Phys. Lett., 85, pp.4666-4668. 2004.

Kanjilal, A., Hansen, J. L., Gaiduk, P., Larsen, A. N., Cherkashin, N., Claverie, A., Normand, P., Kapelanakis, E., Skarlatos, D. and Tsoukalas, D. Structural and electrical properties of silicon dioxide layers with embedded germanium nanocrystals grown by molecular beam epitaxy, Appl. Phys. Lett., 82, pp.1212-1214. 2003.

Kanoun, M., Souifi, A., Baron, T. and Mazen, F. Electrical study of Ge-nanocrystal-based metal-oxide-semiconductor structures for p-type nonvolatile memory applications, Appl. Phys. Lett., 84, pp.5079-5081. 2004.

Kapetanakis, E., Normand, P., Tsoukalas, D. and Beltsios, K. Room-temperature single-electron charging phenomena in large-area nanocrystal memory obtained by low-energy ion beam synthesis, Appl. Phys. Lett., 80, pp.2794. 2002.

Kato, H., Shibata, Y. and Kuwano, H. Effect of the Si-SiO_2 interface state density and the charge in the SiO_2 film on the electrical properties in Pt-diffused mos structure, Electron. Commun. Jpn., Part II: Electronics, 70, pp.65-73. 1987.

Kim, T., Crooks, R. M., Tsen, M. and Sun, L. Polymeric self-assembled monolayers. 2. Synthesis and characterization of self-assembled polydiacetylene mono- and multilayers, J. Am. Chem. Soc., 117, pp.3963-3967. 1995.

Kim, S. H., Medeiros-Ribeiro, G., Ohlberg, D. A. A., Williams, R. S. and Heath, J. R. Individual and collective electronic properties of Ag nanocrystals, J. Phys. Chem. B, 103, pp.10341-10347. 1999.

Kim, T. W., Choo, D. C., Shim, J. H. and Kang, S. O. Single-electron transistors operating at room temperature, fabricated utilizing nanocrystals created by focused-ion beam, Appl. Phys. Lett., 80, pp.2168. 2002.

Kim, D. W., Prins, F. E., Kim, T., Hwang, S., Lee, C. H., Kwong, D. L. and Banerjee, S. K. Reduction of charge-transport characteristics of SiGe dot floating gate memory device with ZrO_2 tunneling oxide, IEEE Trans. Electron Devices, 50, pp.510-513. 2003.

Kim, J. K., Cheong, H. J., Kim, Y., Yi, J. Y., Bark, H. J., Bang, S. H. and Cho, J. H. Rapid-thermal-annealing effect on lateral charge loss in metal-oxide-semiconductor capacitors with Ge nanocrystals, Appl. Phys. Lett., 82, pp.2527-2529. 2003.

Kim, Y.-G., Oh, S.-K. and Crooks, R. M. Preparation and characterization of 1–2 nm dendrimer-encapsulated gold nanoparticles having very narrow size distributions, Chem. Mater., 16, pp.167-172. 2003.

Kim, J. H., Jin, J. Y., Jung, J. H., Lee, I., Kim, T. W., Lim, S. K., Yoon, C. S. and Kim, Y. H. Formation and electrical properties of $Ni_{1-x}Fe_x$ nanocrystals embedded in a polyimide layers for applications as nonvolatile flash memories, Appl. Phys. Lett., 86, pp.1-3. 2005.

Kim, J. H., Baek, K. H., Kim, C. K., Kim, Y. B. and Yoon, C. S. Formation of gold nanoparticles embedded in a polyimide film for nanofloating gate memory, Appl. Phys. Lett., 90, pp.123118. 2007.

Kim, T. W., Shin, J. W., Lee, J. Y., Jung, J. H., Lee, J. W., Choi, W. K. and Jin, S. Electron-beam-induced formation of Zn nanocrystal islands in a SiO_2 layer, Appl. Phys. Lett., 90, 2007.

Kim, C. K., Joo, W. J., Kim, H. J., Song, E. S., Kim, J., Lee, S., Park, C. and Kim, C. Gold nanoparticles passivated with π-conjugated dendrons and their electrical bistability, Synth. Met., 158, pp.359-363. 2008.

Kim, H. C., Park, S. M., Hinsberg, W. D. and Division, I. R. Block copolymer based nanostructures: Materials, processes, and applications to electronics, Chem. Rev., 110, pp.146-177. 2010.

Knecht, M. R., Garcia-Martinez, J. C. and Crooks, R. M. Synthesis, characterization, and magnetic properties of dendrimer-encapsulated nickel nanoparticles containing <150 atoms, Chem. Mater., 18, pp.5039-5044. 2006.

Kolosov, D., English, D. S., Bulovic, V., Barbara, P. F., Forrest, S. R. and Thompson, M. E. Direct observation of structural changes in organic light emitting devices during degradation, J. Appl. Phys., 90, pp.3242-3247. 2001.

Kovacevic, D., van der Burgh, S., de Keizer, A. and Cohen Stuart, M. A. Kinetics of formation and dissolution of weak polyelectrolyte multilayers: Role of salt and free polyions, Langmuir, 18, pp.5607-5612. 2002.

Krishnamoorthy, S., Pugin, R., Brugger, J., Heinzelmann, H. and Hinderling, C. Tuning the dimensions and periodicities of nanostructures starting from the same polystyrene-

block-poly(2-vinylpyridine) diblock copolymer, Adv. Funct. Mater., 16, pp.1469-1475. 2006.

Kuhr W., G. A. R., Manning R. W. and Rhodine C. W. Molecular memories based on a cmos platform, MRS Bulletin 29, pp.838-841. 2004.

Lai, P. Y. and Chen, J. S. Electrical bistability and charge transport behavior in Au nanoparticle/poly(N-vinylcarbazole) hybrid memory devices, Appl. Phys. Lett., 93, pp.153305. 2008.

Lambe, J. and Jaklevic, R. C. Charge-quantization studies using a tunnel capacitor, Phys. Rev. Lett., 22, pp.1371-1375. 1969.

Lang, H., May, R. A., Iversen, B. L. and Chandler, B. D. Dendrimer-encapsulated nanoparticle precursors to supported platinum catalysts, J. Am. Chem. Soc., 125, pp.14832-14836. 2003.

Langhammer, C., Yuan, Z., Zorić, I. and Kasemo, B. Plasmonic properties of supported Pt and Pd nanostructures, Nano Lett., 6, pp.833-838. 2006.

Lauters, M., McCarthy, B., Sarid, D. and Jabbour, G. E. Multilevel conductance switching in polymer films, Appl. Phys. Lett., 89, 2006.

Lee, W. Y., Hostetler, M. J., Murray, R. W. and Majda, M. Electron hopping and electronic conductivity in monolayers of alkanethiol-stabilized gold nano-clusters at the air/water interface, Isr. J. Chem., 37, pp.213-223. 1997.

Lee, C., Meteer, J., Narayanan, V. and Kan, E. C. Self-assembly of metal nanocrystals on ultrathin oxide for nonvolatile memory applications, J. Electron. Mater., 34, pp.1-11. 2005.

Lee, J. J., Harada, Y., Pyun, J. W. and Kwong, D. L. Nickel nanocrystal formation on HfO_2 dielectric for nonvolatile memory device applications, Appl. Phys. Lett., 86, pp.1-3. 2005.

Lee, J. S., Cho, J., Lee, C., Kim, I., Park, J., Kim, Y. M., Shin, H., Lee, J. and Caruso, F. Layer-by-layer assembled charge-trap memory devices with adjustable electronic properties, Nat. Nanotechnol., 2, pp.790-795. 2007.

Lee, C., Kim, I., Shin, H., Kim, S. and Cho, J. Nonvolatile resistive switching memory properties of thermally annealed titania precursor/polyelectrolyte multilayers, Langmuir, 25, pp.11276-11281. 2009.

Lee, D. U., Han, S. J., Seo, K. B., Kim, E. K., Shin, J. W., Cho, W. J. and Kim, Y. H. Electrical characterization of nonvolatile memory with SnO_2 nano-particle in polyimide dielectric layer, Superlattices Microstruct., 46, pp.176-181. 2009.

Leong, W. L., Lee, P. S., Mhaisalkar, S. G., Chen, T. P. and Dodabalapur, A. Charging phenomena in pentacene-gold nanoparticle memory device, Appl. Phys. Lett., 90, pp.042906-3. 2007.

Leong, W. L., Lee, P. S., Lohani, A., Lam, Y. M., Chen, T., Zhang, S., Dodabalapur, A. and Mhaisalkar, S. G. Non-volatile organic memory applications enabled by in situ synthesis of gold nanoparticles in a self-assembled block copolymer, Adv. Mater., 20, pp.2325-2331. 2008.

Lesser, C., Gao, M. and Kirstein, S. Highly luminescent thin films from alternating deposition of CdTe nanoparticles and polycations, Mater. Sci. Eng., C, 8-9, pp.159-162. 1999.

Lim, S. K., Chung, K. J., Kim, Y.-H., Kim, C. K. and Yoon, C. S. Synthesis of iron oxide nanoparticles in a polyimide matrix, J. Colloid Interface Sci., 273, pp.517-522. 2004.

Lin, H. T., Pei, Z., Chen, J. R., Hwang, G. W., Fan, J. F. and Chan, Y. J. A new nonvolatile bistable polymer-nanoparticle memory device, IEEE Electron Device Lett., 28, pp.951-953. 2007.

Ling, Q., Song, Y., Ding, S. J., Zhu, C., Chan, D. S. H., Kwong, D. L., Kang, E. T. and Neoh, K. G. Non-volatile polymer memory device based on a novel copolymer of N-vinylcarbazole and Eu-complexed vinylbenzoate, Adv. Mater., 17, pp.455-459. 2005.

Ling, Q.-D., Chang, F.-C., Song, Y., Zhu, C.-X., Liaw, D.-J., Chan, D. S.-H., Kang, E.-T. and Neoh, K.-G. Synthesis and dynamic random access memory behavior of a functional polyimide, J. Am. Chem. Soc., 128, pp.8732-8733. 2006.

Ling, Q. D., Liaw, D. J., Teo, E. Y. H., Zhu, C., Chan, D. S. H., Kang, E. T. and Neoh, K. G. Polymer memories: Bistable electrical switching and device performance, Polymer, 48, pp.5182-5201. 2007.

Ling, Q. D., Liaw, D. J., Zhu, C., Chan, D. S. H., Kang, E. T. and Neoh, K. G. Polymer electronic memories: Materials, devices and mechanisms, Prog. Polym. Sci., 33, pp.917-978. 2008.

Link, S. and El-Sayed, M. A. Size and temperature dependence of the plasmon absorption of colloidal gold nanoparticles, J. Phys. Chem. B, 103, pp.4212-4217. 1999.

Liu, Y., Wang, Y. and Claus, R. O. Layer-by-layer ionic self-assembly of Au colloids into multilayer thin-films with bulk metal conductivity, Chem. Phys. Lett., 298, pp.315-319. 1998.

Liu, Z., Lee, C., Narayanan, V., Pei, G. and Kan, E. C. Metal nanocrystal memories - Part I: Device design and fabrication, IEEE Trans. Electron Devices, 49, pp.1606-1613. 2002a.

Liu, Z., Lee, C., Narayanan, V., Pei, G. and Kan, E. C. Metal nanocrystal memories - Part II: Electrical characteristics, IEEE Trans. Electron Devices, 49, pp.1614-1622. 2002b.

Liu, F. K., Chang, Y. C., Ko, F. H., Chu, T. C. and Dai, B. T. Rapid fabrication of high quality self-assembled nanometer gold particles by spin coating method, Microelectron. Eng., 67-8, pp.702-709. 2003.

Liu, Z., Yasseri, A. A., Lindsey, J. S. and Bocian, D. F. Molecular memories that survive silicon device processing and real-world operation, Science, 302, pp.1543-1545. 2003.

Lombardo, S., De Salvo, B., Gerardi, C. and Baron, T. Silicon nanocrystal memories, Microelectron. Eng., 72, pp.388-394. 2004.

Luo, Y., Collier, C. P., Jeppesen, J. O., Nielsen, K. A., DeIonno, E., Ho, G., Perkins, J., Tseng, H. R., Yamamoto, T., Stoddart, J. F. and Heath, J. R. Two-dimensional molecular electronics circuits, ChemPhysChem, 3, pp.519-525. 2002.

Ma, L., Liu, J., Pyo, S., Xu, Q. and Yang, Y. Organic bistable devices, Mol. Cryst. Liq. Cryst. Sci. Technol., Sect. A, 378, pp.185-192. 2002a.

Ma, L., Liu, J., Pyo, S. and Yang, Y. Organic bistable light-emitting devices, Appl. Phys. Lett., 80, pp.362-364. 2002b.

Ma, L. P., Liu, J. and Yang, Y. Organic electrical bistable devices and rewritable memory cells, Appl. Phys. Lett., 80, pp.2997-2999. 2002c.

Ma, L., Pyo, S., Ouyang, J., Xu, Q. and Yang, Y. Nonvolatile electrical bistability of organic/metal-nanocluster/organic system, Appl. Phys. Lett., 82, pp.1419-1421. 2003.

Ma, L., Xu, Q. and Yang, Y. Organic nonvolatile memory by controlling the dynamic copper-ion concentration within organic layer, Appl. Phys. Lett., 84, pp.4908. 2004.

Madeley, J. M. and Richmond, C. R. Z. Anorg. Allg. Chem., 389, pp.92. 1972.

Mahapatro, A. K., Agrawal, R. and Ghosh, S. Electric-field-induced conductance transition in 8-hydroxyquinoline aluminum (Alq3), J. Appl. Phys., 96, pp.3583-3585. 2004.

Majumdar, H. S., Bandyopadhyay, A., Bolognesi, A. and Pal, A. J. Memory device applications of a conjugated polymer: Role of space charges, J. Appl. Phys., 91, pp.2433. 2002.

Majumdar, H. S., Bandyopadhyay, A. and Pal, A. J. Data-storage devices based on layer-by-layer self-assembled films of a phthalocyanine derivative, Org. Electron., 4, pp.39-44. 2003.

Majumdar, H. S., Bolognesi, A. and Pal, A. J. Switching and memory devices based on a polythiophene derivative for data-storage applications, Synth. Met., 140, pp.203-206. 2004.

Majumdar, H. S., Baral, J. K., Österbacka, R., Ikkala, O. and Stubb, H. Fullerene-based bistable devices and associated negative differential resistance effect, Org. Electron., 6, pp.188-192. 2005.

Manna, A., Imae, T., Aoi, K., Okada, M. and Yogo, T. Synthesis of dendrimer-passivated noble metal nanoparticles in a polar medium: Comparison of size between silver and gold particles, Chem. Mater., 13, pp.1674-1681. 2001.

Markovich, G., Collier, C. P., Henrichs, S. E., Remacle, F., Levine, R. D. and Heath, J. R. Architectonic quantum dot solids, Acc. Chem. Res., 32, pp.415-423. 1999.

McAloney, R. A., Dudnik, V. and Goh, M. C. Kinetics of salt-induced annealing of a polyelectrolyte multilayer film morphology, Langmuir, 19, pp.3947-3952. 2003.

Morgan, S. E., Jones, P., Lamont, A. S., Heidenreich, A. and McCormick, C. L. Layer-by-layer assembly of pH-responsive, compositionally controlled (Co) polyelectrolytes synthesized via RAFT, Langmuir, 23, pp.230-240. 2006.

Morrison, R. T. and N., B. R. Organic Chemistry. Boston, MA: Allyn and Bacon. 1983.

Muller, C. D., Falcou, A., Reckefuss, N., Rojahn, M., Wiederhirn, V., Rudati, P., Frohne, H., Nuyken, O., Becker, H. and Meerholz, K. Multi-colour organic light-emitting displays by solution processing, Nature, 421, pp.829-833. 2003.

Muller, S., Forrest, S. R., Perlov, C., Jackson, W. and Taussig, C. Electrochromic conductive polymer fuses for hybrid organic/inorganic semiconductor memories, J. Appl. Phys., 94, pp.7811-7819. 2003a.

Muller, S., Perlov, C., Jackson, W., Taussig, C. and Forrest, S. R. A polymer/semiconductor write-once read-many-times memory, Nature, 426, pp.166-169. 2003b.

Mulvaney, P. Surface plasmon spectroscopy of nanosized metal particles, Langmuir, 12, pp.788-800. 1996.

Murray, C. B., Kagan, C. R. and Bawendi, M. G. Synthesis and characterization of monodisperse nanocrystals and close-packed nanocrystal assemblies, Annu. Rev. Mater. Sci., 30, pp.545-610. 2000.

Musick, M. D., Keating, C. D., Lyon, L. A., Botsko, S. L., Pena, D. J., Holliway, W. D., McEvoy, T. M., Richardson, J. N. and Natan, M. J. Metal films prepared by stepwise assembly. 2. construction and characterization of colloidal Au and Ag multilayers, Chem. Mater., 12, pp.2869-2881. 2000.

Nakamoto, M., Yamamoto, M. and Fukusumi, M. Thermolysis of gold(I) thiolate complexes producing novel gold nanoparticles passivated by alkyl groups Chem. Commun. , 15, pp.1622-1623 2002.

Nakano, M., Ishida, T., Sano, H., Sugimura, H., Miyake, K., Ando, Y. and Sasaki, S. Tribological properties of self-assembled monolayers covalently bonded to Si, Appl. Surf. Sci., 255, pp.3040-3045. 2008.

Nicolean, E. H. and Brews, J. R. Metal Oxide Semiconductor Physics and Technology. 1st ed. New York: Wiley. 1992.

Nicollian, E. H. and Brews, J. R. MOS (Metal Oxide Semiconductor) Physics and Technology. New York: Wiley. 1982.

Normand, P., Kapetanakis, E., Tsoukalas, D., Kamoulakos, G., Beltsios, K., Van Den Berg, J. and Zhang, S. MOS memory devices based on silicon nanocrystal arrays fabricated by very low energy ion implantation, Mater. Sci. Eng., C, 15, pp.145-147. 2001.

Oh, S.-K., Kim, Y.-G., Ye, H. and Crooks, R. M. Synthesis, characterization, and surface immobilization of metal nanoparticles encapsulated within bifunctionalized dendrimers, Langmuir, 19, pp.10420-10425. 2003.

Ouyang, J., Chu, C. W., Szmanda, C. R., Ma, L. and Yang, Y. Programmable polymer thin film and non-volatile memory device, Nat. Mater., 3, pp.918-922. 2004.

Ouyang, J., Chu, C. W., Sieves, D. and Yang, Y. Electric-field-induced charge transfer between gold nanoparticle and capping 2-naphthalenethiol and organic memory cells, Appl. Phys. Lett., 86, pp.1-3. 2005a.

Ouyang, J., Chu, C. W., Tseng, R. J. H., Prakash, A. and Yang, Y. Organic memory device fabricated through solution processing, Proc. IEEE, 93, pp.1287-1296. 2005b.

Oyamada, T., Tanaka, H., Matsushige, K., Sasabe, H. and Adachi, C. Switching effect in Cu:TCNQ charge transfer-complex thin films by vacuum codeposition, Appl. Phys. Lett., 83, pp.1252-1254. 2003.

Ozin, G. A., Manners, I., Fournier-Bidoz, S. and Arsenault, A. Dream nanomachines, Adv. Mater., 17, pp.3011-3018. 2005.

Park, B., Cho, K., Moon, B. M. and Kim, S. Memory characteristics of Al nanocrystals embedded in Al_2O_3 layers, Microelectron. Eng., 84, pp.1627-1630. 2007.

Paul, S., Pearson, C., Molloy, A., Cousins, M. A., Green, M., Kolliopoulou, S., Dimitrakis, P., Normand, P., Tsoukalas, D. and Petty, M. C. Langmuir-Blodgett film deposition of metallic nanoparticles and their application to electronic memory structures, Nano Lett., 3, pp.533-536. 2003.

Perego, M., Ferrari, S., Fanciulli, M., Assayag, G. B., Bonafos, C., Carrada, M. and Claverie, A. Detection and characterization of silicon nanocrystals embedded in thin oxide layers, J. Appl. Phys., 95, pp.257-262. 2004.

Pertsin, A. J. and Pashunin, Y. M. An XPS study of the in-situ formation of the polyimide/copper interface, Appl. Surf. Sci., 47, pp.115-125. 1991.

Prakash, A., Ouyang, J., Lin, J. L. and Yang, Y. Polymer memory device based on conjugated polymer and gold nanoparticles, J. Appl. Phys., 100, pp.054309. 2006.

Puniredd, S. R. and Srinivasan, M. P. Covalent molecular assembly in supercritical carbon dioxide: A comparative study between amine- and anhydride-derivatized surfaces, Langmuir, 22, pp.4092-4099. 2006.

Puniredd, S. R. and Srinivasan, M. P. Covalent molecular assembly in a supercritical medium: Formation of nanoparticles encapsulated in immobilized dendrimers, Ind. Eng. Chem. Res., 46, pp.464-471. 2007a.

Puniredd, S. R., Yong, K. W., Satyanarayana, N., Sinha, S. K. and Srinivasan, M. P. Tribological properties of nanoparticle-laden ultrathin films formed by covalent molecular assembly, Langmuir, 23, pp.8299-8303. 2007b.

Puniredd, S. R., Weiyi, S. and Srinivasan, M. P. Pd-Pt and Fe-Ni nanoparticles formed by covalent molecular assembly in supercritical carbon dioxide, J. Colloid Interface Sci., 320, pp.333-340. 2008.

Puniredd, S. R., Yin, C. M., Hooi, Y. S., Lee, P. S. and Srinivasan, M. P. Dendrimer-encapsulated Pt nanoparticles in supercritical medium: Synthesis, characterization, and application to device fabrication, J. Colloid Interface Sci., 332, pp.505-510. 2009.

Pyo, S., Ma, L., He, J., Xu, Q., Yang, Y. and Gao, Y. Experimental study on thickness-related electrical characteristics in organic/metal-nanocluster/organic systems, J. Appl. Phys., 98, pp.1-6. 2005.

Qian, L., Gao, Q., Song, Y., Li, Z. and Yang, X. Layer-by-layer assembled multilayer films of redox polymers for electrocatalytic oxidation of ascorbic acid, Sens. Actuators, B, 107, pp.303-310. 2005.

Rajeshwar, K., de Tacconi, N. R. and Chenthamarakshan, C. R. Semiconductor-based composite materials: Preparation, properties, and performance, Chem. Mater., 13, pp.2765-2782. 2001.

Reed, M. A., Chen, J., Rawlett, A. M., Price, D. W. and Tour, J. M. Molecular random access memory cell, Appl. Phys. Lett., 78, pp.3735-3737. 2001.

Ren, Yang and Zhao. Preparation and tribological studies of C60 thin film chemisorbed on a functional polymer surface, Langmuir, 20, pp.3601-3605. 2004.

Rubira, A. F., Rancourt, J. D., Taylor, L. T., Stoakley, D. M. and Clair, A. K. S. Chemical factors that influence the production of conductive and/or reflective silver-doped polyimide films, J. Macromol. Sci. Part A Pure Appl. Chem., 35, pp.621-636. 1998.

Ruehe, J., Novotny, V. J., Kanazawa, K. K., Clarke, T. and Street, G. B. Structure and tribological properties of ultrathin alkylsilane films chemisorbed to solid surfaces, Langmuir, 9, pp.2383-2388. 1993.

Ruhe, J., Blackman, G., Novotny, V. J., Clarke, T., Street, G. B. and Kuan, S. Terminal attachment of perfluorinated polymers to solid surfaces, J. Appl. Polym. Sci., 53, pp.825-836. 1994.

Saitoh, M., Nagata, E. and Hiramoto, T. Large memory window and long charge-retention time in ultranarrow-channel silicon floating-dot memory, Appl. Phys. Lett., 82, pp.1787-1789. 2003.

Samanta, S. K., Yoo, W. J., Samudra, G., Tok, E. S., Bera, L. K. and Balasubramanian, N. Tungsten nanocrystals embedded in high- k materials for memory application, Appl. Phys. Lett., 87, pp.1-3. 2005.

Sampaio, Beverly, K. C. and Heath, J. R. DC transport in self-assembled 2D layers of Ag nanoparticles, J. Phys. Chem. B, 105, pp.8797-8800. 2001.

Sargentis, C., Giannakopoulos, K., Travlos, A. and Tsamakis, D. Electrical characterization of MOS memory devices containing metallic nanoparticles and a high-k control oxide layer, Surf. Sci., 601, pp.2859-2863. 2007.

Sargentis, C., Giannakopoulos, K., Travlos, A., Normand, P. and Tsamakis, D. Study of charge storage characteristics of memory devices embedded with metallic nanoparticles, Superlattices Microstruct., 44, pp.483-488. 2008.

Satyanarayana, N. and Sinha, S. K. Tribology of PFPE overcoated self-assembled monolayers deposited on Si surface, J. Phys. D: Appl. Phys., 38, pp.3512-3522. 2005.

Satyanarayana, N., Sinha, S. K. and Ong, B. H. Tribology of a novel UHMWPE/PFPE dual-film coated onto Si surface, Sens. Actuators, A, 128, pp.98-108. 2006.

Satyanarayana, N., Gosvami, N. N., Sinha, S. K. and Srinivasan, M. P. Friction, adhesion and wear durability of an ultra-thin perfluoropolyether-coated 3-glycidoxypropyltrimethoxy silane self-assembled monolayer on a Si surface, Philos. Mag., 87, pp.3209 - 3227. 2007.

Satyanarayana, N., Sinha, S. K. and Lim, S. C. Highly wear resistant chemisorbed polar ultra-high-molecular-weight polyethylene thin film on Si surface for micro-system applications, J. Mater. Res., 24, pp.3331-3337. 2009.

Schnippering, M., Carrara, M., Foelske, A., Kötz, R. and Fermín, D. J. Electronic properties of Ag nanoparticle arrays. A Kelvin probe and high resolution XPS study, Phys. Chem. Chem. Phys., 9, pp.725-730. 2007.

Schuetz, P. and Caruso, F. Electrostatically assembled fluorescent thin films of rare-earth-doped lanthanum phosphate nanoparticles, Chem. Mater., 14, pp.4509-4516. 2002.

Scott, R. W. J., Ye, H., Henriquez, R. R. and Crooks, R. M. Synthesis, Characterization, and stability of dendrimer-encapsulated palladium nanoparticles, Chem. Mater., 15, pp.3873-3878. 2003.

Scott, J. C. Is there an immortal memory?, Science, 304, pp.62-63. 2004.

Scott, J. C. and Bozano, L. D. Nonvolatile memory elements based on organic materials, Adv. Mater., 19, pp.1452-1463. 2007.

Sharma, A. K. Advanced semiconductor memories: Architectures, designs and applications. Piscataway, NJ: Wiley. 2003.

Simmons, J. G. and Verderber, R. R. New conduction and reversible memory phenomena in thin insulating films, Proc. R. Soc. London, Ser. A, 301, pp.77-102. 1967.

Sohn, B. H. and Seo, B. H. Fabrication of the multilayered nanostructure of alternating polymers and gold nanoparticles with thin films of self-assembling diblock copolymers, Chem. Mater., 13, pp.1752-1757. 2001.

Sohn, B. H., Choi, J. M., Yoo, S. I., Yun, S. H., Zin, W. C., Jung, J. C., Kanehara, M., Hirata, T. and Teranishi, T. Directed self-assembly of two kinds of nanoparticles utilizing monolayer films of diblock copolymer micelles, J. Am. Chem. Soc., 125, pp.6368-6369. 2003.

Song, Y., Ling, Q. D., Lim, S. L., Teo, E. Y. H., Tan, Y. P., Li, L., Kang, E. T., Chan, D. S. H. and Zhu, C. Electrically bistable thin-film device based on PVK and GNPs polymer material, IEEE Electron Device Lett., 28, pp.107-110. 2007.

Sony. 2008 XEL-1 OLED TV. See http://www.sony.co.uk/product/tvp-oled-tv/xel-1.

Southward, R. E., Boggs, C. M., Thompson, D. W. and St. Clair, A. K. Synthesis of surface-metallized polyimide films via in situ reduction of (perfluoroalkanoato)silver(I) complexes in a poly(amic acid) precursor, Chem. Mater., 10, pp.1408-1421. 1998.

Streetman, B. G. and Banerjee, S. Solid State Electronic Devices. 5th ed. Upper Saddle River, NJ: Prentice Hall. 2000.

Sui, Z. and Schlenoff, J. B. Phase separations in pH-responsive polyelectrolyte multilayers: Charge extrusion versus charge expulsion, Langmuir, 20, pp.6026-6031. 2004.

Sun, L. and Crooks, R. M. Dendrimer-mediated immobilization of catalytic nanoparticles on flat, solid supports, Langmuir, 18, pp.8231-8236. 2002.

Swami, A., Kumar, A., Selvakannan, P. R., Mandal, S., Pasricha, R. and Sastry, M. Highly oriented gold nanoribbons by the reduction of aqueous chloroaurate ions by hexadecylaniline Langmuir monolayers, Chem. Mater., 15, pp.17-19. 2003.

Takimoto, K., Kawade, H., Kishi, E., Yano, K., Sakai, K., Hatanaka, K., Eguchi, K. and Nakagiri, T. Switching and memory phenomena in Langmuir-Blodgett films with scanning tunneling microscope, Appl. Phys. Lett., 61, pp.3032-3034. 1992.

Tan, Z.; Samanta, S. K.; Yoo, W. J. and Lee, S. Self-assembly of Ni nanocrystals on HfO_2 and N-assisted Ni confinement for nonvolatile memory application, Appl. Phys. Lett., 86, pp.013107. 2005.

Tang, W., Shi, H., Xu, G., Ong, B. S., Popovic, Z. D., Deng, J., Zhao, J. and Rao, G. Memory effect and negative differential resistance by electrode-induced two-dimensional single-electron tunneling in molecular and organic electronic devices, Adv. Mater., 17, pp.2307-2311. 2005.

Taranekar, P., Huang, C., Fulghum, T. M., Baba, A., Jiang, G., Park, J. Y. and Advincula, R. C. Nanocomposite films of a polyfluorene copolymer and carbazole-thiol-capped gold nanoparticles: Electrochemical crosslinking and energy-transfer properties, Adv. Funct. Mater., 18, pp.347-354. 2008.

Tirrell, M. V. and Katz, A. Self-assembly in materials synthesis, MRS Bulletin, 30, pp.700-701. 2005.

Tiwari, S., Rana, F., Hanafi, H., Hartstein, A., Crabbé, E. F. and Chan, K. A silicon nanocrystals based memory, Appl. Phys. Lett., 68, pp.1377-1379. 1996.

Tomalia, D. A., Baker, H., Dewald, J., Hall, M., Kallos, G., Martin, S., Roeck, J., Ryder, J. and Smith, P. New class of polymers: Starburst-dendritic macromolecules, Polym. J., 17, pp.117-132. 1984.

Tondelier, D., Lmimouni, K., Vuillaume, D., Fery, C. and Haas, G. Metal/organic/metal bistable memory devices, Appl. Phys. Lett., 85, pp.5763-5765. 2004.

Trindade, T., O'Brien, P. and Pickett, N. L. Nanocrystalline semiconductors: Synthesis, properties, and perspectives, Chem. Mater., 13, pp.3843-3858. 2001.

Tseng, J. Y., Cheng, C. W., Wang, S. Y., Wu, T. B., Hsieh, K. Y. and Liu, R. Memory characteristics of Pt nanocrystals self-assembled from reduction of an embedded PtOx ultrathin film in metal-oxide-semiconductor structures, Appl. Phys. Lett., 85, pp.2595-2597. 2004.

Tseng, R. J., Huang, J., Ouyang, J., Kaner, R. B. and Yang, Y. Polyaniline nanofiber/gold nanoparticle nonvolatile memory, Nano Lett., 5, pp.1077-1080. 2005.

Tseng, R. J., Tsai, C., Ma, L., Ouyang, J., Ozkan, C. S. and Yang, Y. Digital memory device based on tobacco mosaic virus conjugated with nanoparticles, Nat. Nanotechnol., 1, pp.72-77. 2006.

Tsoukalas, D., Dimitrakis, P., Kolliopoulou, S. and Normand, P. Recent advances in nanoparticle memories, Mater. Sci. Eng., B, 124-125, pp.93-101. 2005.

Tsoukalas, D. From silicon to organic nanoparticle memory devices, Philos. Trans. R. Soc. London, Ser. A, 367, pp.4169-4179. 2009.

Tsukruk, V. V. Molecular lubricants and glues for micro- and nanodevices, Adv. Mater., 13, pp.95-108. 2001a.

Tsukruk, V. V. Nanocomposite polymer layers for molecular tribology, Tribol. Lett., 10, pp.127-132. 2001b.

Turkevich, J., Stevenson, P. C. and Hillier, J. A study of the nucleation and growth processes in the synthesis of colloidal gold, Discuss. Faraday Soc., 11, pp.55-75. 1951.

Ulman, A. An introduction to ultrathin organic films from Langmuir-Blogett to self-assembly. New York: Academic Press Inc. 1991.

Underwood, S. and Mulvaney, P. Effect of the solution refractive index on the color of gold colloids, Langmuir, 10, pp.3427-3430. 1994.

Wang, Y. Q., Chen, J. H., Yoo, W. J., Yeo, Y. C., Kim, S. J., Gupta, R., Tan, Z. Y. L., Kwong, D. L., Du, A. Y. and Balasubramanian, N. Formation of Ge nanocrystals in HfAlO high-k dielectric and application in memory device, Appl. Phys. Lett., 84, pp.5407-5409. 2004.

Wang, F., Xu, G., Zhang, Z. and Xin, X. Synthesis of monodisperse CdS nanospheres in an inverse microemulsion system formed with a dendritic polyether copolymer, Eur. J. Inorg. Chem., pp.109-114. 2006.

Wanunu, M., Popovitz-Biro, R., Cohen, H., Vaskevich, A. and Rubinstein, I. Coordination-based gold nanoparticle layers, J. Am. Chem. Soc., 127, pp.9207-9215. 2005.

White, M. H., Adams, D. A. and Bu, J. On the go with SONOS, IEEE Circuits Devices Mag., 16, pp.22-31. 2000.

Yang, Y., Ouyang, J., Ma, L., Tseng, R. J. H. and Chu, C. W. Electrical switching and bistability in organic/polymeric thin films and memory devices, Adv. Funct. Mater., 16, pp.1001-1014. 2006.

Yang, F. M., Chang, T. C., Liu, P. T., Chen, U. S., Yeh, P. H., Yu, Y. C., Lin, J. Y., Sze, S. M. and Lou, J. C. Nickel nanocrystals with HfO_2 blocking oxide for nonvolatile memory application, Appl. Phys. Lett., 90, pp.222104. 2007.

Yano, K., Kyogaku, M., Kuroda, R., Shimada, Y., Shido, S., Matsuda, H., Takimoto, K., Albrecht, O., Eguchi, K. and Nakagiri, T. Nanometer scale conductance change in a Langmuir-Blodgett film with the atomic force microscope, Appl. Phys. Lett., 68, pp.188-190. 1996.

Ye, H., Scott, R. W. J. and Crooks, R. M. Synthesis, characterization, and surface immobilization of platinum and palladium nanoparticles encapsulated within amine-terminated poly(amidoamine) dendrimers, Langmuir, 20, pp.2915-2920. 2004.

Ye, H. and Crooks, R. M. Electrocatalytic O_2 reduction at glassy carbon electrodes modified with dendrimer-encapsulated Pt nanoparticles, J. Am. Chem. Soc., 127, pp.4930-4934. 2005.

Yim, S. S., Lee, M. S., Kim, K. S. and Kim, K. B. Formation of Ru nanocrystals by plasma enhanced atomic layer deposition for nonvolatile memory applications, Appl. Phys. Lett., 89, pp.093115. 2006.

Yoo, D., Shiratori, S. S. and Rubner, M. F. Controlling bilayer composition and surface wettability of sequentially adsorbed multilayers of weak polyelectrolytes, Macromolecules, 31, pp.4309-4318. 1998.

Yuan, C. L., Darmawan, P., Setiawan, Y., Lee, P. S. and Ma, J. Formation of $SrTiO_3$ nanocrystals in amorphous Lu_2O_3 high-k gate dielectric for floating gate memory application, Appl. Phys. Lett., 89, pp.043104. 2006.

Zeng, F. and Zimmerman, S. C. Dendrimers in supramolecular chemistry: From molecular recognition to self-assembly, Chem. Rev., 97, pp.1681-1712. 1997.

Zhang, J. H., Li, X. L., Liu, K., Cui, Z. C., Zhang, G., Zhao, B. and Yang, B. Thin films of Ag nanoparticles prepared from the reduction of AgI nanoparticles in self-assembled films, J. Colloid Interface Sci., 255, pp.115-118. 2002.

Zhang, F. and Srinivasan, M. P. Self-assembled molecular films of aminosilanes and their immobilization capacities, Langmuir, 20, pp.2309-2314. 2004.

Zhang, F. and Srinivasan, M. P. Multilayered gold-nanoparticle/polyimide composite thin film through layer-by-layer assembly, Langmuir, 23, pp.10102-10108. 2007.

Zhang, F. and Srinivasan, M. P. Layer-by-layer assembled gold nanoparticle films on amine-terminated substrates, J. Colloid Interface Sci., 319, pp.450-456. 2008.

Zhen, L., Guan, W., Shang, L., Liu, M. and Liu, G. Organic thin-film transistor memory with gold nanocrystals embedded in polyimide gate dielectric, J. Phys. D: Appl. Phys., 41, 2008.

Zhuravlev, L. T. Concentration of hydroxyl groups on the surface of amorphous silicas, Langmuir, 3, pp.316-318. 1987.

APPENDIX

Publications during Ph.D. Work

1) **Raju Kumar Gupta**, R. Dharmarajan and M. P. Srinivasan "Synthesis of 16-Mercaptohexadecanoic acid capped gold nanoparticles and their immobilization on a substrate" manuscript under review.

2) **Raju Kumar Gupta**, Damar Yoga Kusuma, P. S. Lee and M. P. Srinivasan "Covalent assembly of gold nanoparticles for nonvolatile memory applications" manuscript under review.

3) **Raju Kumar Gupta**, S. Krishnamoorthy, Damar Yoga Kusuma, P. S. Lee and M. P. Srinivasan "Enhancing charge-storage capacity of non-volatile memory device using template-directed assembly of gold nanoparticles" manuscript under review.

4) **Raju Kumar Gupta,** Damar Yoga Kusuma, P. S. Lee and M. P. Srinivasan "Copper nanoparticles embedded in a polyimide film for nonvolatile memory applications" manuscript under review.

5) **Raju Kumar Gupta**, Damar Yoga Kusuma, P. S. Lee and M. P. Srinivasan "Langmuir−Blodgett assembly of 4-methylbenzenethiol functionalized gold nanoparticles for nonvolatile memory applications" manuscript submitted.

6) **Raju Kumar Gupta** and M. P. Srinivasan "Controlled multilayer assembly of gold nanoparticle-polymer composite films through combination of covalent and electrostatic binding" manuscript submitted.

7) **Raju Kumar Gupta** and M. P. Srinivasan "Covalently bound ultrathin polymeric films: An improvement to wear life of the PFPE polymer" manuscript to be submitted.

Conference Presentations during Ph.D. Work

1) Raju Kumar Gupta, P.S. Lee, Damar Yoga Kusuma and **M. P. Srinivasan** "Covalent molecular assembly of gold nanoparticles for nonvolatile memory applications" American Institute of Chemical Engineers (AIChE) 2009 Annual Meeting, November 2009, Nashville, TN, USA.

2) **Raju Kumar Gupta** and M. P. Srinivasan "Covalent multilayer assembly of polymers on silicon with molecular thickness control", 1st Nano Today Conference (Nano Today 2009), August 2009, Biopolis, Singapore.

3) **Raju Kumar Gupta** and M. P. Srinivasan "Controlled multilayer assembly of gold nanoparticle-polymer composite films through combination of covalent and electrostatic binding", 1st Nano Today Conference (Nano Today 2009), August 2009, Biopolis, Singapore.

4) **R. K. Gupta**, D. Y. Kusuma, P. S. Lee, D. Rajarathnam and M. P. Srinivasan "Langmuir−Blodgett film deposition of 4-methylbenzenethiol functionalized gold nanoparticles for nonvolatile memory applications" International conference on materials for advanced applications (ICMAT 2009), July, 2009, Suntec City, Singapore.

5) **Raju Kumar Gupta** and M. P. Srinivasan "Synthesis of short chain thiol capped Au nanoparticles and their stabilization", American Institute of Chemical Engineers (AIChE) 2008 Annual Meeting, November 2008, Philadelphia, USA.

6) **Raju Kumar Gupta** and M. P. Srinivasan "Synthesis of thiol capped gold nanoparticles and their immobilization on a substrate" Asian Conference on Nanoscience and Nanotechnology (AsiaNano 2008), November 2008, Biopolis, Singapore.